THE POWER OF PEROVSKITES: ADVANCING CERAMIC ELECTROCHEMICAL CELL TECHNOLOGY WITH NOVEL CATHODE MATERIALS FOR CLEAN ENERGY

BELLO IDRIS TEMITOPE

PhD

The Hong Kong Polytechnic University

2023

The Hong Kong Polytechnic University

Department of Building and Real Estate

The Power of Perovskites: Advancing Ceramic Electrochemical Cell Technology with Novel Cathode Materials for Clean Energy

BELLO Idris Temitope

A thesis submitted in partial fulfillment of the requirements for the degree of Doctor of Philosophy

June 2023

CERTIFICATE OF ORIGINALITY

I hereby declare that this thesis is my own work and that, to the best of my knowledge and belief, it reproduces no material previously published or written, nor material that has been accepted for the award of another degree or diploma, except where due acknowledgment has been made in the text.

_____________________ (Signed)

Idris Temitope Bello (Name of Student)

DEDICATION

I dedicate this work to my creator ﷲ and then to the memory of my late mother, Mrs. Ganiyat Olabisi Olagunju. Her sacrifices, love, and care have been a constant source of inspiration and motivation throughout my life. I am grateful for the lessons she taught me and the values she instilled in me. Her memory will always be with me.

ABSTRACT

Perovskites have emerged as a promising class of materials for use as cathodes in ceramic electrochemical cells (CECs), which offer a clean and efficient means of energy conversion. The conventional CECs have operated at elevated temperatures (800 – 1000 ^{o}C), which has resulted in rapid material degradation and poor stability, impeding their commercial viability. Reducing the operating temperatures of CECs to 450 – 650 ^{o}C has therefore been proposed as a potential solution. Still, it has often led to suboptimal electrocatalytic reactions at the cathode, necessitating further research and development efforts to overcome them.

Therefore, this research aimed to enhance the oxygen reduction reaction (ORR) kinetics and stability of cathode materials for CECs, focusing on solid oxide fuel cells (SOFCs) and protonic ceramic fuel cells (PCFCs) at reduced operating temperatures (450 – 650 ^{o}C). The objectives of this study were to: - examine the structure-function relationship between lattice strain and ORR activity/CO_2 tolerance in ABO_3 perovskite-based cathodes; - evaluate self-assembly engineering as a viable cathode material developmental strategy in comparison to state-of-the-art methods; and - understand the electrokinetic triple ionic and electronic conductivity (TIEC) dynamics in self-assembled cathodes that enabled their superior performance using electrical conductivity relaxation (ECR) and protonation enthalpy. The present study addressed these objectives to improve the performance and viability of CECs as a clean and sustainable energy generation technology.

The first research objective was accomplished by applying lattice engineering to improve the ORR and CO_2 tolerance of $Ba_{0.5}Sr_{0.5}Co_{0.7}Fe_{0.3}O_{3-\delta}$ (BSCF) functional material for intermediate temperature SOFCs. The introduction of copper-transition metal (Cu-TM) and zinc-transition

metal (Zn-TM) caused a contraction and expansion in the lattice of the BSCF, respectively. Enhanced catalytic ORR and CO_2 tolerance were also correlated with lattice contraction, which was attributed to the shortened pathway for oxygen mobility in the lattice of BSCF and the weakened adsorption energy of the constitutive reactive intermediates. The BSCFC5 cathode, in which lattice contraction occurred, demonstrated the best performance with an area-specific resistance (ASR) of 0.0247 Ω cm^2 and an exceptional peak power density (PPD) of 1715 mW cm^{-2} at 650 ℃ for symmetrical and single cells, respectively. In addition, the material displayed enhanced tolerance to CO_2 infusion, with good recoverability when switched intermittently between pure air and 10-vol% CO_2 infusions for 100 hours. The findings conclude that Cu-TM-doped BSCF (BSCFC5) is a superior substitute for BSCF material in SOFC applications.

The second research objective was actualized by developing a thermodynamically stable self-assembled nanocomposite cathode material with a unique composition $BaCo_{0.5}Ce_{0.3}Fe_{0.1}Yb_{0.1}O_{3-\delta}$ (BCCFYb). Upon calcination, the precursor material separates into a host cubic and ancillary rhombohedral phase. The performance of the TIEC ($O^{2-}/H^+/e^-$) BCCFYb was compared to that of cobalt-rich oxide-ion and electron (O^{2-}/e^-) conducting $BaCo_{0.833}Yb_{0.167}O_{3-\delta}$ (BCYb), cerium-rich proton and electronic (H^+/e^-) conducting $BaCe_{0.75}Fe_{0.25}O_{3-\delta}$ (BCF), and Co-Ce-rich triple ionic and electronic ($O^{2-}/H^+/e^-$) conducting $BaCo_{0.833}Yb_{0.167}O_{3-\delta}$ - $BaCe_{0.75}Fe_{0.25}O_{3-\delta}$ (BCYb-BCF) traditional composite materials. The BCCFYb demonstrates a low TEC, good operational stability, and superior cathodic performance in oxygen ion- and proton-conducting ceramic fuel cell (CFC) modes, making tailored self-assembly engineering a promising cathode material developmental method for CFCs.

In the final objective, the electrokinetic phenomena in a self-assembled cathode material were investigated. A low-cobalt-content self-assembled cubic-rhombohedral TIEC nanocomposite cathode material with the composition $BaCe_{0.4}Co_{0.4}Fe_{0.1}Zr_{0.1}O_{3-\delta}$ (BCCFZ) was synthesized for this purpose. The proton conduction mechanisms of the material were elucidated via hydrogenation and hydration reactions using the ECR method. The BCCFZ exhibited good TIEC properties with a low protonation enthalpy of -30 ± 9 kJ/mol compared to state-of-the-art proton-conducting materials. The material's high cerium and low cobalt content also contributed to its low thermal expansion coefficient (TEC) of 9.6×10^{-6} K^{-1}. The PPD of the anode-supported single cell based on a BCCFZ air electrode reached 1054 mW cm^{-2} at 650 ^{o}C, and the material demonstrated good operational stability over 500 h at 550 ^{o}C. The findings from this study suggest that low enthalpy enabled enhanced proton uptake, and the synergistic phases enabled improved TIEC and low TEC, providing valuable insights as to how tailored self-assembly engineering can revolutionize PCFC cathode material development.

The present study has made significant contributions to the discipline of CEC technology, theoretically and practically. The research outcomes have provided valuable insights, practical strategies, and recommendations for addressing the limitations of current CECs. The results of this investigation will be crucial in improving the performance and viability of CECs as a clean energy generation technology, both regionally and globally. To sum up, the findings of this study have the potential to significantly advance the field through the development of innovative cathode materials for clean energy generation.

LIST OF RESEARCH PUBLICATIONS

1. **Bello, I. T**., Taiwo, R., Esan, O. C., Adegoke, A. H., Ijaola, A., Li, Z., Zhao, S., Chen, W., Shao, Z., & Ni, M. (2023). AI-enabled materials discovery for advanced ceramic electrochemical cells. *Energy and AI*, 100317. https://doi.org/10.1016/j.egyai.2023.100317

2. **Bello, I.T.,** Guan, D., Yu, N., Li, Z., Song, Y., Chen, X., Zhao, S., He, Q., Shao, Z., & Ni, M. (2023). Revolutionizing material design for protonic ceramic fuel cells: Bridging the limitations of conventional experimental screening and machine learning methods. *Chemical Engineering Journal (Lausanne, Switzerland: 1996)*, *477*(147098), 147098. https://doi.org/10.1016/j.cej.2023.147098

3. **Bello, I.T**., Song, Y., Yu, N., Li, Z., Zhao, S., Maradesa, A., Liu, T., Shao, Z., & Ni, M. (2023). Evaluation of the electrocatalytic performance of a novel nanocomposite cathode material for ceramic fuel cells. *Journal of Power Sources*, 560(232722), 232722. https://doi.org/10.1016/j.jpowsour.2023.232722

4. **Bello, I.T.**, Yu, N., Song, Y., Wang, J., Chan, T.-S., Zhao, S., Li, Z., Dai, Y., Yu, J., & Ni, M. (2022). Electrokinetic insights into the triple ionic and electronic conductivity of a novel nanocomposite functional material for protonic ceramic fuel cells. *Small*, 18(40), e2203207. https://doi.org/10.1002/smll.202203207

5. **Bello, I. T.,** Yu, N., Zhai, S., Song, Y., Zhao, S., Cheng, C., Zhang, Z., & Ni, M. (2022). Effect of engineered lattice contraction and expansion on the performance and CO2 tolerance of Ba0.5Sr0.5Co0.7Fe0.3O3-δ functional material for intermediate temperature solid oxide fuel cells. *Ceramics International*, *48*(15), 21416–21427. https://doi.org/10.1016/j.ceramint.2022.04.110

6. **Bello, I.T.**, Zhai, S., He, Q., Cheng, C., Dai, Y., Chen, B., Zhang, Y., & Ni, M. (2022). Materials development and prospective for protonic ceramic fuel cells. *International Journal of Energy Research*, 46(3), 2212–2240. https://doi.org/10.1002/er.7371

7. **Bello, I.T.**, Zhai, S., He, Q., Xu, Q., & Ni, M. (2021). Scientometric review of advancements in the development of high-performance cathode for low and intermediate temperature solid oxide fuel cells: Three decades in retrospect. *International Journal of Hydrogen Energy*, 46(52), 26518–26536. https://doi.org/10.1016/j.ijhydene.2021.05.134

8. **Bello, I.T.**, Zhai, S., Zhao, S., Li, Z., Yu, N., & Ni, M. (2021). Scientometric review of proton-conducting solid oxide fuel cells. *International Journal of Hydrogen Energy*, 46(75), 37406–37428. https://doi.org/10.1016/j.ijhydene.2021.09.061

9. Li, Z., **Bello, I. T.,** Wang, C., Yu, N., Chen, X., Zheng, K., & Ni, M. (2023). Revealing interactions between the operating parameters of protonic ceramic electrolysis cell: A modelling study. *Applied Energy*, *351*(121886), 121886. https://doi:10.1016/j.apenergy.2023.121886

10. Jolaoso, L. A., **Bello, I. T.,** Ojelade, O. A., Yousuf, A., Duan, C., & Kazempoor, P. (2023). Operational and scaling-up barriers of SOEC and mitigation strategies to boost H2 production- a comprehensive review. *International Journal of Hydrogen Energy*. https://doi.org/10.1016/j.ijhydene.2023.05.077

11. Chen, X., Yu, N., **Bello, I. T.,** Guan, D., Li, Z., Liu, T., … Ni, M. (2023). Facile anion engineering: A pathway to realizing enhanced triple conductivity in oxygen electrodes for reversible protonic ceramic electrochemical cells. *Energy Storage Materials*, (103056), 103056. doi:10.1016/j.ensm.2023.103056

12. He, Q., Li, Z., **Bello, I. T.,** Xu, Q., Xia, L., Wang, C., Zhao, S., Zhao, T., & Ni, M. (2023). A comprehensive modelling study of all vanadium redox flow battery: Revealing the combined effects of electrode structure and surface property. *Journal of Energy Storage*, *66*(107427), 107427. https://doi.org/10.1016/j.est.2023.107427

13. Chen X, Yu N, **Bello I.T**, Zhang D, et al. Understanding the oxygen reduction reaction in the hierarchically oriented composite cathode with open, straight pores. *Sep Purif Technology*. 2023;(124713):124713. http://dx.doi.org/10.1016/j.seppur.2023.124713

14. Li, Z., Wang, C., **Bello, I. T.,** Guo, M., Yu, N., Zhu, M., & Ni, M. (2023). Direct ammonia protonic ceramic fuel cell: A modelling study based on elementary reaction kinetics. *Journal of Power Sources*, 556(232505), 232505. https://doi.org/10.1016/j.jpowsour.2022.232505

15. Li, Z., He, Q., Wang, C., Yu, N., **Bello, I. T.,** Guo, M., & Ni, M. (2023). Protonic ceramic fuel cells for power-ethylene cogeneration: A modelling study on structural parameters. *Energy (Oxford, England)*, 264(126193), 126193. https://doi.org/10.1016/j.energy.2022.126193

16. Zhao, S., Liu, T., Wang, J., **Bello, I. T.,**., Zuo, Y., Wei, M., Wang, K., Lau, K. K. S., & Ni, M. (2022). Anti-CO2 strategies for extending Zinc-Air Batteries' Lifetime: A review. *Chemical Engineering Journal* (Lausanne, Switzerland: 1996), 450(138207), 138207. https://doi.org/10.1016/j.cej.2022.138207

17. Zhao, S., Liu, T., Wang, Y., Guo, Z., **Bello, I. T.,** He, Q., Zuo, Y., Wei, M., & Ni, M. (2023). Innovating rechargeable Zn-air batteries for low charging voltage and high energy efficiency. *Energy & Fuels*: An American Chemical Society Journal, 37(2), 1414–1420. https://doi.org/10.1021/acs.energyfuels.2c04025

18. Xu, Q., Guo, Z., Xia, L., He, Q., Li, Z., **Bello, I. T.,**., Zheng, K., & Ni, M. (2022). A comprehensive review of solid oxide fuel cells operating on various promising alternative fuels. *Energy Conversion and Management*, 253(115175), 115175. https://doi.org/10.1016/j.enconman.2021.115175
19. Cheng, C., Wang, S., Wu, Y., **Bello, I. T.,** Dai, Y., Cheng, R., Zhai, S., Wang, Y., Feng, S.-P., & Ni, M. (2021). Thermally regenerative CO_2-induced pH-gradient cell for waste-to-energy conversion. *ACS Energy Letters*, *6*(9), 3221–3227. https://doi.org/10.1021/acsenergylett.1c01000

20. Wang C, Li Z, Guan D, Zhu M, **Bello I.T.,** Han M, et al. Glycerol-assisted co-electrolysis in solid oxide electrolyzer cell (SOEC) for green syngas production: A 2D modelling study. Fuel (Lond). 2023;353(129227):129227. https:// doi:10.1016/j.fuel.2023.129227

21. Li, Z., He, Q., Wang, C., Xu, Q., Guo, M., **Bello, I. T**., & Ni, M. (2022). Ethylene and power cogeneration from proton ceramic fuel cells (PCFC): A thermo-electrochemical modelling study. *Journal of Power Sources*, 536(231503), 231503. https://doi.org/10.1016/j.jpowsour.2022.231503

22. Zhao, S., Liu, T., Dai, Y., Wang, J., Wang, Y., Guo, Z., Yu, J., **Bello, I. T**., & Ni, M. (2023). Pt/C as a bifunctional ORR/iodide oxidation reaction (IOR) catalyst for Zn-air batteries with unprecedentedly high energy efficiency of 76.5%. *Applied Catalysis. B, Environmental*, 320(121992), 121992. https://doi.org/10.1016/j.apcatb.2022.121992

Refereed Conference Paper

Bello, I.T., Ni, M. (2023) Exploring the Conductivity Landscape of Notable Ceramic Electrolytes Under Varying Ambient Conditions. Proceedings of the 15th International Green Energy Conference (IGEC2023-057), 10-13 July 2023, Glasgow, UK.

Honors and Awards

1. **People's Choice Award** at the inaugural PolyU 3MT® Competition organized by the PolyU English Language Centre held at the N003 hall in The Hong Kong Polytechnic University on the 30th of June 2023.

2. **Best Oral Presentation Award** at the International Graduate Student Academic Forum hosted by the China University of Mining and Technology and The Hong Kong Polytechnic University in April 2023.

ACKNOWLEDGEMENTS

"*Then which of the Blessings of your Lord will you both (jinn and men) deny?*" Q55:30. I express my profound gratitude to Almighty Allah for His enormous blessings, granting me the respite to be alive in good health and state of mind to pursue and complete this Ph.D. thesis. I extend my heartfelt appreciation to my chief supervisor, Professor Meng Ni, for his unflagging support, guidance, and expertise throughout my research journey. As a remarkable mentor and role model, he has displayed exceptional kindness and professionalism, and I am grateful for his invaluable contributions to my academic and personal growth. I also appreciate my co-supervisors, including Professor Michael Yam and Dr. Shao-Yuan Leu for their support and assistance. I am grateful to Professor Zongping Shao for his mentorship and contributions during my PhD research sojourn. His expertise and guidance have been very helpful.

I appreciate our highly remarkable research group members for their cooperation and valuable contributions. They were like a family who were always willing to help in whatever way they could. I particularly thank LI Zheng, ZHAO Siyuan, HE Qijiao, YU Na, WANG Chen, CHEN Xi, Dr. SONG Yufei, and Dr. GUAN Daqin for their kind help. Indeed, their support and expertise have been highly instrumental throughout my PhD sojourn. I also acknowledge and appreciate the efforts of Ms. Shing Chloe, Mr. K.K Cheong, Mr. Ken and other administrative members from the Department of Building and Real Estate for their help and assistance. I am eternally grateful for your help and professionalism.

I sincerely thank my family members, including my father, Mr. Tajudeen Orimolade Bello, siblings; Aishat, Abdulmaleek, Nafisah, and Khaleelullah, wife; Sulehat Hamzat, and daughters; Merriam-Al-Batool and Basma, for their unwavering understanding, empathy, and encouragement

throughout my research. Their love and support have played an essential role in enabling me to maintain a healthy mind and spirit. I also express my profound gratitude to all my friends, who have significantly uplifted me and supported me extraordinarily, especially Dr. Mujeeb Adeagbo and Dr. Saka Abdullah. Thank you very much for your brotherly care and love.

I express my sincere gratitude to the Research Institute for Sustainable Urban Development (RISUD), Building and Real Estate Department, and The Hong Kong Polytechnic University for providing me with financial support and a conducive research environment. I am also profoundly grateful to all the individuals who aided and encouraged me throughout my research sojourn. Your invaluable contributions have played a critical role in the success of this intellectual journey.

Finally, I thank my board of examiners, comprising the BOE chair, Professor Liang AN, and the examiners; Professor Hailei ZHAO and Professor Ming CHEN, for accepting to partake in my thesis examination and offering valuable feedback. Thank you very much for your kind support.

TABLE OF CONTENTS

LIST OF FIGURES

LIST OF TABLES

LIST OF ABBREVIATIONS

ASR – Area specific resistance

CEC – Ceramic electrochemical cells

CFC – Ceramic fuel cells

MIEC – Mixed ionic and electronic conductivity

PCEC – Protonic electrolysis cell

PCFC – Protonic ceramic fuel cell

PPD – Peak power density

P-SOFC – Proton conducting solid oxide fuel cells

RePCC – Reversible protonic ceramic cell

RSOC – Reversible solid oxide cells

SOEC – Solid oxide electrolysis cell

SOFC – Solid oxide fuel cell

TEC – Thermal expansion coefficient

TIEC – Triple ionic and electronic conductivity

TM – Transition metals

CHAPTER 1: INTRODUCTION

1.1 Chapter Overview

This chapter provides a detailed account of the research background and motivation that underlie the study. The chapter outlines the research scope and objectives, elucidating the specific research themes to be addressed in the following chapters. Moreover, it explicates the research significance by situating the current study within the larger context of the field and highlighting its potential contributions to advancing knowledge in solid-state electrochemical power generation technologies. The chapter ends by summarizing the structure and contents of the thesis, giving readers an idea of what to expect in the upcoming chapters.

1.2 Background

Since 1965, global energy consumption has increased exponentially and exceeded 160,000 TWh across all energy sources, as reported in the BP Statistical World Energy Review 2020[1]. The surging energy demand is primarily attributed to the growing global population, contemporary urbanization, industrialization, and technological advancements[2]. The principal source of global energy consumption remains fossil fuels, which, being non-renewable, generate greenhouse gas (GHG) emissions that adversely affect the environment, including climate change and respiratory diseases[3]. This detrimental impact of fossil fuels calls for alternative and sustainable energy sources that are clean and safe. Efforts have been made to find alternative energy sources, including solar, wind, geothermal, tidal, and biomass, to mitigate the damage caused by fossil fuels [4,5]. However, these sources have inherent limitations that restrict their use to specific locations, seasons, and times [6]. Therefore, the need for more efficient, cleaner, and safer energy solutions without traditional energy sources' limitations is pressing. Fuel cells could address these limitations, being a promising and emerging energy conversion technology [7]. Fuel cells have the potential to offer clean, efficient, and safe energy, making them a viable option in the quest for sustainable energy.

A fuel cell generates electricity through the direct electrochemical conversion of chemical energy in fuels, such as hydrogen, alcohols, and hydrocarbons, into electrical energy with high efficiency and low emissions [8]. Fuel cells have a higher electricity generation efficiency than traditional thermal power plants because they are not limited by the Carnot cycle [7]. There are various types of fuel cells, which are distinguished by the type of application, electrolyte material used and the operating temperature. **Table 1.1** illustrates the different types of fuel cells in existence.

Table 1.1: Fuel cell varieties and their distinct features.

Fuel Cell	Electrolyte	Operation Temperature	Power Output	Efficiency	Catalyst	Ref.
Alkaline fuel cell	Potassium hydroxide	60 – 120℃	10 kW – 100 kW	35 – 70 %	Platinum	[9,10]
Phosphoric acid fuel cell	Phosphoric acid	150 – 200℃	< 200 kW	40 – 80 %	Platinum	[11]
Proton exchange membrane fuel cell	Polymer membrane	50 – 80℃	50 – 250 kW	40 – 50 %	Platinum	[12,13]
Direct Methanol Fuel Cell	Polymer membrane	50 – 130℃	< 1 kW	20 - 55 %	Platinum	[14]
Molten carbonate fuel cell	Molten lithium or potassium carbonate	≈ 650℃	10 kW – 2 MW	60 – 80 %	Nickel	[15]
Solid oxide fuel cell	Ceramics	500 – 1000℃	kW - MW	> 60 %	Nickel and Perovskites	[16–19]

Among the various types of fuel cells, SOFC stands out in terms of its fuel flexibility, high energy efficiency, low emission, and relatively low cost [7]. Moreover, SOFCs are most suited for stationary power applications, unlike the PEMFCs (polymer electrolyte membrane fuel cells) which are more promising for portable applications [20]. Previously developed SOFCs were high-temperature energy conversion systems operating in the temperature range of 800-1000℃ designed for distributed and centralized power generation in residential buildings and offices. The high operating temperature was designed to promote oxide ion conduction across the solid ceramic electrolyte, thereby increasing the ORR reaction kinetics at the air electrode. However, the high operating temperature has a negative impact on the durability and stability of the cell components [21]. Furthermore, this high operating temperature leads to a continuous decrease in the energy efficiency of the cell from a thermodynamic perspective, as well as an increase in the manufacturing and maintenance cost of the cells due to their rapid degradation [8]. Addressing these issues necessitates developing SOFCs that can operate efficiently at intermediate to low temperatures (usually 300-700℃) [18,21–28]. However, reducing the operating temperatures of SOFCs unavoidably decreases the reaction kinetics of the electrodes and the ionic conductivity in the electrolyte, causing higher overpotential losses. Therefore, measures must be put in place to cushion the effects of the sluggishness of the reaction kinetics at intermediate to low temperatures through the design and proper selection of air electrode materials. The selected materials also have to significantly resist the ohmic losses in the electrolyte and the activation and concentration losses in the cathode [29].

1.3 Research Scope and Objectives

This research aims to explore strategies to enhance the electrocatalytic ORR kinetics of functional cathode materials for ceramic electrochemical fuel cells at reduced operating temperatures (450 – 650 ^{o}C). The specific objectives of this research are as follows:

a. To investigate the effects of lattice engineering (i.e., lattice expansion and contraction) on the electrocatalytic performance and CO_2 tolerance of an established functional cathode material (i.e., $Ba_{0.5}Sr_{0.5}Co_{0.7}Fe_{0.3}O_{3-\delta}$) for intermediate temperature SOFC applications.

b. To investigate how self-assembly nanocomposite engineering affects the TIEC and power output in CFCs, in contrast to the traditional composite and single-phase cathodes.

c. To understand the electrokinetic TIEC mechanisms of cathode materials developed via self-assembly engineering using the ECR and protonation enthalpy.

1.4 Research Significance

This research addresses the limitations of CECs and explores practical ways air electrodes can operate efficiently at reduced temperatures (450 – 650 ^{o}C). The goal is to decrease system start-up time and material degradation and improve operation performance, stability, durability, and efficiency. This research highlighted how novel lattice-engineered contraction and self-assembly nanocomposite engineering can enhance the functionalities of air electrode materials for CFCs. This research contributes to developing clean and efficient energy generation technology, reducing the dependence on non-renewable fossil fuels, and decreasing GHG emissions. This research also has the potential to contribute to the advancement of sustainable energy solutions for various sectors, such as industry and residential.

1.5 Report structure

This thesis is structured into six chapters. **Chapter 1** gives the essential background and challenges in developing air electrode materials for ceramic electrochemical cells. The aim and objectives of the research are clearly highlighted. The significance of the research is also summarized.

Chapter 2 provides a detailed fundamental of CFC technology, highlighting the principles and operation of SOFCs, and how cathode materials play a vital role in the operation of CFCs at reduced temperatures. The chapter thoroughly and systematically examines the electrolyte, cathode, and anode, covering their operational and reaction mechanisms, material classes, synthesis and fabrication methods, performance and stability improvement strategies. Notably, the chapter emphasizes that the design of PCFC cathode materials requires careful consideration of their TIEC, distinguishing them from traditional SOFCs.

Chapter 3 offers a comprehensive summary of the methodology utilized in developing cathode materials tailored for CECs optimized for operation at intermediate and low temperatures. The synthesis process involved the application of the EDTA-citric acid complexing sol-gel method. The chapter presents detailed procedures for fabricating symmetrical cells and anode-supported single cells, encompassing crucial steps such as pressing, sintering, and the application of cathode slurries. Furthermore, the chapter elucidates the procedure for conducting electrochemical measurements. This comprehensive overview of the methodology serves as a foundation for subsequent chapters, establishing the groundwork for further investigations and analyses.

Chapter 4 investigates the effects of lattice engineering on the electrocatalytic performance and CO_2 tolerance of an established functional cathode material, $Ba_{0.5}Sr_{0.5}Co_{0.7}Fe_{0.3}O_{3-\delta}$, for intermediate-temperature SOFC applications. This study entails expanding and contracting the lattice structure of the material to observe its impact on the material's electrocatalytic activity.

Chapter 5 evaluates the performance of a novel self-assembled cathode material, $BaCo_{0.5}Ce_{0.3}Fe_{0.1}Yb_{0.1}O_{3-\delta}$ (BCCFYb), for potential use in ceramic fuel cells, SOFCs, and PCFCs. The performance of the BCCFYb was compared with other novel cathode materials, including cobalt-rich oxide-ion and electron-conducting $BaCo_{0.833}Yb_{0.167}O_{3-\delta}$ (BCYb), cerium-rich proton and electron-conducting $BaCe_{0.75}Fe_{0.25}O_{3-\delta}$ (BCF), and cobalt-cerium-rich triple ionic-conducting $BaCo_{0.833}Yb_{0.167}O_{3-\delta}$ - $BaCe_{0.75}Fe_{0.25}O_{3-\delta}$ (BCYb-BCF).

Chapter 6 focuses on the development and evaluation of a novel cathode material, $Ba(CeCo)_{0.4}(FeZr)_{0.1}O_{3-\delta}$ (BCCFZ), for use in PCFCs. The material was designed through a self-assembly engineering process and consisted of a mixed ionic and electronic conducting phase (M-BCCFZ) and a dominant proton-conducting phase (H-BCCFZ). The electrokinetic phenomena that enabled superior TIEC were thoroughly discussed.

Chapter 7 comprehensively summarizes the key findings, the research significance and contributions, and the limitations encountered during the research process. The chapter serves as an opportunity to reflect on the research outcomes and offers recommendations for future studies in low-temperature operating ceramic fuel cell technology.

1.6 Chapter Summary

This chapter laid the groundwork for the research by providing a comprehensive overview of the background, research aim, objectives, and significance. The chapter identified the problems faced by the research topic's practical and theoretical aspects. Moreover, it highlighted the contributions the study aims to contribute to the field. The structure of the thesis was also outlined, and the chapter established the knowledge gap that the research objectives aim to address. The subsequent chapter will delve into the relevant literature review, which is integral to achieving the research objectives.

CHAPTER 2: LITERATURE REVIEW[1]

2.1 Background

Building upon the foundation established in the previous chapter this chapter provides a detailed review of the current state of CFCs, with a specific focus on perovskite oxide cathode materials, their operational mechanisms, and their practical limitations. This review is intended to provide a comprehensive understanding of the current research landscape and serve as a critical basis for developing novel electrode materials that can enhance the efficiency and practicality of CFCs.

2.2 Fundamentals of ceramic fuel cells

Ceramic fuel cells (CFCs), popularly referred to as SOFCs, are an up-and-coming class of solid-state electrochemical power generation technologies that can convert chemical energy directly into electrical energy in the presence of air and a continuous supply of fuel [30]. The development of SOFCs can be traced back to 1937, when Baur and Preis first demonstrated a fuel cell utilizing a solid ceramic electrolyte [30]. Since then, extensive research on SOFCs has been conducted to advance the technology. Early-generation SOFCs primarily conduct oxide ions in their electrolytes and require high operating temperatures

---

[1] This chapter primarily draws from the following published journal papers:

Bello IT, Zhai S, He Q, Xu Q, Ni M. Scientometric review of advancements in the development of high-performance cathode for low and intermediate temperature solid oxide fuel cells: Three decades in retrospect. International Journal of Hydrogen Energy. 2021 Jul 29;46(52):26518-36.

Bello IT, Zhai S, Zhao S, Li Z, Yu N, Ni M. Scientometric review of proton-conducting solid oxide fuel cells. International Journal of Hydrogen Energy. 2021 Oct 29;46(75):37406-28.

Bello IT, Zhai S, He Q, et al. Materials development and prospective for protonic ceramic fuel cells. Int J Energy Res. 2021; 1-29. doi:10.1002/er.7371 ranging between 800-1000 ℃ to achieve sufficient ionic conductivity. This high temperature requirement generates residual heat during operation, which can be efficiently utilized through integration with a gas turbine or as thermal energy in cogeneration[30]. Furthermore, SOFCs have the advantages of minimal maintenance costs, compatibility with multiple fuels, and modular design, making them an attractive alternative to conventional thermal power plants [21,31,32].

2.2.1 Principles and operation of SOFCs

SOFCs consist of three major components: the anode, cathode, and electrolyte, as illustrated in **Figure 2.1**. Electrons from the anode react with oxygen at the cathode to produce oxide ions, which are transported through the dense ion-conducting electrolyte to the anode side [cathode reaction: $4e^{-} + O_2 \rightarrow 2O^{2-}$]. At the anode, the oxygen ions combine with fuel, such as hydrogen, to generate steam and electrons that flow to the cathode through an external circuit, producing usable electricity [anode reaction: $2H_2 + 2O^{2-} \rightarrow 2H_2O + 4e^{-}$] [30]. The overall reaction of the system will then be $2H_2 + O_2 \rightarrow 2H_2O$.

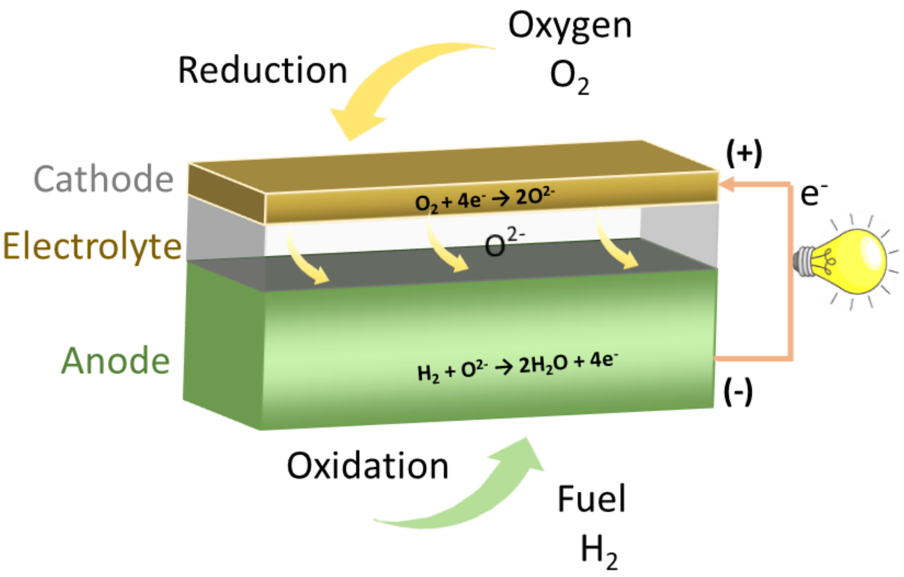

Figure 2.1: Operation of a solid oxide fuel cell.

A significant characteristic of SOFCs is that the ORR kinetics in the cathode are relatively fast, resulting in a lower activation voltage loss, eliminating the need for any noble metals as a catalyst. Moreover, since the operating temperature of SOFCs is high (800-1000°C), the water produced at the anode where hydrogen is supplied as the reactant exists as vapor and does not cause mass transfer loss. This differs from low-temperature fuel cells, such as PEMFCs, where water management is crucial to prevent either drying or flooding of the membrane [30].

2.2.2 Issues associated with high-temperature operating SOFCs

Early-generation SOFCs were primarily designed to conduct oxide ions in their electrolytes, which necessitated high operating temperatures between 800-1000 ℃ to achieve sufficient ionic conductivity[33]. However, such elevated temperatures can result in complicated thermal management and jeopardize the cell's durability due to mismatched thermal expansion coefficients between its components, which may lead to structural and chemical degradation over time [33–

35]. Also, the associated cost due to their high operating temperature is exorbitant considering the rapid rate of component materials degradation, and the incorporation of thermal management systems further raises the cost and impracticality of commercializing this emerging technology[21]. Therefore, recent efforts have been focused on developing SOFCs with lower operating temperatures between 300-600 ℃ to reduce costs, system start-up and shutdown time, and increase the cell's lifetime[36].

2.2.3 Intermediate to low-temperature operating SOFCs

Developing novel electrolyte and electrode materials that can operate effectively at an intermediate or low temperature is crucial to address the limitations of high-temperature SOFCs [26,37–44]. However, lowering the temperature of SOFCs causes high overpotential losses due to the electrolyte's lower ionic conductivity and the significantly reduced electrodes' electrocatalytic activity[45]. Thus, developing novel electrolyte and electrode materials that can operate effectively at an intermediate or low temperature is crucial[18,21–28].

One approach to reducing the ohmic loss of the electrolyte is to utilize alternative materials with high ionic conductivity or to decrease the thickness of the electrolyte, as the ohmic loss is directly proportional to the thickness [21,46]. In addition, improving the cathode through developing new materials with high electrocatalytic activity, optimizing the cathode thickness, or utilizing nanostructured cathodes to increase the surface area and facilitate the ORR can help overcome the activation loss at the cathode and enhance SOFC performance at lower operating temperatures.

For instance, SOFCs with yttria-stabilized zirconia (YSZ) electrolytes that are thick and have a lanthanum strontium manganite (LSM) cathode have demonstrated low power density at intermediate temperatures due to increased polarization resistance (Rp) and ohmic resistance (Ro) of the electrolyte[21,46]. However, utilizing thin film electrolytes for YSZ and doped ceria-based electrolytes, such as Samarium doped Ceria (SDC) and Gadolinium doped Ceria (GDC), has reduced the ohmic resistance to an acceptable level at temperatures ranging from 700 to 550 ℃ [47–49]. Thus, such advancements can enable the development of intermediate and low-temperature operating SOFCs with improved performance[22,47,50–53].

In the preliminary stages of SOFC development, cathodes with high electronic conductivity were necessary to facilitate the exchange reactions at the triple-phase boundary (TPB) between the electrode, electrolyte, and oxidant [33]. Lanthanum strontium-doped manganite (LSM) was commonly used (for the high-temperature operating SOFCs) as cathode material due to its good electronic conductivity and activity toward oxygen reduction reaction (ORR)[63]. However, intermediate to low-temperature operating SOFCs have a more stringent requirement. The cathode materials require mixed ionic and electronic conducting (MIECs) properties to facilitate the extension of the electrochemical reaction region from the TPB to the entire cathode surface to achieve improved cathodic performance [112–121].

Adler [66] outlines the mechanisms governing ORR in SOFC cathodes. He identifies several possible steps that may be involved in the ORR, depending on the materials, microstructure, and conditions of the electrode. **Figure 2.2** illustrates these mechanisms schematically, showing the different phases (α, β, and γ) and the possible reaction pathways.

The steps involved in the ORR include:

i. Incorporation of oxygen into the bulk of the electronic phase (if mixed conducting)
ii. Adsorption and/or partial reduction of oxygen on the surface of the electronic phase

iii. Bulk or surface transport of O^{2-} or O^{n-}, respectively, to the electronic/ionic interface

iv. Electrochemical charge transfer of O^{2-} or combinations of O^{n-} and e^{-}, respectively, across the electronic/ionic interface

v. The rates of one or more of these mechanisms wherein the electrolyte itself is active for generation and transport of electroactive oxygen species.

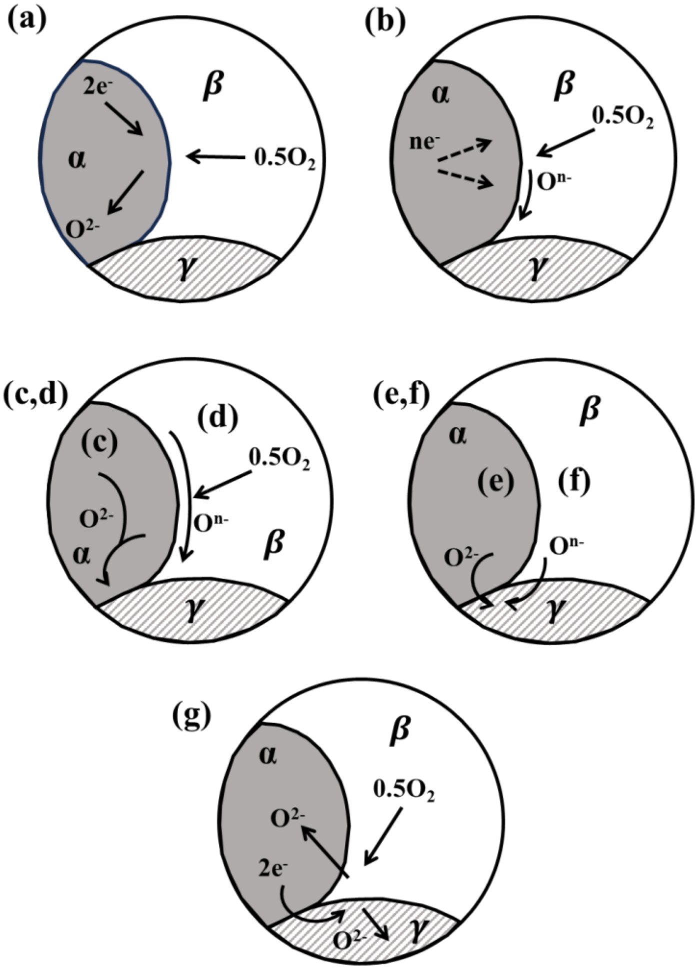

Figure 2.2: Schematic representation of the possible mechanisms of oxygen reduction in SOFC cathodes. Phases α, β, and γ refer to the electronic phase, gas phase, and ionic phase, respectively.

The arrows indicate the transport and reaction of oxygen species in the electrode. Adapted from ref. [66].

Each step is influenced by the material properties and microstructure of the cathode, such as the oxygen vacancy concentration, the surface exchange coefficient, the bulk diffusion coefficient, the surface morphology, and the TPB length [66]. The rate-limiting step of the ORR can vary depending on the operating conditions, such as the temperature, the oxygen partial pressure, and the applied potential [66]. Therefore, a cathode material must meet specific requirements to ensure high performance in intermediate to low-temperature SOFCs. Some of these requirements are:

i. High activity: The cathode material should have a high electrocatalytic activity for the ORR within the desired temperature range of 400 – 750 ^{o}C. This means that the cathode material should have a low ASR of less than 0.3 Ω cm^2, which is the target value to achieve the desired PPD of 1.0 W cm^{-2} [21].

ii. Good durability: The cathode material should maintain its high activity and stability at the operating temperature, even in the presence of impurities or phase transitions [21]. This means that the cathode material should have a low degradation rate and a high tolerance to CO, SO_2, and H_2O [64].

iii. Sufficient electronic and ionic conductivity: The cathode material should have a high electronic conductivity of at least 0.1 S cm^{-1} and a high ionic conductivity of at least 0.01 S cm^{-1} to prevent additional ohmic losses from the electrode [67]. This means that the cathode material should have MIEC property, which can facilitate the extension of the electrochemical reaction region from the TPB to the entire cathode surface [66].

iv. Affordable and reproducible: The cathode material should be cost-effective and easy to synthesize and fabricate for commercial applications. This means that the cathode material should have a low raw material cost, a simple synthesis method, and a scalable fabrication process [64].

Based on these requirements, the cathode materials for intermediate to low-temperature SOFCs can be classified into distinct groups, such as perovskite oxides (which are mostly Co/Fe-based), double perovskite oxides, composite oxides, and others [64]. **Table 2.1** lists some notable cathode materials for intermediate to low-temperature SOFCs from each group.

Table 2.1: Assessment of some notable cathode materials for intermediate to low-temperature SOFCs (where PPD = peak power density, ASR = area-specific resistance, TEC = thermal expansion coefficient

Cathode material	**Configuration**	**Perovskite class**	**PPD ($W\ cm^2$)**	**ASR ($\Omega\ cm^{-1}$)**	**TEC ($10^{-6}\ K^{-1}$)**	**Temp (℃)**	**Ref.**
$BaCo_{0.8}Nb_{0.1}Sc_{0.1}O_{3-\delta}$	BCNS|YSZ| Ni + YSZ	Co-based	0.481	0.0373	18.67	650	[68]
$Ba_{0.5}Sr_{0.5}Co_{0.7}Fe_{0.28}Pr_{0.02}O_{3-\delta}$	BSCFP|YSZ| Ni + YSZ	Co-based	1.083	0.026	16.4	700	[69]
$La_{1.8}Sr_{0.2}CoFeO_{5+\delta}$	LSCF|GDC| Ni + GDC	Double		0.42	19.4	700	[70]
$Nd_{1.9}Ce_{0.1}CuO_4$	NCC|GDC| Ni + GDC	Double	0.283	0.66	11.79	700	[71]
$PrBa_{0.5}Sr_{0.5}Co_{1.5}Fe_{0.5}O_{5+\delta}$	PBSCF|LSGM| Ni + LSGM	Double	0.59	0.067		800	[72]
$Bi_{0.5}Sr_{0.5}Fe_{0.95}P_{0.05}O_{3-\delta}$	BSFP|YSZ| Ni + YSZ	Fe-based	0.56	0.18	13.5	700	[73]
$LaBaCo_2O_{5+\delta}$	LBC|LSGM| Ni + LSGM	Double		0.046	27	700	[74]
$Pr_{0.94}Ba_{0.7}Ca_{0.3}Co_2O_{5+\delta}$	PBCC|YSZ| Ni + YSZ	Double	1.202	0.022		700	[75]
$LaNi_{0.4}Co_{0.6}O_{3-\delta}$	LNC|SDC| Ni + SDC	Co-based	0.45			650	[76]
$La_{1.2}Sr_{0.8}CoO_{4\pm\delta}$	LSC|LSGM| Ni + LSGM	Co-based	0.630	0.062	15	800	[77]
$LaCoO_3$	LC|YSZ| Ni + YSZ	Co-based	0.812	0.34		800	[78]
$SrCo_{0.95}Ir_{0.05}O_{3-\delta}$	SCI|LSGM| Ni + LSGM	Co-based	0.6		16.36	800	[58]
$SmBa_{0.1}Ca_{0.9}Co_2O_{5+\delta}$	SBCC|GDC| Ni + GDC	Double		0.07		700	[79]
$Ba_2YCu_3O_{6+\delta}$	BYC|BZCY| Ni + BZCY	Layered	0.175	0.29		650	[80]

$Sm_{0.5}Sr_{0.5}CoO_{3-\delta}$	SSC|GDC| Ni + GDC	Co-based		0.035		650	[81]
$Sr_{0.9}Y_{0.1}CoO_{3-\delta}$	SYC|LSGM| Ni + LSGM	Co-based	0.3533	0.044	19	700	[82]
$YBa_{0.5}Sr_{0.5}Co_{1.4}Cu_{0.6}O_{5+\delta} - Sm_{0.2}Ce_{0.8}O_{1.9}$	YBSCC-SDC|LSGM| Ni + LSGM	Composite	0.432	0.034	11.2	800	[83]
$La_{0.7}Sr_{0.3}Ti_{0.1}Fe_{0.6}Ni_{0.3}O_{3-\delta}$	LSTFN|LSGM| Ni + LSGM	Fe-based	0.402	0.047		800	[84]
$Bi_{0.5}Sr_{0.5}Fe_{0.9}Sn_{0.1}O_{3-\delta}$	BSFS|YSZ| Ni + YSZ	Fe-based	0.960	0.09	12.9	700	[85]
$BaCe_{0.1}Zr_{0.2}Fe_{0.6}O_{3-\delta}$	BCZF|BCZYYb| Ni + BCZYYb	Fe-based	0.24	0.21		700	[86]

The pursuit of developing highly efficient SOFCs that can operate at intermediate and low temperatures has led to exploring proton-conducting CFCs [87]. The concept of proton conductivity in perovskite oxide-based materials was introduced by Iwahara et al. in 1981[88]. Moreover, later studies have revealed that proton-conducting solid oxide fuel cells (P-SOFCs), popularly referred to as protonic ceramic fuel cells (PCFCs), have higher maximum theoretical efficiency compared to oxide ion conducting SOFCs. This is mainly because of their lower activation energy and lack of fuel dilution at the anode [89,90]. Hence, PCFCs are considered promising alternatives to SOFCs[91].

2.2.4 Detailed comparison between SOFCs and PCFCs

Figure 2.3 illustrates the schematic of SOFC and PCFC. The most distinctive feature which differentiates PCFC from SOFC is the mode of operation of the electrolyte. The electrolyte of PCFC conducts protons, while that of SOFC conducts oxygen ions during operation. SOFCs are characterized by the migration of oxygen ions from the cathode side to the anode side through the dense ceramic electrolyte when the air supplied to the cathode is reduced after reacting with the electrons received from the anode via the externally connected circuit.

In contrast to the traditional oxygen ion-conducting SOFC, where oxygen ions migrate from the cathode to the anode, the PCFC are SOFCs in which the migration species are predominantly protons, which migrate from the anode to the cathode at relatively lower activation energy with the formation of water at the cathode side as illustrated in **Figure 2.3**. The lower activation energy for the migration of protons through the electrolyte and water formation at the cathode is advantageous [92,93]. They give PCFCs an edge over the oxygen ion-conducting SOFC because there will be no fuel dilution problem at the anode since the water formation will only occur at the cathode. Thus, the unreacted hydrogen fuel can be directly recycled for reuse. In addition, the maximum theoretical efficiency of PCFCs is higher than that of SOFC since this theoretical efficiency increases with decreasing temperature. PCFCs are also compatible with multiple fuel types. When hydrocarbon fuel such as methane is used, there can be simultaneous electricity production and valuable byproduct such as ethylene (which helps regulate physiological processes, particularly in plant growth) [21,94]. Another exciting benefit of water formation at the cathode side is that CO_2 capture, and sequestration will be easier since the water formed will be separated from CO_2.

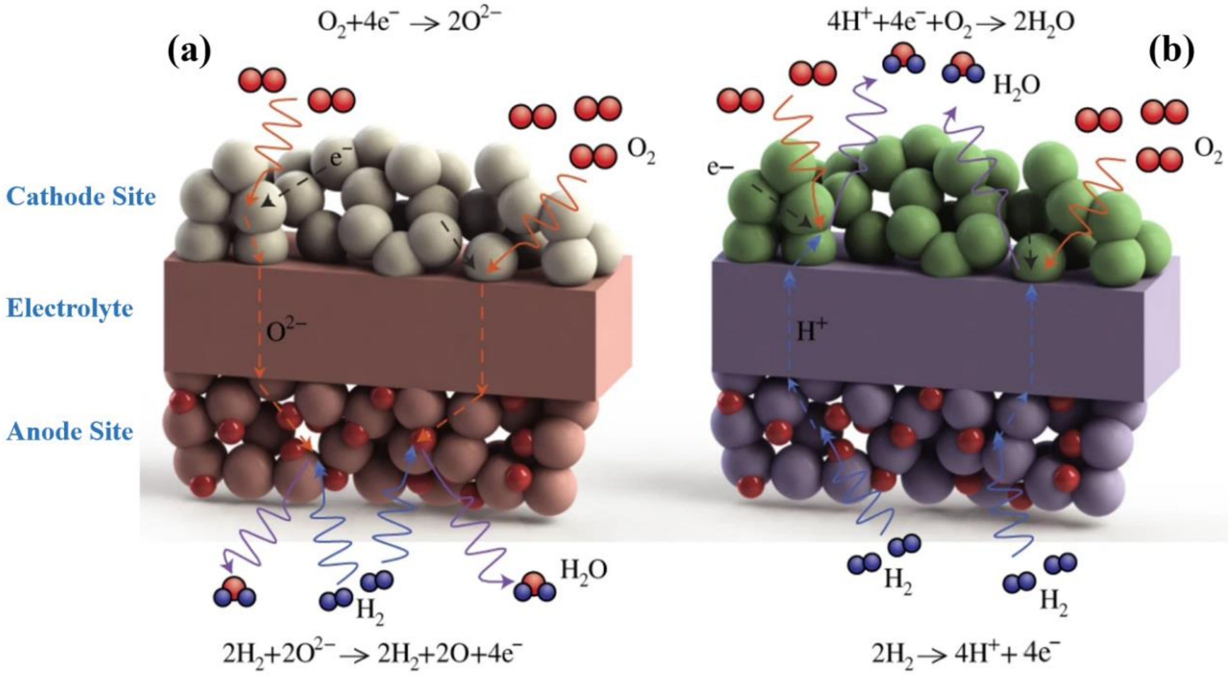

Figure 2.3: Schematic of ceramic fuel cells with (a) oxygen-ion conducting electrolyte and (b) proton conducting electrolyte [95].

Furthermore, several studies have suggested that PCFCs can potentially resist the poisoning effect of H_2S [96]. However, despite the numerous potentials of PCFC in achieving a state-of-the-art energy conversion technology, specific challenges, particularly with the anodic and cathodic reaction processes, need to be thoroughly investigated. For instance, issues related to the sintering, conductivity, stability, and durability of PCFC electrolyte materials are detrimental to the development and commercialization of CFCs.

2.3 Proton conduction mechanisms in PCFC materials

2.3.1 Protonic defects

Proton uptake within the structure of ceramic oxide materials is predominantly due to their oxygen-deficient nature induced by either extrinsic or intrinsic defects. The latter are defects attributed to alterations in the material structure (such as the absence of an atom), while the former are defects due to impurities or substitution of the B-site species with acceptor dopants, as illustrated in Eqn 2.1[97].

$$\mathrm{Acc_2O_3} + 2\mathrm{B_B^{\times}} + 0.5\mathrm{O_2} \rightarrow 2\mathrm{Acc_B'} + \mathrm{V\ddot{o}} + 2\mathrm{BO_2} \qquad (2.1)$$

where Acc stands for the acceptor dopants, a trivalent cation, and B symbolizes the host specie at the B-site.

The above mechanism is predominantly observed for proton defect formation in proton-conducting solid oxide electrolysis and fuel cells. However, a proton defect can also be formed through another means, which involves a non-oxygen defect participating in proton incorporation in the presence of a hydrogen-enriched atmosphere, as shown in Eqn 2.2.

$$\mathrm{H_2} + 2\mathrm{O_O^{\times}} \rightarrow 2\mathrm{OH\dot{o}} + 2\mathrm{e'} \qquad (2.2)$$

Nevertheless, this latter category of materials is not suitable and used as electrolyte materials because of the formation of electronic defects as compensational charges, which eventually trigger electronic conductivity [98].

Hence, in a sodden atmosphere, protonic defects are formed through the dissociation of water into two hydroxyl ions in the presence of oxygen lattice and oxide ion vacancies, as illustrated in Eqn 2.3. The formation of these hydroxyl ions is due to the covalent bond between the lattice oxygen from the structure and a proton and also as a result of the filling of the oxygen ion vacancy by the other hydroxide ion to form a protonic defect [97].

$$\mathrm{H_2O} + \mathrm{O_O^{\times}} + \mathrm{V\ddot{o}} \leftrightharpoons 2\mathrm{OH\dot{o}} \qquad (2.3)$$

where $O_O^{\times}$ *Symbolizes the lattice oxygen,* $V\ddot{o}$ *symbolizes the oxygen vacancy, and* $OH\dot{o}$ *represents the proton defect.*

Based on Equation 3, known as the hydration equation, proton uptake involves an acid-base reaction involving the dissociative incorporation of water into oxide ion vacancies. It implies that an increase in the partial pressure of water will result in an increase in proton uptake and a decrease in oxygen vacancy concentration. The law of mass action can represent the hydration process, as shown in Eqn 2.4.

$$K_{hydration} = \frac{[\mathrm{OH\dot{o}}]^2}{p_{H_2O}[V\ddot{o}][O_O^{\times}]} \qquad (2.4)$$

2.3.2 Proton transport mechanism

The transport mechanism of protons in ceramic oxide materials has been a subject of long-standing debate and research. Among the proposed mechanisms, the Grotthuss mechanism has gained the most acceptance. According to this mechanism, proton migration occurs through a hopping process facilitated by thermally activated rapid rotation, reorientation of the proton, and diffusion from one neighbouring oxygen ion site to another, as depicted in **Figure 2.4**. This concept is supported by experimental measurements of the H/D isotope effect in perovskite oxide materials, as shown in **Figure 2.4**.

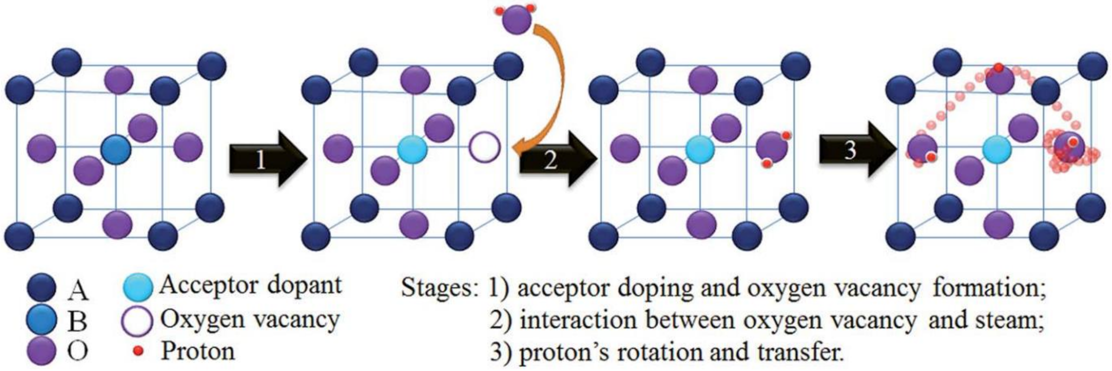

Figure 2.4: Proton transport mechanism in a typical ABO_3 perovskite oxide material [99]. Copyright 2016, Royal Society of Chemistry.

2.4 Overview of P-SOFC/PCFC component materials

PCFCs have three major components, like SOFCs: dense electrolyte, cathode, and anode. However, unlike traditional SOFCs, the electrolytes of P-SOFCs/PCFCs facilitate ionic conduction by promoting swift and efficient migration of protons from the anode to the cathode with minimal ohmic resistance[100]. The electrolyte material must be dense, allowing for maximum conductivity of protons and minimizing reactant crossovers[101]. It is crucial for the electrolyte material to exhibit good chemical and thermo-mechanical compatibility with the other cell components and the atmospheric environment, thereby ensuring reasonable stability and durability[102]. **Section 2.6.1** presents more details about the electrolytes used in PCFCs.

On the other hand, the cathode electrode should have excellent diffusion paths and ionic conductivity (i.e., primarily for protons) to extend the cathode reaction zone throughout the electrode surfaces[103]. The cathode should also possess good electronic and ionic conductivity to reduce polarization resistance. Likewise, it should possess excellent catalytic activity towards ORR since cathode reactions in PCFCs start with oxygen adsorptive dissociation on the catalyst's surface[104]. The other qualities a good cathode material for PCFC should possess are good compatibility with the electrolyte, excellent chemical and physical stability, and sufficient porosity to provide sufficient transport paths for oxygen and stream molecules. An elaborate detail of the cathode requirements and other insightful information can be found in **Section 2.6.2.**

The anode material should possess sufficient porosity (about 20 – 40%) and have good conductivity [105]. It is also desirable that the anode material maintains excellent compatibility with multiple fuels such as hydrogen, natural gas, methanol, ethanol, and other hydrocarbons [21,106,107]. It should possess a good surface area with good electrical conductivity and chemical compatibility with adjoining components under reducing conditions at the operating temperature. In the case of anode-supported cells, the anode material should also have a compatible TEC with other cell components and sufficient mechanical strength to support the cell [108]. See **Section 2.6.3** for more details about the anode materials for P-SOFCs.

The early PCFCs were high-temperature proton-conducting SOFCs. They were often referred to as high-temperature proton conductors (HTPCs) to differentiate them from polymer electrolyte membrane fuel cells (PEMFCs) that operate at low temperatures (< 100 ^{o}C). However, attention is currently shifted to intermediate and low-temperature operating PCFCs. This is because it is cheaper and can potentially increase the durability of CFC components, thereby hastening the commercialization process. Attempts have been made to develop intermediate to low-temperature operating oxygen ion-conducting CFCs, but this has been challenging. Another viable alternative that has drawn much attention lately is the proton-conducting CFCs. It is quite advantageous to SOFC on many fronts. It has lower activation energy and has been reported as coking and sulfur resistant in reputable studies. Despite the benefits of PCFCs, research is still ongoing to improve their performance, stability, and durability.

2.5 Naming conventions for PCFC materials

Duan et al. [107] proposed a naming convention for the various material's stoichiometric compositions to facilitate uniformity and understanding among various researchers focused on PCFC research. If the compound is in the form of $\mathrm{BaCe_{1-x}Y_xO_{3-\delta}}$ and $\mathrm{BaZr_{1-x}Y_xO_{3-\delta}}$, it should be represented with BCYX and BZYX, respectively and the value of X should be $x \times 100$. For instance, the abbreviation for $\mathrm{BaCe_{0.8}Y_{0.2}O_{3-\delta}}$ will be BCY20 and that of $\mathrm{BaZr_{0.8}Y_{0.2}O_{3-\delta}}$ will be BZY20. For other categories of compounds in the form of $\mathrm{BaZr_{1-x-y}Ce_yY_xO_{3-\delta}}$, the format of the abbreviation will indicate the B-site major constituent. If $y < 1 - x - y$, Zr will be the major B-site constituent, and the short form will be BZCYTY, where $T = (1 - x - y) \times 100$. However, if $y > 1 - x - y$, Ce will be the major B-site constituent, and the abbreviation will be BCZYYT, where $Y = y \times 100$ and $T = (1 - x - y) \times 100$. For instance, the abbreviations for $\mathrm{BaCe_{0.6}Zr_{0.2}Y_{0.2}O_{3-\delta}}$ and $\mathrm{BaZr_{0.6}Ce_{0.2}Y_{0.2}O_{3-\delta}}$ will be BCZY62 and BZCY62, respectively. Finally, if the compound happens to be in the form of $\mathrm{BaZr_{1-x-y-z}Ce_yY_xYb_zO_{3-\delta}}$, it will follow the same rule as in $\mathrm{BaZr_{1-x-y}Ce_yY_xO_{3-\delta}}$ compounds earlier described with only an exception that all the percentage constituents of all the B-site compositions will reflect. For instance, the abbreviation of the compounds $\mathrm{BaZr_{0.4}Ce_{0.4}Y_{0.1}Yb_{0.1}O_{3-\delta}}$ and $\mathrm{BaZr_{0.7}Ce_{0.1}Y_{0.1}Yb_{0.1}O_{3-\delta}}$ will be BZCYY4411 and BZCYYb7111, respectively.

2.6 Materials development for various components of PCFCs

2.6.1 Electrolyte materials

Research spanning several decades has identified perovskite oxides with ABO_3 structure as the most promising materials for PCFCs [109,110]. These materials are characterized by A-sites predominantly filled with large ionic-size metals such as Ca, Sr, Ba, and La, and B-sites dominated by smaller tetravalent elements such as Zr and Ce[111–114]. Doping the B-sites with trivalent elements like Yb, Y, Gd, and in creates oxygen vacancies that enhance the proton conductivity of the material. An example of the ABO_3 unit cell structure of a typical proton-conducting perovskite oxide electrolyte material is shown in **Figure 2.5**. A summary of the electrochemical performances of PCFC single cells with proton-conducting electrolyte materials is presented in **Table 2.2.**

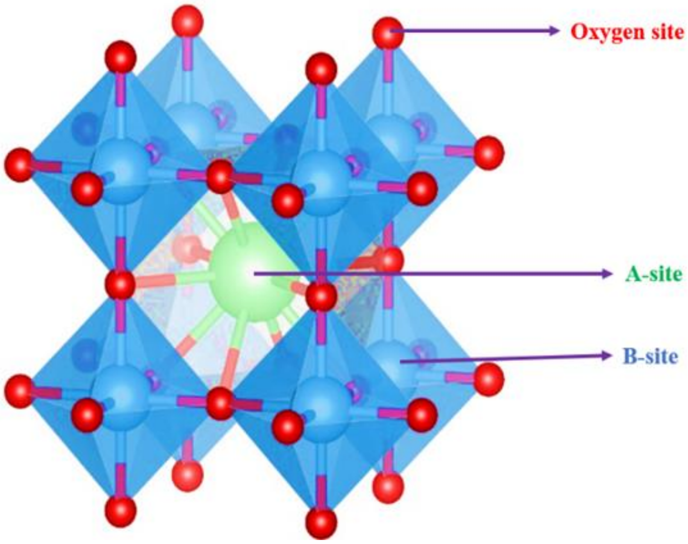

Figure 2.5: ABO_3 structure of a typical protonic ceramic electrolyte material.

Barium cerate-based electrolyte materials

$BaCeO_3$-based oxides are one of the most explored perovskite oxide materials for proton-conducting electrochemical systems [115–122]. These materials exhibit mixed conductivity (i.e., ionic and protonic), and they find application in various systems such as steam electrolyzers for hydrogen production and electrolytes for proton-conducting solid oxide fuel cells. The proton conductivity in this category of protonic electrolyte materials stems from the interaction between oxygen vacancies and water vapor, as described in [123]. Furthermore, an early investigation of proton conductivities of various perovskite oxide-based materials such as indates, hafnates, scandates, yttrates, tantalates, zirconates of alkali-earth elements, and barium cerates, confirms that those based on barium cerates have the highest conductivities [2,97]. The higher proton conductivity in $BaCeO_3$-based oxides (i.e., 10^{-2} S cm^{-1} at 600 ºC [124]) could be due to their relatively low electronegativities, larger ionic radii due to the Ba cation in their A-sites, or/and their lower grain-boundary resistance on the overall resistance of the perovskite oxide material [115]. Also, studies have confirmed that Sr/$CaCeO_3$ and Sr/$CaZrO_3$-based oxides have poor hydration capability and lower proton conductivity than $BaCeO_3$-based oxides, as shown in Figure 2.6.

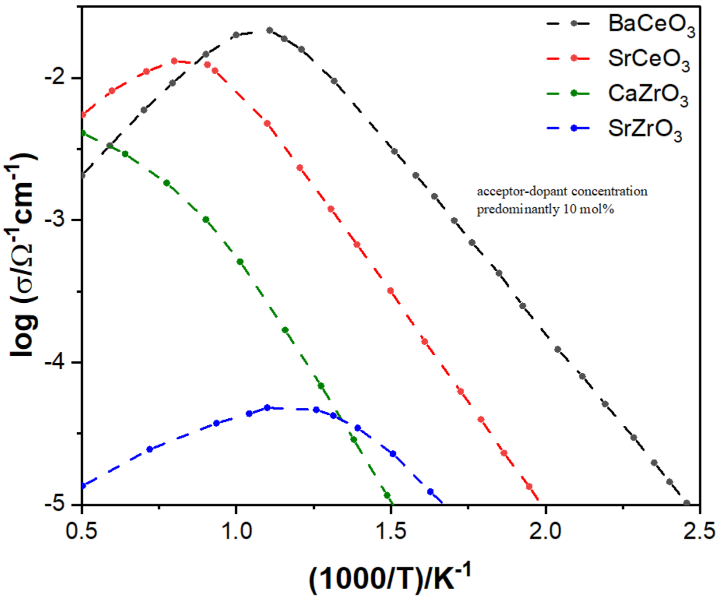

Figure 2.6: Proton conductivities of $BaCeO_3$ electrolyte material relative to other protonic ceramic materials [97].

However, later studies suggested that the high proton conductivity in $BaCeO_3$-based oxides should not be the major yardstick in concluding the viability of their application in electrochemical systems due to their low stability in water and other acidic compounds [120,123,125]. Also, Bhide et al. [126] confirmed that $BaCeO_3$-based electrolyte materials have poor stability relative to other electrolyte materials. Figure 2.7 indicates that $BaCeO_3$-based materials have reaction affinity for atmospheric gases (as illustrated in Eqns 2.5-2.8), and this causes the cerate phase to be decomposed. Eqns 2.5 – 2.8 show what happens when $BaCeO_3$ reacts with water or any acidic compound.

$$BaCeO_3 + H_2O \rightarrow Ba(OH)_2 + CeO_2 \quad (2.5)$$

$$BaCeO_3 + CO_2 \rightarrow BaCO_3 + CeO_2 \quad (2.6)$$

$$BaCeO_3 + SO_2 \rightarrow BaSO_3 + CeO_2 \quad (2.7)$$

$$BaCeO_3 + H_2O \rightarrow BaS + H_2O + CeO_2 \quad (2.8)$$

Due to the challenges encountered with using $BaCeO_3$-based oxides as electrolyte materials for proton-conducting solid oxide fuel cells, efforts were channeled toward developing materials with excellent mixed conductivity and good stability against water and acidic atmospheres[97,99,112,127–133]. Some of those strategies employed were (i) co-doping of $BaCeO_3$ using various suitable elements, which could either be metallic or non-metallic, (ii) introduction of phases with high stability properties to the $BaCeO_3$ based material in the form of composite material development. Based on the outcome of various research works, zirconium was found to be the most suitable element to improve the stability of $BaCeO_3$ [117], although at the expense of other electrical properties of the material as will be discussed in the next section.

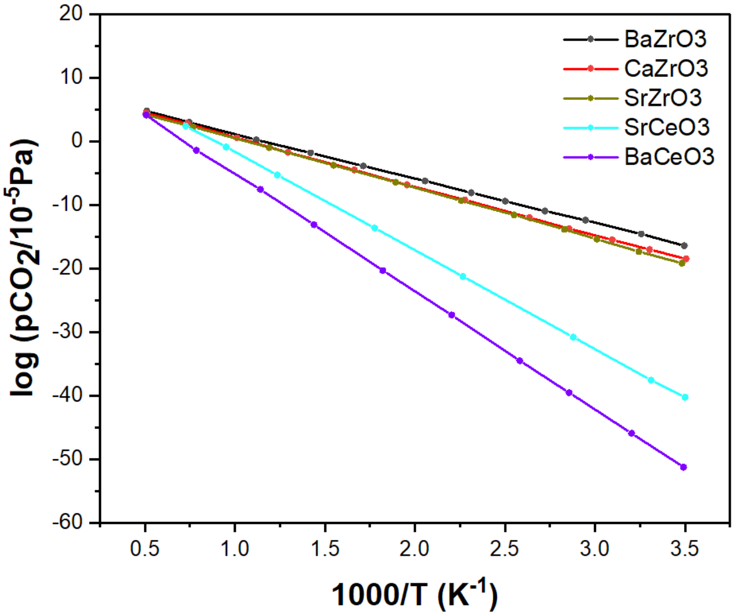

Figure 2.7: Stability of various proton-conducting electrolyte materials based on different pCO_2 and temperatures reproduced from [134]. Copyright Elsevier, 2008.

Barium zirconate-based electrolyte materials

It has been established that the cerate-based perovskite oxide materials exhibit the highest protonic conductivity among all other perovskite oxide materials, with $BaCeO_3$-based oxides being the category of cerates with the highest conductivity. Nevertheless, they are very unstable under practical conditions in electrochemical systems. On the other hand, Zirconium-based oxides are reputable for their high stability under various acidic and atmospheric conditions. $BaZrO_3$-based oxides are chemically stable in water and CO_2 environments. Lu et al. [134] established the relationship between increasing partial pressure of CO_2, Zr content, x, and equilibrium reaction temperature of $BaCe_{1-x}Zr_xO_3$. They confirmed that the stability of $BaCe_{1-x}Zr_xO_3$ increases with increasing Zr content, x, at a given CO_2 partial pressure, as illustrated in Figure 2.8.

Furthermore, $BaCeO_3$ and $BaZrO_3$-based oxides have ionic conductivities of 10^{-2} and 10^{-1} S cm^{-1} at low and intermediate temperatures[135,136]. However, particular challenges limit their application as electrolyte materials in proton-conducting solid fuel cells. $BaZrO_3$-based oxides have issues of significant grain boundary resistance and poor sintering.

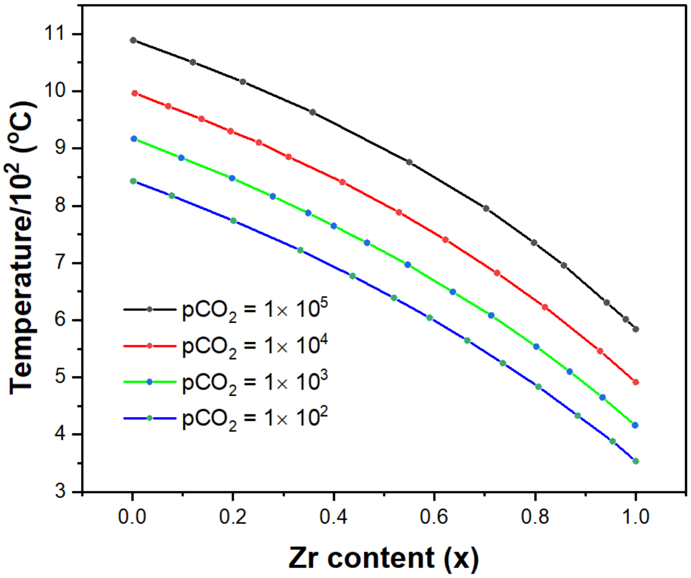

Figure 2.8: Effect of Zr content and partial pressure of CO_2 on equilibrium reaction temperature of $BaCe_{1-x}Zr_xO_3$, reproduced from [134]. Copyright 2008, Elsevier.

Grain boundary characteristics of PCFC electrolyte materials

One significant influencing factor affecting the conductivities of proton-conducting solid oxide fuel cells is their grain boundary characteristics[45,104,137,138]. Grain boundary resistance has been identified as a problem, particularly in the conductivity of $BaZrO_3$-based oxides. Hence, as a rule of thumb, as the grain size increases, the material conductivity increases, and vice versa. $BaZrO_3$-based oxides, on the other hand, are characterized by small-sized grains at the grain boundaries, which is responsible for their high grain boundary resistances and low conductivity

[139]. Grain boundary architecture is often influenced by segregation forces causing acceptor dopants to accumulate around grain boundary core materials and depleting oxygen vacancies and protons. The consequence of this interaction is the formation of space effects that influence ions' transport, as shown in Figure 2.9.

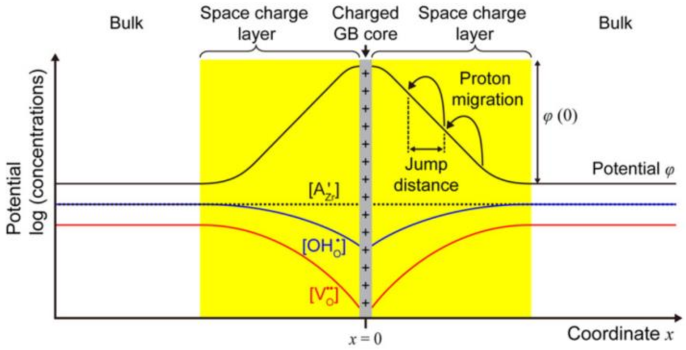

Figure 2.9: Space charge layer model at the grain boundary core of a typical PCFC electrolyte material. Copyright 2013, Elsevier.

Iguchi et al. [140] investigated the effects of grain boundary diameter and microstructure on the electrical conductivities of $BaZrO_3$-based oxides. They notably considered Y-doped $BaZrO_3$ prepared by solid-state reaction process and Pechini method subjected to different sintering conditions. It was confirmed that the sintering duration significantly affected the material's electrical conductivity, with the sample subjected to 200 h sintering time exhibiting the lowest electrical conductivity. However, the sample preparation methods did not affect the grain boundary characteristics [140]. Y-doped $BaZrO_3$ with a 20% doping level has been widely used and considered an excellent candidate for PCFC electrolytes. However, the percentage level of doping of $BaZrO_3$ with Y (i.e., BZY20) often leads to the formation of a secondary phase (i.e., BaY_2NiO_5), thereby compromising the BZY20 as shown in **Figure 2.10**. This implies that the subsequent co-sintering of the supposed BZY20 with NiO will no longer be a 2-phase equilibrium comprising just BZY20 and NiO. Hence, it is proposed that this problem can be solved by limiting the doping level of Y in BZY20 to a maximum of 12% or introducing other dopants such as Yb [141]. The phenomenon described involving foreign phase formations significantly affects the transport of ions around the grain boundaries [142].

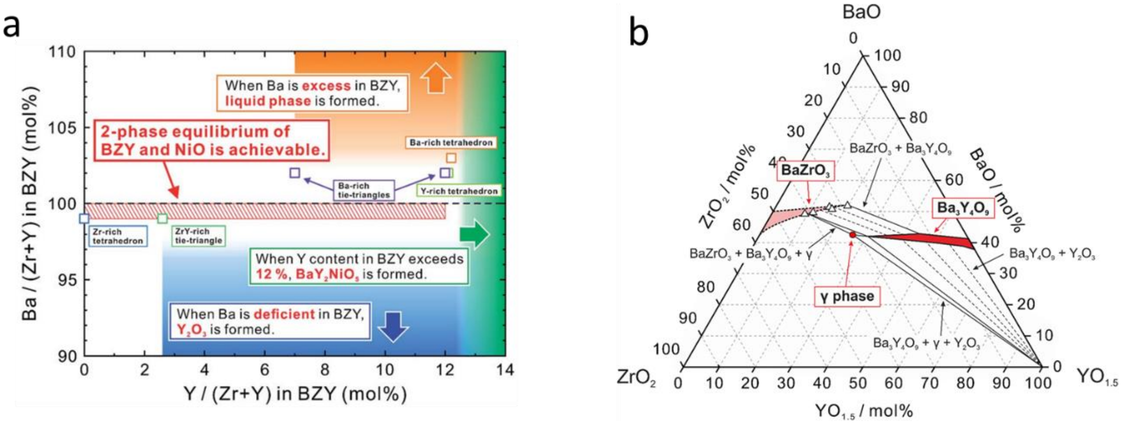

Figure 2.10: (a) Expected secondary phases to be formed when various BZY compositions are co-sintered with NiO [141]. Copyright 2019, Royal Society of Chemistry. (b) Stability of BZY as a function of its composition and heat treatment temperature. The partial phase diagram of the BaO-Y_2O_3-ZrO_2 system at 1600 °C was proposed by Ueno et al. [143].

According to Ueno et al.[143], the stability of BZY ($BaZrO_3$) can be represented as a function of its composition and heat treatment temperature in a BaO-Y_2O_3-ZrO_2 ternary system. They proposed a partial phase diagram of the system at 1600 °C, which is shown in **Figure 2.10b**. The diagram shows that BZY solid solution is continuous in 0–40 mol% in the molar ratio of Y/(Zr + Y) at 1600 °C, but it may separate into two kinds of BZY phases with different Y contents at lower temperatures. The separation region is probably around 10 mol% in the molar ratio of Y/(Zr + Y). They also suggested that the coexistence of two BZY phases could retard the grain growth and affect the conductivity of BZY samples. Therefore, to obtain a homogeneous microstructure with sufficient grain growth and high conductivity, it is desirable to homogenize the distribution of Y in BZY samples before sintering and choose a higher dopant level of Y (> 15 mol%) [143].

Sintering of PCFC electrolyte materials

As earlier discussed in the previous section concerning the grain boundary-resistant problem of $BaZrO_3$-based oxide, various approaches have been employed to address this challenge. The use of several sintering aids, such as NiO, ZnO, and CuO, has been proposed [144–146]. However, Han et al. [131] and others suggested that using sintering aids such as NiO, ZnO, and CuO impedes the proton conductivity in BZY20 and creates hole conduction in an oxidizing atmosphere [145,147,148]. The most investigated doped $BaZrO_3$ oxide is yttrium doped barium zirconate, BZY. There have been co-doping strategies of yttrium barium zirconates with other elements such as Nd, In, Sn, Pr, and Yb to improve the sintering and proton-conducting properties of barium zirconates which has led to specific promising outcomes [149,150]. Asides from the introduction of sintering aids to barium zirconates and co-doping strategies, the use of PLD has also been used to improve the sintering of barium zirconates by Pergolesi et al.[151]. However, PLD is an expensive method and not suitable for large-scale applications. Due to the various challenges enumerated, an alternative approach to getting a superior proton-conducting electrolyte for PCFCs will be a natural combination of yttrium doped barium cerate and yttrium doped barium zirconate to get cerium and yttrium doped barium zirconates as will be explored in the subsequent section.

Other Materials and Challenges

The combination of BCY and BZY has been identified to be a promising approach to getting an improved proton-conducting electrolyte for PCFCs. Katahira et al. [117] investigated the effects of variations in the constituents of BCZY. They observed that increasing the Zr content increases the stability of the compound against CO_2 but sacrifices conductivity. Likewise, they varied the

Ce content and confirmed that its presence increases the conductivity and sinterability of BCZY. Overall, they concluded that BCZY is stable with acceptable conductivity. For instance, Zuo et al. [152] investigated the conductivity and stability of BCZY712 at a low temperature of 500 ^oC. It was discovered that BCZY712 exhibited excellent ionic conductivity of 0.009 S $cm^{-1,}$ which surpassed that of LSGM, GDC, and YSZ. Likewise, in terms of stability, the structure of BCZY712 was confirmed to be the same before and after exposure to CO_2, H_2O, and CO_2 and H_2O. Another innovative product of the combination of BCY and BZY is BCZY442 [153]. This electrolyte material was reported to have a high bulk proton conductivity and an excellent tolerance to CO_2. However, the challenge with is material lies in its high sintering temperature and low grain boundary proton conductivity [154].

Other approaches that researchers have employed are the introduction of several dopants to the B-sites of BCY and BZY. An example of a breakthrough with this approach is the development of BCZYYb7111 in 2009 by Yang et al. [155]. The introduction of Yb into BCZY improved the conductivity and stability of BCZY against sulfide and other hydrocarbons. Later studies revealed that CO_2 affects the stability of BCZYYb7111. The exceptional discovery of another stoichiometric manipulation of BCZY by Choi et al. [156] gave rise to BCZYYb4411. This material was reported to have a high tolerance for $CO_{2,}$ which was attributed to the higher content of Zr. Also, the material has relatively improved performance with high resistance to coking and sulfur atmospheres.

Table 2.2: Selected electrochemical performances of single cells with P-SOFC electrolyte materials operated under humidified hydrogen and ambient air.

Electrolyte	**Power density (mW cm^{-2})**	**OCV (V)**	**Temp. (℃)**	**Cell configuration (cathode | electrolyte | anode)**	**Ref.**
$BaCe_{0.9}Y_{0.1}O_{3-\delta}$	96	1.145	600	PR_2NiO_4 | BCY10(85μm) | Ni + BCY10	[157]
$BaCe_{0.9}Y_{0.1}O_{3-\delta}$	150	0.98	600	LSCF8282- BCYb10 | BCY10(13.4μm) | Ni + BCY10	[158]
$BaZr_{0.8}Y_{0.2}O_{3-\delta}$	169	0.97	600	PBC- BZYP | BZY20(20μm) | Ni + BZY20	[159]
$BaZr_{0.8}Y_{0.2}O_{3-\delta}$	110	0.99	600	LSCF6428- BCYb10| BZY20(4μm) | Ni + BZY20	[160]
$BaZr_{0.3}Ce_{0.55}Y_{0.15}O_{3-\delta}$	1302	1.056	600	BSCF| BZCY3(5μm) | Ni + BZCY3	[161]
$BaZr_{0.1}Ce_{0.7}Y_{0.1}Yb_{0.1}O_{3-\delta}$	690	1.04	600	NBSCF| BZCYYb1711(14.7μm) | Ni + BZCYYb1711	[155]
$BaZr_{0.4}Ce_{0.4}Y_{0.1}Yb_{0.1}O_{3-\delta}$	1098	1.01	600	PBSCF| BZCYYb441(15μm) | Ni + BZCYYb441	[156]
$BaZr_{0.1}Ce_{0.7}Y_{0.2}O_{3-\delta}$	428	1.01	600	SFNb | BZCY172 (20μm) | Ni + BZCY172	[162]
$BaZr_{0.1}Ce_{0.7}Y_{0.1}Yb_{0.1}O_{3-\delta}$	580	0.95	600	LSM-SDC | BZCYYb1711(12μm) | Ni + BZCYYb1711	[163]
$BaZr_{0.1}Ce_{0.7}Y_{0.1}Yb_{0.1}O_{3-\delta}$	700	0.98	600	LSCF6428-SDC | BZCYYb1711(12μm) | Ni + BZCYYb1711	[164]

For cathode.

LSCF8282- BCYb10 = $La_{0.8}Sr_{0.2}Co_{0.8}Fe_{0.2}O_{3-\delta}$ - $BaCe_{0.9}Yb_{0.1}O_{3-\delta}$; PBC- BZYP = $PrBaCo_2O_{5+\delta}$- $BaZr_{0.7}Y_{0.2}Pr_{0.1}O_{3-\delta}$; LSCF6428 - BCYb10 = $La_{0.6}Sr_{0.4}Co_{0.2}Fe_{0.8}O_{3-\delta}$ - $BaCe_{0.9}Yb_{0.1}O_{3-\delta}$; BSCF = $Ba_{0.5}Sr_{0.5}Co_{0.8}Fe_{0.2}O_{3-\delta}$; NBSCF = $NdBa_{0.5}Sr_{0.5}Co_{1.5}Fe_{0.5}O_{5+\delta}$; PBSCF = $PrBa_{0.5}Sr_{0.5}Co_{1.5}Fe_{0.5}O_{5+\delta}$; SFNb = $SrFe_{0.95}Nb_{0.05}O_{3-\delta}$; LSM-SDC = $La_{0.75}Sr_{0.25}MnO_{3-\delta}$ - $Ce_{0.8}Sm_{0.2}O_{2-\delta}$; LSCF6428-SDC = $La_{0.6}Sr_{0.4}Co_{0.2}Fe_{0.8}O_{3-\delta}$ - $Ce_{0.8}Sm_{0.2}O_{2-\delta}$

2.6.2 Cathode Materials development for PCFCs

The cathode is the most explored research area in ceramic fuel cell development because of the high activation loss for ORR at the cathode during low and intermediate-temperature operating conditions. Thus, developing highly active and stable cathode materials could contribute significantly to the performance improvement of PCFCs. Unlike the case of oxygen ion conducting solid oxide fuel cells where the cathode reaction involves oxygen adsorptive dissociation on the catalyst surface followed by the diffusion of oxygen ions to the anode through the electrolyte, in PCFCs, the oxygen adsorptive dissociation first occurs on the catalyst surface, after which the oxygen ions react with the protons that migrated from the anode through the electrolyte to form water. Eqns 2.9 and 2.10 illustrate the adsorptive dissociation reactions in SOFC and PCFCs, respectively. Detailed stepwise elementary reactions at the cathode for PCFCs are presented in Table 2.3**.** In contrast, the reaction pathway for a single-phase proton, electron, and oxygen ion-conducting cathode material for PCFCs is illustrated in **Figure 2.11**.

$$O_2 + 4e^- \rightarrow 2O^{2-} \qquad (2.9)$$

$$O_2 + 4e^- + 4H^+ \rightarrow 2H_2O \qquad (2.10)$$

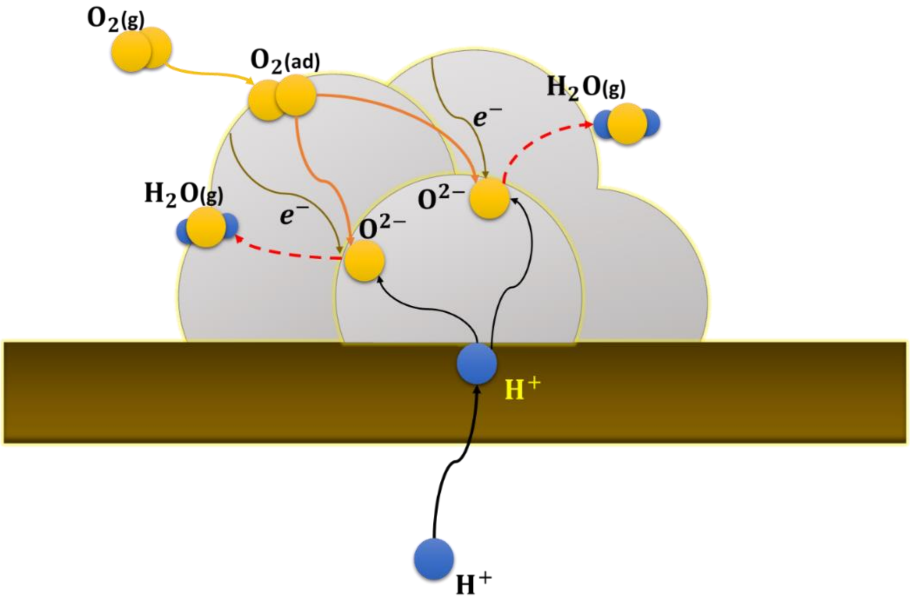

Figure 2.11: Schematic illustrating reactions in a single-phase triple conducting P-SOFC cathode.

There are four types of transfer modes in PCFC cathodes: electron-conducting single-phase, proton and oxygen ion-conducting (either single-phase or composite), oxygen and electron-conducting (MIEC) (as a single-phase or composite), and proton-electron-oxygen ion-conducting single-phase. **Figure 2.12** provides a schematic illustration of these different transfer modes in P-SOFC cathode materials.

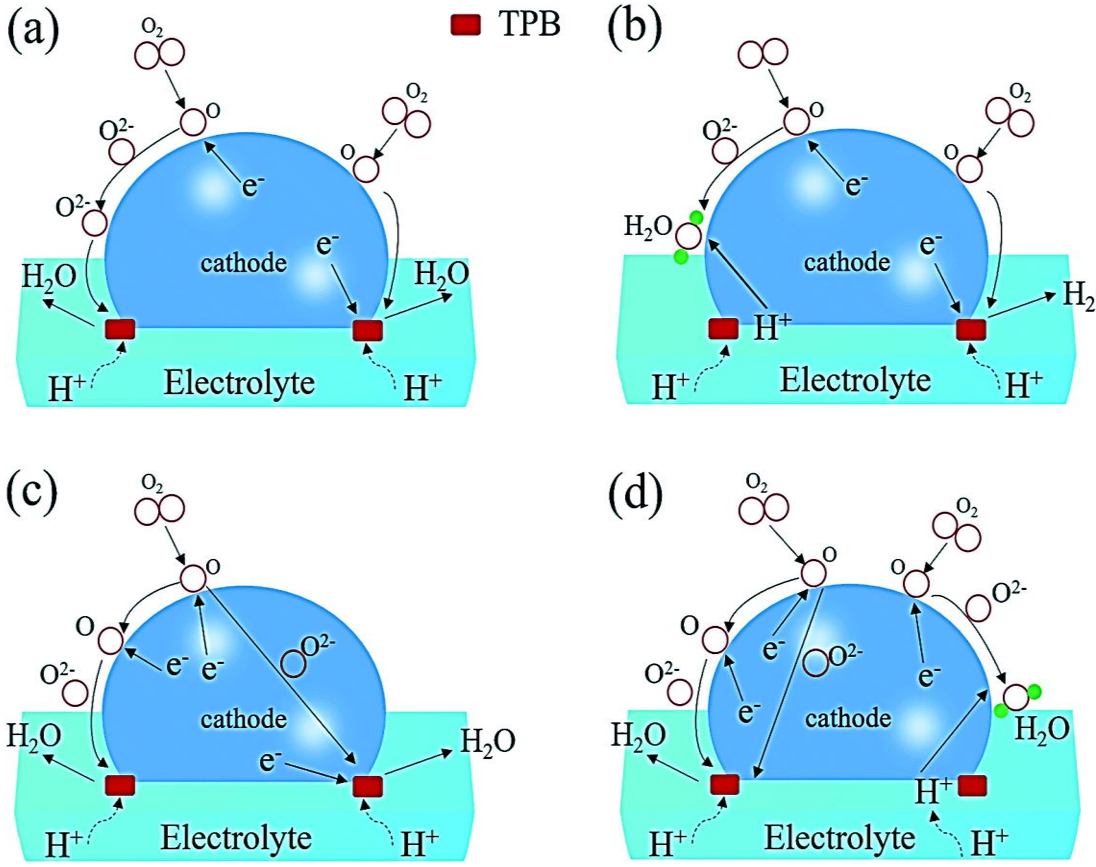

Figure 2.12: Cathodic reactions in PCFCs [165] for (a) Single-phase electron-conducting cathode materials, (b) proton and oxygen ion-conducting cathode materials, (c) MIEC cathode materials, and (d) proton, electron, and oxygen ion-conducting cathode materials: copyright 2018, Royal Society of Chemistry [165].

The foundational concepts for developing cathode materials for PCFCs stem from the knowledge of cathode development for oxygen ion-conducting SOFCs. In the conventional SOFCs, what is currently prominent is the development of single-phase mixed ionic and electronic conducting (MIEC) cathodes which are different from the early traditional SOFCs where cathode reactions are limited to the triple-phase boundary (i.e., the interface where oxygen ion, electrolyte, and cathode coincide)[7,21]. The MIEC concept in SOFCs allows extending the reaction zone beyond the TPB to the whole surface of the cathode, depending on the efficacy of the cathode constitutive elements [64,65]. Some of the most outstanding results of cathode materials developed for SOFC with MIEC are $Ba_{0.5}Sr_{0.5}Co_{0.8}Fe_{0.2}O_{3-\delta}$ (BSCF)[166] and $La_{0.6}Sr_{0.4}Co_{0.2}Fe_{0.8}O_{3-\delta}$ (LSCF)[167]. Besides these materials developed, other categories of materials developed in later years are double perovskites (i.e., $A\acute{A}B_2O_{5+\delta}$ based oxides such as $PrBaCo_2O_{5+\delta}$ [168]), Ruddlesden-Popper (i.e., $A_{n+1}B_nO_{3n+1}$ based oxides such as $La_2NiO_{4+\delta}$ [169]) phases and layered ferrites [170] (e.g., $Sr_2Fe_2O_5$). Other procedures developed to improve the oxygen exchange rate by controlling the cathode morphology include in situ exsolution[129], impregnation[171,172], and atomic layer deposition[76].

PCFCs share standard requirements in cathode development, such as consideration of the cost of constituent cathode materials, compatibility with other cell components, stability, durability, and performance. Some other requirements, such as proton conductivity and TIEC, are peculiar to PCFCs [165].

Activity

For PCFCs, the cathode material must possess effective proton diffusion paths to extend the reaction zone to a higher specific area of active sites, which implies that a PCFC cathode material should have a high catalytic activity toward ORR [173]. The cathode catalyst should be capable of effectively dissociating the adsorbed oxygen on its surface for further reactions at the cathode. One of the strategies for increasing the catalytic activity of PCFC cathode material is substituting the A-sites with lower valence ions which have been proven to increase electronic conductivity and oxygen adsorptive dissociation. Hence, proton conductivity in PCFCs can be achieved by either introducing proton conductivity into an existing conventional MIEC cathode as in the case of $BaCe_{0.8}Sm_{0.2}O_{2.9}$ being introduced into $Sm_{0.5}Sr_{0.5}CoO_3$ to achieve a proton-conducting composite cathode with a highly reduced polarization resistance[174]. Another way of achieving a highly active proton-conducting cathode material is by designing single-phase oxides with a triple conducting capability (i.e., proton, oxygen ion, and electron conductivity) as illustrated in **Figure 2.12 (d)** and **Figure 2.11**. This oxide should have a conductivity up to 1 S/cm to ensure excellent performance. In this case, the reaction is extended to the cathode's entire surface, which improves the cathode's catalytic activity. The stepwise reaction paths for these novel PCFC cathodes with triple conductivity are summarily described in Table 2.3.

Table 2.3: Basic steps and order of reactions at the cathode for a typical P-SOFC.

Step	Reaction(s)	Description
1	$O_2(g) \rightarrow O_{2(ad)}$	Molecular oxygen adsorption
2	$O_{2(ad)} \rightarrow 2O_{(ad)}$	Molecular oxygen dissociation of adsorbed oxygen from the air
3	$O_{(ad)} + e^- \rightarrow O^-_{(ad)}$; $O_{(ad)} + 2e^- \rightarrow 2O^{2-}_{(ad)}$	Oxygen reduction at the cathode
4	$O_{(ad)} \rightarrow O_{TPB}$ $O^-_{(ad)} \rightarrow O^-_{TPB}$	Surface diffusion at the electrode/electrolyte/oxygen ion boundary
5	$O^-_{bulk} \rightarrow O^-_{TPB}$	Bulk diffusion of oxygen throughout the cathode
6	$2H^+_{bulk} \rightarrow 2H^+_{TPB}$	Proton migration toward the anode
7	$2H^+_{TPB} + O^{2-}_{TPB} \rightarrow OH^-_{TPB}$ $OH^-_{TPB} + H^+_{TPB} \rightarrow H_2O_{TPB}$	Formation of water at the triple-phase boundary
8	$H_2O_{TPB} \rightarrow H_2O_{(g)}$	Evaporation of water

Kim et al. [175] developed a single-phase cathode material with triple conductivity, $NdBa_{0.5}Sr_{0.5}Co_{1.5}Fe_{0.5}O_{5+\delta}$ (NBSCF). A low polarization resistance of 0.081 Ωcm^2 was achieved at a temperature of 700 ^oC [175]. Also, proton-conducting cathode materials can be derived from proton-conducting electrolytes such as $BaZrO_3$ and $BaCeO_3$-based electrolytes. The electronic conductivity and catalytic properties of the proposed cathode materials can be improved by doping the B-sites of proton-conducting electrolytes with highly catalytic elements such as Co and Fe as in the case of $BaZr_{1-x}Co_xO_{3-\delta}$ [176] and $BaZr_{1-x}Fe_xO_{3-\delta}$. In 2015, Duan et al. [177] developed the novel cathode material, $BaCo_{0.4}Fe_{0.4}Zr_{0.1}Y_{0.1}O_{3-\delta}$ (BCFZY0.1). This cathode material was reported to have an excellent ORR at low and intermediate temperatures. When hydrogen fuel was used, the peak power density (PPD) was 455 mW cm^{-2} at a low temperature of 500 ^{o}C, and when methane fuel was used, the PPD was 142 mW cm^{-2} at the same temperature. In 2021, Liang et al. [178] doped the high-performance BCFZY cathode material with 5% Ni. This dopant interestingly improved the ASR and PPD of BCFZY material in both SOFC and PCFC as illustrated in **Figure 2.13**. Another exciting strategy for achieving high activity in PCFC cathode materials is the design of self-assembled nanocomposite cathode materials. Self-assembly design of cathode materials is a novel and emerging approach for preparing composite cathode materials with desirable qualities ranging from high activity to excellent thermo-mechanical compatibility with other cell components. Earlier, this strategy was used in preparing cathode materials with excellent MIEC in SOFCs. For instance, Qi et al. [179] employed the strategy of self-assembly cathode design to prepare cubic-hexagonal perovskite nanocomposites (i.e., $BaCo_{0.6}Zr_{0.4}O_{3-\delta}$ (BZC-BC) nanocomposite comprising cubic $BaZr_{0.82}Co_{0.18}O_{3-\delta}$ (BZC) and 12H hexagonal perovskite material, $BaCo_{0.96}Zr_{0.04}O_{2.6-\delta}$ (12H-BC)) for SOFC. The material exhibited excellent compatibility (i.e., TEC) with GDC electrolyte also a high PPD of 1094 mW cm^{-2} at 650 ^{o}C. Recently, Song et al. [180] employed the self-assembly cathode design approach to preparing a nanocomposite cathode material comprising different phases, proton and electronic conductor phase, $BaCe_xY_yCo_zO_{3-\delta}$ (P-BCCY), the MIEC phase, $BaCo_xCe_yY_zO_{3-\delta}$ (M-BCCY) and another MIEC phase, $BaCoO_{3-\delta}$ (BC). The different inherent phases are entwined to achieve a highly active triple conducting material with the active sites extended throughout the cathode material. At 550 °C, a high PPD of 508 mW cm^{-2} was achieved, stable for over 800 h. However, despite the significant progress made in developing PCFC cathodes, the electrochemical processes on the cathode need to be further investigated.

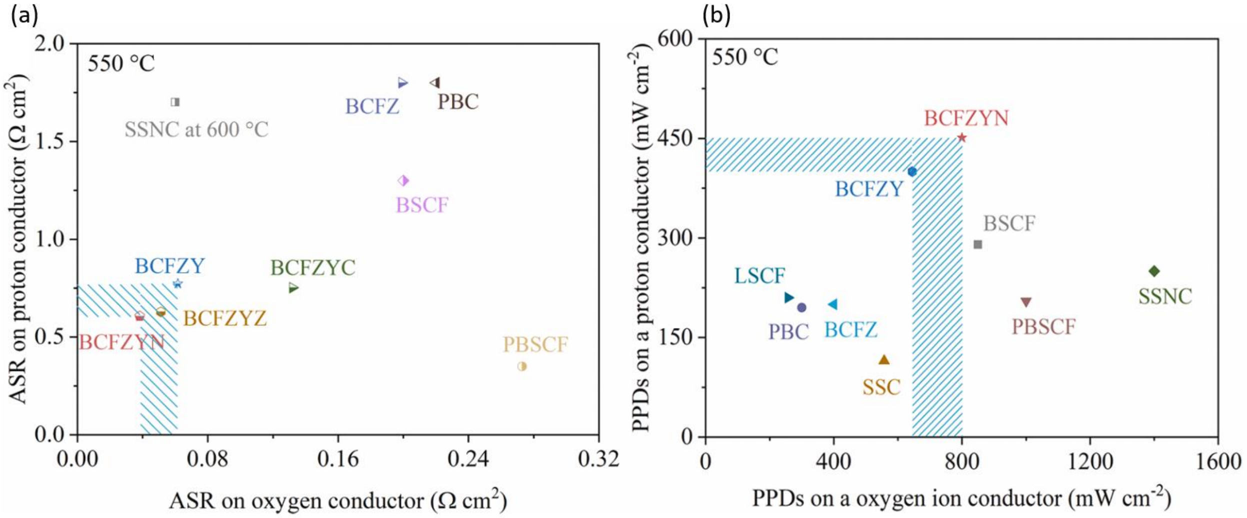

Figure 2.13: The performance of BCFZYN and other classical electrode materials used in both O-SOFCs and PCFCs, respectively (a) ASR in air with SDC and BZCYYb electrolyte (b) PPD with Ni + SDC│SDC│cathodes and Ni + BZCYYb│BZCYYb│cathodes. Copyright 2021, Elsevier [178].

Conductivity improvement strategies for PCFC cathode materials

Another essential requirement for PCFC cathode material is good electronic conductivity. This is important to achieve a cathode material with low ohmic resistance. The idea of electronic conduction stems from the formation and transportation of electron holes which are achieved by introducing transition elements (i.e., Ni, Mn, Fe, Co) in the B-site. The electron holes can be further increased by substituting ions with lower valences, as in the A-site case of Ba^{2+}, Ca^{2+}, and Sr^{2+} [181]. Furthermore, Zohourian et al. [182] and Papac et al. [103] buttressed on mixed and triple conductivity of cathode materials for PCFCs by emphasizing proton uptake mechanisms in perovskite oxide materials which have been elaborately discussed in **Section 2.3**. Specific strategies have been suggested in the literature for developing and designing a high-performance cathode material with superb proton, electron, and oxygen ion conductivity for PCFCs [107,128,183]. The materials that are reported to be most suitable for achieving excellent triple conducting single-phase cathodes are either $\mathrm{ABO_{3-\delta}}$ perovskites, $\mathrm{A\acute{A}B_2O_{5+\delta}}$ double perovskites, and $\mathrm{A_{n+1}B_nO_{3n+1}}$ Ruddlesden-Popper with their A and B sites doped with elements such as Ba, Sr, Zr, Cu, Mn, Co, and Ni[92,184–190]. Considering materials with cubic structures and large lattice volumes is best because they enhance hydration and proton conduction. It is also essential when selecting dopants to consider transition metals with multiple oxidation states because that will significantly enhance redox capability and good electronic conductivity. The B-site cation should possess higher electronegativity than the A-site cation to promote proton uptake and lattice hydration as in the case of specific elements such as Zn, Y, and Zr [182]. Also, the A-site cation should have a larger ionic radius to increase the lattice volume, oxygen vacancy concentration, and mobility. Furthermore, the A-site dopants should be carefully selected because this greatly influences the stability and performance of the material. In Table 2.4, recent articles with new findings on cathode material development for PCFCs are enlisted.

Compatibility with other cell components

A good PCFC cathode material should be compatible with the proton-conducting electrolytes, including chemical and TEC compatibility. The TEC of the cathode material must match reasonably with that of the electrolyte to prevent large thermal stress during thermal cycling, which causes the delamination of the cathode from the electrolyte. TECs of the cathode materials should be reasonably close to those of the electrolytes, usually in the range of 10^{-6} K^{-1}. Past research studies have revealed that Co-based materials usually have good electrocatalytic activity but also significantly higher TECs than Mn-based materials[191]. Hence, reducing the percentage of cobalt in cathode materials by partially replacing it with transition metals can cause a reduction in the material's TEC. Recently, a novel TEC offset approach was proposed by compositing the Co-containing cathode materials with negative thermal expansion (NTE) materials to reduce the overall TEC [192]. As a result, high-performance and durable cathode materials were developed. Although the cathode was for SOFC, the same strategy can also be extended to PCFCs.

Table 2.4: Notable cathode materials for proton-conducting solid oxide fuel cells.

Cathode	**Conductivity (Scm^{-1})**	**R_p ($\Omega\ cm^2$)**	**PPD ($mW\ cm^{-2}$)**	**Cell configuration**	**Ref.**
$Ba_2YCu_3O_{6+\delta}$	0.48	0.29@650	175	BYC│BZCY│Ni - BZCY	[193]
$La_{1.5}Ca_{0.5}NiO_{4+\delta}$		0.053@ 700℃	923	LCN│BZCY│Ni - BZCY	[194]
$Ba_{0.95}La_{0.05}Fe_{0.8}Zn_{0.2}O_{3-\delta}$		0.08@750℃	329	BLFZ│BZCYYb│Ni - BZCYYb	[195]
$Ba_{0.5}Sr_{0.5}Co_{0.8}Fe_{0.2}O_{3-\delta}$ (BSCF)		0.189@ 700℃	356@600℃	BSCF|BZCY721|Ni + $BaZr_{0.2}Ce_{0.7}Y_{0.1}O_{3-\delta}$ (BZCY721)	[196]
BSCF			276@600℃	BSCF|BZCY442|Ni + $BaZr_{0.4}Ce_{0.4}Y_{0.2}O_{3-\delta}$ (BZCY442)	[197]
BSCF			508@600℃	BSCF|BZCY305515|Ni + $BaZr_{0.3}Ce_{0.55}Y_{0.15}O_{3-\delta}$ (BZCY305515)	[198]
BSCF		0.5@600℃	380@600℃	BSCF|BCY|Ni + $BaCe_{0.9}Y_{0.1}O_{3-\delta}$ (BCY)	[199]

BSCF–Ag		245@600℃	BSCF–Ag|BZCY811|Ni + $BaZr_{0.1}Ce_{0.8}Y_{0.1}O_{3-\delta}$ (BZCY811)	[200]
$BaCo_{0.4}Fe_{0.4}Zr_{0.1}Y_{0.1}O_{3-\delta}$	0.2@600℃	970@500℃	BCFZY|BZCYYb + NiO (1 wt %)|Ni + $BaZr_{0.1}Ce_{0.7}Y_{0.1}Yb_{0.1}O_{3-\delta}$ (BZCYYb)	[104]
$Ba(Co_{0.4}Fe_{0.4}Zr_{0.1}Y_{0.1})_{0.95}Ni_{0.05}O_{3-\delta}$	0.607@550 ℃	450@550℃	BCFZYN|BZCYYb4411|Ni + $BaZr_{0.4}Ce_{0.4}Y_{0.1}Yb_{0.1}O_{3-\delta}$	[178]
$PrBaCo_2O_{5+\delta}$		305@600℃	PBC|BZCY721|Ni + BZCY721	[201]
$Ba_{0.9}Co_{0.7}Fe_{0.2}Nb_{0.1}O_{3-\delta}$	0.046@ 600℃	1062@600℃	BCFNb|BZCY721|Ni + BZCY721	[202]
$PrBa_{0.5}Sr_{0.5}Co_{1.5}Fe_{0.5}O_{5+\delta}$	0.056@ 600℃	2160@600℃	PBSCF|BZCYYb4411|Ni + $BaZr_{0.4}Ce_{0.4}Y_{0.1}Yb_{0.1}O_{3-\delta}$ (BZCYYb4411)	[156]
$BaCo_{0.7}(Ce_{0.8}Y_{0.2})O_{3-\delta}$	0.1@600℃	1150@600℃	BCCY|BZCYYb|Ni + BZCYYb	[202]

Chemical and physical stability

Stability is one of the essential yardsticks to assessing the quality of a cathode material used in proton-conducting solid oxide fuel cells. Any material selected as a cathode for PCFC must possess reasonable chemical stability in CO_2 and humid air. Ba and Sr are common A-site elements in cubic ABO_3, and double perovskites are used as cathodes in PCFCs because of their large ionic size and effect on promoting better oxygen pathways. However, these alkaline earth metals are susceptible to reacting with CO_2 in acidic gases-containing environments, thereby causing degradation in the fuel cell performance. Despite stability being a crucial quality in PCFC cathodes, its development has drawn less attention than the effort exerted to improve the performance of PCFC cathodes. Several articles have confirmed that using monovalent ions such as Zr^{4+}, $Hf^{4+,}$ and Yb^{3+} to dope cathode materials can significantly enhance the stability and activity of the cathode material. Tsvetkov et al. [203] hypothesized and investigated if using less reducible cations such as Hf^{4+}, Zr^{4+}, Ti^{4+}, $Nb^{5+,}$ and Al^{3+} can influence the stability of a model perovskite material, $La_{0.8}Sr_{0.2}CoO_3$ (LSC). The study's outcome revealed that these less reducible cations improved the stability and the oxygen exchange kinetics. Also, another potential aspect that could adversely affect the stability of the cathode electrode material is the TEC mismatch between the cathode material and other cell components, such as the anode and electrolyte. This aspect is challenging for cathode material development in conventional SOFCs and PCFCs. For instance, Figure 2.14 illustrates a schematic of various perovskite materials used as either cathode, electrolyte, or anode material for the conventional SOFCs. It is clear from the schematic that different material categories have disparate TECs. Hence, stability does not necessarily increase the ORR but ensures the cathode material's durability. For instance, cobalt-based cathodes possess better ORR and hence better performance, but they exhibit relatively poorer stability than cobalt-free cathode materials.

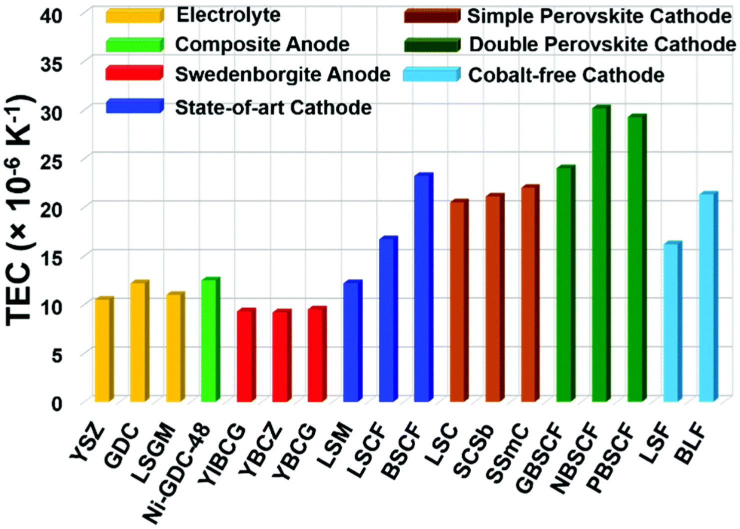

Figure 2.14: TECs for different SOFC component parts with their various constitutive compositions[204] highlighted as follows: $Zr_{0.84}Y_{0.16}O_{1.92}$ (YSZ)[193], $Ce_{0.8}Gd_{0.2}O_{1.9}$ (GDC) [205],$La_{0.8}Sr_{0.2}Ga_{0.8}Mg_{0.2}O_{3-\delta}$ (LSGM) [206], 48 vol% Ni–GDC (Ni-GDC-48, porous, 75% theoretical density) [207], $Y_{0.9}In_{0.1}BaCo_{3.3}Ga_{0.7}O_{7+\delta}$ (YIBCG) [208], $YBaCo_3ZnO_{7+\delta}$ (YBCZ) [208], $YBaCo_{3.2}Ga_{0.8}O_{7+\delta}$ (YBCG)[208], $La_{0.8}Sr_{0.2}MnO_{3-\delta}$ (LSM)[209], $La_{0.6}Sr_{0.4}Co_{0.2}Fe_{0.8}O_{3-\delta}$ (LSCF)[210], $Ba_{0.5}Sr_{0.5}Co_{0.8}Fe_{0.2}O_{3-\delta}$ (BSCF)[211], $La_{0.6}Sr_{0.4}CoO_{3-\delta}$ (LSC)[212], $SrCo_{0.9}Sb_{0.1}O_{3-\delta}$ (SCSb)[213], $Sr_{0.5}Sm_{0.5}CoO_{3-\delta}$ (SSmC)[214], $GdBa_{0.5}Sr_{0.5}Co_{1.5}Fe_{0.5}O_{5+\delta}$ (GBSCF)[215], $NdBa_{0.5}Sr_{0.5}Co_{1.5}Fe_{0.5}O_{5+\delta}$ (NBSCF)[215], $PrBa_{0.5}Sr_{0.5}Co_{1.5}Fe_{0.5}O_{5+\delta}$ (PBSCF)[215], $La_{0.6}Sr_{0.4}FeO_{3-\delta}$ (LSF) [216], and $Ba_{0.95}La_{0.05}FeO_{3-\delta}$ (BLF) [217].

Figure 2.15 illustrates a schematic representation of the different TECs for different cathode and electrolyte materials used in PCFCs, and Table 2.4 provides the details of each electrolyte or cathode compound represented in **Figure 2.15**.

Table 2.5: TECs of different cathode and electrolyte materials for PCFCs.

Material	**Abbrev.**	**TEC ($\times 10^{-6}$) K^{-1}**		**Ref.**
		Cathode	**Electrolyte**	
$La_{0.5}(Ba_{0.75}Ca_{0.25})_{0.5}Co_{0.8}Fe_{0.2}O_{3-\delta}$	LBCCF	21.7		[218]
$BaZr_{0.1}Ce_{0.7}Y_{0.1}Yb_{0.1}O_{3-\delta}$	BZCYYb		10.5	[218]
$Y_{0.8}Er_{0.2}BaCo_{3.2}Ga_{0.8}O_{7+\delta}$	YEBCG	8.41		[219]
$(Ba_{0.85}Sr_{0.15})(Zr_{0.7}Ce_{0.1}Y_{0.2})O_{2.9}$	BSZCY151020		~10	[220]
$BaZrO_3$	BZO		7.13	[119]
$BaCeO_3$	BCO		11.2	[119]

$SrZrO_3$	SZO		9.7	[221]
$SrCeO_3$	SCO		11.1	[221]
$BaZr_{0.80}Y_{0.20}O_{3-d}$	BZY		8.2	[222]
$BaZr_{0.60}Ce_{0.2}Y_{0.2}O_{3-d}$	BZCY		9.1	[222]
$BaZr_{0.1}Ce_{0.7}Y_{0.2}O_{3-d}$	BCZY		10.1	[223]
$Zr_{0.84}Y_{0.16}O_{1.92}$	YSZ		10.5	[193]
$La_{1.5}Ca_{0.5}NiO_{4+\delta}$	LCN	14.6		[194]
$Ba_{0.95}La_{0.05}Fe_{0.8}Zn_{0.2}O_{3-\delta}$	BLFZ	20.4		[195]

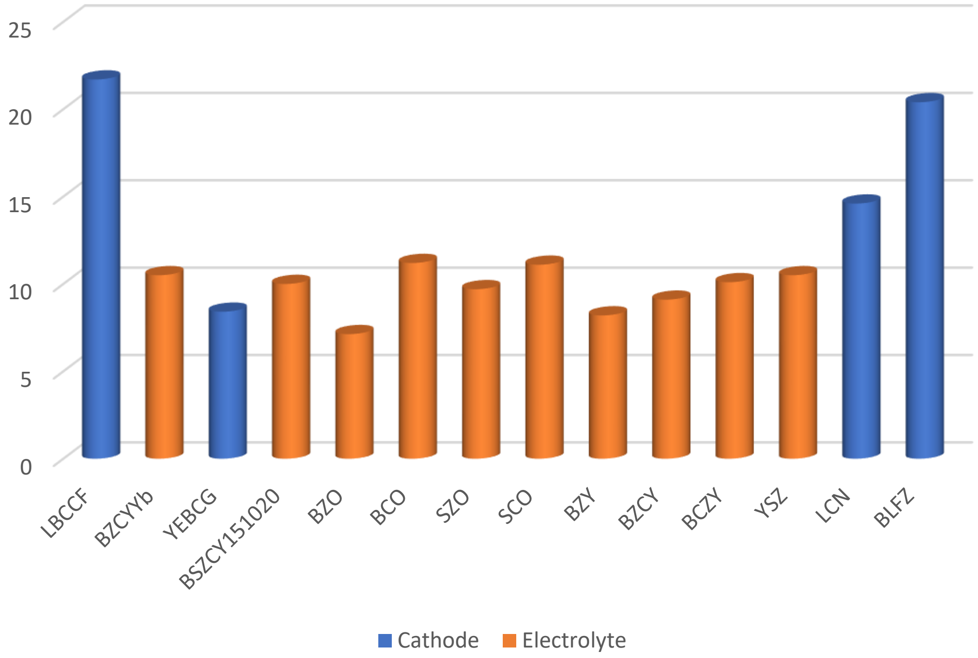

Figure 2.15: TECs of cathode and electrolyte materials for PCFCs.

Finally, it is also expected that PCFC cathode materials should have high porosity. Although, this porosity is not an intrinsic quality achieved by processing. The availability of high porosity will ensure enough transport paths for oxygen and steam molecules diffusion [224].

2.6.3 Anode materials development for PCFCs

The anode is one of the essential components of proton-conducting solid oxide fuel cells. However, it has attracted less attention compared to electrolyte and cathode materials. The anode electrode material for PCFC should have electronic and proton conductivity to increase the number of electrochemically active sites and facilitate an efficient hydrogen oxidation reaction. A hydrogen molecule is oxidized at the anode to produce two protons and two electrons, as illustrated in Eqn 2.11.

$$\mathrm{H_2} \rightarrow 2\mathrm{H^+} + 2\mathrm{e^-} \qquad (2.11)$$

The design of anode materials for proton-conducting solid oxide fuel cells is like that of oxygen ion-conducting solid oxide fuel cells. The PCFC anodes are cermets produced by mixing NiO with a proton-conducting electrolyte in which the NiO is subsequently reduced to Ni. This reduction of NiO to Ni consequently leads to the generation of porosity which is necessary for gas diffusion and continuous electronic pathway. The rule of thumb is that a composite anode material is formed by combining an electronic conducting phase (i.e., Ni) with a proton-conducting oxide. Therefore, the proportion of the electronic and proton-conducting phases, the microstructure, and the particulate size of the anode material must be decided carefully because they significantly influence the cell's performance. The triple-phase boundary increases with an increasing anode surface area which also speeds up the reaction kinetics. This desirable large surface area can be increased by using powders with small average grain sizes. More so, it has been demonstrated that improved symmetric cell performance could be achieved by controlling the anode porosity [225–227].

One of the studies which attempted to gain insights into the reactions at the anode for PCFCs to develop superior anode materials is the research conducted by Pers et al. [225]. They investigated the effect of temperature and atmosphere on the hydrogen oxidation reaction at the Ni-$BaZr_{0.1}Ce_{0.7}Y_{0.1}Yb_{0.1}O_{3-\delta}$ (BZCYYb) interface using impedance spectroscopy at different hydrogen partial pressure in the temperature of 350 – 600 ℃. They asserted that the hydrogen dissociation step is the rate-limiting step for the hydrogen oxidation reaction. Consequently, the polarization resistance of the cermet Ni-BZCYYb was 0.049 Ω cm^2 at *600* ℃ when hydrogen fuel was used.

Also, Essoumhi et al. [228] investigated the microstructure and electrical characteristics of two cermets (ceramic-metal composite) with different Ni content using $BaCe_{0.9}Y_{0.1}O_{2.95}$ ceramic nanopowders. The proportion of Ni in both cermets (i.e., Ni-BCY) is 35 and 45 vol. %, equivalents to 50 and 60 wt% NiO. It was discovered that an increase in Ni content improved the porosity and electrical properties of the electrodes.

Chevallier et al. [229] presented a novel wet-chemical route approach for preparing Ni–$BaCe_{0.9}Y_{0.1}O_{3-\delta}$ cermet. This was achieved by dispersing BCY10 nanocrystalline powder in a nickel nitrate solution and sintering at 1000 ℃. It was found that the resulting cermet was not tolerant to the CO_2 atmosphere at a temperature of 700 ℃ due to the severe degradation encountered. This renders the use of Ni-BCY anode to be restricted to hydrogen fuel and highly unsuitable for hydrocarbon-based fuels.

Plekhanov et al. [108] investigated suitable and possible anode materials for $LaScO_3$-based proton-conducting electrolytes. Ni-LSS5 cermet was produced via solid-state and co-precipitation methods. They then subjected the LSS5 powder to different production and sintering temperatures in the range of 1400 to 1500 ℃ and observed the microstructural features and phase compositions. It was discovered that the electrical conductivity and chemical expansion of Ni-LSS were majorly influenced by its porosity as opposed to the notion of it being influenced by the various methods of synthesis employed. The samples' porosity and average grain size were estimated by scanning electron microscopy (SEM) image analysis. It was discovered that as the sintering temperature increases, the porosity decreases, as shown in Error! Reference source not found..

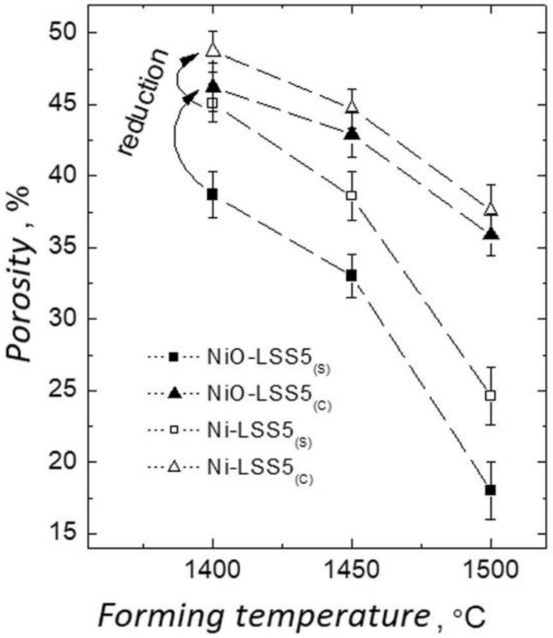

Figure 2.16: Porosity variation of the various specimens with increasing temperature [108]. Copyright 2021, Springer.

Onishi et al. [230] investigated the performance of Ni-BZY20 cermet used with $BaZr_{0.8}Y_{0.2}O_{3-\delta}$ (BZY20) electrolyte. Ni-BZY20 anode symmetrical cells with a 20-70 % NiO content were fabricated and tested. They found that an increase in NiO content complicated the sintering process, with cells failing at 80 wt% NiO. Hence, the proportion of NiO in the proposed cermet was recommended to be less than 70 wt% during cell fabrications.

Ni-based anodes have been vastly employed in SOFC applications due to their suitability and good performance. However, despite the benefits derived from Ni-based anodes, certain drawbacks have been identified especially when the cell operates at a temperature range of 500 – 800 ℃. [231]. Some drawbacks include Ni agglomeration, causing anode performance deterioration with time, and coke formation when hydrocarbon fuel is used. Nevertheless, only a few alternatives have been proposed, as in several instances, hydrogen-permeable metal membranes have been used as supporting anodic structures for protonic SOFCs [232,233].

Sintering of PCFC anode materials

Anode-supported cell construction is often employed in most proton-conducting solid oxide fuel cell fabrications. In this form of cell construction, the anode is made the thickest layer of the cell to provide mechanical support for the other cell components. The thick anode and thin electrolyte layers are often co-sintered at a high temperature. The essence of this is to provide the necessary support for the electrolyte and ensure good sinterability by enhancing the quality densification and conductivity of the electrolyte layer. Several studies have highlighted cermet's roles in ensuring quality sintering in P-SOFC electrolytes[47,144,145].

Duan et al. [104] expounded the use of sintering aids such as CuO and NiO to improve the densification of the various electrolytes investigated, which were $BaCe_{0.7}Zr_{0.1}Y_{0.1}Yb_{0.1}O_{3-\delta}$ (BCZYYb), $BaZr_{0.8}Y_{0.2}O_{3-\delta}$ (BZY20), and $BaCe_{0.6}Zr_{0.3}Y_{0.1}O_{3-\delta}$ (BCZY63). In decreasing order of stability, we have BZY20 > BCZY63 > BCZYYb. BCZY63 has relatively better sinterability and lower grain boundary resistance, while BCZYYb has the highest reported conductivity for P-

SOFCs. With a single-cell composition of 40 wt % BCZYYb + 60 wt % NiO | BCZYYb +1.0 wt % NiO | BCZY63 + BCFZY0.1, a peak power density of 0.455 W/cm^2 was achieved at a temperature of 500 ℃ when hydrogen fuel is used.

Furthermore, the sinterability and performance of the anode electrode are also influenced by the morphology of the electrode. For instance, the effect of the quantity of carbon microspheres pore-former on the porosity, line shrinkage, electrochemical performance, and thermal expansion of NiO-BCZY71 was investigated. It was discovered that electrode support with 30 wt% pore formers exhibited the best performance because of its excellent porosity and good triple-phase boundary reactions [234].

2.7 General synthesis and fabrication of protonic ceramic oxide materials

For years, manufacturing challenges have impeded the development of proton-conducting solid oxide fuel cells until recently, when novel methods of synthesizing and fabricating proton-conducting solid oxide fuels emerged. Some of those newly emerged methods for the processing and fabricating of proton-conducting solid oxide fuel cells are solid-state reactive sintering, anode-assisted densification of the electrolyte, extrusion, and interface modification [107].

The synthesis and fabrication of protonic ceramic oxide materials (PCOM) involve several high-temperature and energy-demanding procedures. These procedures are requisite to achieving the desired phases, microstructures, and other preferable cell component qualities such as porous electrodes, dense electrolytes, and highly stable and durable cells [224]. A study estimated that materials manufacturing cost accounts for about 30 % of the total proton-conducting solid oxide fuel cell manufacturing cost [142]. Therefore, it is essential to devise measures to significantly ameliorate the total manufacturing cost for proton-conducting solid oxide fuel cells by finding alternative and economical fabrication approaches.

Some prominently identified measures to significantly reduce PCOM fabrication cost are lowering various material processing temperatures and spotting compositions that do not require expensive precursors (i.e., salts or rare earth oxides). One of the recommended cost-effective methods of synthesizing and fabricating PCOM is solid-state reactive sintering (SSRS)[235]. With this approach, there is a possibility of reducing the arduous and lengthy manufacturing processes from above ten steps to just three or fewer in addition to the reduced sintering temperatures, time, and energy consumption. What makes the SSRS approach stand out is the fact that it aids the sintering process through the incorporation of a small portion of sintering aids (i.e., NiO, ZnO, and CuO), as expounded in previous sections.

In a study, a homogeneous distribution of ZnO was produced in the intergranular region when 4 wt. % ZnO was added to a well-crystallized BZY powder. The resulting modified grain boundary composition enhances electrolyte sintering and improves grain growth and boundary mobility caused by increased Ba vacancy concentration. Nevertheless, the grain boundary conductivity of unmodified BZY is not improved by introducing ZnO; instead, the grain boundaries are highly tuned. More so, the bulk conductivity of ZnO-modified BZY is relatively lower than that of the unmodified BZY. This work gave insight into the propensity of synthesizing P-SOFCs with lower sintering temperatures and optimized manufacturing processes [236].

Other studies leveraged the foundational concept of SSRS to incorporate phase formation, grain growth, and densification in just a single sintering step which consequently simplified the synthesis and lowered the fabrication cost of P-SOFCs [177,236,237]. Aside from NiO, other sintering aids such as Al_2O_3, LiF, and SnO_2 were investigated to see which significantly reduces sintering temperatures. It was found that NiO is the most effective sintering aid as it reduces the sintering temperature of BZY20 from above 1600 ℃ to 1400 ℃ with a positive densification rating above 95 %[130]. Furthermore, Tong et al. [142]employed a cost-effective SSRS approach to synthesize a high-quality Ni-BZY electrode. A record-breaking conductivity of 0.033 S/cm was achieved at 600 ℃ under a wet argon atmosphere. NiO is the most established and widely used sintering aid in reducing sintering temperatures for P-SOFCs[21,142,144–146,238].

Aside from sintering aids, the other factor which influences the effectiveness of SSRS is the nature of the processing. The effect of four different fabrication processes on the conductivity of BZY10 was studied by Ricote et al. [239]. The various fabrication processes include (a) SSRS (b) conventional sintering using powder prepared by solid-state with NiO as the sintering aid, (c) conventional sintering using powder prepared by solid-state reaction and then annealing at a high temperature of 2200 ℃ (d) spark plasma sintering (SPS). It was discovered that BZY10 prepared by SSRS as in (a) had the least grain boundary resistance while the resistivity of the other samples using the other fabrication methods in increasing order is: (c), (d), and (b). This confirms that the fabrication process does influence the activation energy for proton conduction across the grain boundaries. This suggests that Ni-decorated grain boundaries gotten through SSRS might promote proton conduction across grain boundaries. This phenomenon has been confirmed by Clark et al. [240] and Costa et al. [241]. However, Han et al. [242] asserted that the addition of NiO on BZCY-based electrolytes affects proton conductivity and dehydration temperature, and with time, ionic conductivity will also be affected. Based on this assertion, they concluded that NiO is detrimental to the performance of PCFCs.

Even though tremendous success has been recorded in the adoption and application of the SSRS approach, certain challenges still need to be addressed [243]. One of those challenges is the crossing over of electrons through the electrolyte or leaving residual second phases, which affect the cell performance. The existence of second phases at grain boundaries may negatively influence the cell's durability by reducing the electrolyte's mechanical strength and exposing it to failure. The highlighted challenges, however, do not obviate the recommendation and application of SSRS in the fabrication of PCFCs [104,244]. This is because many highly efficient and relatively cheaper PCOMs have been developed using the SSRS approach, thereby confirming the efficacy of this approach in PCOM synthesis and fabrication.

Another crucial area vital to the PCFC fabrication process is engineering suitable interfaces between the electrodes and electrolytes. Thermal and chemical incompatibility between the electrodes and electrolytes can result in the gradual delamination of PCFC parts, consequently depreciating the cell performance or even leading to cell failure. In curbing this challenge, some research works have suggested and used interfacial layers to improve the contact between the electrolyte and electrode layers[113,156,170,245–248].

The predominant technique for fabricating PCOM-based cells is through the traditional pressing and co-pressing of perovskite oxide powders. Researchers have investigated and attempted using tape casting techniques for cell fabrication in recent years to achieve a larger area, hence higher performance. In 2017, Jin et al.[242] proposed and successfully fabricated anode-supported BZCY-based cells by tape casting and suspension spraying. This is upscale in cell fabrication for PCFCs because it is more established in the traditional SOFCs. Hence, more effort is needed in this capacity to develop further ways to achieve meaningful upscale in the fabrication of PCFCs.

2.8 Prospective for PCFCs

2.8.1 Identified trends and future guidelines for PCFCs

This section summarizes recent progress and directions for protonic ceramic fuel cells. Based on the discussions in the previous sections and recent findings, the progress in the advancement of protonic ceramic fuel cells can be highlighted as follows:

(a) There has been an increasing propensity and drive toward more compositionally complex cathode materials with excellent triple conductivity designed explicitly for PCFCs. More so, it has been observed that most high-performance cathode materials always have an element of Co in their composition. Therefore, it will be prudent to assert that Cobalt-containing compounds are promising in achieving a cathode material with an excellent ORR, especially for low and intermediate-temperature PCFCs.

(b) There has been a dynamic shift from traditional BCY and BZY electrolyte materials to electrolytes with more complex compositions such as BCZYYb and BZCY, with BCZYYb being in the spotlight because of its all-round advantage which involves a balance in the stability, performance, ease of fabrication and performance.

(c) There has been a remarkable improvement in the performance of PCFCs using hydrogen fuels from about 0.3 W/cm^2 to 1.302 W/cm^2 at a temperature of 600 ℃ between 2013 and 2019. This represents a hallmark achievement in the advancement of PCFCs.

(d) Attention has been driven towards cathode development for PCFCs through the design of self-assembled triple-conducting nanocomposite materials.

(e) There has been an increasing interest in developing high-performance bifunctional cathode materials that can be used in PCFCs, PCECs, and RePCCs.

One of the critical future guidelines is the development of PCFCs with high durability under realistic working conditions. To achieve this, efforts must be intensified to develop PCFCs that can function efficiently below 400 ℃. A breakthrough in this regard will facilitate the commercialization process for PCFCs.

Hydrogen is an ideal fuel for fuel cells, including PCFCs. However, hydrogen production and storage efficiently and economically are still challenging. Nevertheless, hydrogen can be generated in the near future through proton-conducting electrolysis cells by using excess energy from renewable energy sources such as solar and wind energy. However, conventional hydrocarbon fuels such as natural gas will remain a primary fuel in the coming decades. Biogas, consisting of methane, hydrogen, carbon monoxide, etc., will increasingly play critical roles in future energy supply. Therefore, it is of practical importance to develop PCFCs running on conventional hydrocarbon fuels and renewable biogas. Direct hydrocarbon fuel can potentially help in this capacity and several studies have explored and demonstrated this possibility [156,177].

Stability and durability are also important considerations in P-SOFC development. The essential roles thermal and chemical stability play in the cell's durability have been addressed in previous sections. Stability is highly correlated with durability in P-SOFC development.

Reversible protonic ceramic cells

These energy storage devices efficiently combine the functionalities of protonic ceramic fuel cells and protonic ceramic electrolysis cells (RePCC). This innovative idea was borne out of the need to offset the intermittent nature of energy from renewable sources such as wind and solar, which have penetrated the energy market in recent years. The excess/waste energy from renewable energy sources during their peak periods can be used to convert electrical energy to chemical energy in the protonic electrolysis cell mode while during periods when the energy demand from the grid exceeds the supply, the stored chemical energy can be converted directly to electrical energy in the protonic ceramic fuel cell mode as illustrated in Figure 2.17. The merits of RePCC are (a) it is relatively more economical than chemical batteries on a larger scale, (b) it has a high round trip efficiency, (c) it does not require precious metals as catalysts as in the case of reversible polymer electrolyte membrane electrolysis cells, (d) it directly produces pure and dry hydrogen thereby saving cost and removing complexities associated with drying and external condensers, among others.

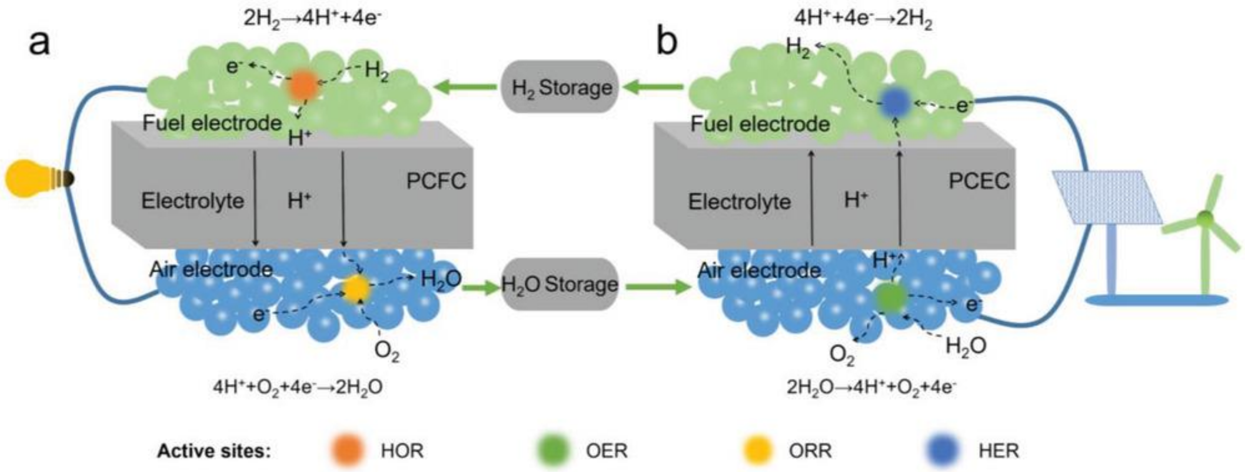

Figure 2.17: *RePCC operating in (a) protonic ceramic fuel cell mode and (b) protonic ceramic electrolysis mode.* Where HER = hydrogen evolution reaction, ORR = oxygen reduction reaction, OER = oxygen evolution reaction, HOR = hydrogen oxidation reaction [249]. Copyright 2021, John Wiley & Sons.

However, despite the numerous advantages of RePCC, one of the major identified challenges to its commoditization is the paucity of bifunctional electrodes which play a vital role in achieving highly stable and active electrodes with excellent oxygen evolution reaction (OER) and oxygen reduction reaction (ORR). High OER in RePCC implies an efficient surface exchange with proton and electron conduction, while a high ORR implies a good adsorptive dissociation and diffusion of oxygen, coupled with triple conductivity (i.e., involving protons, electrons, and oxygen ion). The functional materials' identified requirements cannot be obtained in a single-phase perovskite oxide material. Although some perovskite materials with excellent MIEC can be used as air electrodes for RePCC, they lack proton conductivity and are highly unstable under humid atmospheres [107,250]. Another approach employed for achieving excellent electrode materials for RePCC is the introduction of electronic conductivity into traditional proton conductors such as $BaCeO_3$ and $BaZrO_3$ by doping these materials with transition elements and rare earth metals to achieve materials such as $BaCo_{0.4}Fe_{0.4}Zr_{0.1}Y_{0.1}O_{3-d}$ and $Pr_{0.5}Sr_{0.5}Co_{1.5}Fe_{0.5}O_{5+d}$. Although these materials have excellent performances, there is a thermal mismatch between these electrodes and other components of the cell. Hence, other material improvement strategies must be considered that can cater to these enumerated challenges. Among those strategies to achieve this feat is the development of nanocomposite electrodes. Recently, Song et al.[249] presented an interesting and novel perspective based on nanocomposites for advancing bifunctional reversible protonic ceramic cell electrode materials with outstanding performances. Cerium and Nickel Oxide nanoparticles were used to embellish the surface of a nanocomposite electrode comprising Ruddlesden-Popper (RP) and tetragonal perovskite phases. It was discovered that the RP phases enhanced the proton transfer and hydration while the nanoparticles expedited the surface oxygen exchange and transfer of oxide ions from the surface to the major perovskite. This approach promises to create a pathway for achieving optimal reaction activity in electrolysis and fuel cell electrodes.

2.9 PCFC application and scale-up

PCFCs can be employed for stationary applications, especially as power supplies for residential devices such as combined heat and power (CHP) cogeneration systems, and other applications such as auxiliary power supplies and power sources for vehicles [251,252]. For these applications to be realized, there is a need for a scale-up. This task has been daunting due to various stability issues (such as thermal cycling and chemical incompatibility between the cell components) and insufficient knowledge about stack design and system integration [87,253–255]. There have been attempts to increase the active area of PCFCs from 0.5 cm^2 (often used in the labs) to over 50 cm^2 to explore the feasibility of large-scale production [161]. To achieve a scale-up, there must be a significant improvement in material advancement, improved fabrication procedures, and a better understanding of the various key operation mechanisms of the system. In realizing scale-up in PCFCs, some researchers have reported significant contributions that could aid in achieving this goal. For instance, Mu et al. [256] presented a unique digital approach that integrates precise micro extrusion of 3D printing and fast laser processing to achieve several developmental processes in PCFC fabrication, such as sintering, drying, cutting, and polishing. Tarutin et al. [257] also introduced a one-step sintering process for preparing multilayer PCFCs considering the compatibility of the components and more straightforward cell preparation methods. Likewise, the use of dynamic mechanical analysis to characterize the thermo-mechanical behavior of green tapes has been introduced by Mercadelli et al. [258]. This proposition promises to help achieve optimal lamination viscosity requisite for adhesion between cell parts regardless of the adopted tape formulation. Scaling up SOFCs and PCFCs is very challenging because it requires synergy and expertise contributions from disparate researchers (as observed from some of the scaling up contributing attempts by researchers) from different disciplines such as Material Science, Mechanical Engineering, Electrical Engineering, Control, and Automation, etc. The aspiration of scale-up in PCFC cannot be actualized by a single research group and this makes it even more complicated coupled with the associated costs. Hence, government and philanthropic aids might be required to achieve rapid scale-up in PCFC development.

2.10 Summary and Conclusion

This chapter has comprehensively analyzed the strategies for developing vital components of ceramic fuel cells, focusing on PCFCs. The electrolyte, cathode, and anode were examined in detail, covering their operational mechanisms, synthesis and fabrication methods, and performance and stability improvement strategies. Notably, this chapter has highlighted that the design of PCFC cathode materials requires careful consideration of their TIEC, which sets them apart from traditional SOFCs. In addition, this chapter has discussed the opportunities and challenges that must be overcome for the successful scale-up of PCFCs. The insights and recommendations provided in this review can inform the development of CFC materials that can enable the commercialization of this promising solid-state electrochemical energy conversion technology.

CHAPTER 3: METHODOLOGY

3.1 Background

The preceding chapters have extensively explored the current advancements in CECs, with a particular focus on the materials used in key components of CFCs. Research gaps and potential opportunities in this field have been identified. In this chapter, the essential aspects of the synthesis, fabrication, and electrochemical testing procedures utilized for examining the cathode materials in this study are presented. The subsequent chapters delve into further detailed and comprehensive procedural information, providing a deeper understanding of the methodologies employed.

3.2 Synthesis of cathode materials

All the cathode materials developed in this study were prepared using the EDTA-citric acid complexing sol-gel method. The synthesis of the cathode materials involved utilizing stoichiometric amounts of metal nitrates. A web-based application was developed to simplify the calculation of material weights, which facilitated accurate and efficient calculations. The application can be accessed at gramit.onrender.com. The web-interface of the application is presented in **Figure 4.3 & 3.2.** The web-based application represents the first novel initiative to develop an opensource platform to expedite the synthesis procedure for perovskite oxides using the sol-gel method.

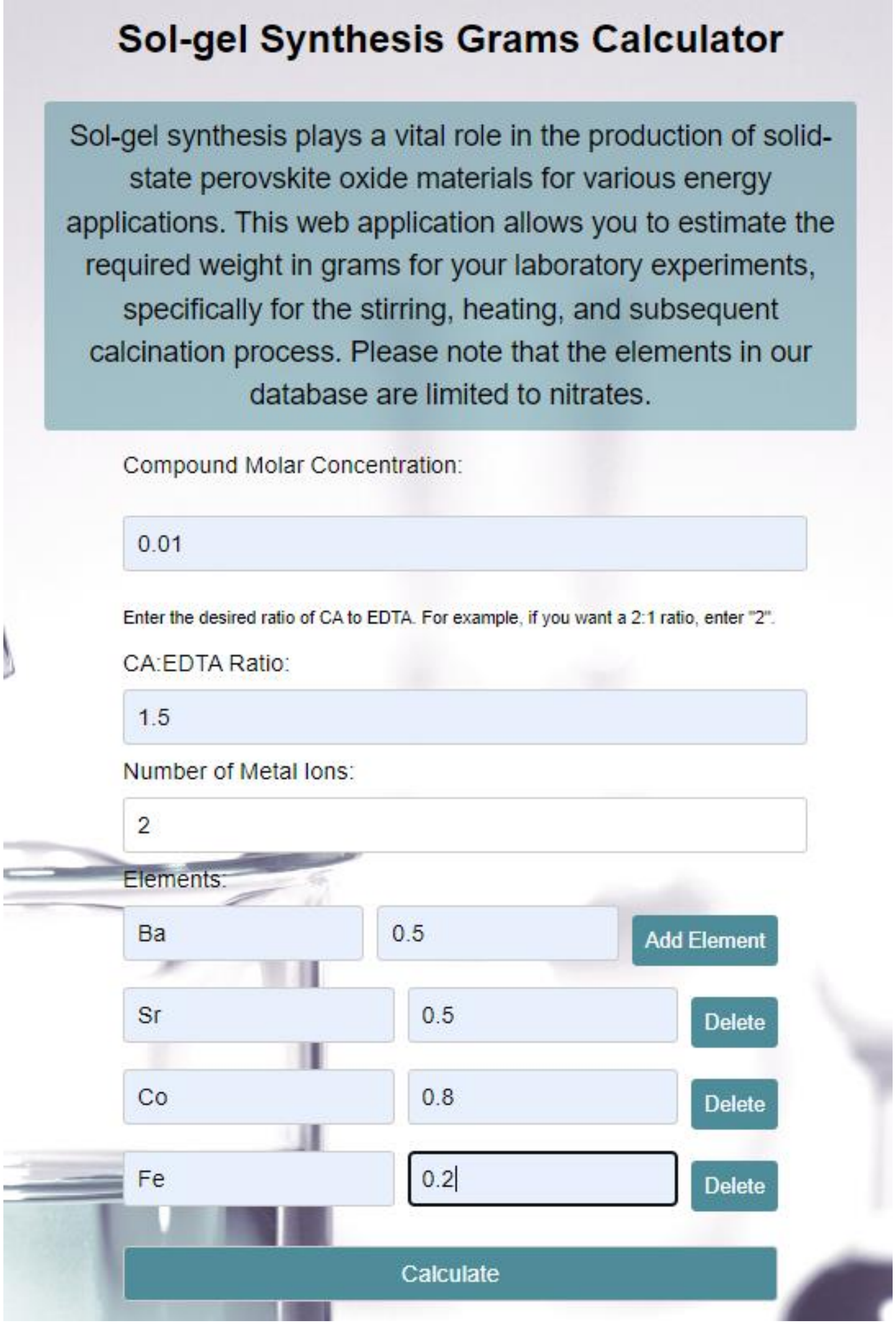

Sol-gel Synthesis Grams Calculator

Sol-gel synthesis plays a vital role in the production of solid-state perovskite oxide materials for various energy applications. This web application allows you to estimate the required weight in grams for your laboratory experiments, specifically for the stirring, heating, and subsequent calcination process. Please note that the elements in our database are limited to nitrates.

Compound Molar Concentration: 0.01

Enter the desired ratio of CA to EDTA. For example, if you want a 2:1 ratio, enter "2".

CA:EDTA Ratio: 1.5

Number of Metal Ions: 2

Elements:

Ba	0.5
Sr	0.5
Co	0.8
Fe	0.2

Figure 3.1: Interface to enter the compound molar concentration, CA: EDTA ratio, element symbols, and their molar fractions.

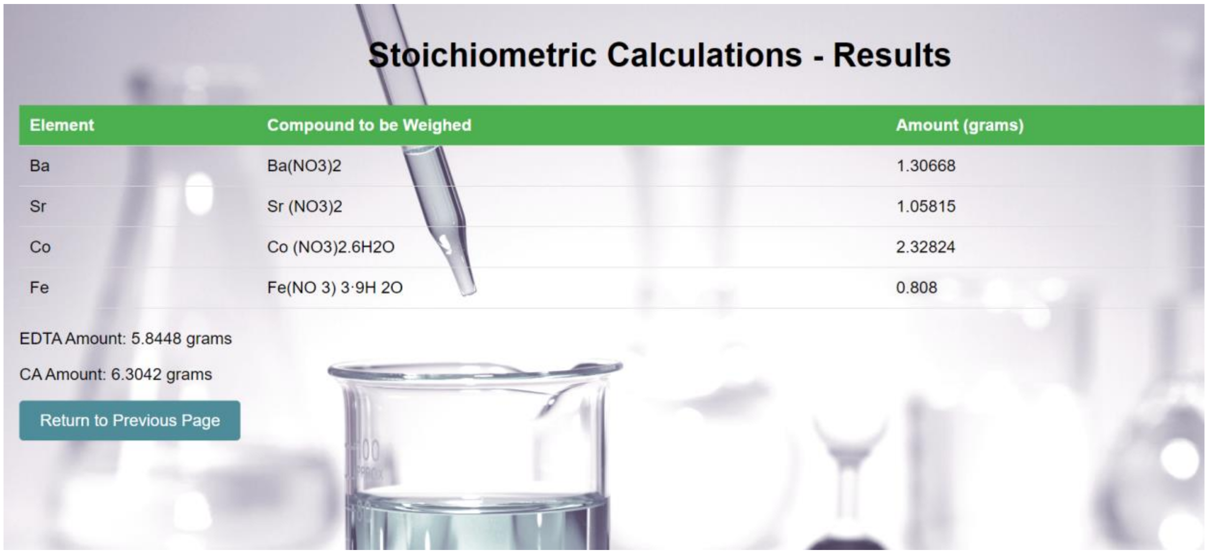

Stoichiometric Calculations - Results

Element	Compound to be Weighed	Amount (grams)
Ba	Ba(NO3)2	1.30668
Sr	Sr (NO3)2	1.05815
Co	Co (NO3)2.6H2O	2.32824
Fe	Fe(NO 3) 3·9H 2O	0.808

EDTA Amount: 5.8448 grams

CA Amount: 6.3042 grams

Figure 3.2: Output interface showing the results from the first page of the application.

Following the derived chemical reagents from **Figure 3.2**, the reagents were weighed and dissolved in deionized water while continuously stirring and heating the solution until a homogeneous mixture was obtained. Under the same conditions, the complexing agents were added to the solution, namely $C_{10}H_{16}N_2O_8$ (EDTA) and $C_6H_8O_7.H_2O$ (citric acid). The pH of the solutions was adjusted to a slightly basic level using NH_4OH. Stirring and heating were maintained until a gel is formed.

Subsequently, the gel was heated in an aerated oven at 180 ℃ for a minimum of 8 hours, forming a solid black precursor. The obtained precursors were then calcined at 1000 ℃ for 5 hours to produce the cathode materials.

3.3 Characterization

The crystal structure of the cathode powders synthesized in this study was investigated using an X-ray diffractometer (Rigaku SmartLab 9kW -Advanced). The diffraction patterns were observed within 20 to 80 degrees at a step size of 0.02 degrees. The diffraction patterns of the cathode powders were refined using FullProf opensource software. Scanning electron microscopy (SEM) was performed using either TESCAN MAIA3, VEGA, or MIRA instruments to examine the morphology of the powders. The microstructure of the calcined cathode powders was probed using high-resolution transmission microscopy (HR-TEM), Field Electron Microscope STEM, and JEOL Model JEM-2100F. For the electrical conductivity measurements, the as-synthesized powders were pressed at a pressure of 200MPa into dense bars with dimensions approximately 20 mm × 5 mm × 2 mm. These bars were sintered for 10 hours. The electrical conductivity was measured using a four-probe DC configuration and a Keithley 2440 source meter. The same bars were also used to determine the surface exchange kinetics (k_{chem}) and bulk diffusion (D_{chem}) coefficients using the electrical conductivity relaxation (ECR) technique. At first, the relative conductivity was determined using the expression:

$$g(t) = \frac{\sigma(t) - \sigma(0)}{\sigma(\infty) - \sigma(0)}$$

$$= 1 - \sum_{n=1}^{\infty}\sum_{m=1}^{\infty}\sum_{p=1}^{\infty} \frac{2C_1^2 \exp\left(-\alpha_{1n}^2 D_{chem}\, {}^{t}/_{l_1^2}\right)}{\alpha_{1n}^2(\alpha_{1n}^2 + C_1^2 + C_1)} \times \frac{2C_2^2 \exp\left(-\alpha_{2m}^2 D_{chem}\, {}^{t}/_{l_2^2}\right)}{\alpha_{2m}^2(\alpha_{2m}^2 + C_2^2 + C_2)} \times \frac{2C_3^2 \exp\left(-\alpha_{3p}^2 D_{chem}\, {}^{t}/_{l_3^2}\right)}{\alpha_{3p}^2(\alpha_{3p}^2 + C_3^2 + C_3)}$$

The coefficients $\alpha_{1n}^2, \alpha_{2m}^2, and\ \alpha_{3p}^2$ are the nth, mth, and pth roots of the following expressions:

$$C_1 = \alpha_{1n} \tan \alpha_{1n},\ C_2 = \alpha_{2m} \tan \alpha_{2m},\ \text{and}\ C_3 = \alpha_{3p} \tan \alpha_{3p}$$

The values of n = m = p was fixed to be 10 to ensure good accuracy of the fitted relaxations. Other details about the ECR procedure in this study can be found elsewhere[259,260].

X-ray absorption spectroscopy (XAS) data around the cobalt K-edge (specifically $Ba(CeCo)_{0.4}(FeZr)_{0.1}O_{3-\delta}$ and $BaCo_{0.4}Fe_{0.4}Zr_{0.1}Y_{0.1}O_{3-\delta}$) and cerium L-edge (specifically BCCFZ and BCZYYb) were collected at the TLS 01C1 beamline of the National Synchrotron Radiation Research Center (NSRRC) in Taiwan. The EXAFS data were processed using the ATHENA module described elsewhere[261].

3.4 Cell fabrication

The fabrication process for symmetrical cells, typically configured as cathode | electrolyte | cathode, involved several steps. Firstly, the electrolyte powders were weighed and pressed uniaxially to form dense pellets. These pellets were then sintered at either 1300 or 1450 ℃ for a duration of 10-12 hours.

Next, the cathode powders were mixed with ethylene glycol, isopropyl alcohol, and glycerol to create a colloidal suspension. The mixture was ball milled using Fritsch Pulverisette 6 at 400 rpm. The resulting colloidal suspensions were uniformly sprayed onto both sides of the dense electrolyte using a compressor pump and spray gun. The sprayed cells were then sintered at 850 ℃ for 2 hours, forming symmetrical cells with porous electrodes and electrolytes. Ag paste was applied evenly to both sides of the cell to serve as the current collector, and Ag wires were attached for electrochemical measurements.

As for the anode-supported single cells, typically configured as NiO-electrolyte | electrolyte | cathode, they were fabricated through dry pressing and co-sintering. Initially, the NiO-electrolyte cermet was produced by ball milling NiO, electrolyte, and starch powders in a ratio of 6.5:3.5:0.8 in pure ethanol for 1 hour. The resulting mixture was dried and then pressed into discs. Pure electrolyte powders were uniformly added and co-pressed onto the cermet at a higher pressure to achieve a dense electrolyte within the single cell. The co-pressed pellets were sintered at a specific temperature in a furnace.

Finally, cathode slurries were sprayed onto the electrolyte, then sintered at 850 ℃ for 2 hours, forming a single cell.

3.5 Electrochemical measurements

The symmetrical cells' ohmic and polarization resistances were determined by a combination of Solarton 1260 frequency response analyzer and Solarton 1287 potentiostat. The measurements were conducted within a temperature range of 400 to 650 ^{o}C. Under open circuit conditions, with no applied DC potential, the measurements were carried out using an AC amplitude of 10-30 mV in the frequency range of 10E6 Hz to 0.1 Hz.

The I-V-P (current-voltage-power) curves were obtained using a four-probe configuration with a Keithley 2440 source meter for the anode-supported single cells. The measurements were performed in the temperature range of 400 to 650 ^{o}C. In this setup, the anode side of the cells was supplied with pure H_2 at a constant specified flow rate, while the cathode side was exposed to ambient air.

3.6 Chapter Summary

This chapter comprehensively summarizes the methodology employed in developing cathode materials for ceramic electrochemical cells, specifically designed to operate at intermediate and low temperatures for clean energy generation. The synthesis process involved utilizing the EDTA-citric acid complexing sol-gel method. Detailed procedures for fabricating symmetrical cells and anode-supported single cells were presented, including steps such as pressing, sintering, and application of cathode slurries. The chapter also covers the procedure for conducting electrochemical measurements. This chapter serves as a comprehensive overview of the methodology, laying the groundwork for further investigations and analyses in subsequent chapters.

CHAPTER 4: LATTICE STRAIN EFFECTS ON ORR/CO_2 TOLERANCE OF PEROVSKITE-BASED CATHODES[2]

4.1 Background

The previous chapter comprehensively summarizes the methodology employed in synthesizing, fabricating, and testing cathode materials for CFCs. Building upon this foundation, the present chapter focuses on applying lattice engineering methodologies. Specifically, the effects of lattice contraction and expansion on the performance and CO_2 tolerance of $Ba_{0.5}Sr_{0.5}Co_{0.7}Fe_{0.3}O_{3-\delta}$ (BSCF), a functional cathode material for intermediate temperature operating SOFCs, are systematically investigated. This chapter aims to provide a detailed analysis of the influence of lattice engineering on the performance of the BSCF material in SOFCs, shedding light on its potential for enhanced functionality in real-world applications.

4.2 Introduction

The universal interest in ameliorating the increasing negative environmental impacts caused by fossil-based products has brought SOFCs to the limelight. Research has revealed that SOFCs are a viable solution to achieving a clean, safe, and highly efficient power source [31,262]. The current trend in the research for SOFCs is the development of low and intermediate temperatures (i.e., 350-700 ℃) SOFCs [7,100]. This is to enhance the service life, minimize material degradation and manufacturing costs, and fast-track the process of overcoming other challenges posed by SOFCs operating at high temperatures (i.e., 800-1000 ℃) [21]. However, the reduction of the operating temperature of SOFCs

---

[2] Fully published chapter:
Bello IT, Yu N, Zhai S, Song Y, Zhao S, Cheng C, et al. Effect of engineered lattice contraction and expansion on the performance and CO2 tolerance of Ba0.5Sr0.5Co0.7Fe0.3O3-δ functional material for intermediate temperature solid oxide fuel cells. Ceram Int 2022:100310. https://doi.org/10.1016/j.ceramint.2022.04.110

significantly decreases the electrolyte conductivity and cathode catalytic activity, causing an increase in the ohmic and polarization resistances of SOFCs [29,263]. The electrolyte ohmic loss can be reduced by fabricating thin-film electrolytes. However, the polarization loss at the cathode for oxygen reduction reaction (ORR) still limits the SOFC performance at reduced temperatures [7]. It is, therefore, paramount to develop cathode materials that can function efficiently at low and intermediate temperatures.

Excellent cathode materials for intermediate to low-temperature operating SOFCs are expected to exhibit mixed ionic and electronic conductivity (MIEC) so that the reaction zones for catalytic ORR can be extended from the traditional triple phase boundaries (TPB) to the entire surfaces of the cathode material [21]. Different categories of compounds, such as perovskite oxides, spinel oxides, Ruddlesden-Popper (RP) oxides, and fluorite oxides, have been proposed and developed as potential candidates to satisfy most or all the requirements of ideal cathode material. Perovskite oxide compounds of the form ABO_3 have been asserted to be the most promising candidates for intermediate and low-temperature SOFCs[7]. This is due to the possibility of modifying these oxides' A- and B- sites by doping by introducing strategic stoichiometric amounts of one or more elements into their A- or B- sites [264]. This doping could cause a change in their catalytic activities, CO_2 tolerance, and electronic structures. Strategic doping has been extensively applied to tailor the structural properties of innumerable perovskite oxide compounds in the form of lattice expansion and contraction for different functional applications. This action could help improve oxygen diffusion in cathode materials during operation, reduce materials' thermal expansion coefficient (TEC), enhance materials' tolerance to CO_2, and increase cathode materials' physical and chemical stability [265–269].

One of the cathode materials for SOFCs that has garnered lots of attention in the past decades is BSCF [270,271]. This material was reported to operate within the temperature range of 500 to 700 ℃ with a PPD of $1.01\ \mathrm{Wcm}^{-2}$, with an ASR of $0.071\ \Omega\ \mathrm{cm}^2$ at 600 ℃, exceeding the performance record achieved by any other cathode material before that time (i.e., 2004) [271]. Since then, it has often been used as the benchmark for assessing the performance of later-developed cathode materials for SOFCs. The major impediment, however, to the universal adoption of this material for commercial SOFC applications is its susceptibility to CO_2 poisoning in a realistic ambiance [272]. Therefore, researchers have adopted different mechanisms and approaches to modify the parent BSCF to improve its catalytic ORR at lower temperatures or enhance its stability and CO_2 tolerance [266,273–278]. No study, however, to the best of our knowledge, has reported the use of lattice engineering in the modification of the performance and CO_2 tolerance of BSCF.

Many studies have employed lattice engineering to influence cathode materials' catalytic ORR, stability, and CO_2 tolerance [269,279,280]. Escudero-Escribano et al.[279] outlined the introduction of contraction mechanisms in the structural lattices of electrocatalysts to tailor their activity, stability, and reactivity. Cai et al. [280] described using lattice engineering for tuning material band structures to achieve materials with improved performance and other desirable properties. Sun et al. [269] modulated the charge density of an active Cobalt atom in $LaCoO_3$ by introducing Ce ions into its lattice, thereby causing a contraction in the lattice structure of the material. This contraction consequently caused an improvement in the performance of the $LaCoO_3$ by reducing the electron tunneling distance, thereby optimizing the charge density distribution of the material.

TMs (i.e., Cu and Zn) are established dopants to optimize the properties of SOFC cathode materials [266,281]. For instance, the phase structure transition of $La_2Ni_{1-x}Cu_xO_4$ has been reported to be altered due to the introduction of Cu dopants [282]. Also, other interesting properties such as ORR and stability have been reported to be enhanced by co-doping Cu with other elements as in the case of Pr_2NiO_4 [283,284]. It has also been asserted that Cu dopants help to enhance the bulk oxygen diffusion and stability of cathode materials by reducing the

TEC of the cathode thereby improving the durability [285]. Zn dopant has also been used to modify the activity and stability of cathode materials [266,286,287]. However, the correlation of the activity and CO_2 tolerance of BSCF with lattice expansion and contraction has not explicitly been reported to the best of our knowledge.

In this study, we have systematically investigated the effects of engineering lattice expansion and contraction on the performance and CO_2 tolerance of the pristine BSCF air electrode functional material. We strategically substituted 5 mol.% Fe-B-site cations of BSCF with TMs, Zn, and Cu, to achieve an expansion and contraction, respectively. We were able to show how lattice engineering is a significant descriptor in illustrating the variability in the catalytic ORR and CO_2 tolerance of BSCF functional air electrode material.

4.3 Material and methods

4.3.2 Powder preparation

$\mathrm{Ba_{0.5}Sr_{0.5}Co_{0.7}Fe_{0.3}O_{3-\delta}}$ (BSCF), $\mathrm{Ba_{0.5}Sr_{0.5}Co_{0.7}Fe_{0.25}Cu_{0.05}O_{3-\delta}}$ (BSCFC5), and $\mathrm{Ba_{0.5}Sr_{0.5}Co_{0.7}Fe_{0.25}Zn_{0.05}O_{3-\delta}}$ (BSCFZ5), powders were synthesized by the EDTA-citric acid complexing sol-gel method. Stoichiometric amounts of the following chemical reagents from Sinopharm: $Ba(NO_3)_2$, $Sr(NO_3)_2$, $Co(NO_3)_2.6H_2O$, $Fe(NO_3)_3.9H_2O$, $Cu(NO_3)_2.3H_20$, and $Zn(NO_3)_2.6H_2O$ were used to synthesize BSCF, BSCFC5, and BSCFZ5, respectively. At first, a homogeneous solution was formed by dissolving stoichiometric amounts of the chemical reagents in deionized water under continuous stirring and heating conditions. After that, the complexing agents; $C_{10}H_{16}N_2O_8$ (EDTA) and $C_6H_8O_7.H_2O$ (citric acid) were added to the solution under the same condition. The pH of the solution was then adjusted using NH_4OH (Ammonium hydroxide) until a slightly basic pH is achieved. The stirring and heating condition was maintained until a gel-like fluid is formed. The gel was then heated in an aerated oven at a temperature of 180 ℃, for at least 8 h, until a solid black precursor is formed. The resulting precursors were then calcined at 1000 ℃ for 5h to generate BSCF, BSCFC5, and BSCFZ5.

4.4 Cell fabrication

4.4.1 Symmetric cells

To fabricate the following cells: BSCF│SDC│BSCF, BSCFC5│SDC│BSCFC5, and BSCFZ5│SDC│BSCFZ5, SDC powder (supplied by Fuel cell materials) were weighed at every instance and then pressed uniaxially to achieve a dense round pellet. The resulting pellets were then sintered at 1300 ℃ for 12 h. After that, the powders of BSCF, BSCFC5, and BSCFZ5 were mixed with ethylene glycol, isopropyl alcohol, and glycerol to form a colloidal suspension by ball milling the mixture using Fritsch Pulverisette 6 at 400 rpm for 30 minutes. With the aid of a compressor pump and spray gun, the resulting colloidal suspensions were then sprayed uniformly on both sides of the dense SDC electrolytes. This was followed by sintering at a temperature of 850 ℃ for 2 h to form symmetric cells comprising porous electrodes (i.e., with a thickness of about 17 µm and an area of 0.5 cm^2) and electrolyte. Afterward, Ag paste was uniformly brushed on both sides of the cell to serve as the current collector, and Ag wires were attached for taking electrochemical measurements.

4.4.2 Anode-supported single cells

The anode-supported single cells with the configurations NiO-SDC│SDC│BSCF, NiO-SDC│SDC│BSCFC5, and NiO-SDC│SDC│BSCFZ5 were fabricated through the process of dry pressing and co-sintering. At first, the NiO-SDC cermet was produced by ball milling NiO, SDC, and starch powders in the ratio of 6.5:3.5:0.8 in pure ethanol for 1 h. The resulting mixture was dried in the oven and then pressed into discs at a pressure of 100 MPa. This was followed by adding and co-pressing pure SDC electrolyte powders uniformly distributed across the cermet at 200 MPa to achieve a dense electrolyte in the single cell. The co-pressed pellets were then sintered in the furnace at a temperature of 1300 ℃ for 5 h. In the end, the cathode slurry was sprayed on the SDC electrolyte like the approach described in Section 0, followed by sintering at a temperature of 850 ℃ for 2h to achieve a single cell. The resulting thickness of the cathode, electrolyte and anode layers for the various cells was an average of $\sim$10 µm, $\sim$20 µm, and $\sim$430 µm, respectively, as illustrated in **Figure S3.2a.**

4.5 Materials characterization

The synthesized powders' phase purity and crystal structure were investigated using x-ray diffraction (XRD, Rigaku SmartLab 9kW). The diffraction patterns were collected through a stepwise scanning process (i.e., 0.02° step size) over 20 – 80°. Rietveld refinement of the XRD patterns for BSCF, BSCFC5, and BSCFZ5 was further carried out using FullProf Suite to get more detailed information about the crystal structures. Scanning electron microscopy (SEM) (TESCAN VEGA3) was used to investigate the material's morphology at an accelerating potential of 20 kV. High-resolution transmission electron microscopy, HR-TEM, FEI Tecnai G2 F20 was also used to characterize the microstructure of the calcined BSCFC5 powder. The powders of BSCF, BSCFC5, BSCFZ5 which were calcined at 1000 ℃ for 5 h were dry pressed at a pressure of 200 MPa into a rectangular shaped block of dimensions $\sim 20\, mm \times 5\, mm\ \times 2\, mm$ followed by sintering at 1050 ℃ for 5 h. Thereafter, the electrical conductivities of the samples were measured in the temperature range of 300 ℃ to 800 ℃ using the four-probe DC configuration with Keithley 2440 source meter at a temperature interval of 10 ℃ [276]. Solarton 1260 frequency response analyzer and Solarton 1287 potentiostat were used to measure the polarization resistances of the symmetric cell samples at a temperature range of 500 ℃ to 700 ℃ in air. The measurements were performed under an open circuit condition with zero applied direct current potential and a 10 mV applied alternating current amplitude under a frequency range of 10 kHz to 0.1Hz. Thereafter, the performance of single button cells based on the cathode materials considered was assessed using *I-V-P* polarization tests in the temperature range of 500 ℃ to 650 ℃ using a four-probe configuration with Keithley 2440 source meter. The anode side of the single cells was fed with H_2 at a constant flow rate of 100 mL/min, while the cathode side was exposed to ambient air.

4.6 Results and discussion

In perovskites, varieties of physicochemical properties related to their electrocatalytic behavior can be extracted from their crystal structure. **Figure 4.3a** illustrates the X-ray diffraction (XRD) profiles of BSCF, BSCFC5, and BSCFZ5 powders after calcination at 1000 ℃ for 5h. The profiles show that the perovskite structures of the powders are all single-phase with unique characteristic peaks. This confirms the successful doping of Zn and Cu into the perovskite lattice of BSCF to yield BSCFZ5 and BSCFC5, respectively. It can be observed from **Figure 4.3b** that the XRD pattern of BSCFZ5 shifted to a lower 2θ angle while that of BSCFC5 shifted to a higher 2θ angle. This confirms that the TMs doped into the Fe-B-site of BSCF led to an expansion and contraction in the unit cell volume. This suggests that the shrinkage and expansion in lattice cell volume could be due to the ionic radius of the substituted B-site element, Fe (Fe^{3+} = 0.645 nm, coordination = VI), relative to the introduced dopants, Zn (Zn^{2+} = 0.74 nm, coordination = VI) and Cu (Cu^{3+} = 0.54 nm, coordination = VI). In addition, the slight disparity in the crystal structures of both doped samples (BSCFC5 and BSCFZ5) could be attributed to the difference in the electronic structures of the dopant elements (Cu and Zn) relative to the main B-site element, Co [288–290]. **Figure 4.3c** illustrates the crystal structural diagram of an idealized cubic BSCFC5 perovskite oxide with its A-site cation being in 12 coordination with O^{2-} and its B-site cation being in six coordination with O^{2-}. Figure **4.3(d-f)** present the XRD refinement patterns for BSCF, BSCFC5, and BSCFZ5, respectively. The samples all have symmetric cubic structures with the same space group ($Pm\bar{3}m$), but different lattice constants as expressed in **Table 4.1**. These values are consistent with those of earlier reported BSCF-based perovskite materials [276,291].

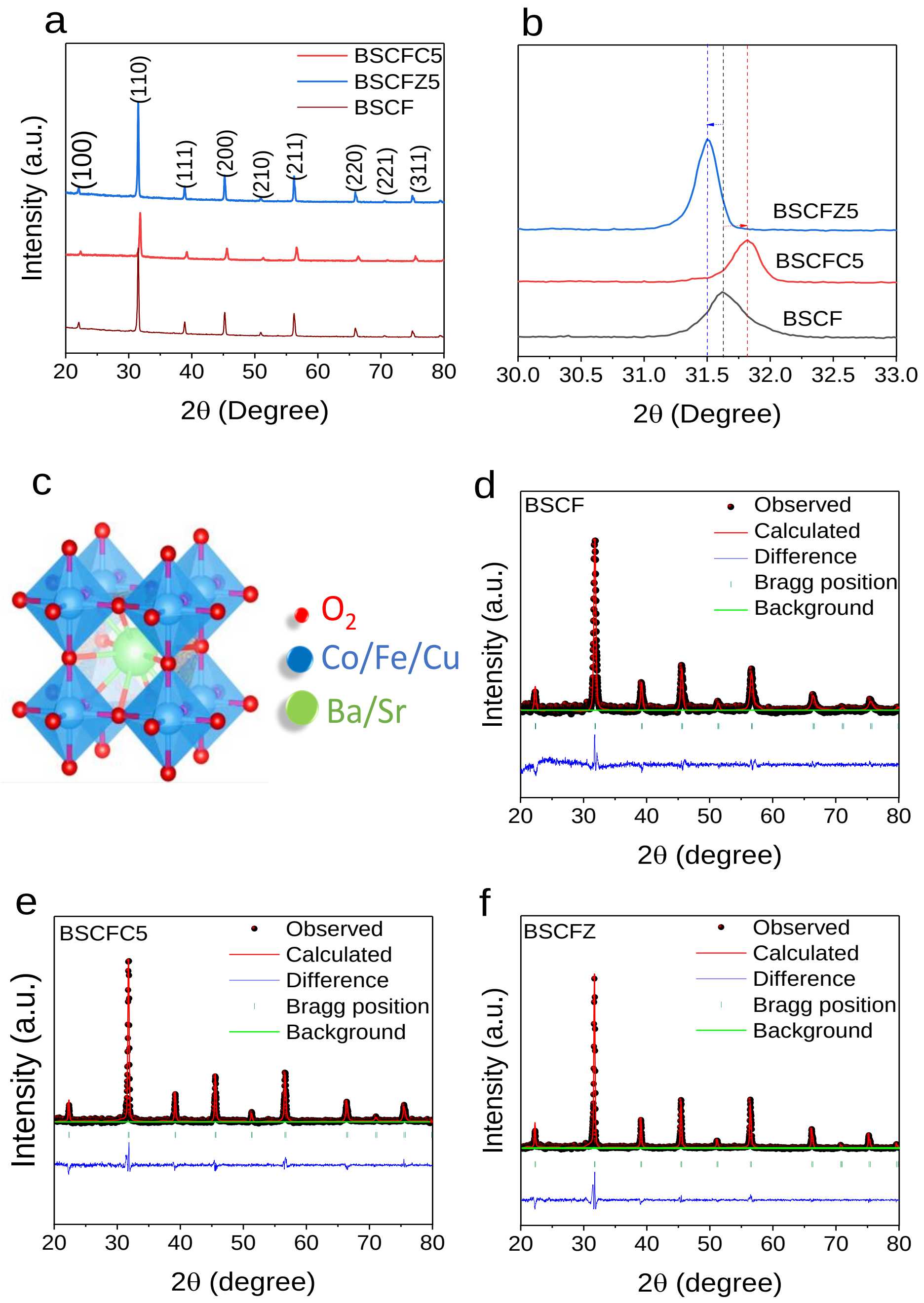

Figure 4.3: XRD patterns illustrating (a) the crystal structures for as-synthesized BSCF, BSCFC5, and BSCFZ5 powders (b) the magnified profile of the (110) plane of all the as-synthesized powders (c) cubic crystal structures of all the samples. Rietveld refinement for (d) BSCF (e) BSCFC5 (f) BSCFZ5.

Table 4.1 presents the lattice parameters, lattice volume, weighted profile reliability factor (wRp), integrated intensity reliability factor (Rp), and goodness of fit (χ^2) for BSCF, BSCFC5 and BSCFZ5. There is a good agreement between the observed pattern and the calculated profile, as illustrated in the data in **Table 4.1**, which establishes the reliability of the structural refinement model. There is an observed contraction and expansion in the lattice volume of BSCF when its Fe-B-site cation is partially substituted with 5 mol.% of Cu and Zn, respectively. This can be confirmed from the shifting of the diffraction peaks of BSCF to a higher and lower diffraction angle when doped with Cu and Zn, respectively, as illustrated in **Figure 4.3a**. This phenomenon is corroborated with the results from the Rietveld calculations presented in **Figure 4.3(d-f)** and **Table 4.1.**

Table 4.1: Refined lattice parameters for all the samples

Sample	a (Å)	b (Å)	c (Å)	V (Å)	wR_p (%)	R_p (%)	χ^2
BSCFC5	3.97944	3.97944	3.97944	63.02	8.44	6.87	1.72
BSCF	3.98116	3.98116	3.98116	63.10	6.18	4.44	1.49
BSCFZ5	3.99232	3.99232	3.99232	63.63	4.59	6.38	1.61

To gain more insights into the influence of the dopants on BSCF in terms of the observed lattice shrinkage and expansion as well as their cationic oxidations states, X-ray photoelectron spectroscopy (XPS) was employed to characterize the surface elemental distribution and composition of BSCF, BSCFC5, and BSCFZ5. **Figure 4.4** illustrates the deconvoluted XPS profiles for Co2p, Fe2p, O1s, Cu2p and Zn2p for BSCF, BSCFC5, and BSCFZ5. XPS core-level spectra of a TM inadvertently provide useful insights into the valence state and electronic structure of the TM ion. Hence, **Figure 4.4a** illustrates the spin-orbital splitting of Co $2p_{1/2}$ and Co $2p_{3/2}$ spectra which were deconvoluted using standard Gaussian-Lorentz. These resulting subpeaks could be designated as Co^{3+} and Co^{4+} as shown in **Figure 4.4a**. The binding energy values are in the range of ~792.97 eV – 795.82 eV at $2p_{1/2}$ and ~777.39 – 779.69 eV at $2p_{3/2,}$ which are consistent with past studies [267,292]. The spin-orbital splitting of Co 2p doublets is congruous with less than ~10 eV binding energy as detailed in **Table S4.2**. There are also no significantly identifiable satellite peaks in the binding energy range of ∼785 – 790 eV suggesting the absence of Co^{2+} in all the samples[267]. **Figure 4.4b** presents the XPS spectra of Fe $2p_{3/2}$ in BSCF, BSCFC5, and BSCFZ5 and specific details can be found in **Table S4.3**. The spin-orbital splitting of Fe 2p electron spectra was fitted into subpeaks corresponding to the valence states Fe^{3+} (708.05 – 709.26 eV) and Fe^{4+} (710.53 – 712.37 eV), respectively. These results conform with existing reports [293,294]. The binding energy values of Co 2p and Fe 2p in BSCFC5 advanced in the higher energy direction while those of BSCFZ5 retreat towards the low energy direction suggesting the existence of expansion and contraction in the lattice volume of the engineered BSCF samples. The higher binding energy advancement could shorten the pathway for oxygen transport thereby enhancing the catalytic performance of BSCF, while the retreat towards the lower energy direction could lengthen the distance for oxygen transport and affect the ORR of BSCF[269,295]. **Figure 4.4c** shows the deconvolution of the O 1s spectra of all the samples considered into two characteristic subpeaks namely: the adsorbed oxygen (OH^-, CO_3^{2-}, O^{2-}, and O^-∼531 eV) and the lattice oxygen (O^{2-}, ∼529 eV) [291,296]. The peak positions and estimated percentages of the surface oxygen for BSCF, BSCFC5, and BSCFZ5 depicted in **Figure 4.4c** are presented in **Table 4. 2.** The surface oxygen in all the specimens transforms in the order outlined in Eq. 4.1.

$$O_2 \leftrightarrow O_2 \xrightarrow{+e^-} O_2^- \xrightarrow{+e^-} O_2^{2-} \leftrightarrow 2O^- \xrightarrow{+2e^-} 2O^{2-} \quad (4.1)$$

Table 4. 2: Percentages of adsorbed and lattice oxygen for BSCF and BSCFC5

Sample	Adsorbed oxygen		Lattice oxygen		Ratio
	Peak position (eV)	Percentage (%)	Peak position (eV)	Percentage (%)	O_{ads}/O_{lat}
BSCF	530.92	81.36	528.82	18.64	4.36
BSCFC5	531.90	83.28	529.66	16.72	4.98
BSCFZ5	530.16	67.67	528.94	32.33	2.09

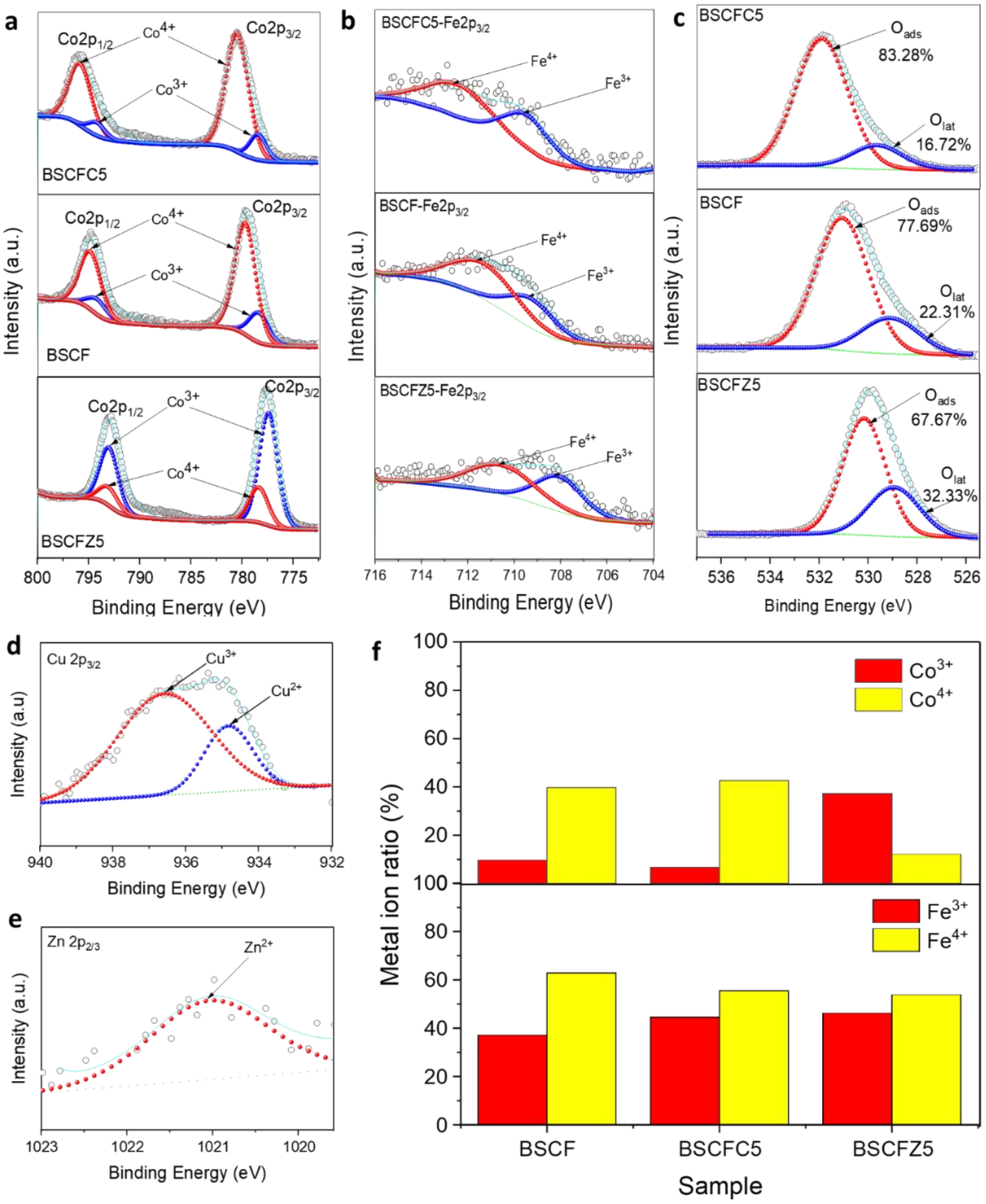

Figure 4.4: XPS spectra of the B-site elements of BSCF, BSCFC5, and BSCFZ5 (a) Co 2p (b) Fe 2p (c) O 1s. XPS spectra for (d) Cu 2p and (e) Zn 2p. (f) Percentage contribution of dominant B-site cations (a) Co$^{3+/4+}$ (b) Fe$^{3+/4+}$.

It can be observed from **Figure 4.4c** that the adsorbed oxygen for BSCFC5 is relatively higher than those of BSCF and BSCFZ5. This is because of the compressive strain on the lattice structure of BSCFC5; therefore, the relative volume of the adsorbates is increased and the pathway for oxygen diffusion in the lattice is shortened which will subsequently promote enhanced catalytic ORR. On the contrary, the smaller percentages of the adsorbed oxygen in BSCF and BSCFZ5 could be attributed to their relatively larger lattice volume since the pathway for oxygen diffusion will be extended. This phenomenon hints that the electrocatalytic performance of BSCFC5 could be better than those of BSCF and BSCFZ5 because of its higher O_{ads}/O_{lat} ratio which has been established in previous studies to influence ORR of cathode materials (i.e., the higher the ratio, the better the ORR)[297,298]. In the case of the Cu element depicted in **Figure 4.4d**, the Cu $2p_{3/2}$ spectra were deconvoluted into two peaks corresponding to Cu^{2+} and Cu^{3+} with binding energy values of ∼934.69 eV and ∼936.62 eV, respectively [299]. The Zn $2p_{3/2}$ spectrum from BSCFZ5 has a single peak which could be designated as Zn^{2+} (∼1021 eV) as depicted in **Figure 4.4e** [300]. The intensities of Co^{3+}/Co^{4+} and Fe^{3+}/Fe^{4+} were calculated from the XPS analysis as illustrated in **Figure 4.4f.** It can be inferred that there is more electroneutrality in BSCFC5 with its B-site cations having a +3/+4 charge (i.e., $[CoFeCu]^{+3/+4}$. This explains the reason for the contraction in the lattice of BSCFC5 because the ionic radius of Cu^{3+} (0.54 nm, coordination = VI) relative to the other B-site elements with +3 charge (Co^{3+} = 0.61 nm, coordination = VI and Fe^{3+} = 0.645 nm, coordination = VI) is lower [301]. This will inadvertently instigate contraction in its lattice. On the other hand, the ionic radius of Zn^{2+} (0.74 nm) is larger than all other B-site cations in BSCFZ5 thereby engendering expansion in its lattice.

The electrical conductivities of BSCF, BSCFC5, and BSCFZ5 with respect to varying temperatures, measured in pure air, are presented in **Figure 4.5**a. The obtained conductivity values (i.e., BSCF) reasonably conform with those reported in previous studies [199,302].

The substitution of Fe-B-site cation of BSCF with Cu leads to the formation of negatively charged defects which requires compensation by positively point charge defects in the form of either holes or oxide ions, as expressed in the mechanistic expression in Eq. 3.2, to achieve a state of equilibrium.

$$CuO \xrightarrow{BSCF} (Cu_{Fe}^{2+})'' + 2\dot{h} + \frac{1}{2}O_2 \qquad (4.2)$$

The resulting balance in Eq. 2 contributes to the redox equilibrium involving the Co and Fe species as expressed in Eq. 3.

$$Cu_{Fe}^{2+} \rightarrow (Cu_{Co}^{3+})' + 2\dot{h} \qquad (4.3)$$

However, the estimation of the conductivity of an MIEC material such as BSCF and its derivatives (BSCFC5 and BSCFZ5) using direct current measurements, as in this case, generates combined electronic and ionic conductivities which coincide with holes and oxide ion migration, respectively. The intensity of this phenomenon, however, is dependent on the temperature variation as expressed in the defect's equilibrium expressions in **Eq. 4.2** and **4.3**. Therefore, from **Figure 4.5**a, it can be inferred that at low temperatures, below the transition point (i.e., around 450-500 ℃), the nature of conductivity is predominantly electronic and above the transition point, the progressive increase of ionic behavior is prevalent as expressed in the mechanistic expression in **Eq. 4.3**.

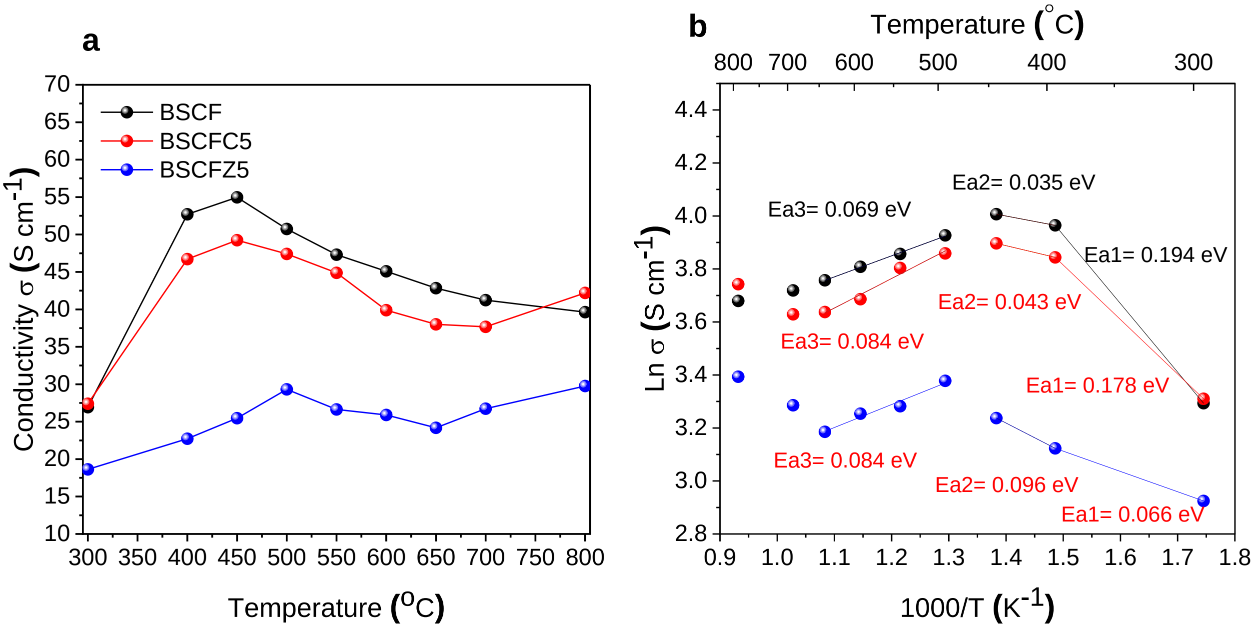

Figure 4.5: Dependence of electrical conductivity on temperature (a) conductivity of all the samples with respect to temperature (b) Arrhenius plots based on the electrical conductivity of the samples.

It can also be inferred from Arrhenius plots in **Figure 4.5b** that the order of decreasing conductivity in the samples studied can be summarized as BSCF>BSCFC5>BSCFZ5, implying that doping of BSCF did not enhance its electrical conductivity. This is because the substitution of Zn and Cu into the B-site of BSCF led to the reduction of Fe^{4+} and Co^{4+} to Fe^{3+} and Co^{3+}, respectively, thereby instigating the reduction in the charge carrier concentrations of BSCFZ5 and BSCFC5. This consequently engenders a decrease in the electrical conductivities of BSCFZ5 and BSCFC5 relative to BSCF. The conductivity behavior in the materials under consideration is non-uniform, hence the activation energies were estimated at several temperature ranges and the cumulative activation energies were summarized in **Table S4.4**. These activation energies were estimated using the expression $\sigma = \sigma_o e^{\frac{-Ea}{kT}}$, where Ea is activation energy and k is Boltzmann constant, T is the absolute temperature and σ_o is the pre-exponential factor. It can be observed that the BSCF has the least activation energy in the intermediate temperature range of (500 – 650 ℃), followed by BSCFC5. However, in the low-temperature range of 300 – 400 ℃, BSCFZ5 has the least activation energy (i.e., 0.084 eV) which makes it eventually possess the smallest cumulative activation energy as depicted in **Table S4.4.**

Figure S4.1 presents the morphology of the BSCFC5 comprising the cross-section of the single cell. In **Figure S4.1a**, the SEM image of the single cell of BSCFC5 shows the layers of the anode, electrolyte, and cathode with their dimensions. The different layers are fused without any apparent significant debonding. It can also be observed that the anode and cathode are reasonably porous enhancing gas diffusion, and the electrolyte is well compacted to allow strictly for the migration of the oxygen ionic species. **Figure 4.6a** shows the Scanning transmission electron microscopy image (STEM) of BSCFC5. **Figure 4.6b** confirms that the distribution of all the elements, within the single grain, in the observed STEM image on the scale of 100 nm from **Figure 4.6a** are homogenous. The Energy dispersive spectroscopy (EDS) mapping in **Figure 4.6c** confirms that all the elements intended to be in BSCFC5 are present. The atomic percentages of the constitutive elements in BSCFC5 are also consistent with the stoichiometric proportion of the as-synthesized perovskite powder described in the materials synthesis section. The d-spacing for the BSCFC5 from the HR-TEM image was estimated to be 0.288 nm, corresponding to the plane (110), as illustrated in **Figure 4.6d.**

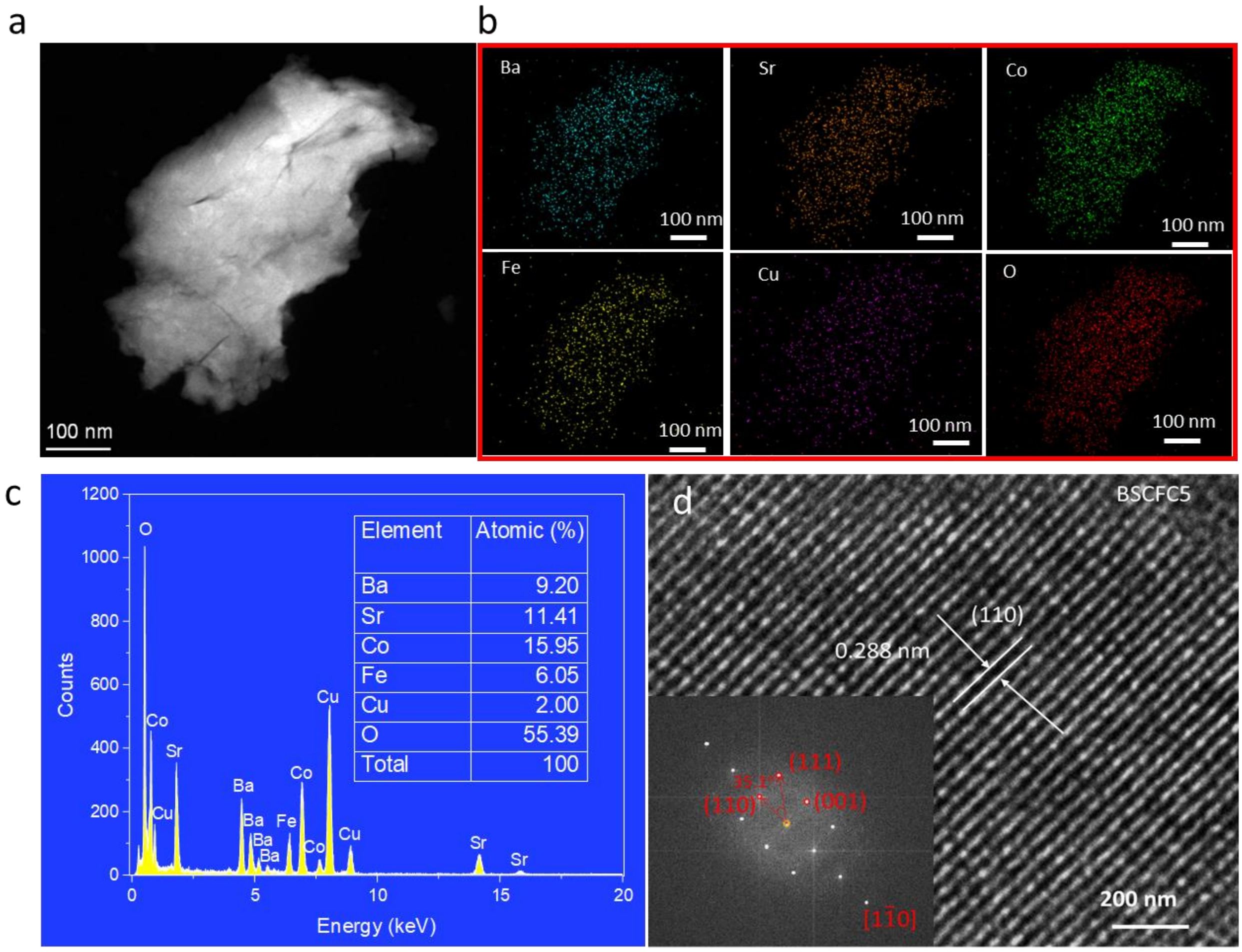

Element	Atomic (%)
Ba	9.20
Sr	11.41
Co	15.95
Fe	6.05
Cu	2.00
O	55.39
Total	100

Figure 4.6: Schematics showing: (a) STEM of BSCFC5 (b) the energy-dispersive X-ray (EDX) of the constitutive elements in BSCFC5 (c) EDS mapping of the constitutive elements in BSCFC5 and their atomic percentages (d) the HR-TEM image of the BSCFC5.

The electrochemical performances of BSCF, BSCFC5, and BSCFZ5 cathode materials were evaluated using symmetric cells with SDC as the electrolyte in each case. The characterization of performances of the cathode materials was achieved by taking electrochemical impedance spectroscopy (EIS) measurements. **Figure 4.** 7**a** presents the Nyquist plots of the EIS data measured at 600 ℃ for all the cathode materials considered. The difference between data points corresponding to high- and low-frequency values intercepting the horizontal axis of the Nyquist plot represents the area-specific resistance as illustrated in **Figure 4.** 7**b**. Based on this, the ASRs for the BSCF, BSCFC5 and BSCFZ5 at 600 ℃ are 0.081 Ω cm^2, 0.054 Ω cm^2 and 0.278 Ω cm^2, respectively. BSCFC5 exhibits the least ASR, followed by BSCF, and then

BSCFZ5. The equivalent circuit model, R_{Ω}-(R_{E1}/CP_{E1})-(R_{E2}/CP_{E2}), was used to fit the EIS results of all the samples. The high-frequency polarization resistance can be attributed to the charge transfer process of oxygen ions at the interface between the electrode and the electrolyte while the low-frequency polarization resistance values can be associated with the oxygen adsorption-dissociation process in the cathode electrode [303]. The ASRs of the cathode electrode materials from 700 ℃ to 500 ℃ are summarized in **Figure 4.** 7**d**. The BSCFC5 material exhibited the lowest ASR values (relative to the other materials) at all temperatures indicating that it has the best electrocatalytic ORR instigated by the contraction in its lattice structure. This suggests that lattice contraction could foster an improved performance of cathode materials as opposed to the supposition that lattice expansion alone promotes improved ORR. This is because the substitution of the Fe-B-site cation of BSCF with 5 mol.% Cu causes a reduction in the oxidation states of Co and Fe. This consequently shortens the pathway for oxygen diffusion thereby accelerating the catalytic ORR kinetics. Also, it could be due to the weakening of the adsorption energy of the reactive intermediates caused by the Cu dopant leading to reduced strength in surface bonds as extensively elaborated in previous studies[304–307]. This could be corroborated by the reduced performance of BSCFZ5 despite the expansion in its lattice volume. The reduced electrocatalytic performance of BSCFZ5 however, could be attributed to the strengthening of the adsorption energy of the constitutive reactive intermediates thereby increasing the strength of the surface bonds in the perovskite structure[304]. Also, the pathway for oxygen diffusion is increased causing a reduction in the catalytic ORR of the parent BSCF material. Further insights into the electroactivity of the materials were investigated by estimating the activation energies for each of the cathode materials using the Arrhenius plots generated from the ASR values of the respective cathode materials in **Figure 4.** 7**c**. BSCFC5 was observed to have the least activation energy of 1.110 eV confirming the superiority of its electrocatalytic performance to BSCF. **Table S4.5** illustrates the comparison of the ASRs of various non-composite single-phase cathode materials that were derived from the traditional BSCF.

Since BSCFC5 demonstrated a better ASR relative to BSCF, and BSCFZ5 the improved ORR can be further expatiated by observing the effects of oxygen partial pressure (PO_2) on the area-specific resistance at different temperatures**. Figure 4.** 7 (**e-f)** illustrates the variation in polarization resistances relative to changes in oxygen partial pressure. The relation $\mathrm{R_p} \propto (\mathrm{PO_2})^{-\mathrm{n}}$ can be used to express the relationship between polarization resistance R_p and oxygen partial pressure (PO_2). The value n represents the rate-limiting step of oxygen reduction reaction as confirmed in previous studies [307–309]. This n exponent value has different connotations regarding the rate-limiting step for ORR depending on its value. When n = 0, 0.25, 0.375, 0.5, and 1, it means the rate-limiting step for ORR is due to ionic oxygen transfer from the triple-phase boundary to the electrolyte, charge transfer process on the electrode, charge transfer process at the triple-phase boundary, surface oxygen adsorptive dissociation and molecular oxygen adsorption and diffusion at the electrode surface, respectively [310]. It can be observed from **Figure 4.** 7 (**e-f)** that the polarization resistance decreases with an increasing oxygen partial pressure. From **Figure 4.** 7**e,** the rate-limiting steps for oxygen reduction reaction of the cathode materials at $600\ ℃$ can be translated to be the charge transfer process on the electrode surface for BSCF and BSCFC5 while a charge transfer process at the triple-phase boundary is the rate-limiting step of ORR for BSCFZ5. However, the rate-limiting steps of ORR for BSCFC5 at $500\ ℃$ in **Figure 4.** 7**f** are predominantly molecular oxygen gas diffusion and partly surface exchange at the electrode surface.

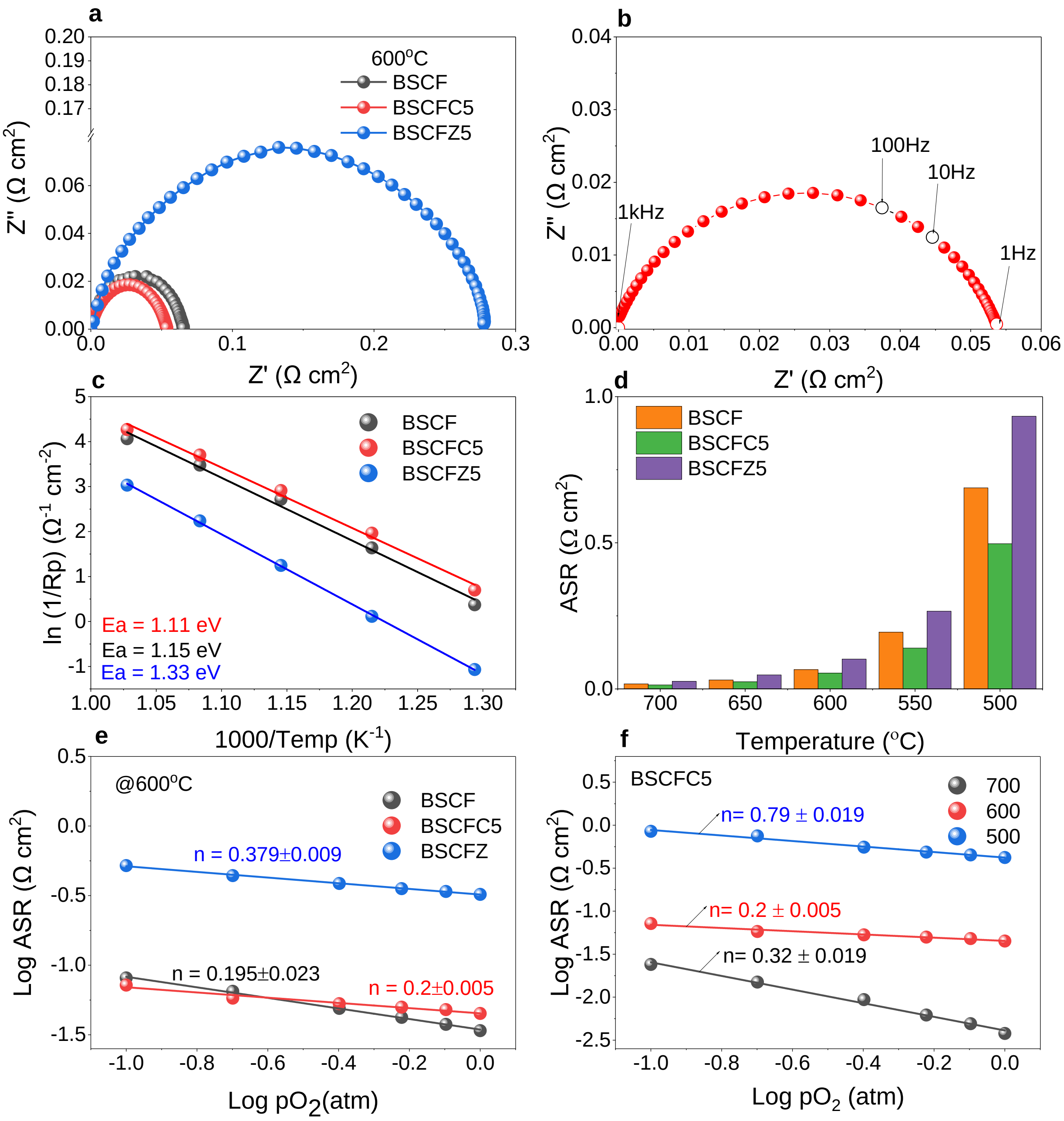

Figure 4. 7: (a) Electrochemical impedance spectra for symmetric cells of BSCF, BSCFC5, and BSCFZ5 at **600** ℃ and (b) Impedance spectrum for the symmetric cell of BSCFC5 showing the frequencies for the charge transfer process and oxygen adsorptive-dissociation (c) Arrhenius plots of area-specific resistance values for BSCF, BSCFC5, and BSCFZ5 showing their various activation energies (d) The comparison of ASR of all the materials at different temperatures. The variation in area-specific resistances with respect to changes in oxygen partial pressures for (e) BSCF, BSCFC5, and BSCFZ5 at 600 ℃ and (f) BSCFC5 at **500** ℃, **600** ℃, and 700 ℃.

To further gain insight into the complex ORR mechanism of BSCFC5 at different operation temperatures, distribution of relaxation time (DRT) analysis was conducted using the DRT tools package developed by Ciucci's lab[311]. From **Figure 4.8**, the plots can be segmented into three parts designated as P1, P2, and P3. The low-frequency region denoted as P3 (with frequency value $\leq 10^1$ Hz) corresponds to oxygen gas diffusion while P2 corresponds to surface exchange and ion diffusion between the electrode and electrolyte and P1(with frequency value $\geq 10^3$ Hz) denotes the charge transfer process at the interfaces as earlier discussed above[79,312–315]. Hence, the predominant rate-limiting step for ORR at $600 - 700$ ℃ in BSCFC5 is the charge transfer process on the electrode, and at the triple-phase boundary as illustrated in **Figure 4.8**. It can also be observed that generally, the rate-limiting process for ORR in region P2 decreases with increasing pO_2 for BSCFC5 at 600 ℃ while the rate-limiting process at region P1 at the same temperature were all fairly the same.

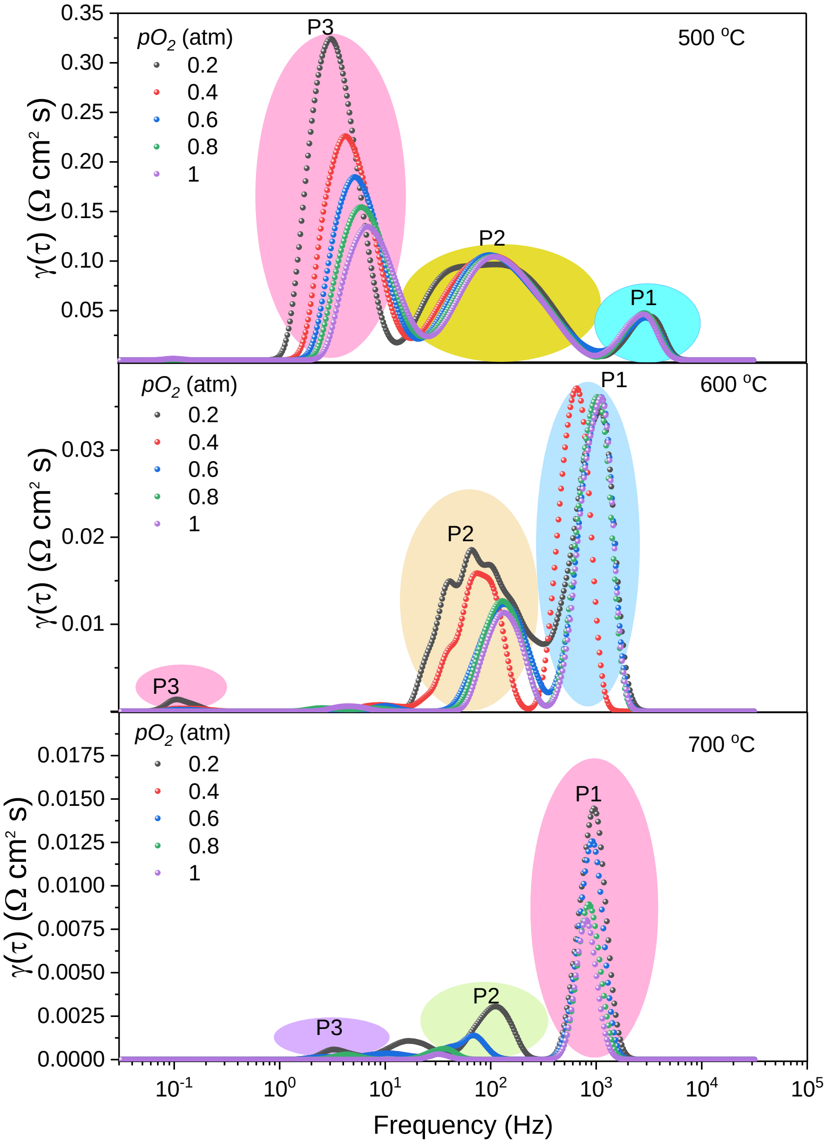

Figure 4.8: Distribution of relaxation time for the partial oxygen pressures of BSCFC5 air electrode material from 500-700 ℃.

The electrochemical performance of the materials can be further evaluated by taking I-V measurements of the anode-supported single cells as illustrated in **Figure 4.9**. The peak power densities of BSCF, BSCFC5, and BSCFZ5 are presented in **Figure 4.9 (a-d)** while **Figure 4.9e** summarizes the contrast between the PPDs of BSCF, BSCFC5, and BSCFZ5 at 500 ℃, 600 ℃, and 650 ℃, respectively. BSCFC5 demonstrated the best performance which implies that the substitution of Fe-TM in the B-site of the traditional BSCF with Cu triggered an increase in the PPD by 31% at 650 ℃ thereby confirming the better suitability of this material as cathode for intermediate temperature operating solid oxide fuel cells. The improved PPD of the BSCFC5 single cell could be attributed to the lattice contraction of the material as earlier explained thereby promoting efficient oxygen diffusion in the material with a shorter oxygen diffusion pathway and an increased O_{ads}/O_{lat} ratio of BSCFC5 from the XPS analysis. Also, **Figure 4.6** confirms that the atomic percentage is high thereby justifying the improved performance of BSCFC5. On the other hand, similar justification can be associated with the poorer performance of BSCFZ5 in the sense that the lattice volume expanded with a longer oxygen diffusion pathway and the O_{ads}/O_{lat} ratio significantly reduced thereby corroborating the reduced ORR of BSCFZ5. Notwithstanding, the observed reduced open-circuit voltage (OCV) of BSCF in **Figure 4.9a** could be attributed to the partial leakage of the supplied fuel during the testing. Nevertheless, the OCV values were all approximately $\sim 0.8\ V$ with the least being 0.77 V. As for the other cells, the OCV values tend to decrease with increasing temperature from 600 ℃ because the electrolyte material is ceria-based so it gets partially short-circuited at temperatures above 600 ℃ causing a reduction and hence, variation in the cell OCV values [316]. More specifically, the density and electrical conductivity of the electrolyte determines a cell OCV. Under reducing conditions, Ce^{4+} will be partially reduced to Ce^{3+} thereby enhancing the electronic conductivity of the cell. Likewise, as the temperature increases the electrical conductivity will increase causing a corresponding decrease in the cell OCV, usually at temperatures above 600 ℃.

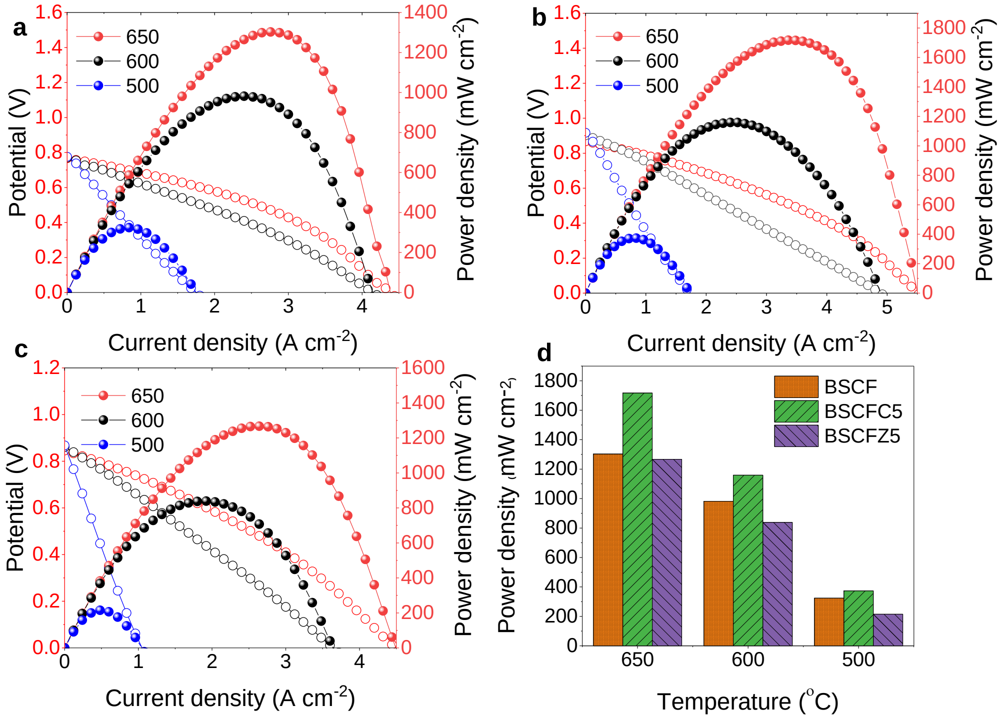

Figure 4.9: The I-V-P curves of single cells from **500** ℃ to **650** ℃ for (a) NiO-SDC│SDC│BSCF (b) NiO-SDC│SDC│BSCFC5 (c) NiO-SDC│SDC│BSCFZ5 and (d) Visual illustrative comparison of the PPDs for the materials at different temperatures.

Durability is another important and basic assessment requirement of cathode materials for SOFC practical applications. The material with superior performance (BSCFC5) was selected for this test. An approximately 185 hours stability test was carried out on the symmetric cell based on BSCFC5 relative to the undoped BSCF material using pure air at a flow rate of 100 mL min^{-1} as illustrated in **Figure 4.10**. The BSCFC5 material exhibited reasonable stability in pure air during the test which suggests that the material has good performance stability.

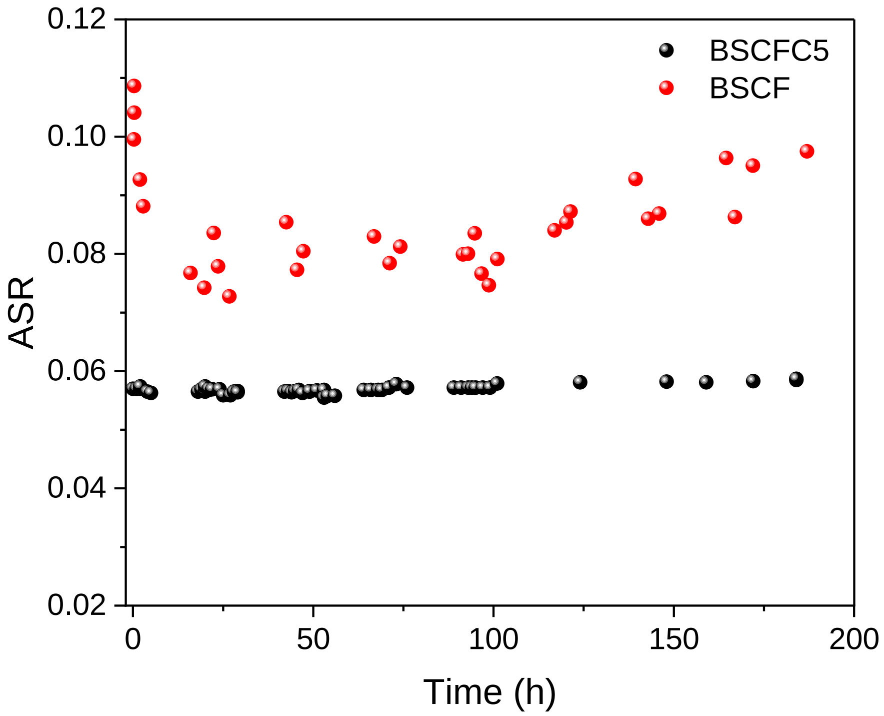

Figure 4.10: Stability of the ASR of BSCFC5 and BSCF after 180 hrs. at **600** ℃.

The initial improvement in BSCF cathode performance, evidenced by the drop in ASR within the first few hours of stability testing at 600°C, followed by fluctuating ASR for the remainder of the 185 hour test, suggests short-term surface activation processes are occurring. The long-term exposure to the air stream may have caused subtle changes to the BSCF surface morphology or grain boundaries that enabled more efficient oxygen adsorption kinetics early on [317]. This could explain the initial enhancement in performance. However, as exposure continued, ongoing microstructural alterations likely caused fluctuations in the population of active sites, resulting in the variability for the rest of the test [318]. The oscillating ASR indicates the surface site density and catalytic rates are dynamically evolving as changes take place at the nanoscale. The mechanisms driving the continued microstructural changes are unclear but may be related to slow cation diffusion or ordering/disordering of oxygen vacancies. While further analysis is needed to elucidate the specific processes, the initial activation and subsequent instability point to complex evolution of the BSCF surface and grain boundary structure over long-term operation.

Thereafter, a CO_2 exposure test was also carried out on BSCF, BSCFC5, and BSCFZ5 powders to observe the degree of the degradation and insurgence of foreign phases in the crystal structures of the perovskite samples. The powders were exposed to 100 % CO_2 gas at the flow rate of 50 mL min^{-1} at 600 ^oC for 24 hrs in a tubular furnace. The resulting crystal structure of the materials is presented in **Figure S4.2** and the refinement in **Figure S4.3**. BSCFZ5 appeared to be more chemically stable in the CO_2 atmosphere even though they all reacted to the CO_2 atmosphere through the formation of $BaCO_3$ phases. The degree of degradation of the exposed BSCF sample, however, is more severe as seen in **Table S4.1** where the lattice volume increased by 0.67 % while those of BSCFC5 and BSCFZ5 increased by 0.36 % and 0.14 %, respectively. Hence, the stabilities of BSCFC5 and BSCFZ5 both improved and the better stability of BSCFZ5 is rational because there has been a trade-off between its performance and stability. Nevertheless, BSCFC5 can be confirmed to be the most optimal material with a simultaneous improvement in its performance and chemical stability thereby promoting it as a superior alternative for intermediate temperature solid oxide fuel cell applications. Moreover, it has been suggested in previous studies that adsorbed oxygen can be linked with CO_2 and functional groups containing oxygen (i.e., OH^-, CO_3^{2-}, O^{2-}, and O^-)[319,320]. It is worthy of note that the adsorbed oxygen content of BSCF increased by 2.36% with Cu substitution in its B-site. Also, the mechanism of the CO_2 reduction reaction has been established to be associated with the valency of oxygen in air electrode materials[321]. Hence the adsorption and reduction reaction of CO_2 in BSCF is improved with Cu-doping.

To further buttress the effect of the CO_2 atmosphere in the samples, the ASRs of their symmetric cells were observed at different intervals with the injection and ejection of 10 vol% CO_2 as shown in **Figure 4.11a.**

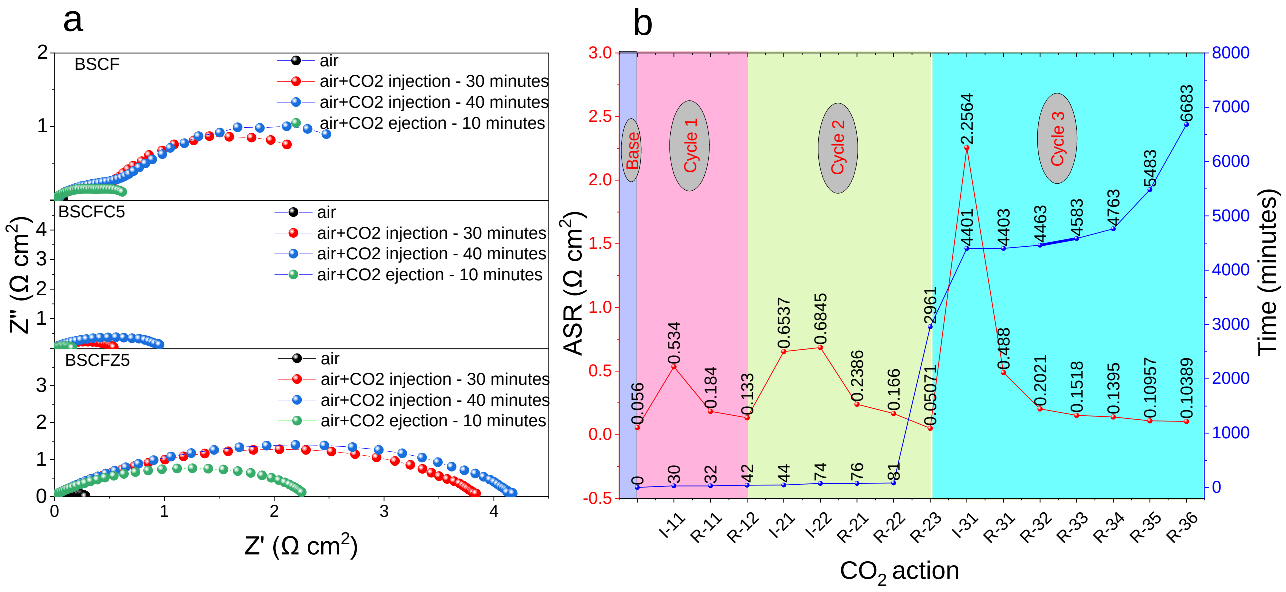

Figure 4.11: (a) Impedance spectra for BSCF, BSCFC5, and BSCFZ5 at **600** ℃ under pure air and injection and ejection of 10 % CO_2. (b) Cyclic Injection and ejection of 10 vol% CO_2 in BSCFC5 at 600 ℃ and different times, where I = Injection and R = Recovery.

The ASRs of BSCF, BSCFC5 and BSCFZ5 were first tested in pure air followed by the injection of 10 vol% CO_2 into the cell for 30 minutes which was later extended to 40 minutes. The performances of all the materials degraded with time when CO_2 was infused into the cells and BSCF appears to be more affected by the CO_2 infusion relative to BSCFZ5 and BSCFC5. This confirms the relative superiority of BSCFC5 and BSCFZ5 to CO_2. After 10 minutes of the ejection of the 10 vol% CO_2 from all the samples, their performances improved. Nonetheless, BSCFC5 can be validated to be the optimal material based on its overall performance during the ASR test in a CO_2-rich atmosphere. The equivalent circuit models can provide valuable insights into the degradation mechanisms and property changes in the cathode materials when exposed to CO_2. The three materials, BSCFC5, BSCF, and BSCFZ5, have different circuit models that represent their physical and electrochemical processes when exposed to CO_2 atmosphere for 40 minutes. The BSCFC5 material has a simple model of LR(C(R(CR))), where L is the lead wire inductance, R1 is the ohmic resistance, C1 and R2 are the charge transfer capacitance and resistance, and C2 and R3 are the oxygen reduction capacitance and resistance. The BSCF material has a similar model, but with higher R1, lower C1, higher R2, lower C2, and higher R3 than the BSCFC5 material. This indicates that the BSCF material has lower conductivity, surface area, catalytic activity, and oxygen diffusion rate than the BSCFC5 material. The BSCFZ5 material has a more complex model of LR(C(R(Q(R(LR)(CR))))), where Q and R4 are the constant phase element and resistance that account for the electrode heterogeneity and polarization loss due to oxygen adsorption. The BSCFZ5 material also has an additional LR(CR) combination that represents the electrolyte and electrode effects. The BSCFZ5 material has lower R1, higher C1, lower R2, higher Q-Yo, lower Q-n, lower R4, higher C2, and lower R3 than the other two materials. This suggests that the BSCFZ5 material has higher surface area, electrode non-ideality, polarization loss, and oxygen diffusion rate than the other two materials. Therefore, the circuit models can provide insights into the degradation mechanisms that affect the material properties, such as sintering, poisoning, or delamination.

To get more insights into BSCFC5 material response to CO_2, a cyclic test was then carried out in which CO_2 was injected and ejected at 600 ℃ and different intervals as shown in **Figure 4.11b**. At first, in the base section, pure air was used for the test to get an ASR of 0.056 Ω cm^2. Secondly, 10 vol% CO_2 was injected into the cell for 30 minutes causing the ASR to increase to 0.534 Ω cm^2 which was then followed by a recovery (ejection of the CO_2) for 2 and 30 minutes. This caused the ASR to reduce to 0.184 Ω cm^2 and 0.133 Ω cm^2, respectively. The 10 vol% CO_2 was passed into the cell for 2 minutes and then another 30 minutes; again, the ASR increased to 0.685 Ω cm^2. The recovery process was initiated, which lasted for 2887 minutes to get an ASR as low as 0.051 Ω cm^2. Again, 10 vol% CO_2 was injected for 1440 minutes. The ASR increased to 2.564 Ω cm^2 and after an ejection process that lasted for 2282 minutes, the ASR reduced to 0.104 Ω cm^2. Hence, after cyclic exposure of CO_2 to BSCFC5 for a total of

6683 minutes, the performance of the material only reduced by 46% from 0.056 Ω cm^2 to 0.104 Ω cm^2 at 600 ℃. This promotes this material as an excellent substitute for BSCF in fuel cell and electrolysis cell applications.

4.7 Summary and Conclusion

In conclusion, we have systematically engineered the lattice expansion and contraction of BSCF functional material by partially substituting the Fe-B-site cation with the TMs, Zn, and Cu, respectively. We were able to show that lattice engineering is a significant descriptor to evince the variability in the catalytic ORR and CO_2 tolerance of BSCF functional material. Enhanced catalytic ORR and CO_2 tolerance were also correlated with lattice contraction due to the shortened pathway for oxygen mobility in the lattice of BSCF and the weakened adsorption energy of the constitutive reactive intermediates. Cu-TM instigated a contraction, while Zn-TM instigated an expansion in the lattice of BSCF. The BSCFC5 cathode, where lattice contraction occurred, exhibits the best performance with an ASR of 0.0247 Ω cm^2 and a high peak power density (PPD) of 1715 mW cm^{-2} at 650 ℃ for the symmetrical and single cells, respectively. The material also displayed enhanced tolerance to CO_2 infusion with satisfactory recoverability when switched intermittently between pure air and 10-vol% CO_2 infusions for 100 hours. Our findings conclude that Cu-TM-doped BSCF (BSCFC5) is a better substitute for BSCF material for SOFC applications.

4.8 Supplementary information

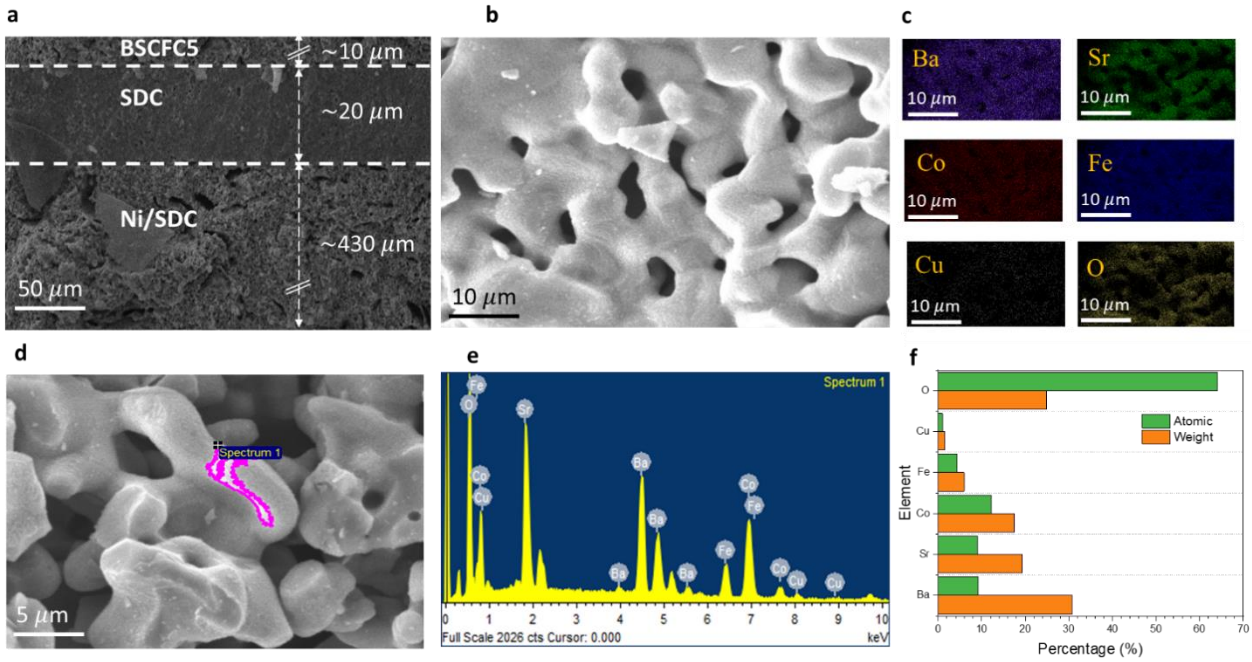

Figure S4. 1: Scanning electron microscopy captures of BSCFC5 showing (a) the cross-section of the single-cell comprising the anode, cathode, and electrolyte (b) the SEM image used for the energy-dispersive x-ray spectroscopy (EDX/EDS) (c) mapping of the constitutive elements (d) the image used for the EDS analysis (e) the spectrum of the constitutive elements (f) the atomic and weight percentages of the constitutive elements.

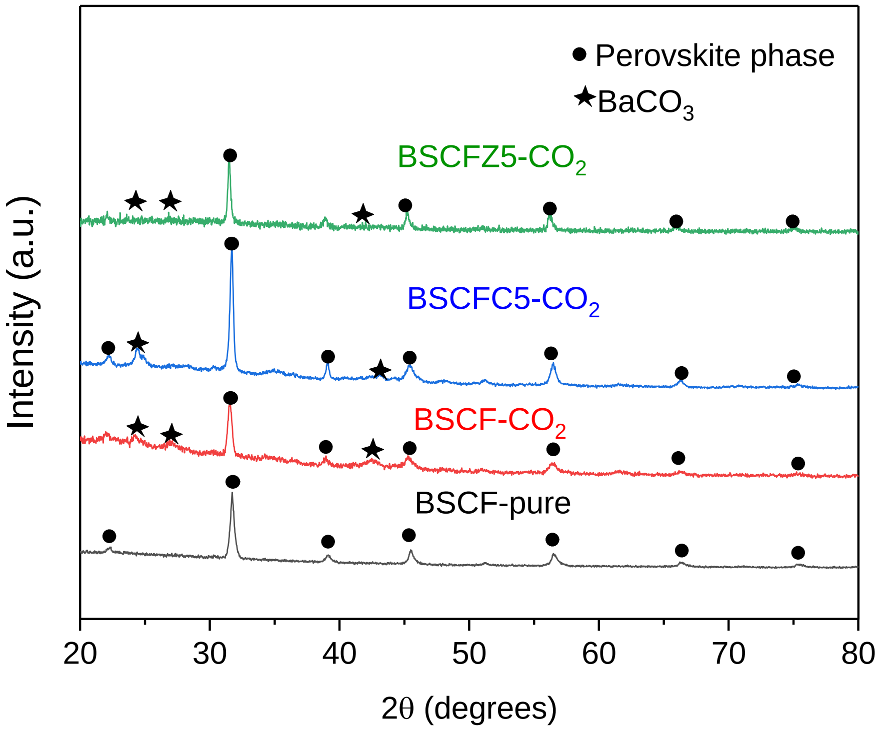

Figure S4.2: XRD pattern of the pure as-synthesized BSCF perovskite powder relative to BSCF, BSCFC5, and BSCFZ5 powders exposed CO_2 at 600 °C for 24 h.

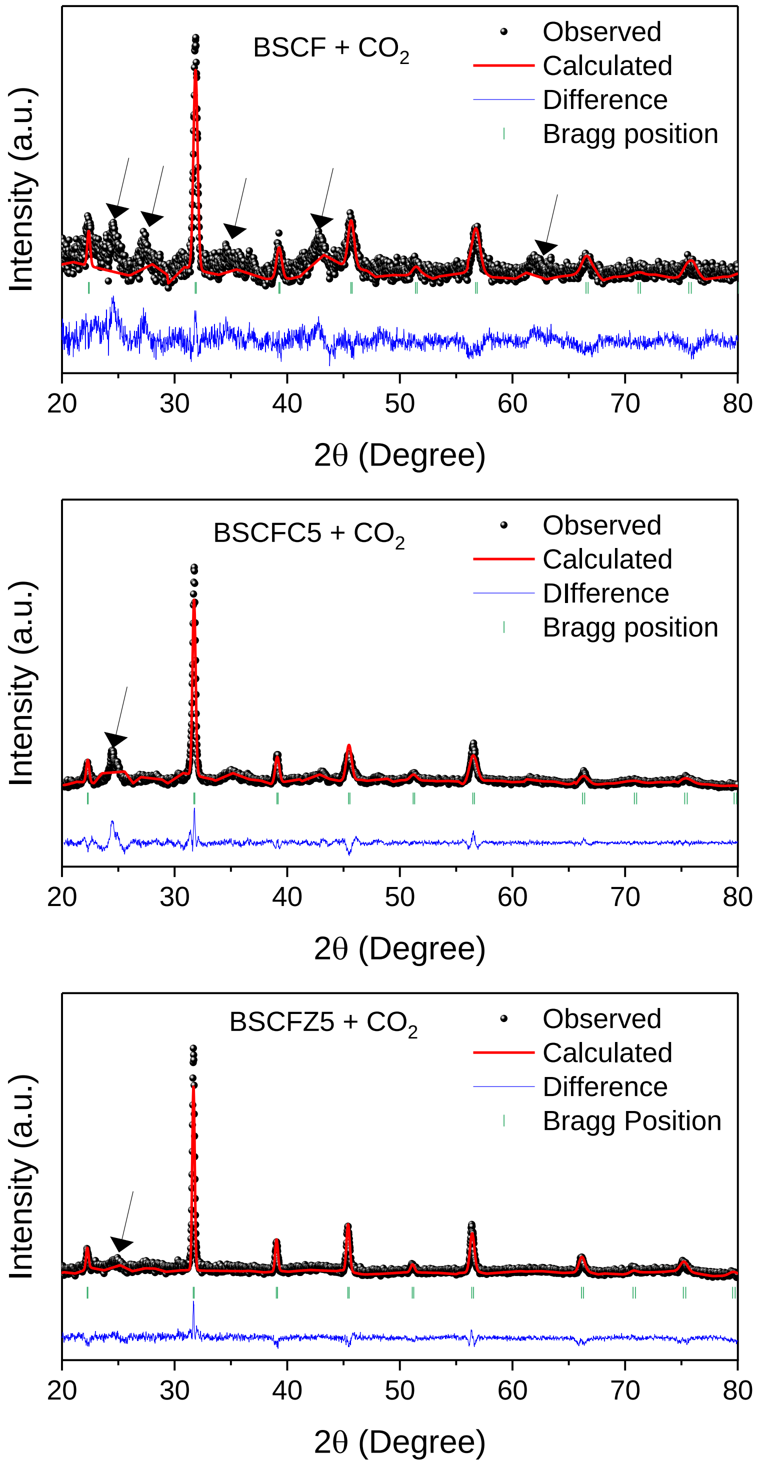

Figure S4.3: Refinement of all the samples exposed to CO_2 from Figure S4.2 with the arrows denoting the $BaCO_3$ phases.

Table S4. 1: Refined lattice parameters for all the samples

Sample	a (Å)	b (Å)	c (Å)	V (Å)	wR_p (%)	R_p (%)	χ^2
BSCFC5	3.98450	3.98450	3.98450	63.25	7.09	5.34	1.94
BSCF	3.98998	3.98998	3.98998	63.52	9.57	7.73	1.61
BSCFCZ5	3.99411	3.99411	3.99411	63.72	7.64	9.36	1.73

From **Figure S4.3** and Table S4. 1**,** it can be inferred that the introduction of CO_2 led to the generation of $BaCO_3$ phases triggering an increase in the lattice volumes of BSCF, BSCFC5 and BSCFZ5 compared to **Table 4.1** in the main article.

Table S4.2: Comparison of Co2p in BSCF, BSCFC5 and BSCFZ5

Sample	$Co^{4+}2p_{1/2}$		$Co^{3+}2p_{1/2}$		$Co^{4+}2p_{3/2}$		$Co^{3+}2p_{3/2}$	
	Peak (eV)	(%)	Peak (eV)	(%)	Peak (eV)	(%)	Peak (eV)	(%)
BSCF	794.14	40.66	794.81	9.95	778.35	39.69	779.69	9.71
BSCFC5	794.20	43.66	795.82	6.95	778.41	42.61	780.76	6.78
BSCFZ5	792.97	12.43	793.04	38.18	777.39	12.14	778.35	37.25

Table S4. 3*:* Comparison of Fe2p in BSCF, BSCFC5 and BSCFZ5

Sample	$Fe^{3+}2p_{3/2}$		$Fe^{4+}2p_{3/2}$	
	Peak (eV)	(%)	Peak (eV)	(%)
BSCF	709.26	37.10	711.30	62.90
BSCFC5	709.50	44.54	712.37	55.46
BSCFZ5	708.05	46.19	710.53	53.81

Table S4.4: Estimation of activation energies for the conductivity of BSCF, BSCFC5 and BSCFZ5

Activation energy	Temperature range (°C)	BSCF (eV)	BSCFC5 (eV)	BSCFZ5 (eV)
Ea1	300 – 400	0.194752	0.177517	0.066353
Ea2	400 – 450	0.035331	0.043087	0.095652
Ea3	500 – 650	0.068939	0.083588	0.08445
Cumulative Ea		0.299021	0.304192	0.246456

Table S4.5: ASR comparison for various non-composite BSCF-based cathode materials with those of this work

Cathode	**Electrolyte**	**ASR (Ω cm^2) @ 600 ℃**	**Ref.**
$Ba_{0.5}Sr_{0.5}Co_{0.8}Fe_{0.2}O_{3-\delta}$	SDC	0.071	[271]
$Ba_{0.5}Sr_{0.5}(Co_{0.8}Fe_{0.2})_{0.96}Zn_{0.04}O_{3-\delta}$	GDC	0.23	[266]
$Ba_{0.5}Sr_{0.5}Co_{0.8}Fe_{0.2}O_{3-\delta}$	GDC	0.150	[322]
$Ba_{0.5}Sr_{0.5}(Co_{0.8}Fe_{0.2})_{0.9}Y_{0.1}O_{3-\delta}$	GDC	0.070	[307]
$Ba_{0.5}Sr_{0.5}Co_{0.8}Fe_{0.2}O_{3-\delta}$	SDC	0.097	[323]
$(Ba_{0.5}Sr_{0.5})_{0.85}Gd_{0.15}Co_{0.8}Fe_{0.2}O_{3-\delta}$	SDC	0.171	[324]
$Ba_{0.5}Sr_{0.5}Co_{0.7}Fe_{0.3}O_{3-\delta}$	SDC	0.081	this work
$Ba_{0.5}Sr_{0.5}Co_{0.7}Fe_{0.25}Cu_{0.05}O_{3-\delta}$	SDC	0.051-0.056	this work
$Ba_{0.5}Sr_{0.5}Co_{0.7}Fe_{0.25}Zn_{0.05}O_{3-\delta}$	SDC	0.288	this work

$\boldsymbol{SDC}: Sm_{0.2}Ce_{0.8}O_{1.9}$; $\boldsymbol{GDC}: Gd_{0.1}Ce_{0.9}O_{1.95}$

CHAPTER 5: SELF-ASSEMBLY CATHODE VERSUS REGULAR COMPOSITES AND SINGLE -PHASE CATHODES[3]

5.1 Background

The previous chapter explored the effects of lattice engineering on the performance and CO_2 tolerance of $Ba_{0.5}Sr_{0.5}Co_{0.7}Fe_{0.3}O_{3-\delta}$ (BSCF) air electrode functional material for intermediate temperature operating SOFCs. The present chapter aims to investigate the development of a thermodynamically stable self-assembled nanocomposite cathode material, $BaCo_{0.5}Ce_{0.3}Fe_{0.1}Yb_{0.1}O_{3-\delta}$ (BCCFYb) and its performance comparison with other unique materials, including a traditional composite material and single-phase material. This chapter will discuss the synthesis and characterization of BCCFYb, and its evaluation in SOFC and PCFC modes. The results will demonstrate the potential of BCCFYb as a promising cathode material for PCFCs.

5.2 Introduction

Humanity continues to rely on energy as a commodity indispensable for survival [3]. However, critical challenges associated with the popular energy sources (i.e., fossils and renewable energy) necessitate seeking alternative technologies with the potential to provide sustainable clean, efficient, and safe energy [325]. Solid oxide fuel cells (SOFCs) are promising alternative power sources that directly convert chemical energy to electrical energy with high efficiency and low emissions [326]. The limiting factor to the commercialization and global adoption of this technology (based on yttria-stabilized zirconia) is its high operation temperature (800 – 1000 ^{o}C)

---

[3] Fully published chapter:
Bello IT, Song Y, Yu N, Li Z, Zhao S, Maradesa A, Liu T, Shao Z, Ni M. Evaluation of the electrocatalytic performance of a novel nanocomposite cathode material for ceramic fuel cells. Journal of Power Sources. 2023 Mar 15;560:232722.

which negatively impacts its performance and durability[21]. Decreasing the operation temperature of SOFCs to 650 – 350 ^{o}C while sustaining reasonable energy efficiency is crucial to attaining commercialization[326].

Numerous advances have been made in accomplishing high-performing SOFCs at reduced temperatures by refining the component materials selection and fabrication processes [161,327–330]. However, recent developments in ceramic fuel cells (CFCs) have led to a renewed interest in protonic ceramic fuel cells (PCFCs) because they are more promising and characterized by lower activation energies and exculpated fuel dilution at the anode during operation [122]. The major challenge with PCFCs is their low power output due to the cathode material's insufficient oxygen reduction reaction (ORR) activity [107]. Extensive research has shown that cathode materials for PCFCs require an optimal triple ionic-electronic conductivity (TIEC) to expand the electrochemical reaction sites for ORR[182,331,332]. However, developing single-phase materials that meet this requirement is challenging[333–336]. The existing body of research has confirmed that composite materials are more auspicious in realizing TIEC in PCFC cathodes [332,336–342].

Composite ceramic oxide materials are either generated mechanically or by the self-ordering procedure. The mechanically generated composites are derived through the ball-milling of already-calcined ceramic oxides in desired proportions. In contrast, self-ordered composites, popularly known as self-assembled materials, are generated through the automatic arrangement of a pre-existing disordered precursor into an organized structure comprising multiple phases after calcination[339]. For instance, the performances of the mechanically generated ceramic oxide composites, $La_{0.6}Ba_{0.4}CoO_{3-\delta}$-$BaZr_{0.1}Ce_{0.7}Y_{0.1}Yb_{0.1}O_{3-\delta}$, $La_{0.6}Sr_{0.4}Co_{0.2}Fe_{0.8}O_{3-\delta}$-$BaZr_{0.5}Pr_{0.3}Y_{0.2}O_{3-\delta}$, $La_{0.6}Sr_{0.4}Co_{0.2}Fe_{0.8}O_{3}$-$BaCe_{0.9}Yb_{0.1}O_{3-\delta}$, and $Ba_{0.5}Sr_{0.5}Co_{0.8}Fe_{0.2}O_{3-\delta}$–$Sm_{0.2}Ce_{0.8}O_{1.9}$ were enhanced by taking advantage of combining two different ceramic oxides with unique properties [343–346]. Likewise, self-ordered composite materials such as $Ba_{0.5}Sr_{0.5}Co_{0.48125}Fe_{0.20625}W_{0.3125}O_{3-\delta}$ (BSCFW), $BaCo_{0.7}(Ce_{0.8}Y_{0.2})_{0.3}O_{3-\delta}$ (BCCY), $BaCe_{0.4}Co_{0.4}Fe_{0.1}Zr_{0.1}O_{3-\delta}$ (BCCFZ), and $BaCe_{0.4}Fe_{0.4}Co_{0.2}O_{3-\delta}$ (BCFC) have also benefitted from the synergistic interactions between the inherent phases in the materials to achieve superior cathodic performances [249,347–351]. Ytterbium (Yb) has been instrumental in tremendously improving the performance of $BaCe_{0.7}Zr_{0.1}Y_{0.1}Yb_{0.1}O_{3-\delta}$ (BCZYYb) electrolyte material for PCFCs [155]. However, little attention has been focused on studying Yb-doped ceramic oxides as cathodes for PCFCs. Therefore, we attempt to study the ORR of materials having two or more of the following cations, Co, Ce, Fe, and Yb, in their B-sites as cathode materials for PCFCs, emphasizing on resulting composite materials. Understanding the ORR mechanisms of materials with these B-site cationic combinations in the PCFC domain will further advance the scope of knowledge in developing multiphasic TIEC cathode materials for PCFCs.

In this study, we investigate the potential of a novel cathode material, a self-ordered nanocomposite, with the composition $BaCo_{0.5}Ce_{0.3}Fe_{0.1}Yb_{0.1}O_{3-\delta}$ (BCCFYb), for use in ceramic fuel cells. The material is generated through a nanoscale auto-biphasic ordering process, which results in a thermodynamically stable material with a host cubic phase (70 %) and an ancillary rhombohedral phase (30 %). We compare the performance of this material to that of other cathode materials with different conductivity properties, including a cobalt-rich oxide-ion and electron (O^{2-}/e^-) conducting $BaCo_{0.833}Yb_{0.167}O_{3-\delta}$ (BCYb), cerium-rich proton and electronic (H^+/e^-) conducting $BaCe_{0.75}Fe_{0.25}O_{3-\delta}$ (BCF), and Co-Ce-rich triple ionic (O^{2-}/H^+/e^-) conducting $BaCo_{0.833}Yb_{0.167}O_{3-\delta}$ - $BaCe_{0.75}Fe_{0.25}O_{3-\delta}$ (BCYb-BCF) traditional composite. Our results demonstrate that the self-ordered nanocomposite material, BCCFYb, exhibits superior ORR activity and good stability, making it a promising material for use in proton-conducting ceramic fuel cells. At 650 ^{o}C, BCCFYb has an area-specific resistance (ASR) of 0.084 Ω cm^2 in 2.5 % air-H_2O, surpassing those of BCYb, BCYb-BCF, and BCF by 24%, 87%, and 100%, respectively. At 650 °C, the peak power density (PPD) of the BCCFYb surpasses 800 and 1200 mW cm^{-2} in PCFC and oxide ion conducting solid oxide fuel cell modes, outperforming many previously developed cathode materials. This study also highlights the potential of self-assembly engineering as a practical approach to developing high-performance cathode materials for ceramic fuel cells.

5.3 Materials and methods

5.3.1 Synthesis

One-pot EDTA-citric acid complexing sol-gel method was used in the synthesis of $BaCo_{0.833}Yb_{0.167}O_{3-\delta}$ (BCYb), $BaCe_{0.75}Fe_{0.25}O_{3-\delta}$ (BCF), $BaCo_{0.5}Ce_{0.3}Fe_{0.1}Yb_{0.1}O_{3-\delta}$ (BCCFYb) nanocomposite powder, $BaCo_{0.75}Ce_{0.05}Fe_{0.1}Yb_{0.1}O_{3-\delta}$ as well as $Sm_{0.2}Ce_{0.8}O_{1.9}$ (SDC) and $BaCe_{0.7}Zr_{0.1}Y_{0.1}Yb_{0.1}O_{3-\delta}$ (BCZYYb) electrolyte powders as discussed elsewhere[352]. Stoichiometric amounts of the chemical reagents $Ba(NO_3)_2$, $Co(NO_3)_2.6H_2O$, $Ce(NO_3)_3.6H_2O$, $Fe(NO_3)_3.9H_2O$, $Yb(NO_3)_3$, $Zr(NO_3)_4$, $Y(NO_3)_3.6H_2O$, and $Sm(NO_3)_3$ procured from Sinopharm were used to prepare BCYb, BCF, BCCFYb, BCZYYb, and SDC. The stoichiometric amounts of the reagents for each case were first dissolved in deionized water under constant stirring and heating conditions (70 °C) until a homogeneous solution was formed. $C_6H_8O_7.H_2O$ (citric acid) and $C_{10}H_{16}N_2O_8$ (EDTA) complexing agents were added to the solution. This was followed by adding enough NH_4OH until a pH of ~8 was achieved. The heating and stirring of the solution are sustained until a gel is formed. This is followed by the transfer of the gel to an aerated oven operating at 170 °C for over 10 h until a dried solid precursor is generated. The precursors are finally calcined in air for 5hrs at 1000 °C to obtain crystalline powders of BCYb, BCF, BCCFYb, SDC, and BCZYYb. The traditional BCYb-BCF composite is generated by ball-milling crystalline powders of BCYb and BCF in a ratio of 60:40.

5.3.2 Characterizations

X-ray diffractometer (Rigaku SmartLab 9kW -Advanced) was used to investigate the crystal structure of the as-synthesized BCCFYb nanocomposite powders. The diffraction patterns were observed over a diffraction angle range of 20 – 80 ^{o} at a step size of 0.02^{o}. FullProf opensource was used to refine the diffraction patterns for BCCFYb. The morphology of BCCFYb was further examined using TESCAN MAIA3, VEGA, and MIRA scanning electron microscopy (SEM). The as-synthesized nanocomposite powders of BCYb, BCF, and BCCFYb were pressed at a pressure of 200MPa into a dense bar with the dimensions $\sim 20\text{ mm} \times 5\text{ mm} \times 2\text{ mm}$ and sintered at 1120 ^{o}C for 10 h was used to measure the electrical conductivity. This was carried out at a temperature range of 400 – 800 ^{o}C using a four-probe DC configuration with a Keithley 2440 source meter. The same bar was used to ascertain the surface exchange kinetics (K_{chem}) and bulk diffusion (D_{chem}) coefficients using the electrical conductivity relaxation (ECR) technique.

5.3.3 Cell Fabrication

Symmetric cells

BCYb│BCZYYb│BCYb, BCF│BCZYYb│BCF, BCYb-BCF│BCZYYb│BCYb-BCF BCCFYb│BCZYYb│BCCFYb, and BCCFYb│SDC│BCCFYb and configurations were used to fabricate the symmetrical cells. The electrolyte powders (SDC and BCZYYb) were weighed and pressed into a dense pellet at a pressure of 200 MPa. The sintering of the pellets follows this at 1300 ^{o}C (SDC) and 1450 ^{o}C (BCZYYb) for 10h. The cathode slurry was prepared by ball milling as-synthesized BCCFYb nanocomposite powders, isopropyl alcohol, ethylene glycol, and glycerol in Fritsch Pulverisette at 400 rpm for 5h to form a colloidal suspension. The cathode slurry was then sprayed on both sides of the electrolyte pellet and co-sintered at 850 ^{o}C for 2h in air. The resulting thickness of the electrode is an average of 18 µm and an average effective area of 0.393 cm^2. Finally, the Ag current collector was brushed on the cathode sides, and Ag wires were affixed to the cells in preparation for electrochemical measurement.

Single cells

NiO-BCZYYb│BCZYYb│BCYb, NiO-BCZYYb│BCZYYb│BCF, NiO-BCZYYb│BCZYYb│BCYb-BCF NiO-BCZYYb│BCZYYb│BCCFYb, and NiO-SDC│SDC│BCCFYb single cells were prepared through the mainstream co-pressing and sintering process[353]. The anode-electrolyte were co-pressed and sintered at 1350 and 1450 ^{o}C for 10h, respectively for SOFC and PCFC, respectively. The anode comprised NiO, starch, and the electrolyte powders in the ratio 6.5:3.5:1. The cathode slurries wereare then sprayed uniformly on the electrolyte side of the already sintered anode-electrolyte, followed by another sintering at 850 ^{o}C for 2h. The average thickness of the SOFC and PCFC is shown in **Figure S5.13**.

5.3.4 Electrochemical Measurements

Solarton 1287 potentiostat and Solarton 1260 frequency response analyzer were used to evaluate the polarization resistances of the symmetrical cells under various atmospheric conditions at a constant rate of 100 sccm. Before each measurement, it was ensured that the system was set to open circuit condition, 30 mV AC amplitude, zero applied DC potential, and a frequency range of 100 kHz to 100 MHz.

A four-probe configuration using Keithley 2440 source meter was used for the I-V-P assessment of the anode-supported single cells. The cathode was exposed to ambient air while the anode was fed with pure hydrogen at a flow rate of 100 sccm.

5.4 Results and discussion

Figure S5.1 presents the X-ray diffraction (XRD) patterns of all the as-synthesized cathode materials after calcination at 1000 °C for 5h. **Figure 5.1a** shows the refined XRD profile of the self-ordered BCCFYb nanocomposite powder. The Rietveld refinement confirms the existence of two distinct phases in BCCFYb, cubic and rhombohedral. The details of the quantitative analysis of the refined crystal structure are illustrated in **Table S5.1**. The vast difference in the ionic radii of the two dominant B-site cations of BCCFYb (Ce and Co) could be regarded as the impelling cause for the separation of the lattice structure into cubic and rhombohedral phases[354]. Under IV coordination, the ionic radii of Co^{4+} and Co^{3+} are 0.53 nm and 0.55 nm, respectively, while those of Ce^{4+} and Ce^{3+} are 0.87 nm and 1.01 nm, respectively, from Shannon's ionic radii table[355]. The cubic phase, estimated to be the host phase (70 %), is based on the Pm-3m space group, equivalent to JCPDS: 75-0227, while the supporting rhombohedral phase (30 %) is based on the R-3c space group, with proximity to JCPDS: 75-0431. The estimated lattice parameters of the cubic phase are a = b = c = 4.1378Å, while those of the rhombohedral phase are a = b = 6.2173 Å and c = 15.1630 Å. The refinements can be confirmed to be reliable because of the low goodness of fit ($\chi^2 = 1.76$), weighted reliability factor (Rwp = 11.1 %), and integrated intensity reliability factor (Rp = 8.41).

The crystallite size (D) of BCCFYb was then calculated from the XRD profile using all peaks associated with each of the constituent phases, as shown in **Figure 5.1a** using the Scherrer equation $\mathrm{D} = 0.94\lambda/\mathrm{L}\cos\theta$, where λ is the X-ray wavelength equivalent to 1.5406 Å, L is the line broadening at the full width of half maxima (FWHM) in radians, and θ is the Bragg's angle in degrees[356]. The calculated crystallite size of the cubic and rhombohedral phases are 27.50 nm and 32.07 nm, respectively.

Figure 5.1b shows the scanning transmission electron microscopy (STEM) image and the energy dispersive x-ray (EDX) mapping of BCCFYb nanocomposite, while **Figure 5.1c** shows the point EDX scanning spectra alongside the element atomic details. These results confirm the existence of two crystalline phases in the BCCFYb nanocomposite. One of the phases is rich in Ce, and the other is rich in Co. **Figure 5.1d** illustrates that the host phase, which is rich in Co, has a cubic structure while the ancillary phase, which is rich in Ce, has a rhombohedral structure. The high-resolution transmission electron microscopy (HR-TEM) images in **Figure 5.1e** show the inter-atomic spacing of the host and cubic phases corresponding to 2.07 and 3.11 Å in planes (200) and (110) of BCCFYb, respectively. More images and details about the microstructure and morphology of BCCFYb can be found in **Figure S5.2-5. Figure S5.2-3** present the unique self-ordered microstructural arrangement of BCCFYb precursor after calcination at 1000 ^{o}C for 5h in ambient air. From **Figure S5.2**, it can be deduced that the white patches represent the Ce-rich phase due to the higher intensity of the Ce-peak relative to Co-peak on the EDS image. **Figure S5.4** represents alternative STEM-EDX images of BCCFYb depicting the Co and Ce-rich phases, while **Figure S5.5** shows the line-EDX scan of the Co and Ce-rich phases from separate STEM images of BCCFYb.

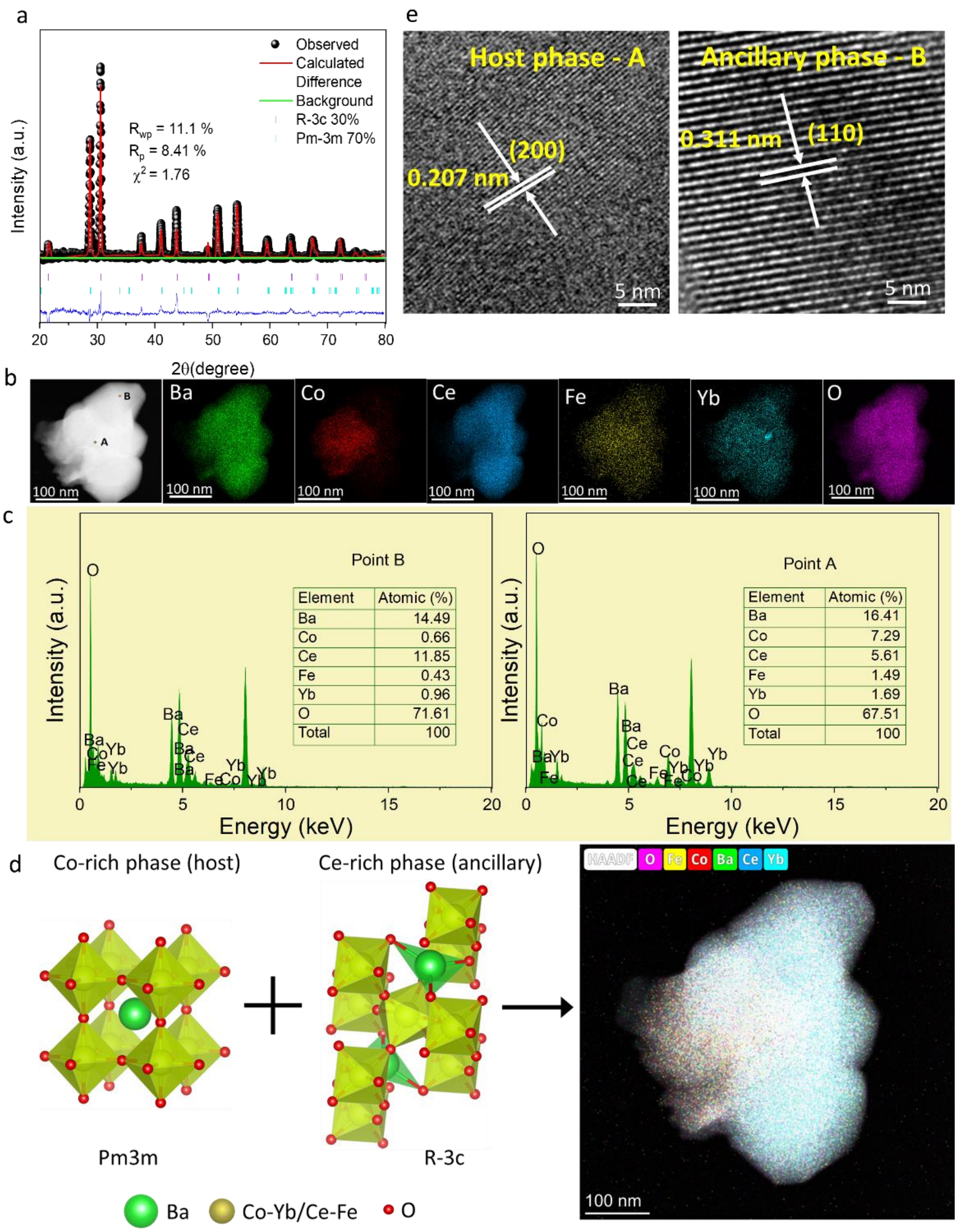

Point B

Element	Atomic (%)
Ba	14.49
Co	0.66
Ce	11.85
Fe	0.43
Yb	0.96
O	71.61
Total	100

Point A

Element	Atomic (%)
Ba	16.41
Co	7.29
Ce	5.61
Fe	1.49
Yb	1.69
O	67.51
Total	100

Figure 5.1: Rietveld refinement of BCCFYb XRD profile. (b) STEM-EDX mapping of BCCFYb. (c) Point EDX results of BCCFYb. (d) Illustration of cubic and rhombohedral integration to generate the biphasic BCCFYb nanocomposite. (e) HR-TEM image of the host and ancillary phases in BCCFYb.

Good thermodynamic stability is an essential feature of cathode material for CFCs to ensure performance stability during operation. This feature was therefore investigated through a high-temperature-XRD (HT-XRD) analysis to observe if the crystal structure of BCCFYb will be altered. **Figure S5.6** presents the HT-XRD patterns of BCCFYb from room temperature to 750 ^oC. There is no disappearance or emergence of foreign peaks at all temperatures, which confirms the thermodynamic phase stability of the self-ordered nanocomposite material. The thermal expansion coefficient (TEC) of BCCFYb nanocomposite estimated from the lattice parameters of the HT-XRD patterns is shown in **Figure S5.7**. The Ce-rich ancillary phase contributed significantly to the reduction of the overall TEC below 13×10^{-6} K^{-1}, suggesting that the cathode material will be thermally compatible with the electrolyte. This TEC value is significantly lower than that of some popular high-performing Co-containing CFC cathode materials such as BSCF, BCFZY, and PBSCF[21,357,358]. Therefore, this study demonstrated an alternative approach to fabricating low TEC Co-containing cathode materials for CFCs.

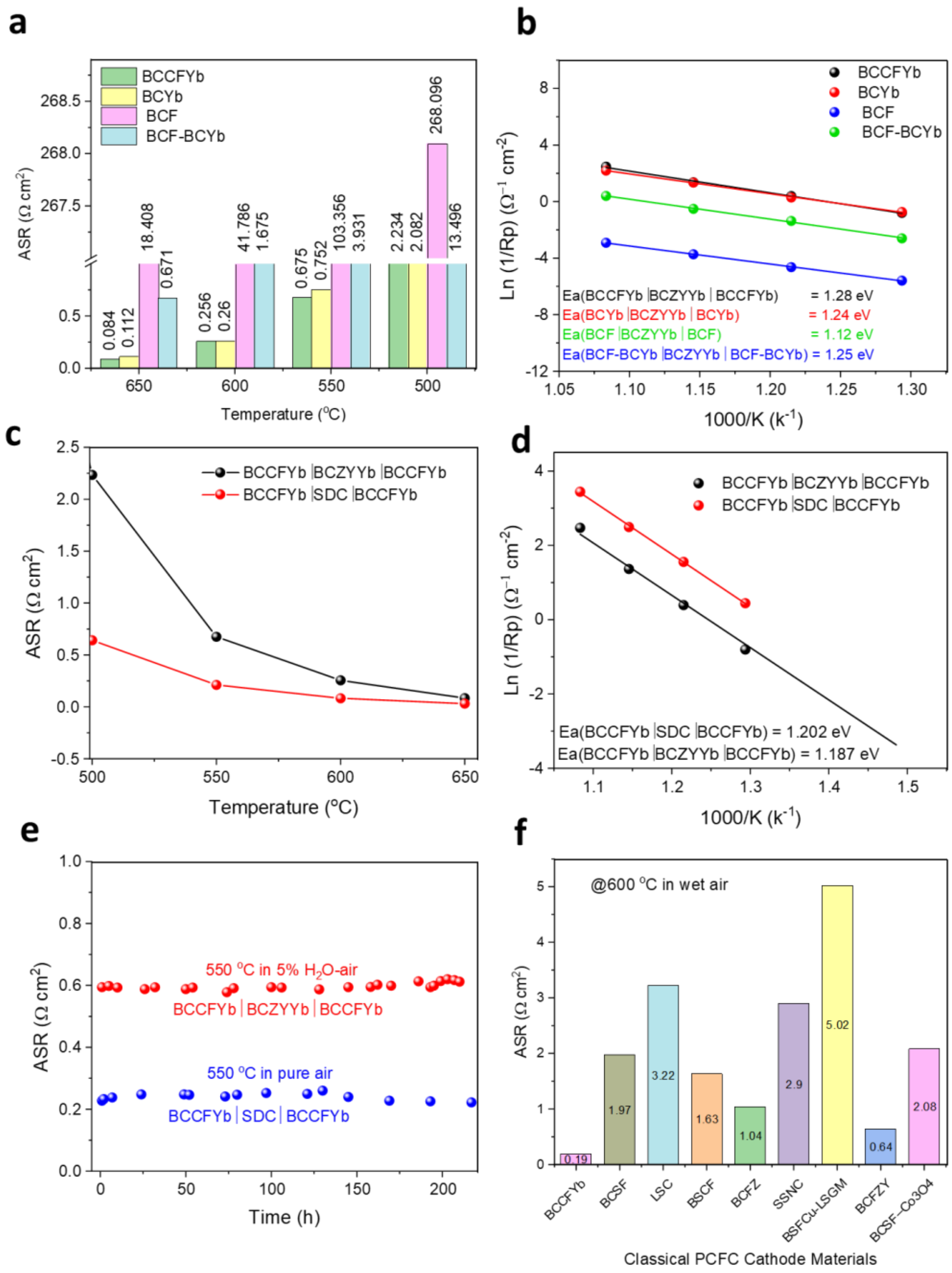

Figure 5.2: (a) Comparison of the ASRs of BCCFYb, BCF, BCYb, and BCYb-BCF from 500 – 650 °C (b) Arrhenius plots of the ASRs of BCCFYb, BCF, BCYb, and BCYb-BCF. (c) Comparison of ASRs of BCCYb-based symmetrical cells in oxygen ion conducting and proton conducting modes. (d) Arrhenius plots of the ASRs of BCCYb-based symmetrical cells in oxygen ion and proton conducting modes. (e) ASR stability of BCCFYb-based symmetrical cells based on SDC and BCZYYb electrolytes at 550 °C. (f) Comparison of ASR of BCCFYb with previously reported cathode materials for PCFCs at 600 °C where BCSF= $BaCe_{0.4}Sm_{0.2}Fe_{0.4}O_{3-\delta}$ [42], LSC = $La_{0.6}Sr_{0.4}CoO_{3-\delta}$ [43], BSCF = $Ba_{0.5}Sr_{0.5}Co_{0.8}Fe_{0.2}O_{3-\delta}$ [44], BCFZ = $BaCo_{0.4}Fe_{0.4}Zr_{0.2}O_{3-\delta}$ [45], SSNC = $SrSc_{0.175}Nb_{0.025}Co_{0.8}O_{3-\delta}$ [46], BSFCu-LSGM = $Ba_{0.5}Sr_{0.5}Fe_{0.8}Cu_{0.2}O_{3-\delta}$ -

$La_{0.8}Sr_{0.2}Ga_{0.8}Mg_{0.2}O_{3-\delta}$ [47], BCFZY = $BaCo_{0.4}Fe_{0.4}Zr_{0.1}Y_{0.1}O_{3-\delta}$ [48], BCSF–Co_3O_4 = $BaCe_{0.4}Sm_{0.2}Fe_{0.4}O_{3-\delta}$ - Co_3O_4 [49].

The chemical compatibility of BCCFYb nanocomposite with the electrolytes (SDC and BCZYYb) was investigated by mechanically mixing the cathode powder with the electrolyte powders in the ratio of 1:1 followed by calcination at 900 °C for 2h. **Figure S5.8** suggests that BCCFYb is more compatible with the BCZYYb electrolyte powders compared with SDC, due to the small impurity phase that surfaced in the calcinated mixture of SDC and BCCFYb.

The catalytic ORR of BCCFYb, BCF, BCYb, and BCYb-BCF in 2.5% H_2O-air, was first evaluated using proton conducting symmetrical cells, as shown in **Figure 5.2a.** BCCFYb exhibited the lowest ASR at all temperatures suggesting its superior catalytic ORR to the cobalt-rich BCYb, cerium-rich BCF, and BCF-BCYb traditional composite. At 650 °C, the performance of BCCFYb surpasses those of BCYb, BCYb-BCF, and BCF by 24%, 87%, and 100%, respectively. The performance of BCYb is inferior to BCCFYb under BCZYYb electrolyte because it is a mixed ionic and electronic material, most suited for SOFCs. The BCF, on the other hand, is highly rich in cerium which impedes the transport of electron-hole carriers but with excessive oxygen vacancy concentration, thus significantly decreasing its performance as a cathode material for PCFCs[359]. The poorer performance of the BCYb-BCF traditional composite relative to the self-ordered BCCFYb could be due to the poor percolation between the inherent phases[351,360]. The superior performance of BCCFYb could be attributed to the beneficial coactivity of the cubic and rhombohedral phases. The cubic phase (rich in Co) facilitates the transport of oxygen vacancy and electron holes, while the rhombohedral phase (rich in Ce) facilitates the hydration of the oxygen vacancies and hence, promotes the transport of protonic carriers and electron holes[334]. Combining these two phases reinforces the expansion of the active reaction sites for electrochemical ORR beyond the triple phase boundary, which is customary to MIEC SOFC cathode materials. To confirm that the superior performance of BCCFYb nanocomposite was due to the synergy of the Co and Ce-rich phases, we significantly reduced the amount of Ce in the B-site to 5% to create a Co-rich 97% cubic phase $BaCo_{0.75}Ce_{0.05}Fe_{0.1}Yb_{0.1}O_{3-\delta}$ **(Figure S5.10)**. We then compared the performance of the BCCFYb nanocomposite to the resulting 97%-BCCFYb cubic phase material. Our findings demonstrated that the BCCFYb nanocomposite outperformed the 97%-BCCFYb cubic phase material under the SOFC and PCFC modes **(Figure S5.11-12)**. Under the PCFC mode, the performance of the 97%-BCCFYb cubic phase material was lower due to the dominant MIEC characteristic of the material and its lack of sufficient active site for ORR **(Figure S5.11-12)**. This result further substantiates the theory that the complementarity of the Co and Ce-rich phases is the main contributor to the enhanced ORR in the BCCFYb nanocomposite.

The Arrhenius plots in **Figure 5.2b** compare the activation energies of the materials tested in **Figure 5.2a**. BCCFYb was further assessed on O-SOFC electrolyte, SDC (in synthetic air with 0.21% O_2 concentration), and proton conducting BCZYYb (in 5% H_2O-air) electrolytes from 500-650 ^oC, as summarized in **Figure 5.2c**. The ASRs of the BCCFYb on SDC and BCZYYb at 650 ^oC are 0.032 and 0.063 Ω cm^2, respectively, which signifies outstanding performance. The EIS spectra of the symmetrical cells in the temperature range of 550-650 ^oC are illustrated in **Figure S5.9**. The Arrhenius plots in **Figure 5.2d** compare the activation energies of BCCFYb-based symmetrical cells on SDC and BCZYYb electrolytes. It can be observed that the activation energy in the PCFC operating mode is slightly lower (by 1.25%), thereby substantiating the need to develop PCFCs for low-temperature operations. The ASR stabilities of BCCFYb on SDC and BCZYYb were also observed for over 200h, as shown in **Figure 5.2e**. It can be deduced that BCCFYb is favorably stable under the described testing conditions in **Figure 5.2e**. **Figure 5.2f** contrasts the ASR of BCCFYb at 600 ^{o}C with other prominent PCFC cathode materials under wet air testing conditions. BCCFYb displays the least ASR, validating it as a highly enhanced cathode material for PCFCs.

X-ray photoelectron spectroscopy (XPS) was used to study the valency and electronic structure of the B-site cations, Co, Ce, Fe, Yb, and O, acquired from the core-level spectra of the cations, as shown in **Figure S5.13-14**. This purpose was to ascertain the rationale behind the improved electrocatalytic ORR of BCCFYb and provide insights into the oxygen vacancy concentration of the material. The XPS profiles were deconvoluted using standard Gaussian-Lorentz[361]. **Figure S5.13** shows the XPS deconvolution of the major B-site cations in BCCFYb; Co 2p3/2 and Ce 3d3/2 & 3d5/2. The binding energies and concentrations of Co^{3+} and Co^{4+} are ~776.85 eV (~13 %) and 777.82 eV (~87 %), respectively. The Ce 3d3/2 & 3d5/2 sub-peaks were designated to Ce^{3+} (~9 %) and Ce^{4+} (~91 %) at different binding energies as shown in **Figure S5.13**[362]**.** It can be observed that the binding energies of the cations in BCCFYb are relatively lower compared to those of BCYb, BCF, and BCYb-BCF composite, as shown in **Figure S5.14**. The O1s spectra of the four samples illustrated in **Figure 5.3a** were deconvoluted into four peaks: the O^{2-} (lattice oxygen), O_2^{2-}/O^- (highly oxidative oxygen), OH^-/O_2 (adsorbed oxygen) and H_2O (adsorbed water), as vividly described in **Table S5.2**. BCCFYb has a high adsorbed species with significantly lower binding energy than the other samples, as shown in **Figure 5.3a**. It can also be observed that there is a relative decrease in the signal of the highly oxidative oxygen in the fitted O1s spectra for BCYb-BCF and BCCFYb compared with the other samples, likewise a closeness in the percentages of their O_2^{2-}/O^- peaks. This phenomenon could be due to the co-existence of Co- and Ce-rich phases in the composite materials, engendering similar O_2^{2-}/O^- concentrations, yet contrasting binding energies. The process for oxygen vacancy formation based on the Co and Ce-rich sites for all the samples, where $Fe_{Ce}^{\times}$ and $F\dot{e}_{Ce}$ equate to Fe^{3+} and Fe^{4+}, is described using Kroger-Vink notations in Eqns. 1 and 2.

$$Yb_2O_3 + 2Co_{Co}^{\times} + O_O^{\times} \leftrightharpoons 2Yb'_{Co} + V\ddot{o} + 2CoO_2 \qquad 1$$

$$O_O^{\times} + 2F\dot{e}_{Ce} \leftrightharpoons 2Fe_{Ce}^{\times} + V\ddot{o} + \frac{1}{2}O_2 \qquad 2$$

Electrical conductivity is one of the yardsticks for assessing the performance of cathode materials for ceramic fuel cells[7]. **Figure 5.3b** presents the electrical conductivity of BCCFYb relative to BCF and BCYb in the temperature range of 400 – 800 °C using the direct current (DC) measurement method. This approach has been established to generate a combination of ionic and electronic conductivity with $\sigma_{ionic} << \sigma_{electronic}$[182]. In a non-humid atmosphere, however, the σ_{ionic} corresponds to oxygen ion defects transport while the $\sigma_{electronic}$ corresponds to electron-hole defects transport. Nevertheless, all the samples displayed a typical p-type semiconductor behavior since the electrical conductivities increased with temperature due to the small polaron hopping phenomenon [363]. The electrical conductivity of the BCYb outperforms all other samples due to its high cobalt content, followed by BCCFYb and BCF. The electrical conductivity of BCCFYb exceeds the conductivity threshold (0.1 S cm^{-1}) for CFCs throughout the temperature range it was tested at, while those of BCF are very low (<0.02 S cm^{-1}) at all temperatures[21]. The activation energy of the electrical conductivity of BCCFYb was estimated to be 0.08 eV, which is very low compared to BCF, BCYb, and to other prominent cathode materials for CFCs, as shown in **Figure 5.3c** [100,334,364].

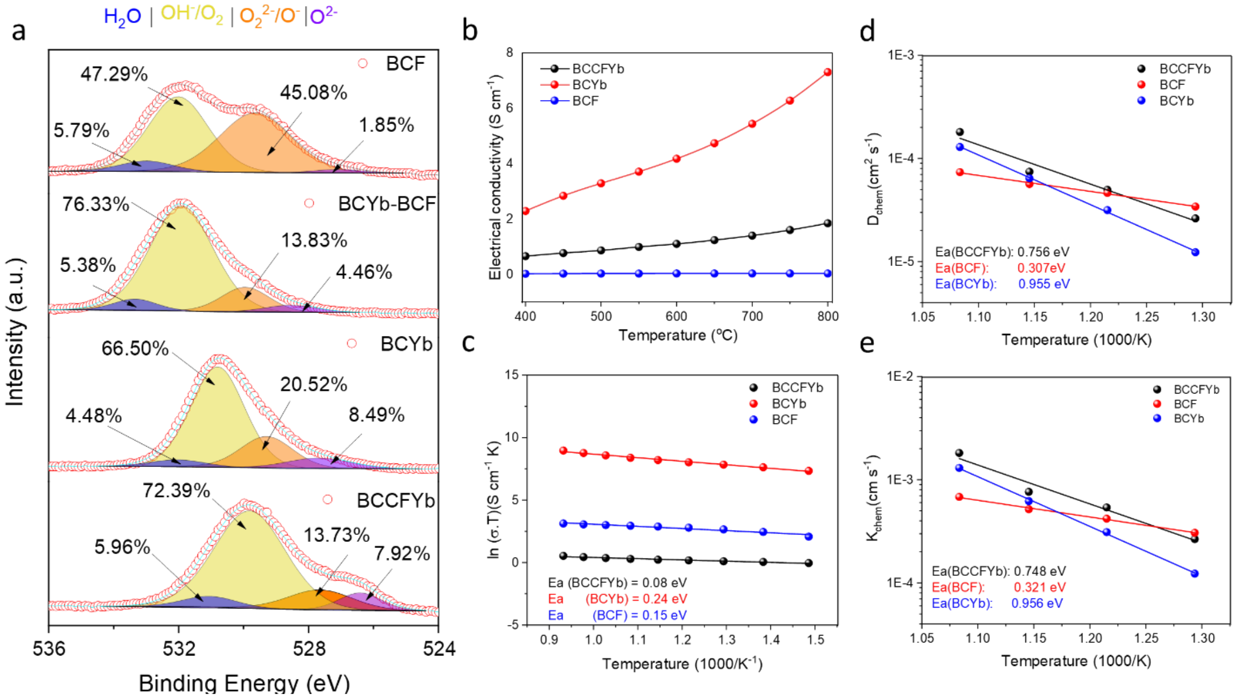

Figure 5.3: (a) The deconvolution of the O1s XPS spectra of BCCFYb, BCYb, BCYb-BCF, and BCF. (b) Electrical conductivity of BCCFYb, BCYb, and BCF from 400-800 °C. (c) Arrhenius plots of electrical conductivities of BCCFYb, BCYb, and BCF from 400-800 °C. (d,e) Bulk diffusion and surface exchange coefficients of BCCFYb, BCF, and BCYb.

The oxygen exchange in BCCFYb, BCYb, and BCF was studied using electrical conductivity relaxation (ECR). The dense bars of the samples were subjected to a change in atmospheric condition from an oxygen partial pressure of 0.21 to 0.1 atm in the temperature range of 500-650 °C, as shown in **Figure S5.15**. Following Fick's second law, the coefficients of bulk diffusion and surface exchange constants were estimated using the ECR data, as shown in **Figure 5.3**(d,e)[365,366]. At 650 °C, the D_{chem} and K_{chem} for BCCFYb surpass those of BCF and BCYb by 145 % and 40 %, respectively, reinforcing BCCFYb as the superior cathode material at intermediate temperatures. However, BCF has the lowest activation energy, which could be attributed to its low electron-hole concentration and high cerium content[367].

Since BCCFYb exhibited the best performance, the distribution of relaxation time (DRT) of the EIS data at various testing conditions were examined, as illustrated in **Figure 5.4.** The purpose was to study the kinetics of the electrochemical processes responsible for the improved catalytic ORR of BCCFYb self-ordered nanocomposite [368,369]. The DRT method involves deconvoluting complex electrochemical impedance spectra data to study the kinetics of the catalytic ORR processes[369]. The deconvolution process helps to understand the electrokinetic mechanisms of the ORR in BCCFYb by separating the different steps in the electrode electrochemical reactions based on frequency segregation. The DRT peaks are customarily partitioned into low, medium, and high-frequency regions denoted as LF, MF, and HF. The LF peak represents the rate-limiting step for ORR, which is typically associated with gas diffusion due to the transport of ionic/electronic defects within the electrode. The MF peak represents resistance from bulk diffusion and surface exchange processes, while the HF represents resistance due to charge transfer processes at the electrode-electrolyte interface[370]. The area of the peaks within the segmented frequency ranges can be correlated with the corresponding resistance of the electrochemical process[371].

At first, the electrochemical processes for BCCFYb nanocomposite on SDC oxygen ion-conducting electrolyte at different oxygen partial pressures (pO_2) were studied using DRT at a constant temperature of 550 ^oC, as shown in **Figure 5.4a.** All the peaks fall in the MF region (10^0 – 10^4 Hz), although with depressing intensity as the oxygen concentration increases, suggesting that the electrochemical processes of the cathode were generally insensitive to changes in pO_2 on phase electrolyte. This phenomenon implies that the resistance in the cell is either due to oxygen adsorption and dissociation or surface exchange. It could even be a combination of the processes. A similar test was conducted using the BCCFYb cathode on BCZYYb proton-conducting electrolyte at the same temperature of 550 ^{o}C, as shown in **Figure 5.4b.** This time, the rate-limiting steps for ORR spread across the three regions: HF ($\geq 10^{4}$ Hz), M.F., and L.F. ($\leq 10^{0}$ Hz), with the MF peaks dominating the electrochemical resistance processes. Nevertheless, the intensity of the resistances decreased with increasing oxygen concentration, but the cathode was also insensitive to pO_2 variation on the BCZYYb electrolyte since a similar pattern of rate-limiting processes was observed throughout.

Figure 5.4c presents a more complicated series of DRT peaks derived from EIS data of tests conducted under different atmospheric conditions and electrolytes to reveal the various electrochemical processes at 650 ^{o}C for the BCCFYb nanocomposite-based cathode. Under synthetic air, the peaks in the MF and LF were almost completely depressed when the test was conducted using an SDC electrolyte, confirming the predominance of ORR resistance from charge transfer processes. When the electrolyte was changed to BCZYYb using the same synthetic air, the resistance source shifted to MF with very high intensities suggesting that the limiting step for ORR was due to bulk diffusion and surface exchange processes at the electrode interface. When 0.025 pH_2O concentration was introduced into the cell, an additional peak emerged at the LF, with most of the peaks at the MF. When the pH_2O was further increased to 0.05 atm, the intensity of the peak at the LF increased while those of the peaks at the MF slightly decreased.

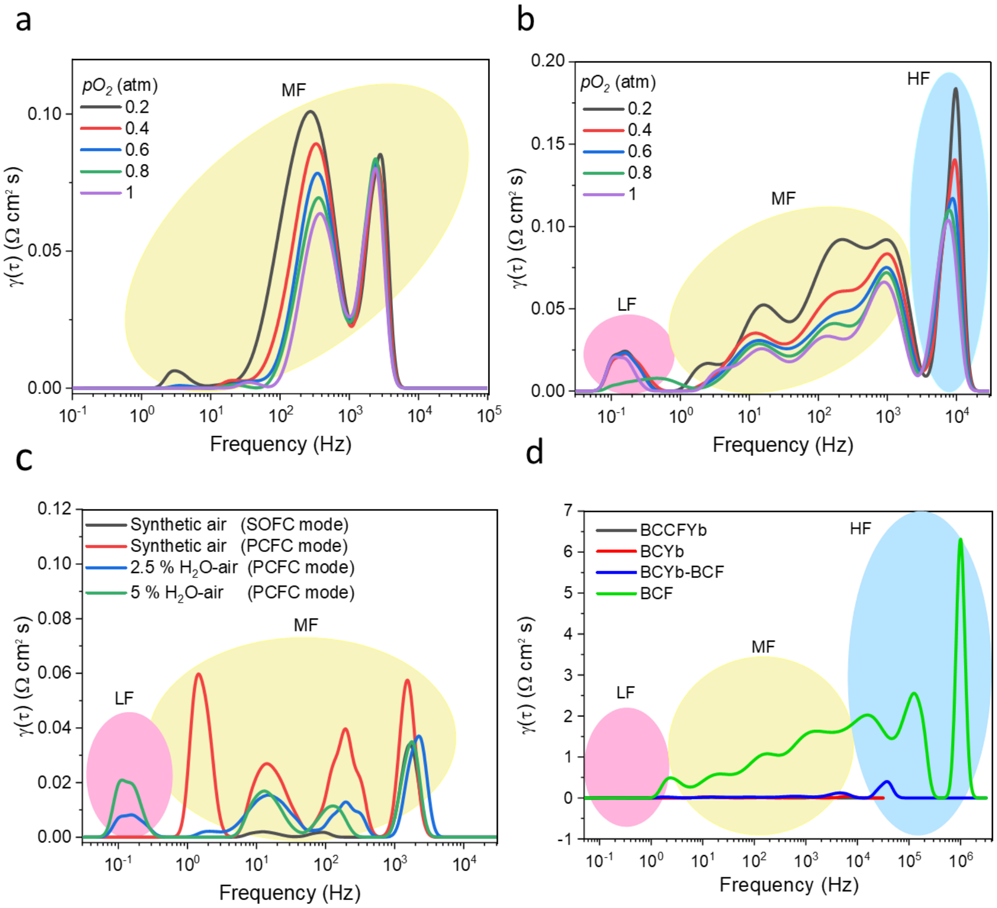

Figure 5.4: DRT spectra of pO$_2$ variation (0.2-1 atm) of (a) BCCFYb | SDC | BCCFYb symmetrical cell at 550 °C in air (b) BCCFYb | BCZYYb | BCCFYb symmetrical cell at 550 °C in 2.5 % H$_2$O-air (c) DRT spectra comparing the electrochemical processes of BCCFYb in oxygen ion and proton conducting symmetrical cells at different testing conditions (air, 2.5% H$_2$O-air, and 5% H$_2$O-air) at 650 °C. (d) DRT spectra of BCCFYb relative to BCF, BCYb, and BCYb-BCF at 650 °C in 2.5 H$_2$O-air.

Figure 5.4d attempts to contrast the electrochemical processes in BCCFYb relative to BCF, BCYb, and BCYb-BCF traditional composite at 650 °C in H$_2$O-air. The BCCFYb DRT profile is not visible due to its relatively low resistance. Nevertheless, the rate-limiting processes for ORR in the other cathode materials, especially BCF and BCYb-BCF, are excessive resistance to charge transfer, bulk diffusion, and surface exchange at the electrode-electrolyte interface.

Summarily, increasing pO_2 concentration decreases the intensity of rate-limiting steps for ORR but does not lead to the emergence or disappearance of a new ORR rate-limiting process for BCCFYb cathode on both SDC and BCZYYb electrolytes. Introducing humid air into the BCCFYb cathode on BCZYYb decreases the intensity of the cell resistance but introduces a rate-limiting process due to gas diffusion because the hydrated electrode surface will exhibit decreased capability for O_2 adsorption. Hence, increasing the pH_2O further will decrease the total cell resistance but trigger an increase in the intensity of cell resistance resulting from a hindrance to the transport of electronic defects.

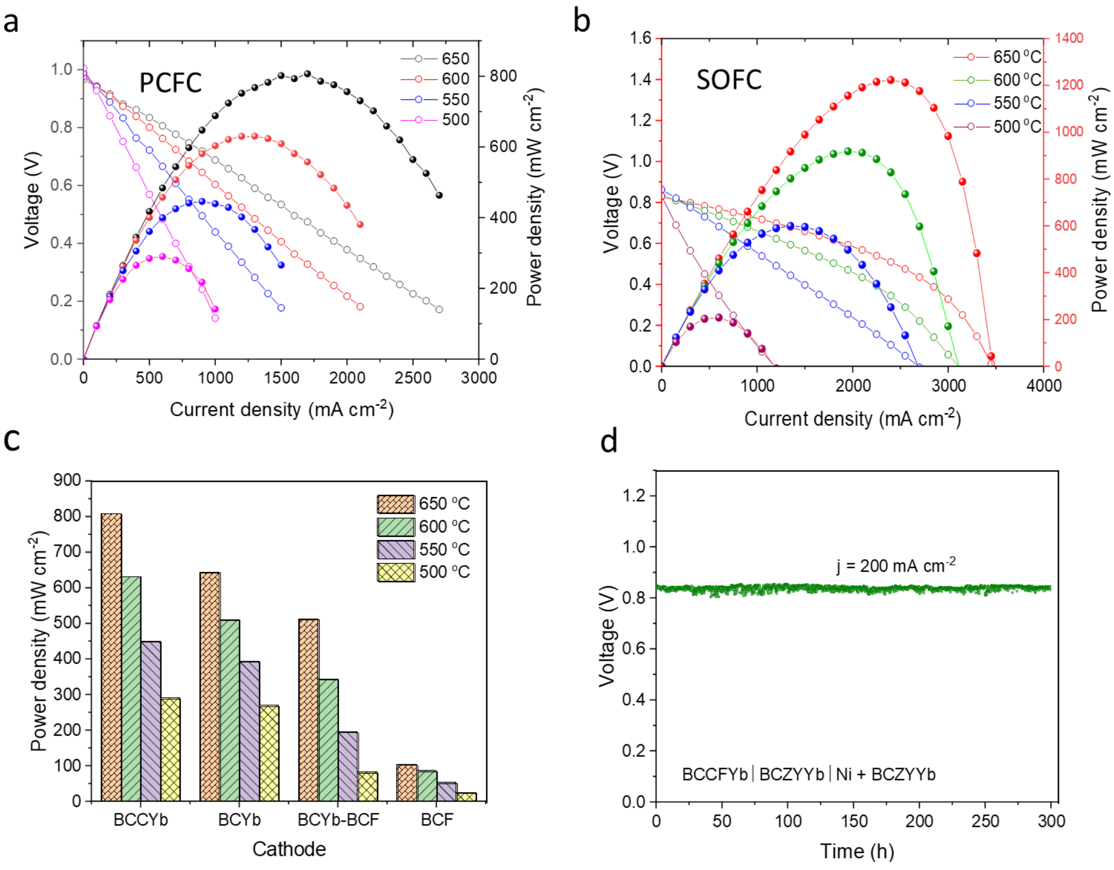

Figure 5.5: I-V-P curves of anode-supported single cells with the anode being fed with H_2 and the cathode exposed to ambient air (a) BCCFYb│BCZYYb│Ni-BCZYYb. (b) BCCFYb│SDC│Ni-

SDC. (c) Comparison of PCFCs based on BCCFYb, BCYb, BCF, and BCYb-BCYb cathodes (f) Stability of BCCFYb│BCZYYb│Ni-BCCFYb single cell in H_2 at 550 °C.

Figure 5.4(a,b) show the I-V-P curves of BCCFYb│BCZYYb│Ni-BCZYYb and BCCFYb│SDC│Ni-BCCFYb anode-supported single cells tested under pure H_2 fuel. The cross-section of the tested cell is illustrated in **Figure S5.17**. The peak power densities of the cells exceed 1200 mW cm^{-2} and 800 mW cm^{-2}, respectively, under SOFC and PCFC modes at 650 °C. The power output of BCCFYb exceeds that of the mechanically generated BCYb-BCF composite and those of BCYb and BCF, as shown in **Figure 5.5c and Figure S5.16**. This confirms the superiority of self-ordered nanocomposites compared to other classes of materials for PCFCs. The comparison of the performance of CFCs based on BCCFYb cathode relative to other cathode materials is also shown in **Table S5.3-4.** The PPD values of BCCFYb-based single cells surpass those of famous cathode materials for SOFC and PCFCs. As earlier buttressed, the high performance of the BCCFYb-based CFCs is due to the synergy of the host and ancillary phases. It can also be observed that the open-circuit voltage (OCV) of the SOFC is lower than that of the PCFC.

Similarly, the performance of the PCFC is slightly higher than that of the SOFC at 500 °C. However, during the examination of the performance of the symmetrical cell based on the BCCFYb cathode on an oxide-ion conducting electrolyte (**Figure 5.2**c), the performance was better than when it was used as a cathode on a proton-conducting electrolyte at 500 °C. The reduced performance of the single cell based on SDC electrolyte at 500 °C and its lower OCV could be attributed to the high current leakage in the SOFC resulting from the internal shorting of the SDC electrolyte and the lower activation energy characteristic of PCFCs [107,372]. Generally, better performance can be achieved for the PCFC with improved single-cell fabrication techniques. The PPD values attained confirm the potential of the BCCFYb nanocomposite cathode as a promising candidate for PCFCs and the suitability of self-assembly engineering for cathode development. The stability of the single cell under PCFC mode at a current density of 200 mA cm^{-2} for 300h is illustrated in **Figure 5.4d,** which also showcases the prospects of BCCFYb as a suitable candidate for ceramic electrochemical cell applications.

5.5 Conclusion and summary

In this work, the performance of a self-ordered nanocomposite cathode material was evaluated in relation to various cathode materials with different conductivity properties. The thermodynamically stable self-ordered nanocomposite material was created through a nanoscale auto-biphasic ordering process using the ceramic precursor $BaCo_{0.5}Ce_{0.3}Fe_{0.1}Yb_{0.1}O_{3-\delta}$ (BCCFYb). The resulting material consists of a host cubic phase (∼70 %) and an ancillary rhombohedral phase (∼30 %), which synergistically enhance its ORR activity. The performance of the BCCFYb material was compared to that of cobalt-rich oxide-ion and electron (O^{2-}/e^-) conducting $BaCo_{0.833}Yb_{0.167}O_{3-\delta}$ (BCYb), cerium-rich proton and electron (H^+/e^-) conducting $BaCe_{0.75}Fe_{0.25}O_{3-\delta}$ (BCF), and Co-Ce-rich triple ionic ($O^{2-}/H^+/e^-$) conducting $BaCo_{0.833}Yb_{0.167}O_{3-\delta}$ - $BaCe_{0.75}Fe_{0.25}O_{3-\delta}$ (BCYb-BCF) traditional composite materials. The BCCFYb material showed superior performance in terms of power output and stability compared to the other materials. These results demonstrate the effectiveness of self-assembly engineering as a simple approach for manipulating triple ionic and electronic conductivity in cathode materials for ceramic electrochemical cells.

5.6 Supplementary section

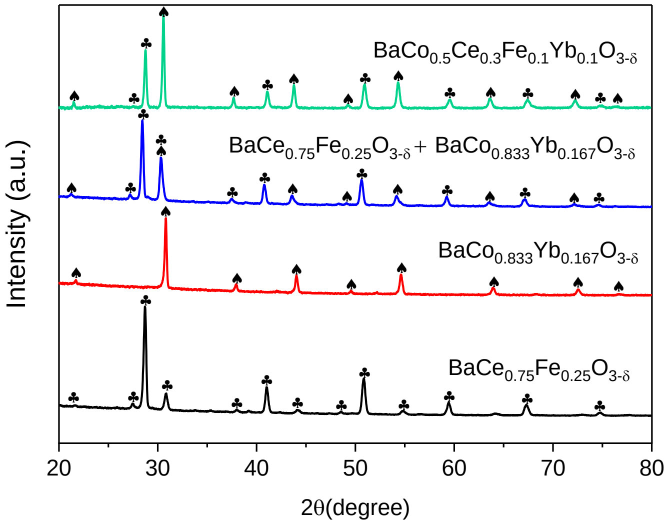

Figure S5.1: XRD profiles of all as-synthesized cathode materials.

Table S5.1: Rietveld refinement output generated from as-synthesized BCCFYb XRD pattern.

Element	Wyckoff Symbol	x	y	z
Phase 1 (Pm-3m; a=b=c=4.1378Å, 70 wt.%)				
Ba	1a	0	0	0
Co	1b	0.5	0.5	0.5
Yb	1b	0.5	0.5	0.5
O	3c	0	0.5	0.5
Phase 2 (R-3c; a=b=6.2173 Å c=15.1630 Å, 30 wt.%)				
Ba	6a	0	0	-0.25
Ce	6b	0	0	0
Fe	6b	0	0	0
O	18e	0.4487	0	0.25

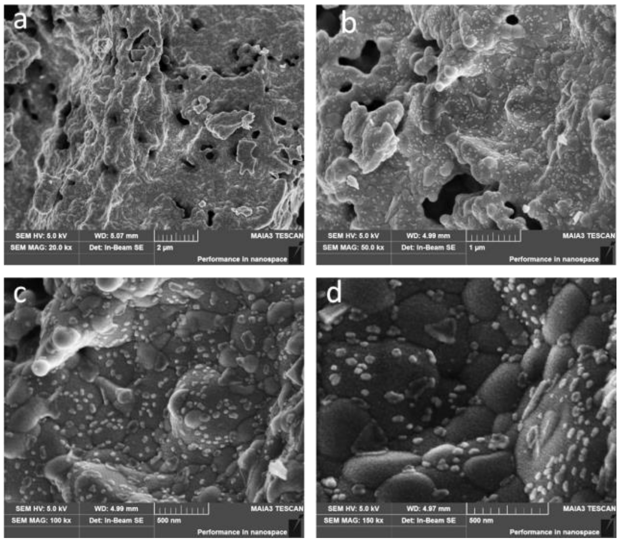

Figure S5.2: SEM micrograph of BCCFYb nanocomposite after undergoing calcination for 5h at 1000 ^{o}C.

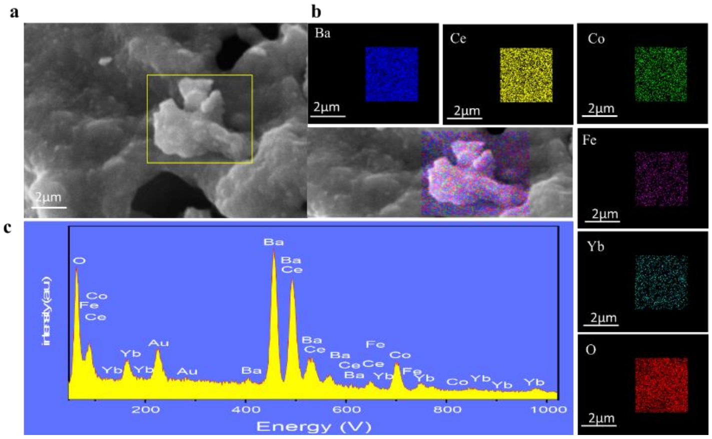

Figure S5.3: (a) SEM image of BCCFYb after undergoing calcination at 1000 ^{o}C in ambient air. (a) EDX mapping of the SEM image in (a). (c) SEM-EDS spectrum summary.

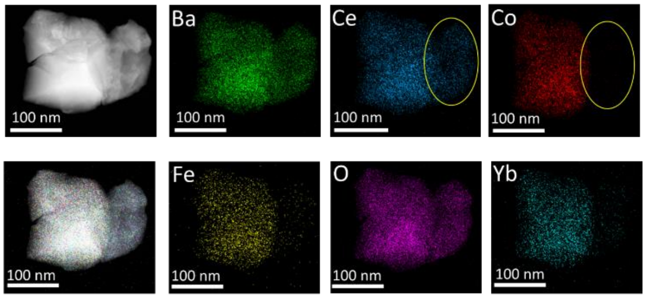

Figure S5.4: EDS mapping results of BCCFYb calcined at 1000 ^{o}C for 5h in ambient air.

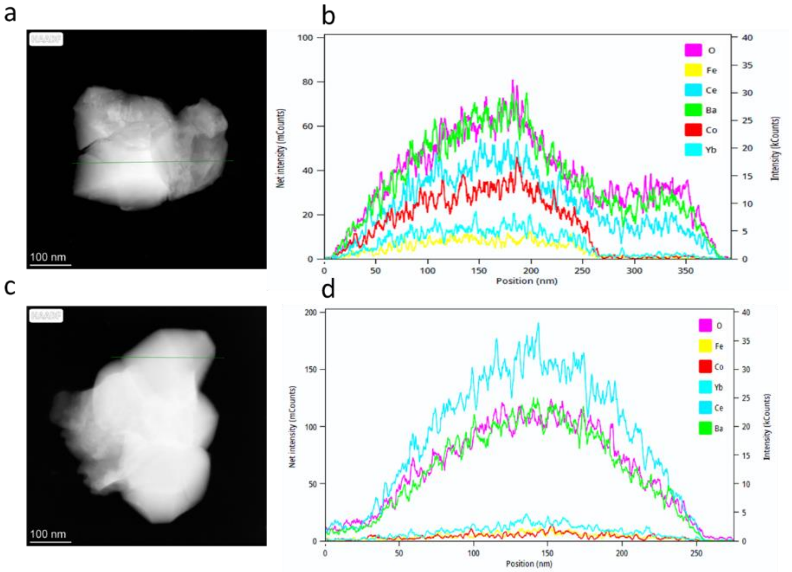

Figure S5.5: (a) Scanning transmission electron microscopy (STEM) image of BCCFYb nanocomposite (b) line energy dispersive X-ray (EDX) scan of (a) showing a Co-rich phase (c) STEM image of BCCFYb (d) line EDX scan of image (c) showing Ce rich phase.

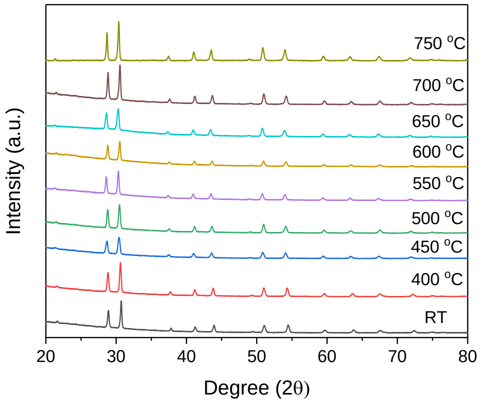

Figure S5.6: HT-XRD for BCCFYb nanocomposite powders from room temperature to 750 ^oC.

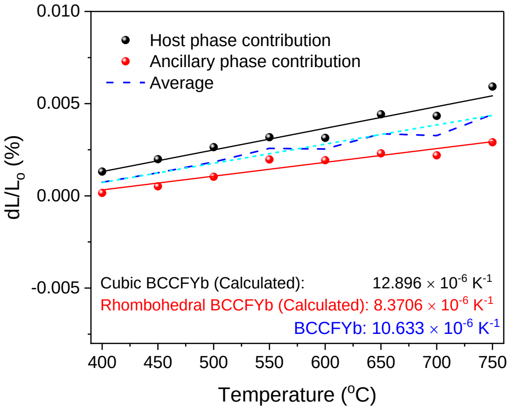

Figure S5.7: Calculated TEC of BCCFYb from the HT-XRD patterns in Figure S5.6.

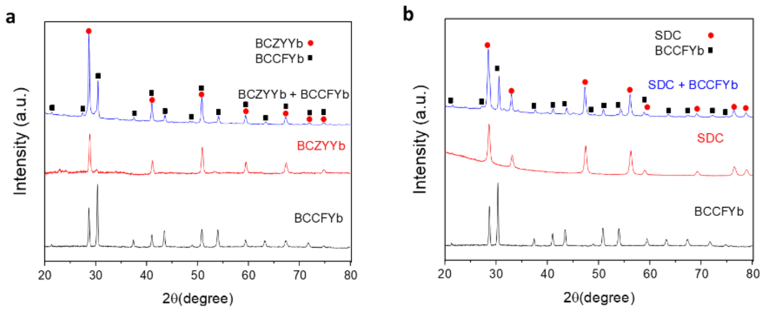

Figure S5.8: XRD patterns of (a) BCCFYb, BCZYYb, and mechanically mixed BCCFYb + BCZYYb (50:50 weight ratio) calcined at 850 °C for 2h in air and (b) BCCFYb, SDC, and mechanically mixed BCCFYb + SDC (50:50 weight ratio) calcined at 850 °C for 2h in air.

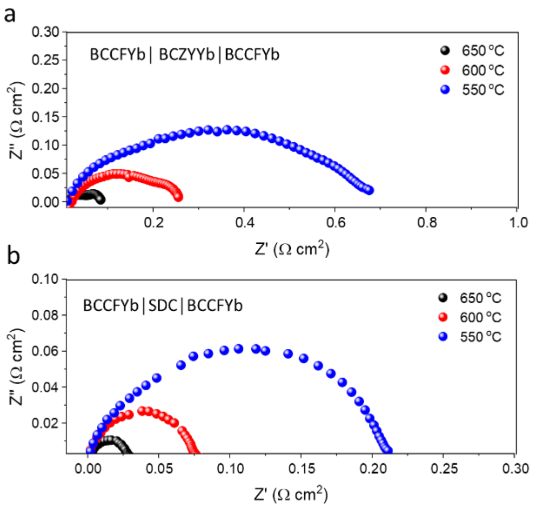

Figure S5.9: EIS spectra of symmetrical cells with the configurations (a) BCCFYb│ BCZYYb│BCCFYb and (b) BCCFYb│SDC│BCCFYb.

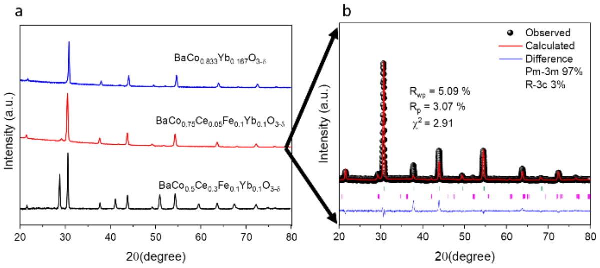

Figure S5.10: (a) XRD patterns showing different cathode materials with decreasing rhombohedral phase as Ce content is reduced (b) Refinement of 97 % cubic BCCFYb.

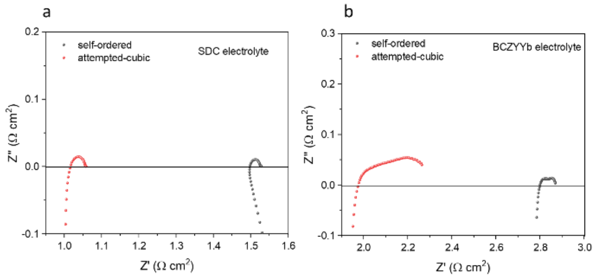

Figure S5.11: EIS spectra of symmetrical cells with the configurations (a) BCCFYb-97% cubic│SDC│BCCFYb-97% cubic and (b) BCCFYb-97% cubic│ BCZYYb│BCCFYb-97% cubic.

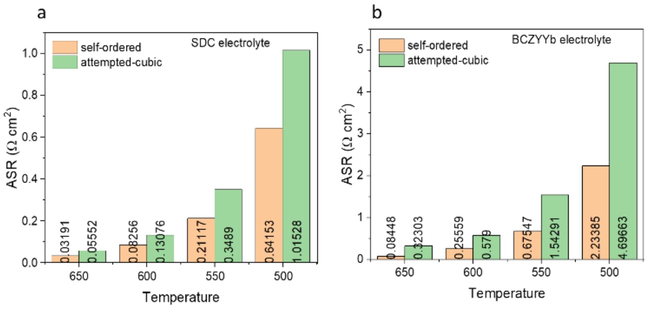

Figure S5.12: Comparison of the ASRs of the self-ordered and 97 % cubic phase BCCFYb under (a) SOFC and (b) PCFC.

Table S5.2: The composition of the deconvoluted O1s spectra for BCCFYb, BCF, BCYb and BCF-BCYb.

		Position (eV)	FWHM (eV)	Area	Atomic %
BCCFYb	$O_{lattice}$	526.41	1.55	5894.37	7.92
	O_{ox}	527.65	2.37	10220.22	13.73
	O_{ad}	529.81	2.59	53904.52	72.39
	H_2O_{ad}	531.05	1.94	4441.75	5.97
BCY	$O_{lattice}$	528.69	2.36	7050.72	8.51
	O_{ox}	530.29	1.9	17019.05	20.54
	O_{ad}	531.8	1.95	55079.16	66.48
	H_2O_{ad}	533.03	1.99	3707.47	4.47
BCF	$O_{lattice}$	527.11	1.79	2021.19	1.85
	O_{ox}	529.64	2.62	49228.28	45.13
	O_{ad}	532.01	2.18	51541.88	47.25
	H_2O_{ad}	532.98	1.94	6301.28	5.78
BCYb-BCF	$O_{lattice}$	527.21	1.94	4445.68	4.46
	O_{ox}	528.61	1.75	13776.24	13.83
	O_{ad}	530.57	2.3	76050.22	76.33
	H_2O_{ad}	532	1.55	5360.06	5.38

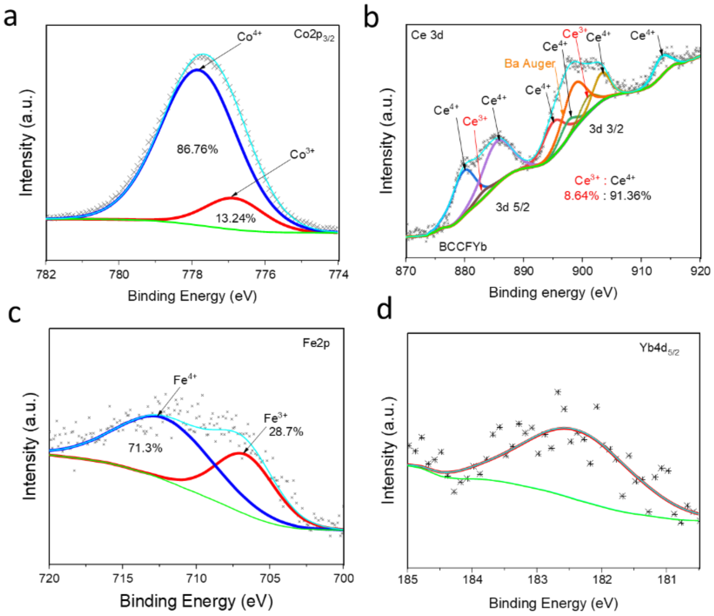

Figure S5.13: Deconvoluted XPS spectra of BCCFYb nanocomposite B-site cations (a) Co 2p (b) Ce 3d (c) Fe 2p and (d) Yb 4d.

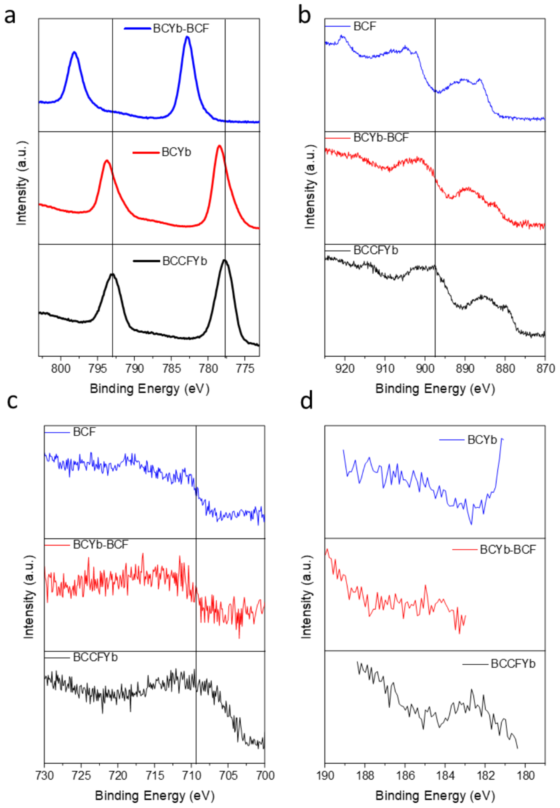

Figure S5.14: XPS spectra of BCCFYb, BCF, BCYb, and BCYb-BCF (a) Co 2p (b) Ce 3d (c) Fe 2p and (d) Yb 4d.

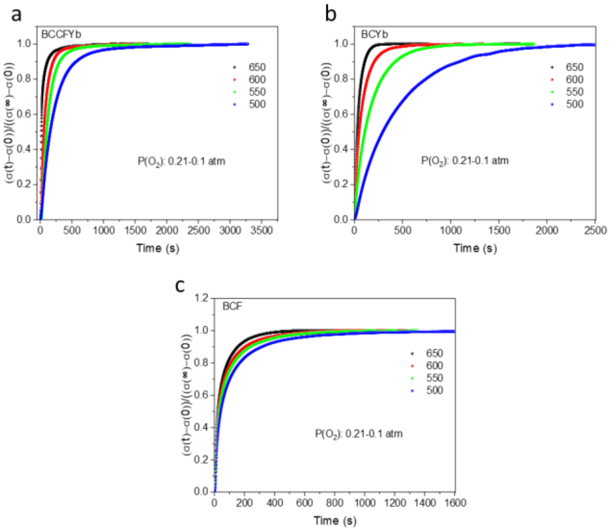

Figure S5.15: ECR curves for (a) BCCFYb (b) BCYb and (c) BCF.

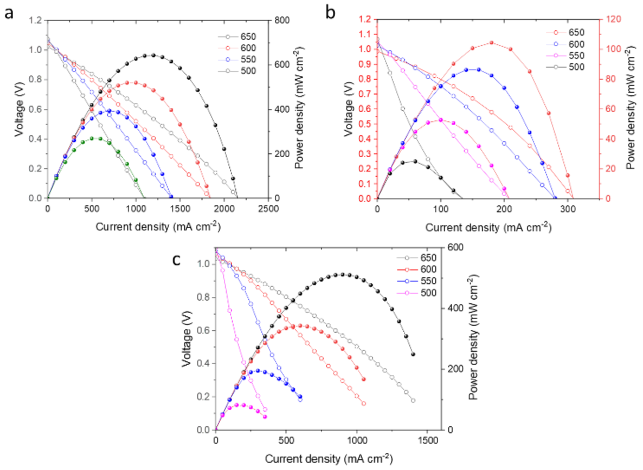

Figure S5.16: Single cells tested under H_2 fuel and ambient air. (a) BCYb│BCZYYb│Ni-BCZYYb (b) BCF│BCZYYb│Ni- BCZYYb (c) BCYb-BCF│BCZYYb│Ni- BCZYYb.

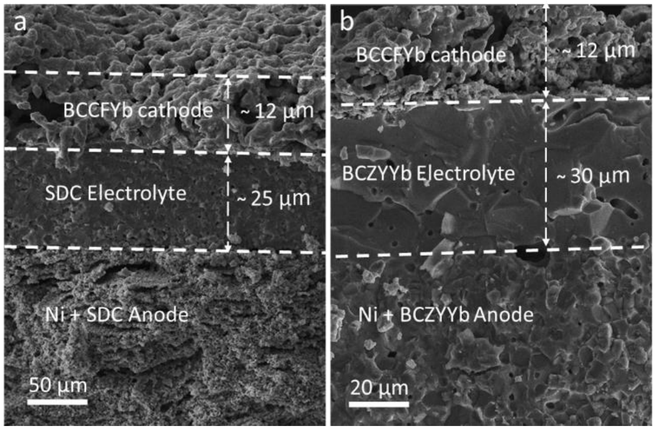

Figure S5.17: Cross-sectional SEM images of tested anode-supported ceramic fuel cells based on BCCFYb cathode. (a) SOFC (b) PCFC.

Table S5.3: PPDs of anode-supported single cells at 550 °C with different cathode materials based on O-SOFCs.

Cathode	Electrolyte	PPD, mW cm^{-2} (550 °C)	Ref.
LSCF	GDC	257	[22]
SSC	SDC (4)/ScSZ	557	[373]
PBC	SDC	300	[374]
BCFZ	SDC	400	[375]
SCNT	GDC	1150	[329]
BBSC	SDC (5)/YSZ	220 (600)	[376]
BCFZY	SDC	645	[178]
PBSCF	SDC/LSGM	697@850 ^{o}C	[358]
BCCFYb	SDC	600	This work

* LSCF: $La_{0.6}Sr_{0.4}Co_{0.2}Fe_{0.8}O_{3-\delta}$, SSC: $Sm_{0.5}Sr_{0.5}CoO_{3-\delta}$, PBC: $PrBaCo_2O_{5+\delta}$, BCFZ: $BaCo_{0.4}Fe_{0.4}Zr_{0.2}O_{3-\delta}$, SCNT: $SrCo_{0.8}Nb_{0.1}Ta_{0.1}O_{3-\delta}$, BBSC: $Ba_{0.8}Bi_{0.2}Sc_{0.1}Co_{0.9}O_{3-\delta}$, GDC: $Gd_{0.1}Ce_{0.9}O_{1.95}$, ScSZ: $Sc_{0.1}Zr_{0.89}Ce_{0.01}O_{2-x}$, YSZ: yttria-stabilized zirconia. PBSCF: $PrBa_{0.5}Sr_{0.5}Co_{1.5}Fe_{0.5}O_{5+\delta}$

Table S5.4: PPDs of anode-supported single cells at 550 °C with different cathode materials based on PCFCs.

Cathode	Electrolyte	PPD at 550 °C (mW cm^{-2})	Ref.
LSCF	BZCY	210	[377]
SSC	BZCYYb	115	[378]
BSCF	BZCY	276@600 ºC	[379]
SSNC	BZCY	250	[380]
PBC	BZCY	195	[381]
NBSCF	BCZYYb	690@600 ºC	[382]
BCFZ	BZCYYb	200	[383]
PBSCF	BZCYYb	630	[156]
BCFZY	BZCYYb	~515	[104]
PBSCF	BZCYYb	205	[384]
BCFZY	BZCYYb	400	[178]
BCYb	BZCYYb	403	This work
BCYb-BCF	BZCYYb	195	This work
BCCFYb	BZCYYb	449	This work

NBSCF: $NdBa_{0.5}Sr_{0.5}Co_{1.5}Fe_{0.5}O_{5+\delta}$, LSCF: $La_{0.6}Sr_{0.4}Co_{0.2}Fe_{0.8}O_{3-\delta}$, SSC: $Sm_{0.5}Sr_{0.5}CoO_{3-\delta}$, PBC: $PrBaCo_2O_{5+\delta}$, BCFZ: $BaCo_{0.4}Fe_{0.4}Zr_{0.2}O_{3-\delta}$, SCNT: $SrCo_{0.8}Nb_{0.1}Ta_{0.1}O_{3-\delta}$, BBSC: $Ba_{0.8}Bi_{0.2}Sc_{0.1}Co_{0.9}O_{3-\delta}$, PBSCF: $PrBa_{0.5}Sr_{0.5}Co_{1.5}Fe_{0.5}O_{5+\delta}$, BSCF: $Ba_{0.5}Sr_{0.5}Co_{0.8}Fe_{0.2}O_{5+\delta}$,

CHAPTER 6: PROBING ELECTROKINETIC PHENOMENA IN TAILORED NANOCOMPOSITE CATHODE MATERIALS[6]

6.1 Background

The preceding chapter evaluates the electrocatalytic performance of a novel TIEC nanocomposite cathode material developed through self-assembly engineering for ceramic fuel cells. The material was thermodynamically stable with superior catalytic performance in SOFC and PCFC modes. This chapter focuses on the electrokinetic mechanism of proton defect formation and transport in an optimized self-assembled cathode material for protonic ceramic cells.

6.2 Introduction

Solid oxide fuel cells (SOFCs) have gained prominence in the past decades due to their propensity to compensate for the limitations of fossil-based and renewable energy sources with higher efficiency and lower greenhouse gas emissions[30]. Their commercialization, however, is stifled due to their high operating temperature, especially when the traditional yttria-stabilized zirconia (YSZ) is used as the electrolyte, causing accelerated system degradation and high cost[385]. Thus, reducing their operating temperatures (< 700 °C), without significantly affecting their power output, is an essential obligation to attain commercialization.

Past studies have explored approaches to achieve a significant reduction in the operating temperature of SOFCs [7,386–388]. In recent times, proton-conducting solid oxide fuel cells (P-

---

[4] Fully published chapter:
Bello IT, Yu N, Song Y, Wang J, Chan TS, Zhao S, Li Z, Dai Y, Yu J, Ni M. Electrokinetic Insights into the Triple Ionic and Electronic Conductivity of a Novel Nanocomposite Functional Material for Protonic Ceramic Fuel Cells. Small. 2022 Oct;18(40):2203207.

SOFCs), otherwise known as protonic ceramic fuel cells (PCFCs), have been confirmed to stand better chances of operating efficiently at lower temperatures (up to 350 ^{o}C) relative to the traditional oxygen ion conducting SOFCs [20]. This is primarily because of their lower activation energies and the non-fuel dilution of fuel at their anodes [95,122].

The cathode is one of the core cell components that facilitate the operation of PCFCs at low temperatures. This is because it is the center where oxygen reduction reaction (ORR) takes place[62]. Lowering the operation temperature, however, implies that the kinetics for ORR will become sluggish and the performance of the cell will be impacted negatively[389]. The mixed ionic-electronic conductivity (MIEC) is an essential property requisite for low-temperature operating oxygen ion-conducting SOFCs because it helps to extend reaction sites beyond the triple-phase boundary (TPB) thereby enhancing the electrochemical activities of the cathode at lower temperatures[76]. Triple ionic and electronic conductivity (TIEC), however, has been established to be more suited for PCFCs because they can facilitate the broader spatial transmission of active reaction sites for electrochemical reactions in the cell through the introduction and enhancement of proton conductivity in the cathode [103,390]. For proton transport to take place in PCFCs, however, a proton transport enabling atmospheres, such as H_2 and H_2O, is needed so that the desired protonic defects can be formed alongside oxygen vacancy and electronic defects. A protonic conductivity up to 10^{-5} Scm^{-1} has been deemed sufficient for reasonable protonic carrier formation and transport in a TIEC material [359,391]. This implies that cathode materials that can simultaneously transport protonic carriers, oxygen vacancy, and electron holes, can function more efficiently at reduced temperatures without noticeably trading off their electrocatalytic performance[103]. The attainment of this feat in PCFC cathodic materials design promises to substantially reduce PCFC degradation and make the transition of this technology to the stage of commercialization smoother.

Several approaches have been attempted in the attainment of TIEC in PCFC cathode materials. This could be through the enhancement of proton conductivity in MIEC materials by strategically co-doping base materials (such as $BaFeO_{3-\delta}$, $BaCoO_{3-\delta}$, and $BaZrO_{3-\delta}$) to derive proton-conducting single-phase materials such as $BaCo_{0.4}Fe_{0.4}Zr_{0.1}Y_{0.1}O_{3-\delta}$, $BaCo_{0.7}Fe_{0.2}Nb_{0.1}O_{3-\delta}$ among others [104,387]. It could also be through the traditional mixing of as-synthesized materials with other materials with various dominant conductivities as delineated in the percolation theory used to describe $La_{0.6}Sr_{0.4}Co_{0.2}Fe_{0.8}O_{3-\delta}$(LSCF)-$Sm_{0.8}Ce_{0.2}O_{3-\delta}$-$BaZr_{0.1}Ce_{0.7}Y_{0.2}O_{3-\delta}$ composite material [392]. For instance, the dual-phase composite material $Sm_{0.5}Sr_{0.5}CoO_{3-\delta}$ - $BaZr_{0.1}Ce_{0.7}Y_{0.2}O_{3-\delta}$ was prepared using this traditional mechanical approach[393]. The self-assembly approach is an emerging technique recently incorporated into the design of cathode materials for ceramic fuel cells[394]. This approach entails the formation of an organized structure through the spontaneous amalgamation of constituent phases resulting from the special interaction between the constitutive elements. This results in the generation of a unique structure combining the inherent properties of the constitutive phases. $BaCo_{0.7}(Ce_{0.8}Y_{0.2})_{0.3}O_{3-\delta}$, $BaCe_{0.5}Fe_{0.4}Ni_{0.1}O_{3-\delta}$, $BaCe_{1-(x+z)}Fe_{x}Y_{z}O_{3-\delta}$ and $Ba_{0.5}Sr_{0.5}Co_{0.48125}Fe_{0.20625}W_{0.3125}O_{3-\delta}$ are some of the few recently reported self-assembled cathodic materials for PCFCs [249,347–349,395,396]. The self-harmonization of distinct compatible phases with different conductivity characteristics and the thermal expansion compatibility of these materials with PCFC electrolytes make them stand out in terms of performance and durability. There are certain challenges, however, associated with this technique such as phase transition under varying temperature conditions as in the case of $BaCo_{0.7}Ce_{0.24}Y_{0.06}O_{3-\delta}$ [337]; imbalanced rationing and selection of elements which results in weak synergistic interaction between the different phases and hence, low electrocatalytic performance, as in the case of $BaCe_{0.5}Fe_{0.4}Ni_{0.1}O_{3-\delta}$ and $Ba_{0.5}Sr_{0.5}Co_{0.48125}Fe_{0.20625}W_{0.3125}O_{3-\delta}$ [347,349]. In addition, the estimation and description of the mechanism of proton uptake in TIEC materials have been daunting and vague[97]. These are some of the salient issues that need to be addressed in the incorporation of self-assembly engineering in the development of cathode materials for PCFCs.

This study, therefore, presents a newly designed nanocomposite material with triple ionic-electronic conductivity for reduced temperature PCFCs via self-assembly engineering. The nanocomposite material with the configuration, $Ba(CeCo)_{0.4}(FeZr)_{0.1}O_{3-\delta}$ (BCCFZ) was strategically developed via a one-pot synthesis. It comprises a cubic and rhombohedral phase spontaneously composited into a unique crystal structure. A combination of electrical conductivity relaxation (ECR), X-ray absorption spectroscopy (XAS), and distribution of relaxation times (DRT) mathematical tool was used to provide insights into the mode of proton uptake as well as the thermodynamic enthalpy of protonic defects formation and transport in the nanocomposite material relative to the single-phase $BaCo_{0.4}Fe_{0.4}Zr_{0.1}Y_{0.1}O_{3-\delta}$ (BCFZY). The underlying electrokinetic mechanisms and characteristics of BCCFZ that made it perform optimally and thus, recommended for reduced temperature protonic ceramic applications are discussed.

6.3 Results and discussion

The crystal and microstructural characterization of the one-pot as-synthesized BCCFZ powders at room temperature after calcination at 1000 ^{o}C for 5h in air is shown in **Figure 6.1**. The Rietveld refinement of the X-ray diffraction spectroscopy (XRD) pattern illustrated in **Figure 6.1a** shows that the material is biphasic containing two distinct crystalline phases, a rhombohedral and cubic phase. The phase separation of BCCFZ into a rhombohedral-cubic structure could be due to the wide difference between the ionic radius of the two key B-site elements (Ce and Co) based on their stoichiometric configuration during the synthesis of the BCCFZ (4411) nanocomposites [397]. The Ce and Co both with coordination of VI have an ionic radius of 0.87 nm and 0.53 nm, respectively based on Shannon estimation[355]. Based on the Rietveld refinement results, the rhombohedral phase (space group = R-3c, JCPDS: 75-0431) is the dominant phase (60 wt. %) with the lattice parameters a = b = 6.167753 Å and c = 15.056063 Å while the cubic phase (40 wt. %, space group = Pm-3m, JCPDS: 75-0227), has the lattice parameters a = b = c = 4.1060143 Å. **Table S6.1** presents a more vivid description of the Rietveld refinement data of the XRD pattern for BCCFZ.

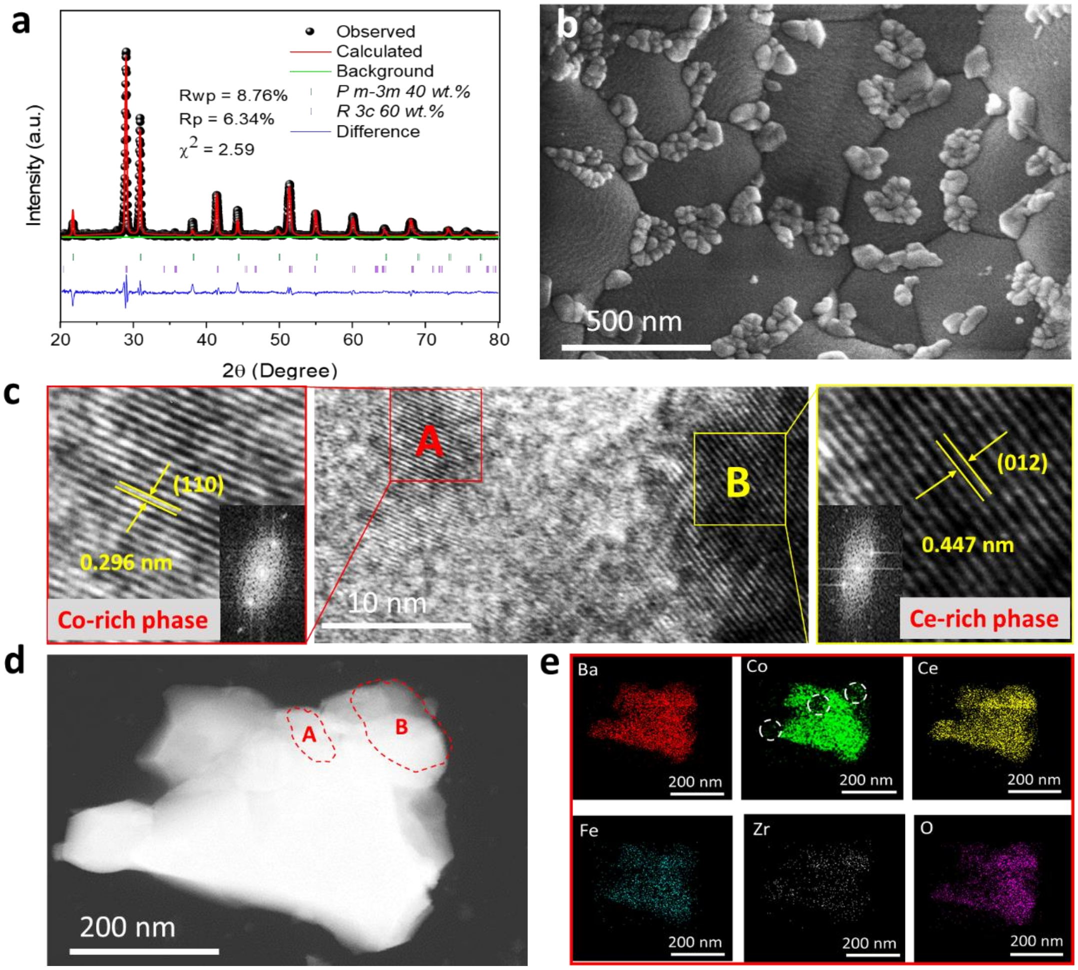

Figure 6.1: Biphasic structure and microstructural characterization of self-assembled BCCFZ after calcination at 1000 °C for 5h showing (a) the Rietveld refinement of the as-synthesized BCCFZ nanocomposites (b) the HR-SEM of BCCFZ nanocomposites (c) the HR-TEM image of BCCFZ nanocomposites (d) the STEM image and (e) the EDX mapping of BCCFZ nanocomposites.

The weighted residual (Rwp), residual of least squares (Rp), and goodness of fit (χ^2) of the refined diffraction pattern of BCCFZ powders corresponding to 8.76 %, 6.34 %, and 2.59 %, respectively confirm the reliability of the refinement results. This indicates that the calculated profile agrees intimately with the observed XRD pattern of the as-synthesized BCCFZ nanocomposite powders. The lattice parameters of the rhombohedral phase, similar to BaCe$_{0.8}$Zr$_{0.2}$O$_{3-\delta}$ [398]with the occupancy data from the refined results in **Table S6.1** confirm that the phase is rich in cerium.

This suggests that the phase is mainly proton-conducting. The lattice parameters of the cubic phase, $BaCo_{0.8}Fe_{0.2}O_{3-\delta}$ derived from cubic $BaCoO_{2.23}$[399], with B-site occupancy similar to that of the traditional $Ba_{0.5}Sr_{0.5}Co_{0.8}Fe_{0.2}O_{3-\delta}$ material [400], suggests that the cobalt-rich phase is dominantly mixed oxygen-ion and electronic conducting phase. It can therefore be inferred from refinement results that the BCCFZ is predominantly proton-conducting combined with a mixed ionic conducting phase. Since the peaks of the two phases have been determined and identified from the refinement of the XRD profile in **Figure 6.1a**, the crystallite sizes of both phases were then estimated using the identified peaks of the observed pattern of the XRD result. The Scherrer equation ($D = K\lambda/L\cos\theta$) was used in the estimation of the crystallize sizes[356]. The crystallite sizes of the rhombohedral and cubic phases were 23.80 nm and 44.01 nm, respectively. **Figure 6.1b** is the HR-SEM image showing the unique arrangement of O-BCCFZ and H-BCCZF phases to form the BCCFZ biphasic crystal structure. The meandrous nanocomposite particles in **Figure 6.1b** can be inferred to be dominantly rich in cerium from the estimated crystallite sizes and they are concentrated at the particle boundaries of the other H-BCCZF phase which contains varying amounts of Co and Ce in a self-assembled fashion as shown in **Figure S6.1-3)** and **Figure 6.1b**. From the HR-SEM image, the grain sizes of the cerium-rich phase lie within 0.140 – 0.224 µm while those of the cobalt-rich phase are within the range of 0.547 – 0.768 µm. The two distinct phases are illustrated in **Figure 6.1c.** It can be observed that the d-spacings (2.96 Å and 4.47 Å) of the two phases in BCCFZ estimated from the HR-STEM images correspond to plane (110) of the cobalt-rich phase and plane (012) of the cerium-rich phase. This result conforms with the d-spacing result estimated from the Rietveld refinement of the BCCFZ XRD pattern in **Figure 6.1a.** The STEM image and the associated EDX mapping results are represented in **Figure 6.1(d-e).** The elemental distribution was not uniform due to the existence of multiple phases. However, there seem to be a fragment of each constitutive element in all the phases as evident in the EDX mapping results in **Figure 6.1 (d&e)** and **Figure S6.2&3)**. The Ce-rich phases are circled in **Figure S6.3 and Figure 6.1e** to buttress the fact that the dominant B-site elements (Ce and Co) were not distributed uniformly due to the formation of separate phases. A high-temperature HT-XRD analysis was then carried out on the BCCFZ material to investigate its phase structural stability at varying elevated temperatures. This is because sporadic lattice expansion could occur during a phase transition, and this could eventually lead to the detachment of the cathode from the electrolyte during operation thereby affecting the durability of the cell [401]. The surface features, as well as the bulk diffusion of the cathode during operation, may also be altered due to phase transition and this will negatively impact the electrochemical activity of the cathode[402]. Therefore, it is prudent to investigate the presence and severity of this phenomenon. In BCCFZ, there was no abrupt change observed in its biphasic structure as the temperature was elevated from room temperature up to 750 ^{o}C. This confirms that the material has good phase stability and hence, the potential to be used for long hours without fast degradation. The minimal change observed in the diffraction angles of the characteristic peaks in **Figure S6.4,** however, is customary because as the temperature of a perovskite oxide increases, the crystal structure tends to adjust in response to the change in the environment[403].

The oxidation state of metals at the B-site of a perovskite material can be correlated with the oxygen vacancy concentration[404–407]. Hence, X-ray photoelectron spectroscopy (XPS) and X-ray absorption near edge structure (XANES) were used to investigate the valency of Co and Ce in BCCFZ nanocomposite. **Figure 6.2(a,b)** present the X-ray absorption spectroscopy (XAS) of Co and Ce in BCCFZ relative to BCFZY and BCZYYb. From the XANES spectra in **Figure 6.2a**, the oxidation state of Cobalt in BCCFZ is lower than in BCFZY which suggests that BCCFZ has a higher oxygen vacancy concentration[407]. The XANES spectra of Ce in BCCFZ and BCZYYb presented in **Figure 6.2b** appear to be closely interwoven. This implies that the oxidation states are close with the binding energy of Ce in BCCFZ at the rising edge slightly lower than that of BCZYYb. The bond length information of Co and Ce in BCCFZ relative to BCFZY and BCZYYb based on information from the extended x-tray absorption fine structure (EXAFS) can be found in **Figure S6.5**. The deconvolution of the XPS profiles of the major B-site elements (Ce 3d5 and Co 2p) as well as that of the O1s spectrum are illustrated in **Figure 6.2 (c-e)** while those of the other minor B-site elements (Fe 2p and Zr3d3 & Zr3d5) can be found in **Figure S6.6.** Standard Gaussian-Lorentz was used in the deconvolution of the XPS profiles of all the spectra. The core-level spectra of the elements provided insight into the electronic structure and valence state of the prevailing B-site ions. It can be deduced from the XPS results that there is reasonable electroneutrality in BCCFZ with the B-site cations dominantly having a +4 charge (i.e., $[CeCoFeZr]^{4+}$). The deconvolution of the O1s spectra resulted in three characteristics peaks: highly oxidative oxygen (O_2^{2-}/O^-), the lattice oxygen (O^-) and the adsorbed oxygen (OH^-/O_2). The higher percentage of the adsorbed oxygen sub-peak suggests that the oxygen vacancy concentration is large which means that there will be a high proton uptake resulting from hydration reaction if the material is exposed to controlled humidified conditions [103].

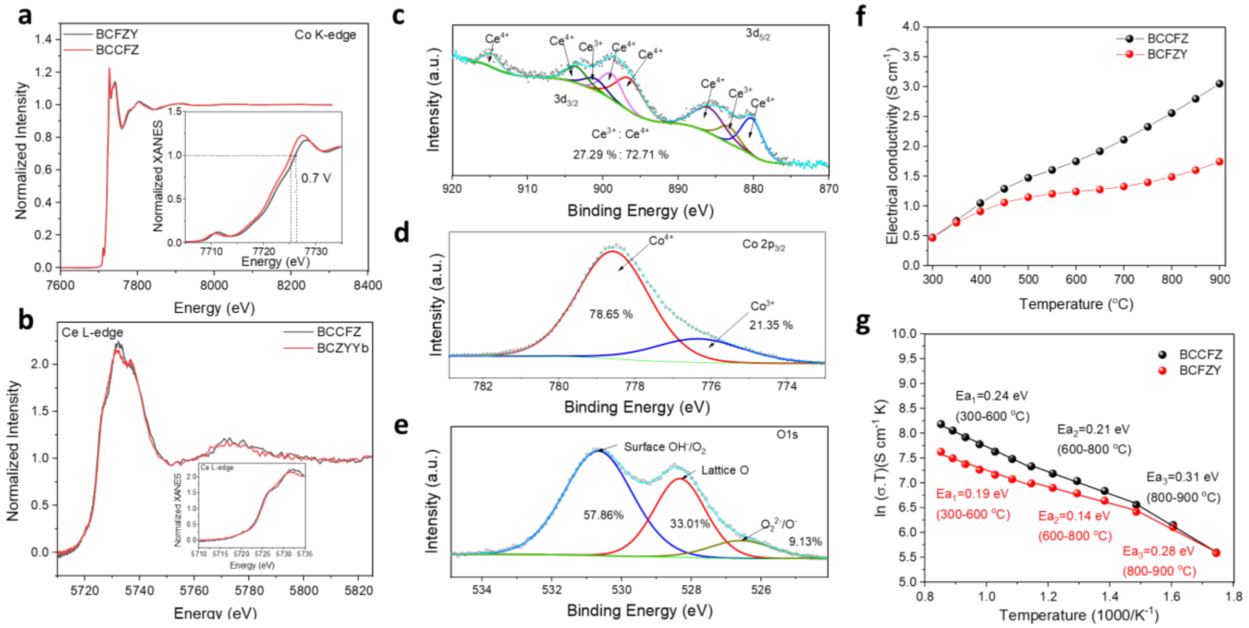

Figure 6.2: (a) XAS of Co K-edge showing the XANES for BCFZY and BCCFZ (b) The XAS of Ce L-edge showing the XANES for BCCFZ and BCZYYb. The XPS spectra of the major B-site elements of BCCFZ composite material, which are: (c) Co 2p (d) Ce 3d5, and (e) the O1s spectrum. (f) The conductivity of BCCFZ composite material was measured in air from 300 ^{o}C to 900 ^{o}C (g) The Arrhenius plots of BCCFZ and BCFZY showing their activation energies.

Figure 6.2f presents the electrical conductivity of the novel BCCFZ composite material relative to the single-phase BCFZY measured in pure air in the temperature range of 300 ^{o}C to 900 ^{o}C. The conductivity behavior of both materials is that of a typical p-type semiconductor resulting from small-polaron hopping under a temperature-activated condition. The evaluated electrical conductivity values are within 0.47-3.05 S cm^{-1} and 0.46-1.74 S cm^{-1} from 300 ^{o}C to 900 ^{o}C for BCCFZ and BCFZY, respectively. BCCFZ appears to maintain higher electrical conductivity throughout the test temperature range relative to BCFZY. However, the activation energy of BCFZY is lower by a small margin as shown in the Arrhenius plot in **Figure 6.2g** which could be due to its lower oxygen vacancy concentration**.** More so, the activation energies of both samples generally decrease as the temperature increases up to a focal point (i.e., 800 ^{o}C) where the dynamics begin to change. This could be attributed to the dominant conduction of electron-hole defects below the observed focal point. The successive increase in ionic conduction above the focal point could be attributed to the increasing activation energies above 800 ^oC. The measurement of electrical conductivity in pure air using the direct measurement approach often provides a net value equivalent to the combination of electron defects and oxygen vacancy concentration[182]. The higher electrical conductivity of BCCFZ could therefore be due to its higher oxygen vacancy concentration which will be buttressed in the later part of this study[103].

Since the electrocatalytic activity of cathode materials can be correlated with bulk oxygen diffusion and surface exchange properties, the bulk diffusion coefficient (D_{chem}) and surface exchange constant (k_{chem}) of BCCFZ were estimated using the electrical conductivity relaxation (ECR) as expressed in **Figure 6.3f.** The D_{chem} and k_{chem} values of BCCFZ at 650 ^oC are 4.49E-4 $cm^2\ s^{-1}$ and 5.30E-3 cm s^{-1} which are significantly higher than those of BCFZY by over 40% [337]. This confirms that the bulk diffusion and surface exchange of oxygen in BCCFZ is highly enhanced due to the synergistic interaction between the Ce and Co-rich phases in BCCFZ.

These findings prompted the initial investigation of the performance of the BCCFZ nanocomposites in symmetrical cells relative to the single-phase BCFZY material. The catalytic ORR of BCCFZ nanocomposite material was first investigated using symmetrical cells based on SDC and BCZYYb electrolytes as shown in **Figure S6.8**. Before this, the possibility of phase reaction between SDC and BCZYYb electrolyte and BCCFZ was investigated. According to the results in **Figure S6.7**, there was no phase reaction between the components of the cell. The symmetrical cells were tested and the generated Nyquist plots for the P-SOFC based cells were all fitted using the circuit model L-R_o-(R_1/CP_1)-(R_2/CP_2) while the SOFC symmetric cells based on SDC were also fitted using the simple R_o-(R_1/CP_1) model illustrated in **Figure S6.8**. For the PCFC with BCCFZ nanocomposites cathode, the ASR values of 0.089, 0.232, 0.573, 1.491, 4.347, and 14.296 Ω cm^2 were obtained at 650, 600, 550, 500, 450, and 400 ^oC, respectively, in 2.5 % H_2O-air. These values are relatively better compared to the single-phase BCFZY material tested under the same condition as shown in **Table 6S (2-3)** as well as other reported materials reported[347,404,408,409]. **Figure 6.3a** shows the electrochemical impedance spectroscopy (EIS) plots of BCCFZ and BCFZY based on the proton-conducting electrolyte at 650 ^oC in 2.5 % H_2O-air. The performance comparison between the BCCFZ composite electrode and single-phase BCFZY electrode tested under the same condition from 650 - 400 ^oC is illustrated in **Figure 6.3b**. The ASR stability of BCCFZ is shown in **Figure 6.3d.** The result indicates that BCCFZ is stable after testing for over 200h in 2.5 % H_2O-air.

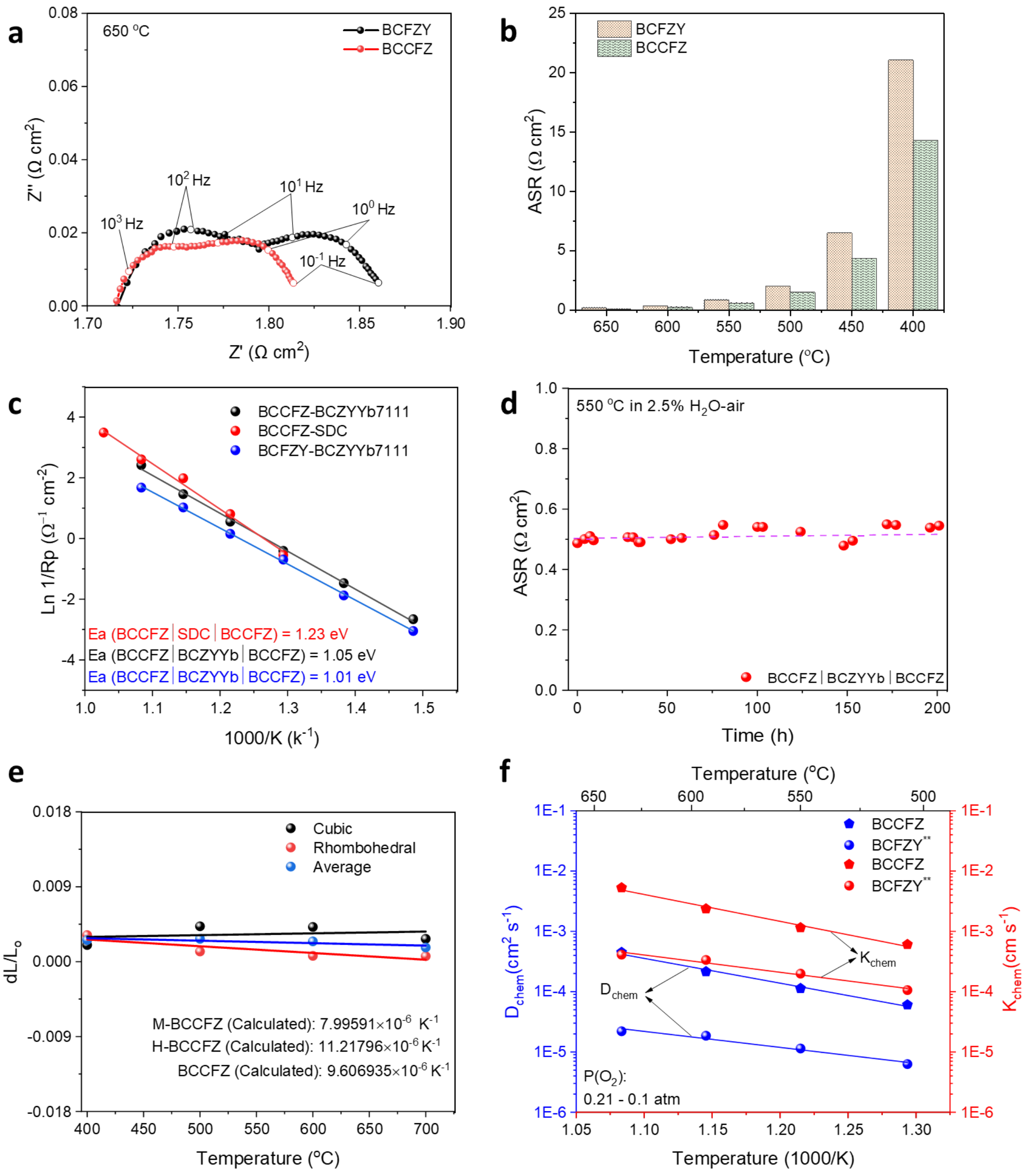

Figure 6.3: (a) Nyquist plots of symmetrical cells based on BCCFZ air electrode relative to BCFZY at 650 °C using 2.5% H_2O-air and BCZYYb7111 electrolyte material (b) ASR performance comparison between BCCFZ and BCFZY cathode from 650-400 °C (c) Arrhenius plots of the EIS data based on ASR values from O-SOFC and P-SOFC of BCCFZ and BCFZY symmetrical cells (d) ASR stability of BCCFZ-based symmetrical cell using BCZYYb electrolyte in 2.5 % H_2O-air. (e) The TEC of BCCFZ was calculated using the refinement data of the HT-XRD between 400 °C and 700 °C. (f) The comparison of the D_{chem} and k_{chem} values of BCCFZ nanocomposites and BCFZY.

The better performance of the BCCFZ nanocomposite electrode signifies that the synergistic interplay between the dominant proton-conducting and mixed ionic conducting active sites in the two inherent phases led to a superior triple ionic and electronic characteristic. The higher percentage of the adsorbed species from the XPS results also suggests that the improved proton uptake in BCCFZ nanocomposite led to an optimal catalytic ORR. One of the advantages of P-SOFCs relative to SOFC is lower activation energy[20]. This phenomenon is verified from the results in **Figure 6.3c**. Although the SOFC-based cells have lower ASR values, their activation energies are higher than those of their proton-conducting counterparts.

Another essential requirement of cathode materials for PCFCs, which is requisite for cell durability, is thermal compatibility with the other cell components. Single-phase cathode materials rich in Co and Fe with high activity are characterized by high thermal expansion coefficients (TECs), usually above $19 \times 10^{-6}\, K^{-1}$ [104,410]. The common SOFC and PCFC electrolytes have significantly lower TEC values [100]. This usually results in strain build-up at the electrolyte-electrode interface due to a thermal mismatch between the electrolyte and the electrode[411]. The TEC of BCCFZ was calculated from the HT-XRD result in **Figure S6.4** (following a similar approach in [412]) illustrated in **Figure 6.3f.** Remarkably, the estimated TEC of BCCFZ is only $9.607 \times 10^{-6}\, K^{-1}$ which is very close to the TEC of BCZYYb7111 ($10.5 \times 10^{-6}\, K^{-1}$) [100] and $BaCe_{0.5}Zr_{0.3}5In_{0.1}Zn_{0.05}O_{3-\delta}$ ($9.49 \times 10^{-6}\, K^{-1}$) [413]. The striking reduction in TEC of BCCFZ could be attributed to the Ce-rich phase, which is dispersed in the form of clustered nanoparticles at the grain boundaries of the Co-rich phase. The coactive interaction between the two inherent phases in BCCFZ resulted in a significant reduction in the TEC.

Having ascertained the initial electrocatalytic performances of BCFZY and BCCFZ based on symmetrical cells in PCFC and SOFC modes, the mechanism of proton diffusion in BCCFZ relative to BCFZY in the PCFC mode was then investigated using the ECR technique. For p-type MIEC materials, the use of direct current measurement in the estimation of their electronic conductivity mostly gives a combined electronic and ionic conductivity due to the transport of electronic defects (holes) and oxygen ions during the measurement [182,403]. To estimate the proton conductivity of TIEC materials (which are also mostly p-type like the MIECs) using direct measurement, humidified air needs to be introduced[339]. When humidified air is injected during the measurement of the electronic conductivity of a typical p-type TIEC material, the electronic defect concentration decreases resulting in the reduction of the net output value of the electrical conductivity[94]. The degree of electronic defects suppression can be correlated with the amount and extent of the predominant mode of proton conduction, which could either be hydration or hydrogenation [182]. Eqns. 1&2 illustrate hydration and hydrogenation reactions requisite for proton conduction in TIEC materials, respectively.

$$\mathrm{H_2O + O_O^{\times} + V\ddot{o} \leftrightharpoons 2OH\dot{o}} \qquad 1$$

$$\mathrm{H_2O + 2O_O^{\times} + 2\ddot{h} \leftrightharpoons 2OH\dot{o}} + \frac{1}{2}O_2 \qquad 2$$

In a humid atmosphere, proton conduction through hydration in an acid-base reaction occurs when a material sufficiently has a higher oxygen vacancy ($\mathrm{V\ddot{o}}$) concentration than the electronic defects ($\ddot{h}$) concentration so that proton defects ($\mathrm{OH\dot{o}}$) are conducted as shown in Eqn. 1[414]. Materials that fall in this category (such as PCFC electrolyte materials with the configuration $\mathrm{BaCe_{1-x-y}Zr_xY_yO_{3-\delta}}$) are bound to have insignificant or very low electrical conductivities but when pH_2O is increased, their $\mathrm{OH\dot{o}}$ concentration increases while their $\mathrm{V\ddot{o}}$ concentration decreases[103]. On the other hand, proton conduction in humid atmospheres through hydrogenation occurs when electronic defect concentration is sufficiently higher than oxygen vacancy concentration[260]. In this case, when pH_2O is increased, $\mathrm{OH\dot{o}}$ concentration increases while $\dot{h}$ concentration decreases[103]. Therefore, the conduction of proton carriers in TIEC materials in a humid atmosphere could be facilitated through the indirect or direct sacrifice of oxygen vacancies or electron holes depending on the predominant inherent concentration in the material.

Therefore, the electrical conductivity relaxation (ECR) technique was used to study the mode of proton conductivity in the self-assembled BCCFZ, single-phase BCFZY, and BCZYYb proton conducting electrolyte. The various materials were considered to have a better discernment of the mode of proton uptake in the BCCFZ nanocomposites. A constant oxygen partial pressure of 21% was used while varying the pH_2O concentration intermittently between 0 and 10%. **Figure 6.4a** shows the ECR curves of BCCFZ and BCFZY upon varying the humid conditions. It can be observed that when pH_2O (0.1) was introduced, the net conductivity of both samples dropped systematically until an equilibrium is reached where the conductivity becomes constant. Upon switching pH_2O to zero, the net conductivity of both samples begins to increase again until it reaches the equilibrium point where the net conductivity becomes constant again. The drop in the net conductivity values in BCFZY and BCCFZ is due to the occupation of the electron holes by the proton carriers which implies that hydrogenation is partially taken place [260]. Taking the changes in the net conductivity values to be equivalent to proton uptake due to hydrogenation reaction, the enthalpy and entropy of protonic defects uptake can be estimated using Vant's Hoff equation illustrated in Eqn. 3.

$$\ln(K_{OH}) = \frac{-\Delta H}{R}\frac{1}{T} + \frac{\Delta S}{R} \qquad 3$$

Where K_{OH} is the equilibrium constant, ΔH is the enthalpy change, R is the ideal gas constant, T is the absolute temperature, and ΔS is the change in entropy. **Figure 6.4d** clearly shows that both reactions are exothermic, and lower energy is needed for the generation and transport of protonic defects in the BCCFZ nanocomposite cathode materials relative to the single-phase BCFZY. In **Figure 6.4c**, however, the net conductivity of BCZYYb increases upon the introduction of humid air and decreases sharply when pH_2O is switched back to zero. This confirms that hydration reaction majorly takes place in BCZYYb since the oxygen vacancy concentration far exceeds the electron-hole concentration which is customary in electrolyte materials[182,367]. As for BCCFZ and BCFZY, the degree of suppression of electron-hole concentration is illustrated in **Figure 6.4b**. Even though BCFZY initially had lower net conductivity values under pure air, when it got abruptly exposed to humidified conditions, its net conductivity changes became higher than those of BCCFZ due to the occupation of the electron holes by protonic defects. Therefore, BCFZY has about three times higher electron-hole concentration than BCCFZ as shown in **Figure 6.4b.** The observed low electron-hole concentration in BCCFZ could be attributed to its high percentage of Ce-rich phase as verified in previous studies[367,397]. This phenomenon confirms that the oxygen vacancy concentration in BCCFZ is greater than in BCFZY as earlier deduced from the XANES spectra of Co Kedge in **Figure 6.2a**. Proton conduction through hydration can be inferred to be the dominant mode of proton uptake in BCCFZ nanocomposites since the holes sacrificed are insignificant as shown in **Figure 6.4d** but their electrochemical performances in symmetrical cells from **Figure 6.3** are superior to those of BCFZY under PCFC mode testing conditions [260,391].

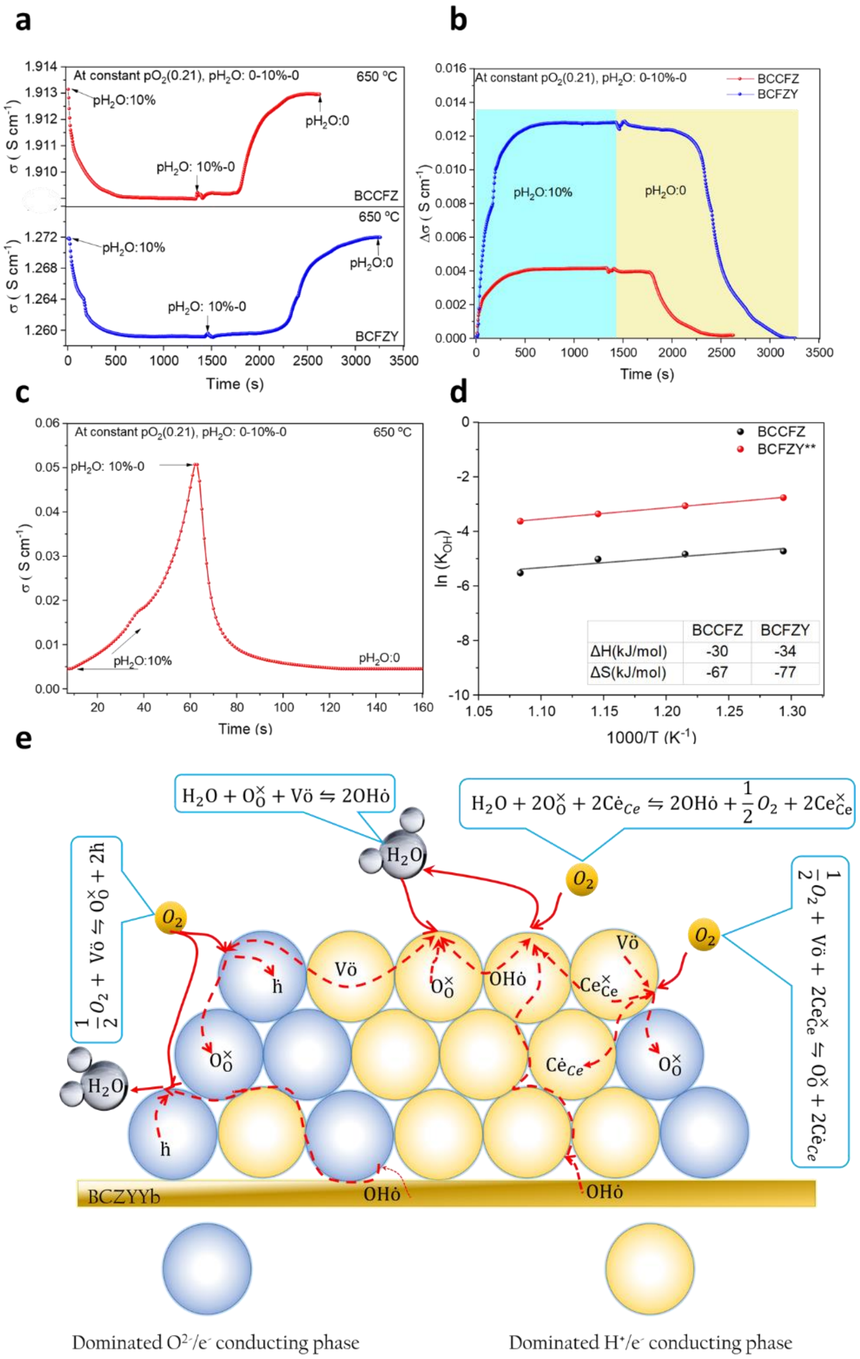

Figure 6.4: (a) ECR curves of BCCFZ and BCFZY at constant pO_2(0.21) and pH_2O (0-0.1-0) concentration at 650 °C. (b) Comparison of the change in the observed conductivities of BCCFZ and BCFZY from the ECR measurement in (a). (c) The observed ECR curve of BCZYYb at constant pO_2(0.21) and pH_2O (0-0.1-0) concentration at 650 °C. (d) Arrhenius plot showing the comparison of the enthalpy and entropy of formation of protonic defects in BCCFZ and BCFZY based on the hydrogenation reaction taken place with BCFZY** data from [131] (e) summary of the mechanism of proton uptake in the BCCFZ nanocomposite cathode in a symmetric cell.

The electronic defects in BCCFZ can be assumed to be predominantly localized at the Ce ions (based on the results from the ECR) where $\mathrm{Ce}^{\times}_{\mathrm{Ce}}$ and $\mathrm{C\dot{e}}_{Ce}$ correspond to Ce^{3+} and Ce^{4+}. The combination of Eqn. 1&4 yields Eqn. 6 which illustrates how proton uptake takes place at the expense of electron holes using a redox reaction. The transport mechanism of the various defects is summarized in **Figure 6.4e.**

$$\frac{1}{2}O_2 + \mathrm{V\ddot{o}} + 2\mathrm{Ce}^{\times}_{\mathrm{Ce}} \leftrightharpoons \mathrm{O}^{\times}_{\mathrm{O}} + 2\mathrm{C\dot{e}}_{Ce} \tag{4}$$

$$K_{o\times} = \frac{[\mathrm{O}^{\times}_{\mathrm{O}}][\mathrm{C\dot{e}}_{Ce}]^2}{(pO_2)^{0.5}[\mathrm{V\ddot{o}}][\mathrm{Ce}^{\times}_{\mathrm{Ce}}]^2} \tag{5}$$

$$\mathrm{H_2O} + 2\mathrm{O}^{\times}_{\mathrm{O}} + 2\mathrm{C\dot{e}}_{Ce} \leftrightharpoons 2\mathrm{OH\dot{o}} + \frac{1}{2}O_2 + 2\mathrm{Ce}^{\times}_{\mathrm{Ce}} \tag{6}$$

It is imperative to mention that no specific threshold has been set for each of the conductivities in a TIEC cathode material to achieve an optimal result since lots of factors are involved. A computational study, however, may accelerate the process of determining optimal values for each of the conducting species in a TIEC cathode material using reliable and sufficient experimental data. Nonetheless, previous studies have recommended a minimum of 10E-5 S/cm proton conductivity to be sufficient to increase electrode reaction active sites[331,359,391]. Other studies opined that a minimum of 0.1 S/cm electronic conductivity is still tenable for cathode materials for ceramic fuel cells [21,415]. Furthermore, ionic conductivity can be correlated with oxygen vacancy concentration[416]. Materials with optimal oxygen vacancy will therefore foster the production and mobility of protons and oxygen ions[331,417]. Of the three collective desired conductivities in cathode materials for ceramic cells, electronic conductivity is usually the highest[418]. Substituting more electronic conductivity with ionic conductivities in an already high electron conducting material, therefore, is highly recommended to achieve enhanced TIEC and general cell performance.

To gain a deeper perception of the mechanism of the electrocatalytic activity of BCCFZ nanocomposite electrode material, the electrochemical processes at various operation temperatures were investigated using the mathematical tools package, distribution of relaxation times (DRT) [311]. This tool functions by deconvoluting complex electrochemical processes of the Nyquist plot data into various peaks with significant electrochemical connotations (based on frequency ranges) as shown in **Figure S6.9.** Based on this, the DRT peaks in **Figure 6.5(a-b)** are segmented into the high-frequency region denoted as P1, the intermediate frequency region denoted as P2, and the low-temperature region denoted as P3. The high-frequency region designated as P1 connotes the transfer of charges in form of ions from the electrolyte to the interface of the cathode at the triple-phase boundary (TPB) [369,370,408]. The intermediate frequency region, P2 represents the bulk diffusion and surface exchange processes at the electrode-electrolyte interface while the low-frequency region, P1 denotes the gas diffusion process [419,420]. The equivalent area of each designated peak corresponds to the resistance of the electrochemical process [249,421]. **Figure 6.5a** presents the EIS plots of symmetrical cells based on BCCFZ under varying H_2O concentrations (0-5%) at 550 ^oC while the corresponding DRT plots are shown in **Figure 6.5b.** The ASRs estimated from these plots are 1.12 Ω cm^2, 0.57 Ω cm^2, and 0.33 Ω cm^2 at 0 %, 2.5 % and 5 % water concentrations, respectively. When the injected water concentration was zero, bulk diffusion and surface exchange, P2, predominantly limited the electrochemical reaction followed by the charge transfer process in P3. When the water concentration, however, got increased to 2.5%, the charge transfer, P3, dominated the rate-limiting process, and some initially non-existent resistances due to gas diffusion in P1 surfaced. At 5% water concentration, the overall resistances reduced significantly and the peak representing the dominating rate-limiting process, P2, was uniquely stretched over a frequency range of 10^1-10^3 Hz as highlighted in **Figure 6.5b**. This implies that the performance of BCCFZ is enhanced with increasing water concentration. The dominant rate-limiting step for the electrochemical reaction in the BCCFZ nanocomposite electrode can therefore be deduced to be the charge transfer process at the interface of the electrode and the TPB as shown in **Figure 6.5 (b-d)**. **Figure 6.5c** presents a comparative DRT description of the electrochemical reaction processes in symmetrical cells based on BCCFZ and BCFZY at 650 ^oC in 2.5% H_2O-air. BCFZY appears to be more significantly limited by the charge transfer process. Even with the variation in the oxygen partial pressures of BCCFZ at 550 ^oC in 2.5% H_2O-air, the electrochemical processes appear to be unchanged as shown in **Figure 6.5d** which confirms that protonic defect transport is dominant in the electrochemical reaction process.

The performance of the BCCFZ nanocomposite was finally investigated using an anode-supported single-cell comprising a 30 µm thick BCZYYb7111 electrolyte, a 495 µm thick Ni-BCZYYb7111, and 15 µm thick BCCFZ cathode as shown in **Figure S6.10**. Ambient air and H_2 (50 mL/min) were supplied to the air and fuel electrode, respectively. The layered structure of the anode-supported cell based on BCCFZ cathode after the stability test is shown in **Figure S6. 11**. Peak power densities (PPDs) of 1054, 683, 380, 212, and 121 mW cm^{-2} were recorded at 650, 600, 550, 500, and 450 ^oC, respectively as shown in **Figure 6.5c**. This performance is better than that of the single-cell fabricated and tested under the same condition using BCFZY cathode material as shown in **Figure S6.12**. The comparison of the performance of the anode-supported single cell based on BCCFZ electrode relative to some previously developed cathode materials is also shown in **Table S6.4**. The single-cell based on BCCFZ nanocomposite electrode conclusively exhibited operational stability spanning over 500 h at 0.2 and 0.3 A cm^{-2} current densities as shown in **Figure 6.5f**.

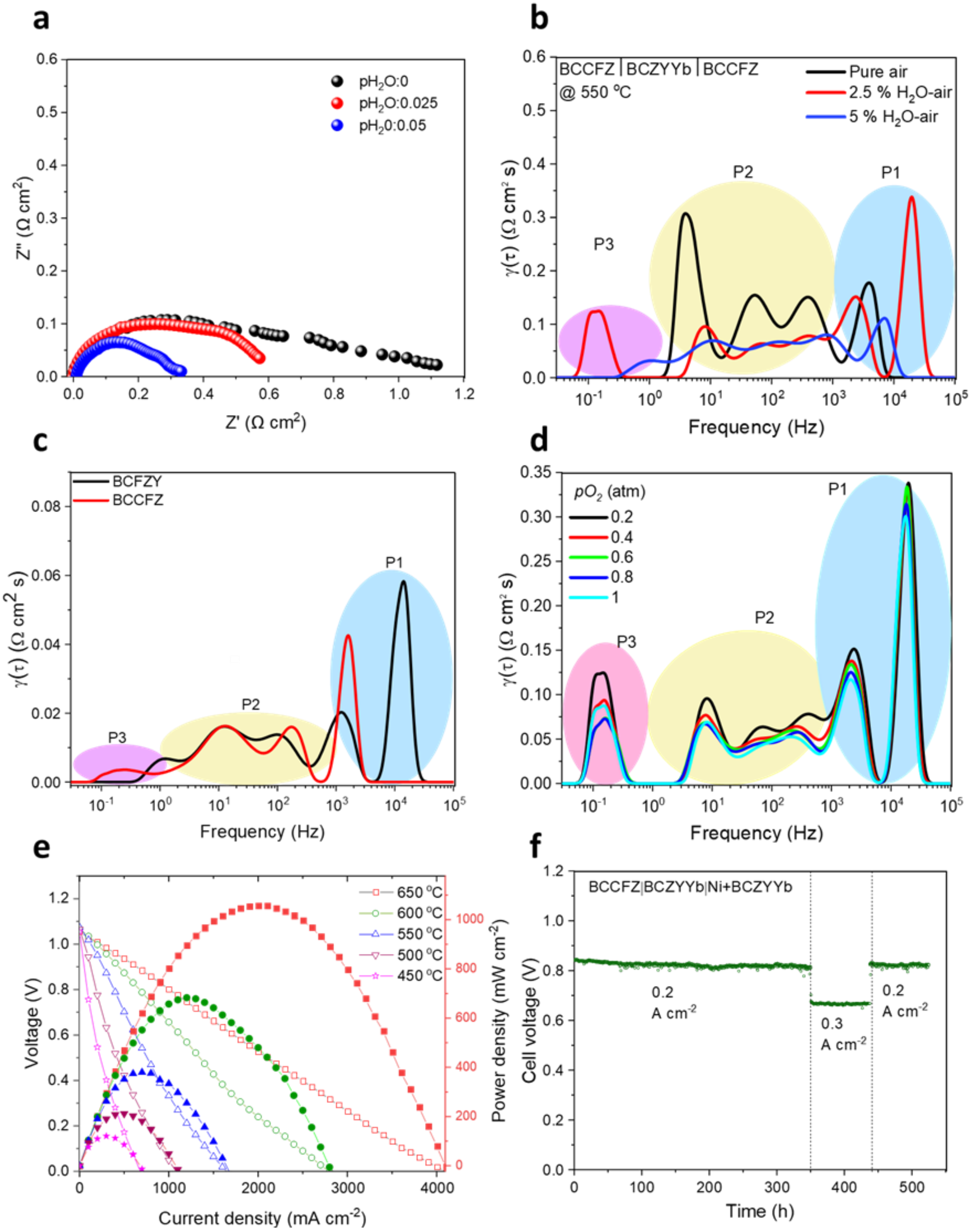

Figure 6.5: (a) Impedance spectra of symmetrical cells with the configuration BCCFZ│BCZYYb7111│ BCCFZ in 0%, 2.5% and 5% H_2O-air at 550 ºC. (b) DRT analysis of the cells in (a). (c) Comparative DRT analysis of BCCFZ and BCFZY-based symmetrical cells in

2.5 % H_2O-air at 650 ^{o}C. (d) DRT analysis of partial oxygen pressures of BCCFZ electrode in 2.5 % H_2O-air at 550 ^{o}C (e) I-V-P curves of the anode supported Ni-BCZYYb7111 cell with BCCFZ as the air electrode with H_2 fuel from 650 – 450 ^{o}C (f) Operational stability of the anode supported Ni-BCZYYb7111 single cell with BCCFZ as the cathode at 0.2 A cm^{-2} and 0.3 A cm^{-2} current densities at 550 ^{o}C for over 500h.

The cell did not display any erratic degradation after the stability test as shown in **Figure S6.11.** The good stability of this material could be attributed to the thermal compatibility of the electrolyte with the cathode material as earlier discussed. This confirms the suitability of this material and its fabrication method as a highly recommended approach for the development and construction of cathode materials for PCFCs.

6.4 Conclusion and summary

We have systematically designed and demonstrated the application of materials self-assembly engineering in the development of a new biphasic nanocomposite air electrode material with triple ionic and electronic conductivity for PCFCs. The low-cobalt-content self-assembled cubic-rhombohedral TIEC nanocomposite cathode material developed has the configuration $Ba(CeCo)_{0.4}(FeZr)_{0.1}O_{3-\delta}$ (BCCFZ). The material has good TIEC properties with an interestingly low enthalpy of protonation of -30 ± 9 kJ/mol compared to present-day competitive proton-conducting materials. The material's high cerium and low cobalt content favored its low TEC, 9.6 $\times 10^{-6}$ K^{-1}. The peak power density (PPD) of the anode-supported single cell based on BCCFZ air electrode reached 1054 mW cm^{-2} at 650 ^{o}C with good stability spanning over 500 h at 550 ^{o}C. This promotes BCCFZ nanocomposite material as a highly befitting cathode material for PCFC applications.

6.5 Supplementary section

6.5.1 Powder synthesis

$Ba(CeCo)_{0.4}(FeZr)_{0.1}O_{3-\delta}$ (BCCFZ) and $BaCo_{0.4}Fe_{0.4}Zr_{0.1}Y_{0.1}O_{3-\delta}$ (BCFZY) powders were synthesized through a one-pot sol-gel EDTA-citric acid complexing method. The required stoichiometric amounts of the chemical reagents supplied by Sinopharm, $Ba(NO_3)_2$, $Ce(NO_3)_3.6H_2O$, $Co(NO_3)_2.6H_2O$, $Fe(NO_3)_3.9H_2O$, $Zr(NO_3)_4$, and $Y(NO_3)_3.6H_2O$ were used to synthesize BCCFZ and BCFZY according to the same procedure described elsewhere with the resulting precursor powders of both materials calcined at 1000 °C for 5h in the air[394]. The same approach was used to synthesize the electrolyte powders, $Sm_{0.2}Ce_{0.8}O_{1.9}$ (SDC) and $BaCe_{0.7}Zr_{0.1}Y_{0.1}Yb_{0.1}O_{3-\delta}$ (BCZYYb7111) where the resulting precursors were calcined for 5h in the air at 700 °C and 1000 °C, respectively.

6.5.3 Cell fabrication

The configuration *cathode*│*SDC or BCZYYb7111*│*cathode* was used in the fabrication of the symmetrical cells. At first, the SDC or BCZYYb7111 powders were weighed and pressed uniaxially into dense pellets which are then sintered at 1350 °C and 1450 °C for 10h, respectively. The cathode slurry was prepared by mechanically mixing (using Fritsch Pulverisette) the calcined cathode powders with ethylene glycol, isopropyl alcohol, and glycerol to form a colloidal suspension. An air compressor pump was then used to uniformly spray the colloidal cathode slurry on both sides of the electrolyte followed by a sintering process at 850 °C for 2h air. The current collectors were then applied on both sides of the symmetric cell using an Ag paste.

The anode supported cells with the configuration *cathode*│*BCZYYb7111*│ *NiO+BCZYYb7111* were prepared through the dry co-pressing and sintering method. The *NiO+BCZYYb7111* cermet powders were first produced by ball milling NiO, BCZYYb7111, and starch powders in the ratio of 6.5:3.5:0.8 in pure ethanol for 1 h and then dried at 170 ^oC. About 0.35 g of the anode powder is weighed in each case followed by pressing at a pressure of 1 MPa. About 0.02 g of the electrolyte powder is then spread uniformly on the anode followed by pressing at a pressure of 2MPa. The co-pressed dense pellets are then sintered at 1450 ^oC for 10h in air. The cathode slurry is then sprayed uniformly on the electrolyte side followed by another sintering at 850 ^oC for 2h air.

6.5.4 Materials characterization

X-ray diffraction (XRD, Rigaku SmartLab 9kW) was used to examine the phase structure of the as-synthesized BCCFZ powders. A step-scan with 0.02^o intervals over a range of 20 – 80^o was used to collect the diffraction patterns. Opensource Fullprof Suite was used to refine the obtained diffraction patterns to get more detailed information about the crystal structures. TESCAN MAIA3 scanning electron microscopy (SEM) was used to examine the material's morphology at an accelerating potential of 5 kV. The microstructure of the calcined BCCFZ powder was probed using high-resolution transmission microscopy (HR-TEM), Field Electron Microscope STEM, JEOL Model JEM-2100F. A dense rectangular-shaped block with the dimensions $\sim 20\, mm \times 5\, mm\ \times 2\, mm$, prepared by dry pressing 5.5g of BCCFZ and BCFZY at a pressure of 1MPa and sintered at 1100 ^oC for 10h in air, was used to ascertain the electrical conductivity. The temperature range of 300 – 900 ^oC was used to carry out this measurement using a standard four-probe DC configuration with Keithley 2440 source meter. The same block was used for the electrical conductivity relaxation (ECR) test to determine the surface exchange kinetics (K_{chem}) and the bulk diffusion coefficient (D_{chem}). The XAS data around the cobalt K-edge (i.e., BCCFZ and BCFZY) and cerium L-edge (i.e., BCCFZ and BCZYYb) were collected at the TLS 01C1 beamline of the National Synchrotron Radiation Research Center (NSRRC), Taiwan.

6.5.4 Electrochemical measurements

The ohmic and polarization resistances of the symmetrical cells were measured using the combination of Solarton 1260 frequency response analyzer and Solarton 1287 potentiostat within the temperature range of 400 – 650 ^oC using 2.5% H_2O-air. This was carried out under an open circuit condition with 30 mV AC amplitude but no applied DC potential in the 10E6 Hz to 0.1 Hz frequency range.

The *I-V-P* curves of the anode-supported single cells were ascertained using a four-probe configuration with a Keithley 2440 source meter in the temperature range of 400 – 650 ^oC. The anode side of the cells was fed with pure H_2 at a constant flow rate of 50 sccm, while the cathode side was exposed to ambient air.

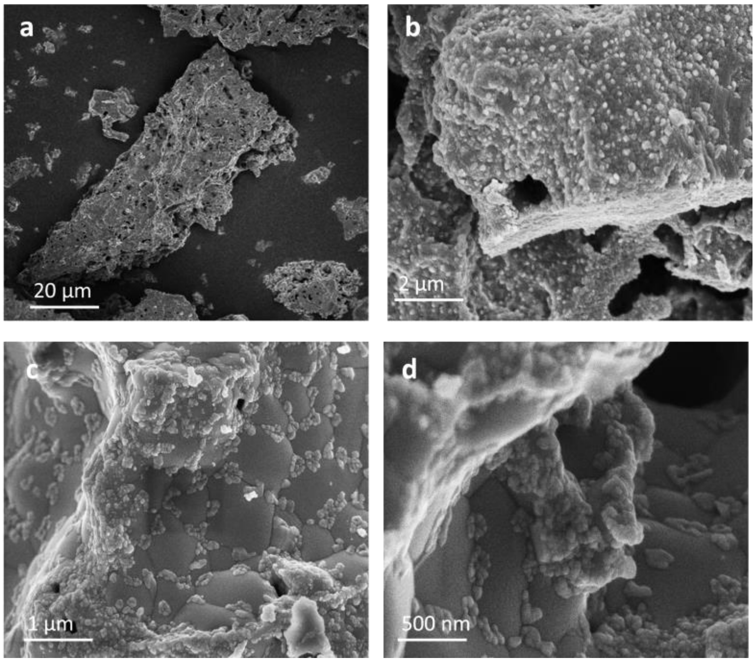

Figure S6.1: SEM images of BCCFZ nanocomposites with different views and magnifications after undergoing calcination at 1000 ^{o}C in the air for 5h.

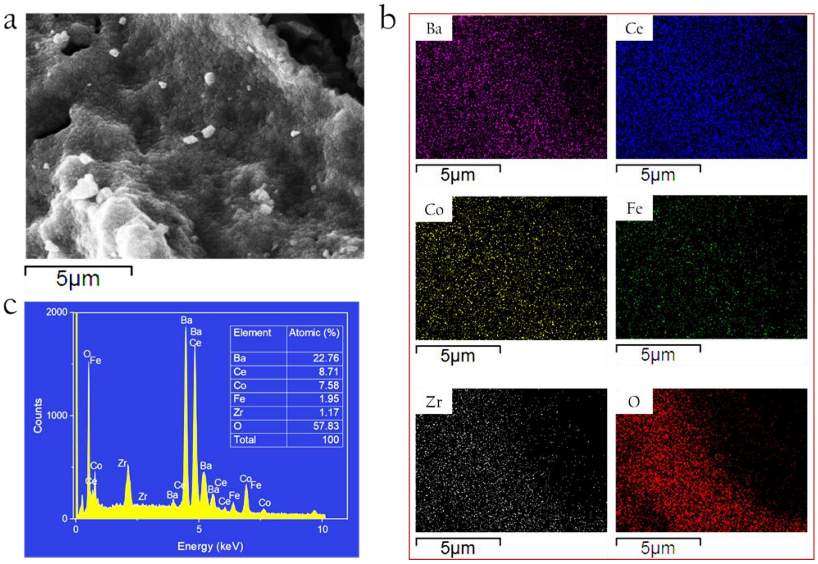

Element	Atomic (%)
Ba	22.76
Ce	8.71
Co	7.58
Fe	1.95
Zr	1.17
O	57.83
Total	100

Figure S6.2: (a) SEM image of BCCFZ as-synthesized powder (b) EDX mapping of the SEM image (c) point EDX scanning image of (a)

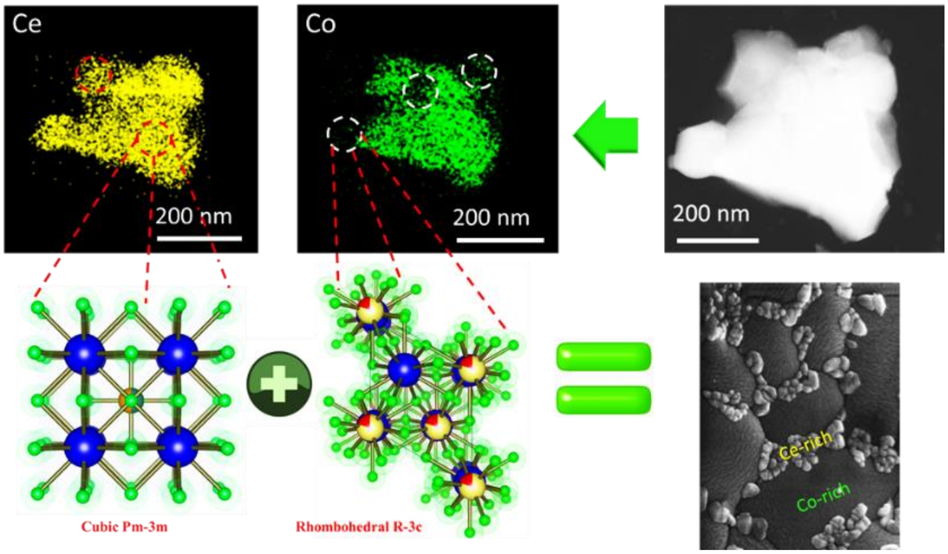

Figure S6.3: Schematic images elaborating the self-assembled nature of BCCFZ with the Co and Ce rich faces clearly highlighted.

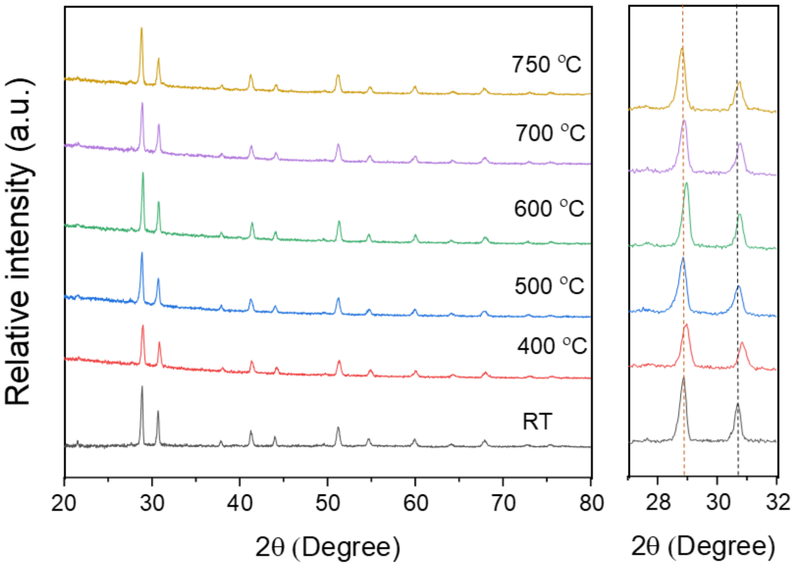

Figure S6.4: High-temperature XRD pattern of BCCFZ from room temperature to 750 °C.

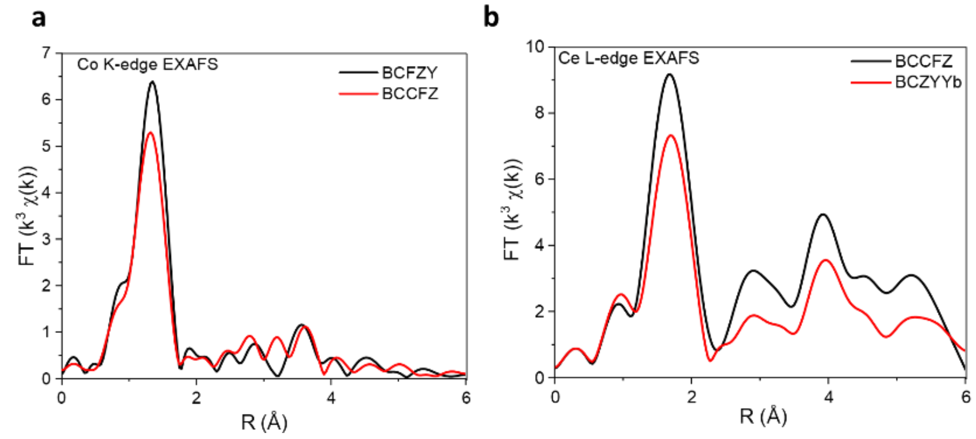

Figure S6.5: The EXAFS of (a) Co K-edge in BCFZY and BCCFZ and (b) Ce L-edge in BCCFZ and BCZYYb.

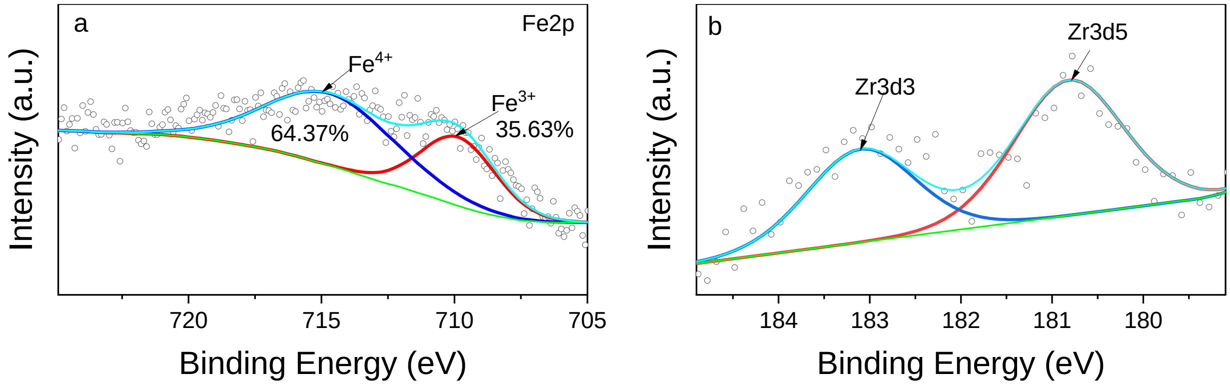

Figure S6.6: XPS spectra of the minor B-site elements in BCCFZ (a) Fe 2p (b) Zr3d3 and Zr3d5.

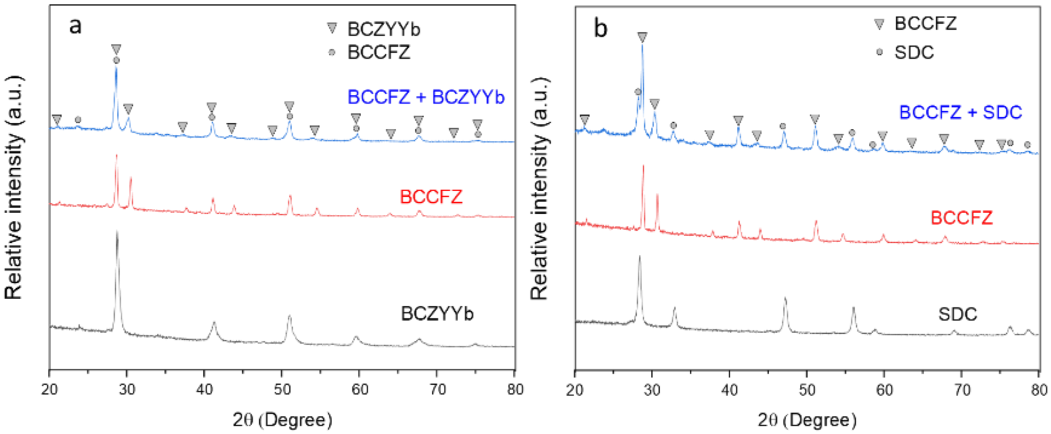

Figure S6.7: XRD profiles of (a) BCCFZ, BCZYYb711, and mechanically mixed BCCFZ + BCZYYb7111 (1:1 weight ratio) calcined at 850 °C for 2h in air and (b) BCCFZ, SDC, and mechanically mixed BCCFZ + SDC (1:1 weight ratio) calcined at 850 °C for 2h in air.

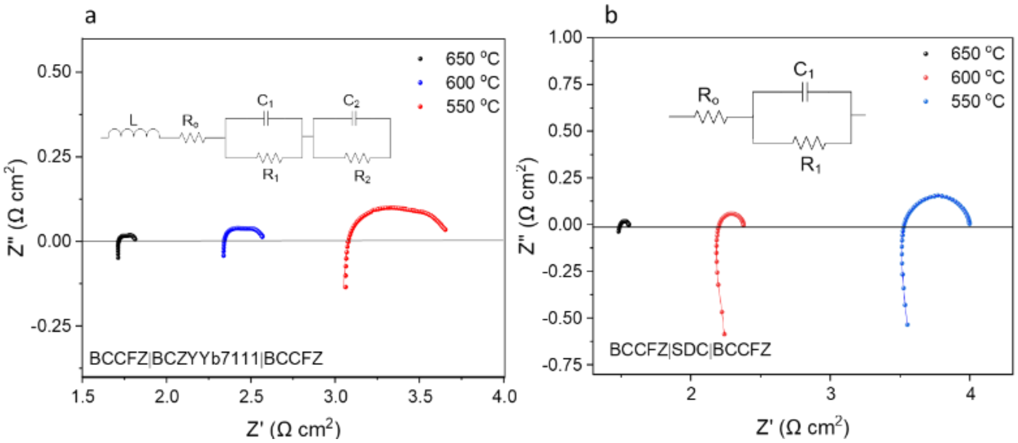

Figure S6.8: Impedance spectra of symmetrical cells with (a) BCCFZ│BCZYYb7111│ BCCFZ configuration and (b) BCCFZ│SDC│ BCCFZ configuration.

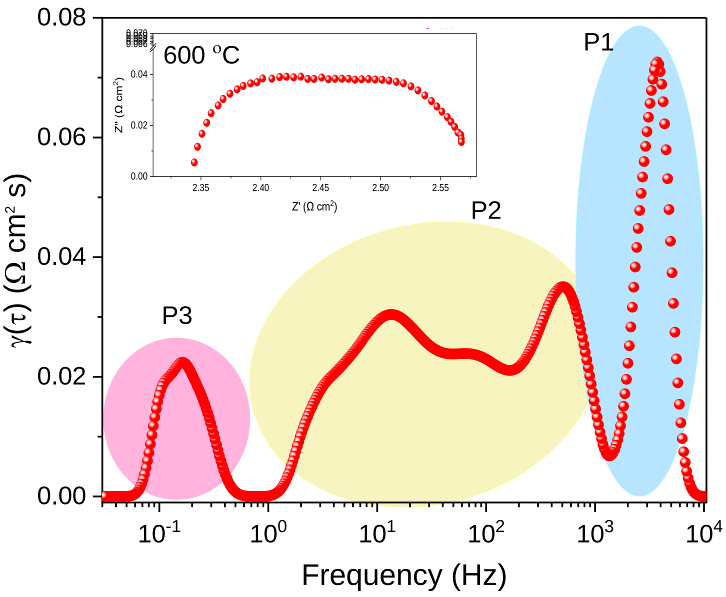

Figure S6.9: Distribution of relaxation time for BCCFZ nanocomposite electrode at 600 °C in 2.5 % H_2O.

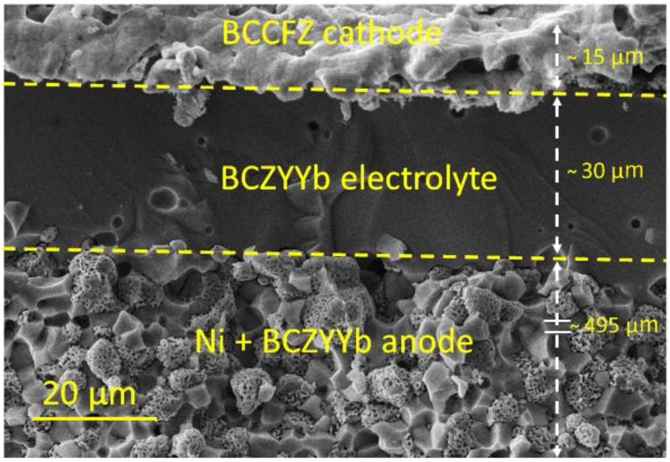

Figure S6.10: Cross-sectional image of a typical Ni + BCZYYb anode-supported single cell with BCCFZ cathode.

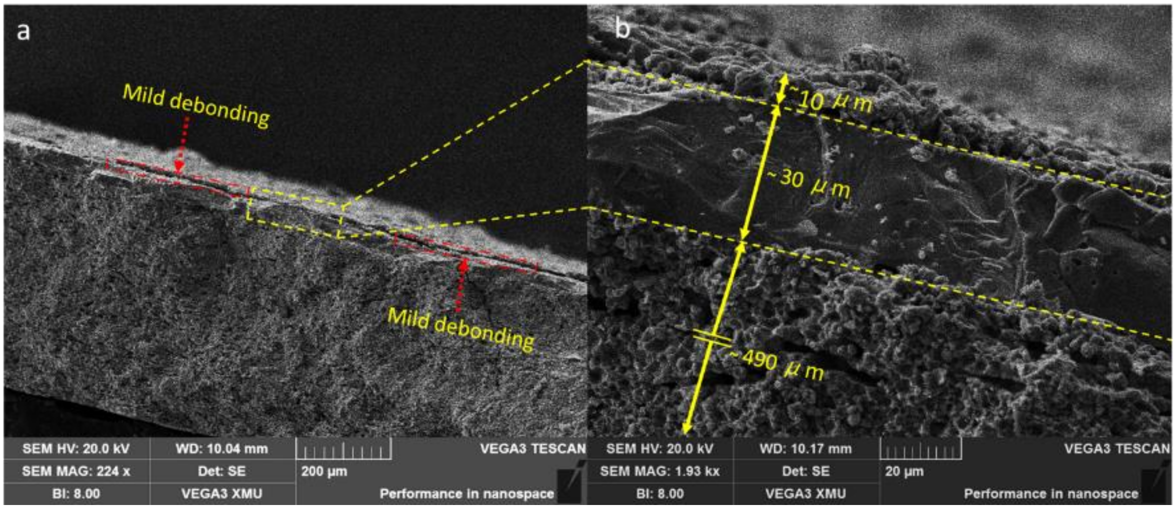

Figure S6.11: SEM images of anode-supported BCCFZ|BCZYYb7111|Ni+BCZYYb7111 single-cell cross-section after undergoing stability test for over 500 h with areas of mild detachment highlighted.

Table S6.1: Refined results of the XRD pattern of as-synthesized BCCFZ nanocomposites at room temperature

Element	Wyck Symbol	x	y	z	Occupancy
Phase 1 (Pm-3m; a=b=c=4.1060143, 40 wt.%)					
Ba	1a	0	0	0	1
Co	1b	0.5	0.5	0.5	0.8
Fe	1b	0.5	0.5	0.5	0.2
O	3c	0	0	0	1
Phase 2 (R-3c; a=b=6.167753 c=15.056063, 60 wt.%)					
Ba	6a	0	0	-0.25	1
Ce	6b	0	0	0	0.8
Zr	6b	0	0	0	0.2
O	18e	0.4487	0	0.25	1

Table S6.2: ASR values of BCCFZ nanocomposite electrode and BCFZY based on SDC electrolyte in air.

Temperature (^oC)	BCCFZ ASR (Ω cm^2)	BCFZY ASR (Ω cm^2)
700	0.030436	0.029192
650	0.073657	0.057925
600	0.137207	0.134069
550	0.446657	0.452478
500	1.726584	1.638229

Table S6.3: ASR values of BCCFZ nanocomposite electrode and BCFZY based on BCZYYb7111 electrolyte in 2.5% H_2O-Air.

Temperature (^oC)	BCCFZ (2.5% H_2O-Air) ASR (Ω cm^2)	BCFZY (2.5% H_2O-Air) ASR (Ω cm^2)
650	0.089082	0.186735
600	0.231607	0.35913
550	0.572737	0.857809
500	1.499541	2.005399
450	4.346633	6.513171
400	14.29618	21.0689

Table S6.4: Performance comparison of BCCFZ cathode with previously developed cathode materials.

Cathode	Electrolyte	Anode	PPD (mW cm^{-2})		Ref.
			650 ^{o}C	600 ^{o}C	
BCCFZ	BCZYYb7111	Ni+ BCZYYb7111	1054	683	This work
BCFZY	BCZYYb7111	Ni+ BCZYYb7111	807	672	This work
BCFN	BCZY721	Ni+BCZY721	70	40	[347]
LNO-LNF	BCZY721	Ni+BCZY721	364	266	[422]
$Ba_2YCu_3O_{6+\delta}$	BCZY721	Ni+BCZY721	175	-	[193]
BSCF	BCZY721	Ni+BCZY721	-	356	[196]
$PrBaCo_2O_{5+\delta}$	BCZY721	Ni+BCZY721	-	305	[201]
SFNb	BCZY721	Ni+BCZY721	-	428	[162]
LSM-SDC	BCZYYb7111	Ni+ BCZYYb7111	-	580	[163]
LSCF6428-BCYb10	BCY91	Ni+ BCY91	-	150	[158]
PBC- BZYP	BZY20	Ni+BZY20	-	169	[159]

BCCFZ: $BaCe_{0.4}Co_{0.4}Fe_{0.1}Zr_{0.1}O_{3-\delta}$, BCFZY: $BaCo_{0.4}Fe_{0.4}Zr_{0.1}Y_{0.1}O_{3-\delta}$, LNO-LNF: $La_2Ni\ O_{4+\delta}$-$LaNi_{0.6}Fe_{0.4}O_{3-\delta}$, BCZYYb7111: $BaCe_{0.7}Zr_{0.1}Y_{0.1}Yb_{0.1}O_{3-\delta}$, BCZY721: $BaCe_{0.7}Zr_{0.2}Y_{0.1}O_{3-\delta}$, BSCF: $Ba_{0.5}Sr_{0.5}Co_{0.8}Fe_{0.2}O_{3-\delta}$, ; SFNb: $SrFe_{0.95}Nb_{0.05}O_{3-\delta}$, LSM-SDC: $La_{0.75}Sr_{0.25}MnO_{3-\delta}$ - $Ce_{0.8}Sm_{0.2}O_{2-\delta}$, BCY91: $BaCe_{0.9}Y_{0.1}O_{3-\delta}$, LSCF6428- BCYb91: BCFN: $BaCe_{0.5}Fe_{0.4}Ni_{0.1}O_{3-\delta}$, $La_{0.8}Sr_{0.2}Co_{0.8}Fe_{0.2}O_{3-\delta}$ - $BaCe_{0.9}Yb_{0.1}O_{3-\delta}$, PBC- BZYP: $PrBaCo_2O_{5+\delta}$- $BaZr_{0.7}Y_{0.2}Pr_{0.1}O_{3-\delta}$

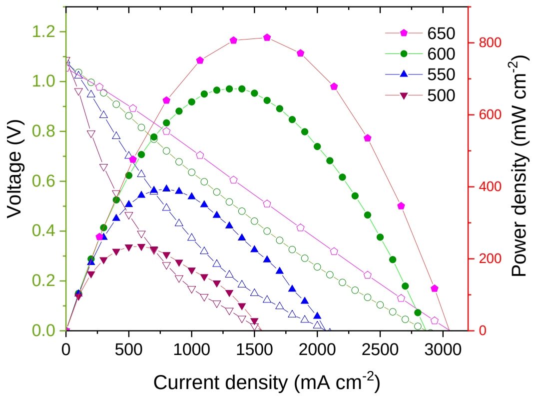

Figure S6.12: I-V and I-P curves of the anode-supported Ni+BCZYYb7111 single cell based on BCFZY cathode which was used to compare the novel BCCFZ composite material operating at 500 – 650 ^{o}C.

CHAPTER 7: CONCLUSIONS AND RECOMMENDATIONS

7.1 Background

The preceding chapters of this study have focused on investigating cathode material development strategies for CFCs, specifically SOFCs and PCFCs, capable of operating at intermediate and low temperatures. The research objectives were meticulously addressed and explored, providing new insights and understanding of this field. In this final chapter, the key findings and contributions of the study will be consolidated and presented clearly and concisely. The purpose of this chapter is to provide a comprehensive summary of the work conducted, draw meaningful conclusions, and offer commendations for future research.

7.2 Summary of Research Objectives and Key Findings

This research aims to address the challenges associated with the reduced temperature operation of CECs by exploring strategies to enhance the electrocatalytic performance of their functional cathode materials. The project has three objectives that contribute to improving the performance and practicality of CFCs.

i. The first objective is to investigate the effects of lattice engineering on the electrocatalytic performance and CO_2 tolerance of an established functional cathode material, $Ba_{0.5}Sr_{0.5}Co_{0.7}Fe_{0.3}O_{3-\delta}$, for intermediate-temperature SOFC applications. This objective entails expanding and contracting the lattice structure of the material to observe its impact on the material's electrocatalytic activity. The results of this objective will contribute to developing new strategies for improving the performance of functional air electrode materials for SOFCs.

ii. The second objective of this research project is to investigate how self-assembly engineering affects the TIEC and power output in CFCs relative to regular composites and single-phase cathodes. This objective focuses on understanding the effects of phasic interactions on TIEC and suitability of nanocomposite self-assembly engineering for CEC cathodic applications. Four distinct materials, including a self-assembled, regular composite, and single-phase cathode materials with different dominant conductivities, were evaluated for their performance in SOFC and PCFC applications.

iii. The final objective is to understand the electrokinetic phenomena in self-assembled cathodes that enabled their superior performance in PCFCs. This objective entails optimizing TIEC of cathode materials for PCFCs at reduced temperatures using self-assembly cathode engineering. The proton conduction mechanisms of the material were elucidated via hydrogenation and hydration pathways using the tailored ECR approach. The findings from this study will inform better understanding of the conductivity interplay between multi-phases that promote superior cathodic performance in PCFCs.

The ultimate goal of this research project is to contribute to developing new, efficient, and cost-effective cathode materials for CFCs that can be operated at reduced temperatures, thereby increasing their practicality, and making them more accessible to a broader range of applications. This research's findings and contributions will be summarized and presented along with recommendations for future research.

7.2.1 Key Findings from Objective 1

BSCF is a well-known cathode material for SOFCs due to its high catalytic activity for the ORR at low and intermediate temperatures. However, its poor stability in a CO_2-rich environment limits its practical use. In addressing this issue, the effects of lattice contraction and expansion on the performance and CO_2 tolerance of $Ba_{0.5}Sr_{0.5}Co_{0.7}Fe_{0.3}O_{3-\delta}$ air electrode material were systematically investigated in this study.

In achieving lattice expansion and contraction, 5 mol.% of the Fe-B site cations in BSCF were substituted with TMs, i.e., Zn and Cu, respectively. The results showed that the $Ba_{0.5}Sr_{0.5}Co_{0.7}Fe_{0.25}Cu_{0.05}O_{3-\delta}$ (BSCFC5) cathode, which experienced lattice contraction, exhibited the best performance with an ASR of 0.0247 Ω cm^2 and a PPD of 1715 mW cm^{-2} at 650°C for symmetrical and single cells, respectively. Furthermore, the material displayed improved CO_2 tolerance compared to BSCF, as it survived several rounds of 10% CO_2 injection and ejection over 100 hours (about 4 days).

This study highlights the importance of lattice engineering in optimizing the properties of SOFC cathode materials. The correlation between the ORR and CO_2 tolerance of BSCF and lattice expansion and contraction has not been reported previously. This study showed that lattice engineering is crucial in determining the variability in the catalytic ORR and CO_2 tolerance of BSCF functional material. The shortened pathway for oxygen mobility and weakened adsorption energy of reactive intermediates in the lattice of BSCF were responsible for the improved ORR and CO_2 tolerance of the BSCFC5 cathode.

In conclusion, the study demonstrated that Cu-TM-doped BSCF (BSCFC5) is a better alternative to BSCF material for SOFC applications due to its improved performance and CO_2 tolerance.

These findings provide valuable insights into optimizing SOFC cathode materials using lattice engineering.

7.2.2 Key Findings from Objective 2

The second objective focuses on evaluating the performance of a novel cathode material, $BaCo_{0.5}Ce_{0.3}Fe_{0.1}Yb_{0.1}O_{3-\delta}$ (BCCFYb), for potential use in CFCs (i.e., SOFCs and PCFCs). The material was created through a nanoscale auto-biphasic ordering process and consisted of a host cubic phase (70%) and an ancillary rhombohedral phase (30%) that synergistically enhances its ORR activity.

The results of the comparison between BCCFYb and other cathode materials, including cobalt-rich oxide-ion and electron-conducting $BaCo_{0.833}Yb_{0.167}O_{3-\delta}$ (BCYb), cerium-rich proton and electron-conducting $BaCe_{0.75}Fe_{0.25}O_{3-\delta}$ (BCF), and cobalt-cerium-rich triple ionic-conducting $BaCo_{0.833}Yb_{0.167}O_{3-\delta}$ - $BaCe_{0.75}Fe_{0.25}O_{3-\delta}$ (BCYb-BCF), showed that BCCFYb outperforms all of these materials in terms of ORR activity and stability. At 650 °C, BCCFYb had an ASR of 0.084 $\Omega\ cm^2$ in 2.5% air-H_2O, surpassing the ASRs of BCYb, BCYb-BCF, and BCF by 24%, 87%, and 100%, respectively. In addition, at 650 °C, the PPD of BCCFYb exceeded 800 and 1200 $mW\ cm^{-2}$ in PCFC and SOFC modes, respectively, and outperformed many previously developed cathode materials. This study highlights the potential of self-assembly engineering as a more practical approach to developing high-performance cathode materials for CFCs, especially the protonic CFCs.

7.2.3 Key Findings from Objective 3

The third objective of this study focuses on optimizing and understanding the electrokinetic TIEC in the cathode material with the unique composition $Ba(CeCo)_{0.4}(FeZr)_{0.1}O_{3-\delta}$ (BCCFZ). The material was designed through a self-assembly engineering process and consisted of a mixed ionic and electronic conducting phase (M-BCCFZ) and a dominant proton-conducting phase (H-BCCFZ). The cerium-rich H-BCCFZ phase significantly enhanced the material's oxygen vacancy concentration and proton defects formation and transport, resulting in a low enthalpy of protonation of -30 ± 9 kJ mol^{-1}. The ASR of the BCCFZ symmetrical cell was 0.089 Ω cm^2 at 650 °C in 2.5% H_2O-air. The PPD of the anode-supported single cell based on the BCCFZ cathode reached 1054 mW cm^{-2} at 650 °C, demonstrating good operation stability over 500 hours at 550 °C. The low cobalt content and high cerium content in the BCCFZ material also favored its low TEC of 9.6×10^{-6} K^{-1}. The findings from this study suggest that low enthalpy enabled enhanced proton uptake and synergistic phases enabled improved TIEC and low TEC, demonstrating the practicality and effectiveness of self-assembly engineering as a method for developing superior cathode materials.

7.3 Research Significance and Contributions

The research project aimed to address the challenges associated with the low-temperature operation of CFCs by exploring strategies to enhance the electrocatalytic performance of their functional cathode materials. Through the examination of ABO_3 perovskite oxide materials as cathode materials, the investigation of lattice engineering on the electrocatalytic performance and CO_2 tolerance of established functional cathode material, and the optimization of the TIEC of cathode materials through nanocomposite self-assembly engineering, this research project has made several significant contributions to the field of CFCs.

The findings of this research project have provided a comprehensive understanding of the strengths and weaknesses of using certain perovskite oxide materials in CFCs, which will inform future research efforts in this area. The investigation of lattice engineering has led to new insights into how the structure of functional air electrode materials can impact their electrocatalytic activity. The optimization of TIEC through nanocomposite self-assembly engineering has resulted in the development of new biphasic nanocomposite air electrode materials with improved ORR, which has the potential to significantly improve the performance and stability of CFCs at reduced operating temperatures. The results of this research can be used to develop new, efficient, and cost-effective cathode materials for CFCs that can be operated at reduced temperatures, making them more accessible and practical for a broader range of applications. Recommendations for future research are presented, building upon the foundation laid by this research project, and further advancing the field of CFCs.

7.4 Limitations of the study

Despite the comprehensive nature of this research project, it is essential to acknowledge its limitations. These limitations provide valuable insights into potential avenues for future research and improvement. The following are the fundamental limitations of this study:

1. Limited mechanistic analysis in lattice engineering study: The first study in this thesis focused on investigating the effects of lattice engineering on the performance and CO_2 tolerance of the BSCF cathode material. While lattice contraction was found to improve catalytic activity and CO_2 resistance, the analysis did not thoroughly examine the concurrent effects of changes in valence states and oxygen vacancy concentration induced by Cu-doping. This represents a limitation of the lattice engineering study and an area for

future work to build a more nuanced understanding of how multiple concurrently changed factors affect the material's performance.

2. Sample Size: The sample size of this study was limited, which could have impacted the generalizability of the results. To further validate the findings of this research, larger sample sizes and a more significant number of replications should be considered in future studies.
3. Methodological Limitations: The study was designed with a specific research design and methodology. While every effort was made to ensure that the methodology was appropriate for the research objectives, there may have been limitations in the design or execution of the study that impacted the results. In particular, the limitations of the methods used to measure the microstructural properties and electrocatalytic performance of the cathode materials should be considered.
4. Time Constraints: This research project was carried out within a specified time frame (less than three years). The time constraints may have limited the ability of the study to fully explore all of the relevant factors that could impact the electrocatalytic performance of cathode materials for ceramic fuel cells.
5. Lack of Control Variables: There may have been variables that were not considered or controlled in this study that could have impacted the results, such as sintering, calcination, ball milling, and stability time variables. Future studies should consider the potential impact of these variables and attempt to control for them as much as possible.
6. Limited Scope: The scope of this research project was limited to a specific set of cathode materials and their performance in CFCs. While the findings of this research are significant and contribute to the existing literature, they are not exhaustive and may not be applicable

to other materials or applications, such as ceramic electrolysis cells and reversible ceramic cells.

7.5 Recommendations for Future Research

The current research project has explored strategies for enhancing the electrocatalytic performance of functional cathode materials for CFCs to address the challenges associated with the low-temperature operation of CECs. The project has achieved a comprehensive understanding of the challenges and limitations of using perovskite oxide materials as cathode materials, investigated the effects of lattice engineering on the electrocatalytic performance and CO_2 tolerance of functional cathode material, and optimized the TIEC of cathode materials through the adoption of nanocomposite self-assembly engineering. Based on the results of this research, the following recommendations are made for future research in this area:

i. Optimization of Lattice Engineering Techniques: The first objective of this research project aimed to investigate the effects of lattice engineering on the electrocatalytic performance and CO_2 tolerance of an established functional cathode material for intermediate-temperature SOFC applications. A more comprehensive mechanistic study considering how lattice contraction interacts with alterations in valence states and oxygen vacancies is needed to gain deeper insight into the underlying mechanisms responsible for the enhanced properties of Cu-doped BSCF. Likewise, further research is needed to understand the lattice engineering techniques used in this study and to explore their potential for improving the performance of other functional cathode materials.

ii. Enhancement of TIEC: The second and third objectives of this research project aimed to optimize the TIEC of cathode materials for PCFCs at lower temperatures through the adoption of nanocomposite self-assembly engineering. Although this research has made significant strides in developing new biphasic nanocomposite air electrode materials with improved TIECs and better understanding of their electrokinetic phenomena, there is still room for future research to continue refining and optimizing these materials to achieve even higher performance levels and stability.

iii. It would be beneficial to comprehensively evaluate the performance and stability of the nanocomposite cathode materials developed in this study in real-world operating conditions, including testing in full-scale CFC systems.

iv. Finally, further research is needed to explore the potential of CFCs for a broader range of applications, including small-scale and large-scale systems, and to identify the critical challenges associated with their commercialization and deployment.

7.6 Chapter Summary

This chapter provides a comprehensive summary of the key findings, the research significance and contributions, and the limitations encountered during the research process. The chapter serves as an opportunity to reflect on the research outcomes and offers recommendations for future studies in cathode development for low-temperature operating CFC technology.

REFERENCES

[1] Ritchie H, Roser M. Energy 2020. Our World Data.

[2] Fabbri E, Pergolesi D, Traversa E. Materials challenges toward proton-conducting oxide fuel cells: A critical review. Chem Soc Rev 2010;39:4355–69. https://doi.org/10.1039/b902343g.

[3] Cozzi L, Gould T, Bouckart S, Crow D, Kim T-Y, McGlade C, et al. World Energy Outlook 2020;2050:1–461.

[4] Günes S, Neugebauer H, Sariciftci NS. Conjugated Polymer-Based Organic Solar Cells. Chem Rev 2007;107:1324–38. https://doi.org/10.1021/cr050149z.

[5] Green MA, Ho-Baillie A, Snaith HJ. The emergence of perovskite solar cells. Nat Photonics 2014;8:506–14. https://doi.org/10.1038/nphoton.2014.134.

[6] Notton G, Nivet M-L, Voyant C, Paoli C, Darras C, Motte F, et al. Intermittent and stochastic character of renewable energy sources: Consequences, cost of intermittence and benefit of forecasting. Renew Sustain Energy Rev 2018;87:96–105. https://doi.org/10.1016/j.rser.2018.02.007.

[7] Bello IT, Zhai S, He Q, Xu Q, Ni M. Scientometric review of advancements in the development of high-performance cathode for low and intermediate temperature solid oxide fuel cells: Three decades in retrospect. Int J Hydrogen Energy 2021;46:26518–36. https://doi.org/10.1016/j.ijhydene.2021.05.134.

[8] Stambouli AB, Traversa E. Solid oxide fuel cells (SOFCs): a review of an environmentally clean and efficient source of energy. Renew Sustain Energy Rev

2002;6:433–55. /https://doi.org/10.1016/S1364-0321(02)00014-X.

[9] Merle G, Wessling M, Nijmeijer K. Anion exchange membranes for alkaline fuel cells: A review. J Memb Sci 2011;377:1–35. https://doi.org/10.1016/j.memsci.2011.04.043.

[10] Varcoe JR, Slade RCT. Prospects for Alkaline Anion-Exchange Membranes in Low Temperature Fuel Cells. Fuel Cells 2005;5:187–200. https://doi.org/10.1002/fuce.200400045.

[11] Stonehart P. Development of alloy electrocatalysts for phosphoric acid fuel cells (PAFC). J Appl Electrochem 1992;22:995–1001. https://doi.org/10.1007/BF01029576.

[12] Li Q, Jensen JO, Savinell RF, Bjerrum NJ. High temperature proton exchange membranes based on polybenzimidazoles for fuel cells. Prog Polym Sci 2009;34:449–77. https://doi.org/10.1016/j.progpolymsci.2008.12.003.

[13] Li H, Tang Y, Wang Z, Shi Z, Wu S, Song D, et al. A review of water flooding issues in the proton exchange membrane fuel cell. J Power Sources 2008;178:103–17. https://doi.org/10.1016/j.jpowsour.2007.12.068.

[14] Liu H, Song C, Zhang L, Zhang J, Wang H, Wilkinson DP. A review of anode catalysis in the direct methanol fuel cell. J Power Sources 2006;155:95–110. https://doi.org/10.1016/j.jpowsour.2006.01.030.

[15] Kulkarni A, Giddey S. Materials issues and recent developments in molten carbonate fuel cells. J Solid State Electrochem 2012;16:3123–46. https://doi.org/10.1007/s10008-012-1771-y.

[16] Jacobson AJ. Materials for Solid Oxide Fuel Cells. Chem Mater 2010;22:660–74.

https://doi.org/10.1021/cm902640j.

[17] Mahato N, Banerjee A, Gupta A, Omar S, Balani K. Progress in material selection for solid oxide fuel cell technology: A review. Prog Mater Sci 2015;72:141–337. https://doi.org/10.1016/j.pmatsci.2015.01.001.

[18] Minh NQ. Solid oxide fuel cell technology—features and applications. Solid State Ionics 2004;174:271–7. https://doi.org/10.1016/j.ssi.2004.07.042.

[19] Laguna-Bercero MA. Recent advances in high temperature electrolysis using solid oxide fuel cells: A review. J Power Sources 2012;203:4–16. https://doi.org/10.1016/j.jpowsour.2011.12.019.

[20] Bello IT, Zhai S, He Q, Cheng C, Dai Y, Chen B, et al. Materials development and prospective for protonic ceramic fuel cells. Int J Energy Res 2021:1–29. https://doi.org/10.1002/er.7371.

[21] Yang G, Su C, Shi H, Zhu Y, Song Y, Zhou W, et al. Toward reducing the operation temperature of solid oxide fuel cells: Our past 15 years of efforts in cathode development. Energy and Fuels 2020;34:15169–94. https://doi.org/10.1021/acs.energyfuels.0c01887.

[22] Leng Y, Chan SH, Liu Q. Development of LSCF–GDC composite cathodes for low-temperature solid oxide fuel cells with thin film GDC electrolyte. Int J Hydrogen Energy 2008;33:3808–17. https://doi.org/10.1016/j.ijhydene.2008.04.034.

[23] de Larramendi I, Lamas DG, Cabezas MD, de Larramendi JI, de Reca NE, Rojo T. Development of electrolyte-supported intermediate-temperature single-chamber solid oxide fuel cells using Ln0.7Sr0.3Fe0.8Co0.2O3-δ (Ln = Pr, La, Gd) cathodes. J Power

Sources 2009;193:774–8. https://doi.org/10.1016/j.jpowsour.2009.04.069.

[24] Jiang SP. Development of lanthanum strontium manganite perovskite cathode materials of solid oxide fuel cells: A review. J Mater Sci 2008;43:6799–833. https://doi.org/10.1007/s10853-008-2966-6.

[25] Zhou W, Ran R, Shao Z. Progress in understanding and development of Ba0.5Sr0.5Co0.8Fe0.2O3-δ-based cathodes for intermediate-temperature solid-oxide fuel cells: A review. J Power Sources 2009;192:231–46. https://doi.org/10.1016/j.jpowsour.2009.02.069.

[26] He W, Wu X, Yang G, Shi H, Dong F, Ni M. BaCo0.7Fe0.22Y0.08O3-δ as an Active Oxygen Reduction Electrocatalyst for Low-Temperature Solid Oxide Fuel Cells below 600 °c. ACS Energy Lett 2017;2:301–5. https://doi.org/10.1021/acsenergylett.6b00617.

[27] Zhou W, Shao Z, Liang F, Chen Z-G, Zhu Z, Jin W, et al. A new cathode for solid oxide fuel cells capable of in situ electrochemical regeneration. J Mater Chem 2011;21:15343–51. https://doi.org/10.1039/c1jm12660a.

[28] Hashim SS, Liang F, Zhou W, Sunarso J. Cobalt-Free Perovskite Cathodes for Solid Oxide Fuel Cells. ChemElectroChem 2019;6:3549–69. https://doi.org/10.1002/celc.201900391.

[29] Sasaki K, Wurth J -P., Gschwend R, Gödickemeier M, Gauckler LJ. Microstructure-Property Relations of Solid Oxide Fuel Cell Cathodes and Current Collectors: Cathodic Polarization and Ohmic Resistance. J Electrochem Soc 1996;143:530–43. https://doi.org/10.1149/1.1836476.

[30] Revankar S, Majumdar P. FUEL CELLS: Principles, Design and Analysis. 1st ed. CRC Press; 2014.

[31] Carrette L, Friedrich KA, Stimming U. Fuel Cells - Fundamentals and Applications. Fuel Cells 2001;1:5–39. https://doi.org/10.1002/1615-6854(200105)1:1<5::aid-fuce5>3.0.co;2-g.

[32] Abd Aziz AJ, Baharuddin NA, Somalu MR, Muchtar A. Review of composite cathodes for intermediate-temperature solid oxide fuel cell applications. Ceram Int 2020;46:23314–25. https://doi.org/10.1016/j.ceramint.2020.06.176.

[33] Jiang SP. Development of lanthanum strontium manganite perovskite cathode materials of solid oxide fuel cells: A review. J Mater Sci 2008;43:6799–833. https://doi.org/10.1007/s10853-008-2966-6.

[34] Hartley A, Sahibzada M, Weston M, Metcalfe IS, Mantzavinos D. La0.6Sr0.4Co0.2Fe0.8O 3 as the anode and cathode for intermediate temperature solid oxide fuel cells. Catal Today 2000;55:197–204. https://doi.org/10.1016/S0920-5861(99)00239-4.

[35] Gupta RK, Choi IJ, Cho YS, Lee HL, Hyun SH. Characterization of perovskite-type cathode, La0.75Sr0.25 Mn0.95-xCox Ni0.05O3+δ ($0.1 \le x \le 0.3$), for intermediate-temperature solid oxide fuel cells. J Power Sources 2009;187:371–7. https://doi.org/10.1016/j.jpowsour.2008.10.136.

[36] Ni M, Shao Z. Fuel cells that operate at 300° to 500°C. Science 2020;369:138 LP – 139. https://doi.org/10.1126/science.abc9136.

[37] Li W, Cheng Y, Zhou Q, Wei T, Li Z, Yan H, et al. Evaluation of double perovskite Sr2FeTiO6−δ as potential cathode or anode materials for intermediate-temperature solid oxide fuel cells. Ceram Int 2015;41:12393–400. https://doi.org/10.1016/j.ceramint.2015.06.074.

[38] Li X, Jiang X, Xu H, Xu Q, Jiang L, Shi Y, et al. Scandium-doped PrBaCo2-xScxO6-δ oxides as cathode material for intermediate-temperature solid oxide fuel cells. Int J Hydrogen Energy 2013;38:12035–42. https://doi.org/10.1016/j.ijhydene.2013.07.024.

[39] Pang S, Su Y, Yang G, Shen X, Zhu M, Wu X, et al. Enhanced electrochemical performance of Ca-doped NdBa1-xCaxCoCuO5+δ as cathode material for intermediate-temperature solid oxide fuel cells. Ceram Int 2018;44:21902–7. https://doi.org/10.1016/j.ceramint.2018.08.301.

[40] Huang S, Gao F, Meng Z, Feng S, Sun X, Li Y, et al. Bismuth-Based Pervoskite as a High-Performance Cathode for Intermediate-Temperature Solid-Oxide Fuel Cells. ChemElectroChem 2014;1:554–8. https://doi.org/10.1002/celc.201300070.

[41] Meng F, Xia T, Wang J, Shi Z, Zhao H. Praseodymium-deficiency Pr0.94BaCo2O6-δ double perovskite: A promising high performance cathode material for intermediate-temperature solid oxide fuel cells. J Power Sources 2015;293:741–50. https://doi.org/10.1016/j.jpowsour.2015.06.007.

[42] Jun A, Kim J, Shin J, Kim G. Perovskite as a Cathode Material: A Review of its Role in Solid-Oxide Fuel Cell Technology. ChemElectroChem 2016;3:511–30. https://doi.org/10.1002/celc.201500382.

[43] Jang I, Lee H, Tamarany R, Yoon H, Kim C, Kim S, et al. Tailoring the Ratio of A-Site

Cations in Pr1- xNd xBaCo1.6Fe0.4O5+δto Promote the Higher Oxygen Reduction Reaction Activity for Low-Temperature Solid Oxide Fuel Cells. Chem Mater 2020;32:3841–9. https://doi.org/10.1021/acs.chemmater.9b05378.

[44] Sayers R, Flack NLO, Alaria J, Chater PA, Palgrave RG, McMitchell SRC, et al. Epitaxial growth and enhanced conductivity of an it-sofc cathode based on a complex perovskite superstructure with six distinct cation sites. Chem Sci 2013;4:2403–12. https://doi.org/10.1039/c3sc21931c.

[45] Shi H, Su C, Ran R, Cao J, Shao Z. Electrolyte materials for intermediate-temperature solid oxide fuel cells. Prog Nat Sci Mater Int 2020;30:764–74. https://doi.org/10.1016/j.pnsc.2020.09.003.

[46] Li M, Zhou W, Zhu Z. Recent development on perovskite-type cathode materials based on SrCoO3 -δ parent oxide for intermediate-temperature solid oxide fuel cells. Asia-Pacific J Chem Eng 2016;11:370–81. https://doi.org/10.1002/apj.2009.

[47] Gu H, Ran R, Zhou W, Shao Z. Anode-supported ScSZ-electrolyte SOFC with whole cell materials from combined EDTA-citrate complexing synthesis process. J Power Sources 2007;172:704–12. https://doi.org/10.1016/j.jpowsour.2007.07.056.

[48] Ren H, Lee YH, Wu EA, Chung H, Meng YS, Fullerton EE, et al. Nano-Ceramic Cathodes via Co-sputtering of Gd-Ce Alloy and Lanthanum Strontium Cobaltite for Low-Temperature Thin-Film Solid Oxide Fuel Cells. ACS Appl Energy Mater 2020;3:8135–42. https://doi.org/10.1021/acsaem.0c01147.

[49] Zhang L, Yang W. High-performance low-temperature solid oxide fuel cells using thin proton-conducting electrolyte with novel cathode. Int J Hydrogen Energy 2012;37:8635–

40. https://doi.org/10.1016/j.ijhydene.2012.02.140.

[50] Zhang L, Yang W. High-performance low-temperature solid oxide fuel cells using thin proton-conducting electrolyte with novel cathode. Int J Hydrogen Energy 2012;37:8635–40. https://doi.org/10.1016/j.ijhydene.2012.02.140.

[51] Rousseau F, Nickravech M, Awamat S, Morvan D, Amouroux J. Optical emission spectroscopy of a supersonic low-pressure plasma reactor used to synthesis SOFC cathodes thin layers. High Temp Mater Process 2006;10:431–44. https://doi.org/10.1615/HighTempMatProc.v10.i3.70.

[52] Sun W, Yan L, Shi Z, Zhu Z, Liu W. Fabrication and performance of a proton-conducting solid oxide fuel cell based on a thin BaZr0.8Y0.2O3-δ electrolyte membrane. J Power Sources 2010;195:4727–30. https://doi.org/10.1016/j.jpowsour.2010.02.012.

[53] Ju Y-W, Inagaki T, Ida S, Ishihara T. Sm(Sr)CoO3 cone cathode on LaGaO3 thin film electrolyte for IT-SOFC with high power density. J Electrochem Soc 2011;158:B825–30. https://doi.org/10.1149/1.3592427.

[55] He W, Wu X, Yang G, Shi H, Dong F, Ni M. BaCo0.7Fe0.22Y0.08O3-δ as an Active Oxygen Reduction Electrocatalyst for Low-Temperature Solid Oxide Fuel Cells below 600 °c. ACS Energy Lett 2017;2:301–5. https://doi.org/10.1021/acsenergylett.6b00617.

[56] Tarancón A, Skinner SJ, Chater RJ, Hernández-Ramírez F, Kilner JA. Layered perovskites as promising cathodes for intermediate temperature solid oxide fuel cells. J Mater Chem 2007;17:3175–81. https://doi.org/10.1039/b704320a.

[57] Lee KT, Manthiram A. Characterization of Nd0.6Sr0.4Co1-yFe yO3-δ (0 ≤ y ≤ 0.5)

cathode materials for intermediate temperature solid oxide fuel cells. Solid State Ionics 2005;176:1521–7. https://doi.org/10.1016/j.ssi.2005.05.002.

[58] Cascos V, Troncoso L, Larralde AL, Fernandez-Diaz MT, Alonso JA. Performance of SrCo1- xIrxO3-δ(x = 0.10 and 0.15) Perovskites as Potential Cathode Materials for Intermediate-Temperature Solid Oxide Fuel Cells (IT-SOFC). ACS Appl Energy Mater 2020;3:6709–16. https://doi.org/10.1021/acsaem.0c00848.

[59] Ding D, Li X, Lai SY, Gerdes K, Liu M. Enhancing SOFC cathode performance by surface modification through infiltration. Energy Environ Sci 2014;7:552–75. https://doi.org/10.1039/c3ee42926a.

[60] Hashim SS, Liang F, Zhou W, Sunarso J. Cobalt-Free Perovskite Cathodes for Solid Oxide Fuel Cells. ChemElectroChem 2019;6:3549–69. https://doi.org/10.1002/celc.201900391.

[61] Agun L, Abd. Rahman H, Ahmad S, Muchtar A. Durability and stability of LSCF composite cathode for intermediate-low temperature of solid oxide fuel cell (IT-LT SOFC): Short review. Adv Mater Res 2014;893:732–7. https://doi.org/10.4028/www.scientific.net/AMR.893.732.

[62] He W, Wu X, Yang G, Shi H, Dong F, Ni M. BaCo0.7Fe0.22Y0.08O3-δ as an Active Oxygen Reduction Electrocatalyst for Low-Temperature Solid Oxide Fuel Cells below 600 °c. ACS Energy Lett 2017;2:301–5. https://doi.org/10.1021/acsenergylett.6b00617.

[63] Wang WG, Mogensen M. High-performance lanthanum-ferrite-based cathode for SOFC. Solid State Ionics 2005;176:457–62. https://doi.org/10.1016/j.ssi.2004.09.007.

[64] Sun C, Hui R, Roller J. Cathode materials for solid oxide fuel cells: A review. J Solid State Electrochem 2010;14:1125–44. https://doi.org/10.1007/s10008-009-0932-0.

[65] Dong F, Ni M, Chen Y, Chen D, Tadé MO, Shao Z. Structural and oxygen-transport studies of double perovskites PrBa1-xCo2O5+δ (x = 0.00, 0.05, and 0.10) toward their application as superior oxygen reduction electrodes. J Mater Chem A 2014;2:20520–9. https://doi.org/10.1039/c4ta04372c.

[66] Adler SB. Factors governing oxygen reduction in solid oxide fuel cell cathodes. Chem Rev 2004;104:4791–843. https://doi.org/10.1021/cr020724o.

[67] Gao Z, Mogni L V., Miller EC, Railsback JG, Barnett SA. A perspective on low-temperature solid oxide fuel cells. Energy Environ Sci 2016;9:1602–44. https://doi.org/10.1039/c5ee03858h.

[68] Niu Y, Yin X, Sun C, Song X, Zhang N. Adjusting surface oxygen vacancies prompted perovskite as high performance cathode for solid oxide fuel cell. J Alloys Compd 2021;865:158746. https://doi.org/10.1016/j.jallcom.2021.158746.

[69] Liu D, Dou Y, Xia T, Li Q, Sun L, Huo L, et al. B-site La, Ce, and Pr-doped Ba0.5Sr0.5Co0.7Fe0.3O3-δ perovskite cathodes for intermediate-temperature solid oxide fuel cells: Effectively promoted oxygen reduction activity and operating stability. J Power Sources 2021;494:229778. https://doi.org/https://doi.org/10.1016/j.jpowsour.2021.229778.

[70] Costilla-Aguilar SU, Escudero MJ, Cienfuegos-Pelaes RF, Aguilar-Martínez JA. Double perovskite La1.8Sr0.2CoFeO5+δ as a cathode material for intermediate temperature solid oxide fuel cells. J Alloys Compd 2021;862.

https://doi.org/10.1016/j.jallcom.2020.158025.

[71] Bo L, Na L, Liping S, Qiang L, Lihua H, Hui Z. Rare-earth elements doped Nd2CuO4 as Cu-based cathode for intermediate-temperature solid oxide fuel cells. J Alloys Compd 2021;870:159397. https://doi.org/10.1016/j.jallcom.2021.159397.

[72] Zan J, Wang S, Zheng D, Li F, Chen W, Pei Q, et al. Characterization and functional application of PrBa0.5Sr0.5Co1.5Fe0.5O5+ cathode material for IT-SOFC. Mater Res Bull 2021;137:111173. https://doi.org/10.1016/j.materresbull.2020.111173.

[73] Gao J, Li Q, Sun L, Huo L, Zhao H. Enhanced electrocatalytic activity and CO2 tolerant Bi0.5Sr0.5Fe1-xTaxO3-δ as cobalt-free cathode for intermediate-temperature solid oxide fuel cells. Ceram Int 2019;45:20226–33. https://doi.org/10.1016/j.ceramint.2019.06.295.

[74] Wang S, Zan J, Qiu W, Zheng D, Li F, Chen W, et al. Evaluation of perovskite oxides LnBaCo2O5+δ (Ln = La, Pr, Nd and Sm) as cathode materials for IT-SOFC. J Electroanal Chem 2021;886:115144. https://doi.org/10.1016/j.jelechem.2021.115144.

[75] Zhang X, Xia T, Li Q, Sun L, Huo L, Zhao H. A highly active and CO2-tolerant perovskite cathode for solid oxide fuel cells operating below 700 °C. J Alloys Compd 2021;858. https://doi.org/10.1016/j.jallcom.2020.157743.

[76] Irshad M, Idrees R, Siraj K, Shakir I, Rafique M, Ain QU, et al. Electrochemical evaluation of mixed ionic electronic perovskite cathode LaNi1-xCoxO3-δ for IT-SOFC synthesized by high temperature decomposition. Int J Hydrogen Energy 2021;46:10448–56. https://doi.org/10.1016/j.ijhydene.2020.09.180.

[77] Li F, Xu Y, Zhao D, Jiang L, Wu Q, Shen H, et al. Structural, transport, thermal, and

electrochemical properties of (La1−xSrx)2CoO4±δ cathode in solid-oxide fuel cells. J Appl Electrochem 2021. https://doi.org/10.1007/s10800-020-01514-0.

[78] Rehman SU, Song R-H, Lim T-H, Park S-J, Hong J-E, Lee J-W, et al. High-performance nanofibrous LaCoO3 perovskite cathode for solid oxide fuel cells fabricated: Via chemically assisted electrodeposition. J Mater Chem A 2018;6:6987–96. https://doi.org/10.1039/c7ta10701c.

[79] Song KE, Woo SH, Baek SW, Kang H, Choi WS, Park JY, et al. SmBa1-xCaxCo2O5+d Layered Perovskite Cathodes for Intermediate Temperature-operating Solid Oxide Fuel Cells. Front Chem 2021;8. https://doi.org/10.3389/fchem.2020.628813.

[80] Zhang Z, Xie D, Ni J, Ni C. Ba2YCu3O6+δ-based cathode material for proton-conducting solid oxide fuel cells. Ceram Int 2021. https://doi.org/10.1016/j.ceramint.2021.01.242.

[81] Lee J, Choi M, Lee W. Encapsulation of Metal Catalysts for Stable Solid Oxide Fuel Cell Cathodes. Int J Precis Eng Manuf - Green Technol 2021. https://doi.org/10.1007/s40684-020-00290-8.

[82] Liu J, Jin F, Yang X, Niu B, Yu S, Li Y, et al. Synergistic electron doping and ion conductive phase incorporating of SrCoO3-δ as desirable cathode materials for intermediate-temperature solid oxide fuel cells. Ceram Int 2020;46:28332–41. https://doi.org/10.1016/j.ceramint.2020.07.337.

[83] Liu M, Fu X, Meng X, Lü S, Ren S, Liu X, et al. Enhanced electrochemical performance of the YBa0.5Sr0.5Co1.4Cu0.6O5+δ cathode material by Sm0.2Ce0.8O1.9 incorporation for solid oxide fuel cells application. J Sol-Gel Sci Technol 2020;96:742–52. https://doi.org/10.1007/s10971-020-05409-6.

[84] Hanif MB, Gao J-T, Shaheen K, Wang Y-P, Yasir M, Zhang S-L, et al. Performance evaluation of highly active and novel La0.7Sr0.3Ti0.1Fe0.6Ni0.3O3-δ material both as cathode and anode for intermediate-temperature symmetrical solid oxide fuel cell. J Power Sources 2020;472. https://doi.org/10.1016/j.jpowsour.2020.228498.

[85] Xia W, Li Q, Sun L, Huo L, Zhao H. Electrochemical performance of Sn-doped Bi0.5Sr0.5FeO3-δ perovskite as cathode electrocatalyst for solid oxide fuel cells. J Alloys Compd 2020;835. https://doi.org/10.1016/j.jallcom.2020.155406.

[86] Tarutina LR, Vdovin GK, Lyagaeva JG, Medvedev DA. BaCe0.7–xZr0.2Y0.1FexO3–δ derived from proton-conducting electrolytes: A way of designing chemically compatible cathodes for solid oxide fuel cells. J Alloys Compd 2020;831. https://doi.org/10.1016/j.jallcom.2020.154895.

[87] Hassan D, Janes S, Clasen R. Proton-conducting ceramics as electrode/electrolyte materials for SOFC's—part I: preparation, mechanical and thermal properties of sintered bodies. J Eur Ceram Soc 2003;23:221–8. https://doi.org/10.1016/S0955-2219(02)00173-5.

[88] Iwahara H, Esaka T, Uchida H, Maeda N. Proton conduction in sintered oxides and its application to steam electrolysis for hydrogen production. Solid State Ionics 1981;3–4:359–63. https://doi.org/10.1016/0167-2738(81)90113-2.

[89] An H, Shin D, Ji H Il. Pr2NiO4+d for cathode in protonic ceramic fuel cells. J Korean Ceram Soc 2018;55:358–63. https://doi.org/10.4191/kcers.2018.55.4.06.

[90] Strandbakke R, Cherepanov VA, Zuev AY, Tsvetkov DS, Argirusis C, Sourkouni G, et al. Gd- and Pr-based double perovskite cobaltites as oxygen electrodes for proton ceramic fuel cells and electrolyser cells. Solid State Ionics 2015;278:120–32.

https://doi.org/10.1016/j.ssi.2015.05.014.

[91] Wang N, Tang C, Du L, Zhu R, Xing L, Song Z, et al. Advanced Cathode Materials for Protonic Ceramic Fuel Cells: Recent Progress and Future Perspectives. Adv Energy Mater 2022;2201882:1–29. https://doi.org/10.1002/aenm.202201882.

[92] Wang Q, Hou J, Fan Y, Xi X-A, Li J, Lu Y, et al. Pr2BaNiMnO7-: δ double-layered Ruddlesden-Popper perovskite oxides as efficient cathode electrocatalysts for low temperature proton conducting solid oxide fuel cells. J Mater Chem A 2020;8:7704–12. https://doi.org/10.1039/c9ta11212j.

[93] Da′as EH, Bi L, Boulfrad S, Traversa E. Nanostructuring the electronic conducting La0.8Sr0.2MnO3−δ cathode for high-performance in proton-conducting solid oxide fuel cells below 600°C. Sci China Mater 2018;61:57–64. https://doi.org/10.1007/s40843-017-9125-1.

[94] Wang P, Xu D, Cheng J, Hong T. Proton uptake kinetics and electromotive force in BaCo0.4Fe0.4Zr0.1Y0.1O3-δ cathode material with e−/O2−/H+ three mobile carriers for protonic ceramic fuel cells. Ionics (Kiel) 2021;27:1185–92. https://doi.org/10.1007/s11581-021-03914-4.

[95] Shim JH. Ceramics breakthrough. Nat Energy 2018;3:168–9. https://doi.org/10.1038/s41560-018-0110-7.

[96] Sun S, Cheng Z. H 2 S Poisoning of Proton Conducting Solid Oxide Fuel Cell and Comparison with Conventional Oxide-Ion Conducting Solid Oxide Fuel Cell . J Electrochem Soc 2018;165:F836–44. https://doi.org/10.1149/2.0841810jes.

[97] Kreuer KD. Proton-Conducting Oxides. Annu Rev Mater Res 2003;33:333–59. https://doi.org/10.1146/annurev.matsci.33.022802.091825.

[98] Thabet K, Le Gal La Salle A, Quarez E, Joubert O. Protonic-based ceramics for fuel cells and electrolyzers. INC; 2020. https://doi.org/10.1016/b978-0-12-818285-7.00004-6.

[99] Kochetova N, Animitsa I, Medvedev D, Demin A, Tsiakaras P. Recent activity in the development of proton-conducting oxides for high-temperature applications. RSC Adv 2016;6:73222–68. https://doi.org/10.1039/c6ra13347a.

[100] Bello IT, Zhai S, He Q, Cheng C, Dai Y, Chen B, et al. Materials development and prospective for protonic ceramic fuel cells. Int J Energy Res 2022;46:2212–40. https://doi.org/10.1002/er.7371.

[101] Bian W, Wu W, Wang B, Tang W, Zhou M, Jin C, et al. Revitalizing interface in protonic ceramic cells by acid etch. Nature 2022;604:479. https://doi.org/10.1038/s41586-022-04457-y.

[102] Choi M, Paik J, Kim D, Woo D, Lee J, Kim SJ, et al. Exceptionally high performance of protonic ceramic fuel cells with stoichiometric electrolytes. Energy Environ Sci 2021. https://doi.org/10.1039/d1ee01497h.

[103] Papac M, Stevanović V, Zakutayev A, O’Hayre R. Triple ionic–electronic conducting oxides for next-generation electrochemical devices. Nat Mater 2021;20:301–13. https://doi.org/10.1038/s41563-020-00854-8.

[104] Duan C, Tong J, Shang M, Nikodemski S, Sanders M, Ricote S, et al. Readily processed protonic ceramic fuel cells with high performance at low temperatures. Science (80-)

2015;349:1321–6. https://doi.org/10.1126/science.aab3987.

[105] Rafique M, Nawaz H, Shahid Rafique M, Bilal Tahir M, Nabi G, Khalid NR. Material and method selection for efficient solid oxide fuel cell anode: Recent advancements and reviews. Int J Energy Res 2019;43:2423–46. https://doi.org/10.1002/er.4210.

[106] Ye Y, Sun X, Zhou M, Chen Y. A mini review on the application of proton-conducting solid oxide cells for CO2 conversion. Energy and Fuels 2020;34:13427–37. https://doi.org/10.1021/acs.energyfuels.0c02899.

[107] Duan C, Huang J, Sullivan N, O'Hayre R. Proton-conducting oxides for energy conversion and storage. Appl Phys Rev 2020;7:011314. https://doi.org/10.1063/1.5135319.

[108] Plekhanov MS, Lesnichyova AS, Stroeva AY, Ananyev M V, Farlenkov AS, Bogdanovich NM, et al. Novel Ni cermets for anode-supported proton ceramic fuel cells. J Solid State Electrochem 2019;23:1389–98. https://doi.org/10.1007/s10008-019-04233-5.

[109] Iwahara H. Oxide-ionic and protonic conductors based on perovskite-type oxides and their possible applications. Solid State Ionics 1992;52:99–104. https://doi.org/10.1016/0167-2738(92)90095-7.

[110] Roth RS. Classification of perovskite and other ABO3-type compounds. J Res Natl Bur Stand 1957;58:75. https://doi.org/10.6028/jres.058.010.

[111] Duan C, Kee RJ, Zhu H, Karakaya C, Chen Y, Ricote S, et al. Highly durable, coking and sulfur tolerant, fuel-flexible protonic ceramic fuel cells. Nature 2018;557:217–22. https://doi.org/10.1038/s41586-018-0082-6.

[112] Sun W, Liu M, Liu W. Chemically stable yttrium and tin co-doped barium zirconate electrolyte for next generation high performance proton-conducting solid oxide fuel cells. Adv Energy Mater 2013;3:1041–50. https://doi.org/10.1002/aenm.201201062.

[113] Fabbri E, Bi L, Tanaka H, Pergolesi D, Traversa E. Chemically stable Pr and y Co-doped barium zirconate electrolytes with high proton conductivity for intermediate-temperature solid oxide fuel cells. Adv Funct Mater 2011;21:158–66. https://doi.org/10.1002/adfm.201001540.

[114] Zhang W, Hu YH. Progress in proton-conducting oxides as electrolytes for low-temperature solid oxide fuel cells: From materials to devices. Energy Sci Eng 2021;n/a. https://doi.org/https://doi.org/10.1002/ese3.886.

[115] Xu X, Bi L. Proton-conducting electrolyte materials. vol. 96. 2019. https://doi.org/10.1016/B978-0-12-817445-6.00003-X.

[116] Ranran P, Yan W, Lizhai Y, Zongqiang M. Electrochemical properties of intermediate-temperature SOFCs based on proton conducting Sm-doped BaCeO3 electrolyte thin film. Solid State Ionics 2006;177:389–93. https://doi.org/10.1016/j.ssi.2005.11.020.

[117] Katahira K, Kohchi Y, Shimura T, Iwahara H. Protonic conduction in Zr-substituted BaCeO3. Solid State Ionics 2000;138:91–8. https://doi.org/10.1016/S0167-2738(00)00777-3.

[118] Wang CC, Luo D, Jiang SP, Lin B. Highly sulfur poisoning-tolerant BaCeO3-impregnated La0.6Sr0.4Co0.2Fe0.8O3-δ cathodes for solid oxide fuel cells. J Phys D Appl Phys 2018;51. https://doi.org/10.1088/1361-6463/aadf4c.

[119] Yamanaka S, Fujikane M, Hamaguchi T, Muta H, Oyama T, Matsuda T, et al. Thermophysical properties of BaZrO3 and BaCeO3. J Alloys Compd 2003;359:109–13. https://doi.org/10.1016/S0925-8388(03)00214-7.

[120] Loureiro FJA, Nasani N, Reddy GS, Munirathnam NR, Fagg DP. A review on sintering technology of proton conducting BaCeO3-BaZrO3 perovskite oxide materials for Protonic Ceramic Fuel Cells. J Power Sources 2019;438:226991. https://doi.org/10.1016/j.jpowsour.2019.226991.

[121] Bi L, Zhang S, Fang S, Tao Z, Peng R, Liu W. A novel anode supported BaCe0.7Ta0.1Y0.2O3-δ electrolyte membrane for proton-conducting solid oxide fuel cell. Electrochem Commun 2008;10:1598–601. https://doi.org/10.1016/j.elecom.2008.08.024.

[122] Bello IT, Zhai S, Zhao S, Li Z, Yu N, Ni M. Scientometric review of proton-conducting solid oxide fuel cells. Int J Hydrogen Energy 2021;46:37406–28. https://doi.org/10.1016/j.ijhydene.2021.09.061.

[123] Medvedev DA, Lyagaeva JG, Gorbova E V., Demin AK, Tsiakaras P. Advanced materials for SOFC application: Strategies for the development of highly conductive and stable solid oxide proton electrolytes. Prog Mater Sci 2016;75:38–79. https://doi.org/10.1016/j.pmatsci.2015.08.001.

[124] Ma G, Matsumoto H, Iwahara H. Ionic conduction and nonstoichiometry in non-doped BaxCeO3-α. Solid State Ionics 1999;122:237–47. https://doi.org/10.1016/S0167-2738(99)00074-0.

[125] Medvedev D, Murashkina A, Pikalova E, Demin A, Podias A, Tsiakaras P. BaCeO3: Materials development, properties and application. Prog Mater Sci 2014;60:72–129.

https://doi.org/10.1016/j.pmatsci.2013.08.001.

[126] Atmospheres W, Bhide S V, Virkar A V. Stability of BaCeO 3 - Based Proton Conductors in Water - Containing Atmospheres Stability of BaCeO 3 -Based Proton Conductors in 1999:3–10.

[127] Bi L, Da'as EH, Shafi SP. Proton-conducting solid oxide fuel cell (SOFC) with Y-doped BaZrO3 electrolyte. Electrochem Commun 2017;80:20–3. https://doi.org/10.1016/j.elecom.2017.05.006.

[128] Hossain S, Abdalla AM, Jamain SNB, Zaini JH, Azad AK. A review on proton conducting electrolytes for clean energy and intermediate temperature-solid oxide fuel cells. Renew Sustain Energy Rev 2017;79:750–64. https://doi.org/10.1016/j.rser.2017.05.147.

[129] Rioja-Monllor L, Bernuy-Lopez C, Fontaine ML, Grande T, Einarsrud MA. Processing of high performance composite cathodes for protonic ceramic fuel cells by exsolution. J Mater Chem A 2019;7:8609–19. https://doi.org/10.1039/c8ta10950h.

[130] Nikodemski S, Tong J, O'Hayre R. Solid-state reactive sintering mechanism for proton conducting ceramics. Solid State Ionics 2013;253:201–10. https://doi.org/https://doi.org/10.1016/j.ssi.2013.09.025.

[131] Han D, Uemura S, Hiraiwa C, Majima M, Uda T. Detrimental Effect of Sintering Additives on Conducting Ceramics: Yttrium-Doped Barium Zirconate. ChemSusChem 2018;11:4102–13. https://doi.org/10.1002/cssc.201801837.

[132] Xia Y, Xu X, Teng Y, Lv H, Jin Z, Wang D, et al. A novel BaFe0.8Zn0.1Bi0.1O3−δ

cathode for proton conducting solid oxide fuel cells. Ceram Int 2020;46:25453–9. https://doi.org/10.1016/j.ceramint.2020.07.015.

[133] Wang D, Xia Y, Lv H, Miao L, Bi L, Liu W. PrBaCo2-xTaxO5+δ based composite materials as cathodes for proton-conducting solid oxide fuel cells with high CO2 resistance. Int J Hydrogen Energy 2020;45:31017–26. https://doi.org/10.1016/j.ijhydene.2020.08.094.

[134] LÜ J, WANG L, FAN L, LI Y, DAI L, GUO H. Chemical stability of doped BaCeO3-BaZrO3 solid solutions in different atmospheres. J Rare Earths 2008;26:505–10. https://doi.org/10.1016/S1002-0721(08)60127-1.

[135] Azad AK, Irvine JTS. Synthesis, chemical stability and proton conductivity of the perovksites Ba(Ce,Zr)1-x Scx O3 - δ. Solid State Ionics 2007;178:635–40. https://doi.org/10.1016/j.ssi.2007.02.004.

[136] Azad AK, Irvine JTS. High density and low temperature sintered proton conductor BaCe 0.5Zr0.35Sc0.1Zn0.05O 3-δ. Solid State Ionics 2008;179:678–82. https://doi.org/10.1016/j.ssi.2008.04.036.

[137] Malavasi L, Fisher CAJ, Islam MS. Oxide-ion and proton conducting electrolyte materials for clean energy applications: Structural and mechanistic features. Chem Soc Rev 2010;39:4370–87. https://doi.org/10.1039/b915141a.

[138] Wang W, Qu J, Julião PSB, Shao Z. Recent Advances in the Development of Anode Materials for Solid Oxide Fuel Cells Utilizing Liquid Oxygenated Hydrocarbon Fuels: A Mini Review. Energy Technol 2019;7:33–44. https://doi.org/10.1002/ente.201700738.

[139] Jarry A, Jackson GS, Crumlin EJ, Eichhorn B, Ricote S. The effect of grain size on the hydration of BaZr0.9Y0.1O3-: δ proton conductor studied by ambient pressure X-ray photoelectron spectroscopy. Phys Chem Chem Phys 2019;22:136–43. https://doi.org/10.1039/c9cp04335g.

[140] Iguchi F, Yamada T, Sata N, Tsurui T, Yugami H. The influence of grain structures on the electrical conductivity of a BaZr0.95Y0.05O3 proton conductor. Solid State Ionics 2006;177:2381–4. https://doi.org/10.1016/j.ssi.2006.07.008.

[141] Ueno K, Hatada N, Han D, Uda T. Thermodynamic maximum of y doping level in barium zirconate in co-sintering with NiO. J Mater Chem A 2019;7:7232–41. https://doi.org/10.1039/c8ta12245h.

[142] Tong J, Clark D, Bernau L, Sanders M, O'Hayre R. Solid-state reactive sintering mechanism for large-grained yttrium-doped barium zirconate proton conducting ceramics. J Mater Chem 2010;20:6333–41. https://doi.org/10.1039/C0JM00381F.

[143] Ueno K, Hatada N, Han D, Toyoura K, Uda T. Reexamination of the phase diagram of the BaO-ZrO2-Y2O3 system: investigation of the presence of separate region in Y-doped BaZrO3 solid solution and the dissolution of Zr in Ba3Y4O9. J Solid State Electrochem 2020;24:1523–38. https://doi.org/10.1007/s10008-020-04716-w.

[144] Tong J, Clark D, Hoban M, O'Hayre R. Cost-effective solid-state reactive sintering method for high conductivity proton conducting yttrium-doped barium zirconium ceramics. Solid State Ionics 2010;181:496–503. https://doi.org/https://doi.org/10.1016/j.ssi.2010.02.008.

[145] Babilo P, Haile SM. Enhanced sintering of yttrium-doped barium zirconate by addition of

ZnO. J Am Ceram Soc 2005;88:2362–8. https://doi.org/10.1111/j.1551-2916.2005.00449.x.

[146] Bi L, Fabbri E, Sun Z, Traversa E. Sinteractive anodic powders improve densification and electrochemical properties of BaZr0.8Y0.2O3-δ electrolyte films for anode-supported solid oxide fuel cells. Energy Environ Sci 2011;4:1352–7. https://doi.org/10.1039/c0ee00387e.

[147] Tao S, Irvine JTS. A stable, easily sintered proton-conducting oxide electrolyte for moderate-temperature fuel cells and electrolyzers. Adv Mater 2006;18:1581–4. https://doi.org/10.1002/adma.200502098.

[148] Tao S, Irvine JTS. Conductivity studies of dense yttrium-doped BaZrO3 sintered at 1325 °C. J Solid State Chem 2007;180:3493–503. https://doi.org/10.1016/j.jssc.2007.09.027.

[149] Sun W, Shi Z, Liu M, Bi L, Liu W. An Easily Sintered, Chemically Stable, Barium Zirconate-Based Proton Conductor for High-Performance Proton-Conducting Solid Oxide Fuel Cells. Adv Funct Mater 2014;24:5695–702. https://doi.org/10.1002/adfm.201401478.

[150] Uhlenbruck S, Tietz F, Haanappel V, Sebold D, Buchkremer H-P, Stöver D. Silver incorporation into cathodes for solid oxide fuel cells operating at intermediate temperature. J Solid State Electrochem 2004;8:923–7. https://doi.org/10.1007/s10008-004-0510-4.

[151] Pergolesi D, Fabbri E, D’Epifanio A, Di Bartolomeo E, Tebano A, Sanna S, et al. High proton conduction in grain-boundary-free yttrium-doped barium zirconate films grown by pulsed laser deposition. Nat Mater 2010;9:846–52. https://doi.org/10.1038/nmat2837.

[152] Zuo C, Zha S, Liu M, Hatano M, Uchiyama M. Ba(Zr0.1Ce0.7Y0.2)O3-δ as an electrolyte for low-temperature solid-oxide fuel cells. Adv Mater 2006;18:3318–20. https://doi.org/10.1002/adma.200601366.

[153] Vázquez S, Davyt S, Basbus JF, Soldati AL, Amaya A, Serquis A, et al. Synthesis and characterization of La0.6Sr0.4Fe0.8Cu0.2O3-δ oxide as cathode for Intermediate Temperature Solid Oxide Fuel Cells. J Solid State Chem 2015;228:208–13. https://doi.org/10.1016/j.jssc.2015.04.044.

[154] Basbus JF, Arce MD, Prado FD, Caneiro A, Mogni L V. A high temperature study on thermodynamic, thermal expansion and electrical properties of BaCe0.4Zr0.4Y0.2O3−δ proton conductor. J Power Sources 2016;329:262–7. https://doi.org/10.1016/j.jpowsour.2016.08.083.

[155] Yang L, Wang S, Blinn K, Liu M, Liu Z, Cheng Z, et al. Enhanced Sulfur and Coking Tolerance of a Mixed Ion Conductor for SOFCs: BaZr 0.1 Ce 0.7 Y 0.2– x Yb x O 3–δ. Science (80-) 2009;326:126–9. https://doi.org/10.1126/science.1174811.

[156] Choi S, Kucharczyk CJ, Liang Y, Zhang X, Takeuchi I, Ji H-I, et al. Exceptional power density and stability at intermediate temperatures in protonic ceramic fuel cells. Nat Energy 2018;3:202–10. https://doi.org/10.1038/s41560-017-0085-9.

[157] Taillades G, Dailly J, Taillades-Jacquin M, Mauvy F, Essouhmi A, Marrony M, et al. Intermediate Temperature Anode-Supported Fuel Cell Based on BaCe0.9Y0.1O3 Electrolyte with Novel Pr2NiO4 Cathode. Fuel Cells 2010;10:166–73. https://doi.org/https://doi.org/10.1002/fuce.200900033.

[158] Zunic M, Chevallier L, Deganello F, D’Epifanio A, Licoccia S, Di Bartolomeo E, et al.

Electrophoretic deposition of dense BaCe0.9Y0.1O3−x electrolyte thick-films on Ni-based anodes for intermediate temperature solid oxide fuel cells. J Power Sources 2009;190:417–22. https://doi.org/https://doi.org/10.1016/j.jpowsour.2009.01.046.

[159] Bi L, Fabbri E, Sun Z, Traversa E. A novel ionic diffusion strategy to fabricate high-performance anode-supported solid oxide fuel cells (SOFCs) with proton-conducting Y-doped BaZrO3 films. Energy Environ Sci 2011;4:409–12. https://doi.org/10.1039/c0ee00353k.

[160] Pergolesi D, Fabbri E, Traversa E. Chemically stable anode-supported solid oxide fuel cells based on Y-doped barium zirconate thin films having improved performance. Electrochem Commun 2010;12:977–80. https://doi.org/https://doi.org/10.1016/j.elecom.2010.05.005.

[161] An H, Lee HW, Kim BK, Son JW, Yoon KJ, Kim H, et al. A 5 × 5 cm2 protonic ceramic fuel cell with a power density of 1.3 W cm–2 at 600 °C. Nat Energy 2018;3:870–5. https://doi.org/10.1038/s41560-018-0230-0.

[162] Yuan R, He W, Zhang C, Ni M, Leung MKH. Cobalt free SrFe0.95Nb0.05O3−δ cathode material for proton-conducting solid oxide fuel cells with BaZr0.1Ce0.7Y0.2O3−δ electrolyte. Mater Lett 2017;200:75–8. https://doi.org/https://doi.org/10.1016/j.matlet.2017.04.103.

[163] Chen C, Dong Y, Li L, Wang Z, Liu M, Rainwater BH, et al. High performance of anode supported BaZr0.1Ce0.7Y0.1Yb0.1O3-δ proton-conducting electrolyte micro-tubular cells with asymmetric structure for IT-SOFCs. J Electroanal Chem 2019;844:49–57. https://doi.org/10.1016/j.jelechem.2019.05.001.

[164] Chen C, Dong Y, Li L, Wang Z, Liu M, Rainwater BH, et al. Electrochemical properties of micro-tubular intermediate temperature solid oxide fuel cell with novel asymmetric structure based on BaZr0.1Ce0.7Y0.1Yb0.1O3−δ proton conducting electrolyte. Int J Hydrogen Energy 2019;44:16887–97. https://doi.org/10.1016/j.ijhydene.2019.04.264.

[165] Hou J, Miao L, Hui J, Bi L, Liu W, Irvine JTS. A novel: In situ diffusion strategy to fabricate high performance cathodes for low temperature proton-conducting solid oxide fuel cells. J Mater Chem A 2018;6:10411–20. https://doi.org/10.1039/c8ta00859k.

[166] Darab M, Toprak MS, Syvertsen GE, Muhammed M. Nanoengineered BSCF cathode materials for intermediate-temperature solid-oxide fuel cells. J Electrochem Soc 2009;156:K139–43. https://doi.org/10.1149/1.3142430.

[167] Xi X, Kondo A, Kozawa T, Naito M. LSCF-GDC composite particles for solid oxide fuel cells cathodes prepared by facile mechanical method. Adv Powder Technol 2016;27:646–51. https://doi.org/10.1016/j.apt.2016.02.022.

[168] Zhu C, Liu X, Yi C, Yan D, Su W. Electrochemical performance of PrBaCo2O5+δ layered perovskite as an intermediate-temperature solid oxide fuel cell cathode. J Power Sources 2008;185:193–6. https://doi.org/10.1016/j.jpowsour.2008.06.075.

[169] Jeong C, Lee J-H, Park M, Hong J, Kim H, Son J-W, et al. Design and processing parameters of La2NiO4+δ-based cathode for anode-supported planar solid oxide fuel cells (SOFCs). J Power Sources 2015;297:370–8. https://doi.org/10.1016/j.jpowsour.2015.08.023.

[170] Tarancón A, Burriel M, Santiso J, Skinner SJ, Kilner JA. Advances in layered oxide cathodes for intermediate temperature solid oxide fuel cells. J Mater Chem 2010;20:3799–

813. https://doi.org/10.1039/b922430k.

[171] Jiang Z, Xia C, Chen F. Nano-structured composite cathodes for intermediate-temperature solid oxide fuel cells via an infiltration/impregnation technique. Electrochim Acta 2010;55:3595–605. https://doi.org/10.1016/j.electacta.2010.02.019.

[172] Li L, Jin F, Shen Y, He T. Cobalt-free double perovskite cathode GdBaFeNiO5+δ and electrochemical performance improvement by Ce0.8Sm0.2O1.9 impregnation for intermediate-temperature solid oxide fuel cells. Electrochim Acta 2015;182:682–92. https://doi.org/10.1016/j.electacta.2015.09.146.

[173] Huan D, Shi N, Xie Y, Li X, Wang W, Xue S, et al. Cathode materials for proton-conducting solid oxide fuel cells. INC; 2019. https://doi.org/10.1016/B978-0-12-817445-6.00008-9.

[174] Wu T, Peng R, Xia C. Sm0.5Sr0.5CoO3 - δ-BaCe0.8Sm0.2O3-δ composite cathodes for proton-conducting solid oxide fuel cells. Solid State Ionics 2008;179:1505–8. https://doi.org/10.1016/j.ssi.2007.12.005.

[175] Kim J, Sengodan S, Kwon G, Ding D, Shin J, Liu M, et al. Triple-Conducting Layered Perovskites as Cathode Materials for Proton-Conducting Solid Oxide Fuel Cells. ChemSusChem 2014;7:2811–5. https://doi.org/10.1002/cssc.201402351.

[176] Wang Z, Yang W, Zhu Z, Peng R, Wu X, Xia C, et al. First-principles study of O2 reduction on BaZr1-xCoxO3 cathodes in protonic-solid oxide fuel cells. J Mater Chem A 2014;2:16707–14. https://doi.org/10.1039/c4ta01652a.

[177] Duan C, Tong J, Shang M, Nikodemski S, Sanders M, Ricote S, et al. Readily processed

protonic ceramic fuel cells with high performance at low temperatures. Science (80-) 2015;349:1321 LP – 1326. https://doi.org/10.1126/science.aab3987.

[178] Liang M, He F, Zhou C, Chen Y, Ran R, Yang G, et al. Nickel-doped BaCo0.4Fe0.4Zr0.1Y0.1O3-δ as a new high-performance cathode for both oxygen-ion and proton conducting fuel cells. Chem Eng J 2021;420:127717. https://doi.org/10.1016/j.cej.2020.127717.

[179] Qi H, Zhao Z, Wang X, Tu B, Cheng M. Self-assembled cubic-hexagonal perovskite nanocomposite as intermediate-temperature solid oxide fuel cell cathode. Ceram Int 2020;46:22282–9. https://doi.org/10.1016/j.ceramint.2020.05.307.

[180] Song Y, Chen Y, Wang W, Zhou C, Zhong Y, Yang G, et al. Self-Assembled Triple-Conducting Nanocomposite as a Superior Protonic Ceramic Fuel Cell Cathode. Joule 2019;3:2842–53. https://doi.org/10.1016/j.joule.2019.07.004.

[181] Mather GC, Muñoz-gil D, Zamudio-garc J, Porras-v M, Marrero-l D, Domingo P. applied sciences Perspectives on Cathodes for Protonic Ceramic Fuel Cells 2021.

[182] Zohourian R, Merkle R, Raimondi G, Maier J. Mixed-Conducting Perovskites as Cathode Materials for Protonic Ceramic Fuel Cells: Understanding the Trends in Proton Uptake. Adv Funct Mater 2018;28:1–10. https://doi.org/10.1002/adfm.201801241.

[183] Fabbri E, Bi L, Pergolesi D, Traversa E. Towards the next generation of solid oxide fuel cells operating below 600 °c with chemically stable proton-conducting electrolytes. Adv Mater 2012;24:195–208. https://doi.org/10.1002/adma.201103102.

[184] Ding P, Li W, Zhao H, Wu C, Zhao L, Dong B, et al. Review on Ruddlesden–Popper

perovskites as cathode for solid oxide fuel cells. J Phys Mater 2021;4:022002. https://doi.org/10.1088/2515-7639/abe392.

[185] Li W, Guan B, Zhang X, Yan J, Zhou Y, Liu X. New mechanistic insight into the oxygen reduction reaction on Ruddlesden-Popper cathodes for intermediate-temperature solid oxide fuel cells. Phys Chem Chem Phys 2016;18:8502–11. https://doi.org/10.1039/c6cp00056h.

[186] Boulahya K, Muñoz-Gil D, Gómez-Herrero A, Azcondo MT, Amador U. Eu2SrCo1.5Fe0.5O7 a new promising Ruddlesden-Popper member as a cathode component for intermediate temperature solid oxide fuel cells. J Mater Chem A 2019;7:5601–11. https://doi.org/10.1039/c8ta11254a.

[187] Miao L, Hou J, Gong Z, Jin Z, Liu W. A high-performance cobalt-free Ruddlesden-Popper phase cathode La1·2Sr0·8Ni0·6Fe0·4O4+Δ for low temperature proton-conducting solid oxide fuel cells. Int J Hydrogen Energy 2019;44:7531–7. https://doi.org/10.1016/j.ijhydene.2019.01.255.

[188] Li W, Guan B, Zhang X, Yan J, Zhou Y, Liu X. New mechanistic insight into the oxygen reduction reaction on Ruddlesden-Popper cathodes for intermediate-temperature solid oxide fuel cells. Phys Chem Chem Phys 2016;18:8502–11. https://doi.org/10.1039/c6cp00056h.

[189] Huan D, Zhang L, Li X, Xie Y, Shi N, Xue S, et al. A Durable Ruddlesden-Popper Cathode for Protonic Ceramic Fuel Cells. ChemSusChem 2020;13:4994–5003. https://doi.org/10.1002/cssc.202001168.

[190] Chen Z, Wang J, Huan D, Sun S, Wang G, Fu Z, et al. Tailoring the activity via cobalt

doping of a two-layer Ruddlesden-Popper phase cathode for intermediate temperature solid oxide fuel cells. J Power Sources 2017;371:41–7. https://doi.org/10.1016/j.jpowsour.2017.10.011.

[191] Bilal Hanif M, Motola M, qayyum S, Rauf S, khalid A, Li CJ, et al. Recent advancements, doping strategies and the future perspective of perovskite-based solid oxide fuel cells for energy conversion. Chem Eng J 2022;428:132603. https://doi.org/10.1016/j.cej.2021.132603.

[192] Zhang Y, Chen B, Guan D, Xu M, Ran R, Ni M, et al. Thermal-expansion offset for high-performance fuel cell cathodes. Nature 2021;591:246–51. https://doi.org/10.1038/s41586-021-03264-1.

[193] Zhang Z, Xie D, Ni J, Ni C. Ba2YCu3O6+δ-based cathode material for proton-conducting solid oxide fuel cells. Ceram Int 2021;47:14673–9. https://doi.org/https://doi.org/10.1016/j.ceramint.2021.01.242.

[194] Gu C-Y, Wu X-S, Cao J-F, Hou J, Miao L-N, Xia Y-P, et al. High performance Ca-containing La2-xCaxNiO4+δ(0≤x≤0.75) cathode for proton-conducting solid oxide fuel cells. Int J Hydrogen Energy 2020;45:23422–32. https://doi.org/https://doi.org/10.1016/j.ijhydene.2020.06.106.

[195] Wang Z, Lv P, Yang L, Guan R, Jiang J, Jin F, et al. Ba0.95La0.05Fe0.8Zn0.2O3-δ cobalt-free perovskite as a triple-conducting cathode for proton-conducting solid oxide fuel cells. Ceram Int 2020;46:18216–23. https://doi.org/10.1016/j.ceramint.2020.04.144.

[196] Wan T-T, Zhu A-K, Li H-B, Wang C-C, Guo Y-M, Shao Z-P, et al. Performance variability of Ba0.5Sr0.5Co0.8Fe0.2O3−δcathode on proton-conducting electrolyte

SOFCs with Ag and Au current collectors. Rare Met 2018;37:633–41. https://doi.org/10.1007/s12598-017-0942-5.

[197] Liu Y, Guo Y, Ran R, Shao Z. A novel approach for substantially improving the sinterability of BaZr0.4Ce0.4Y0.2O3−δ electrolyte for fuel cells by impregnating the green membrane with zinc nitrate as a sintering aid. J Memb Sci 2013;437:189–95. https://doi.org/10.1016/j.memsci.2013.03.002.

[198] Bae K, Noh H-S, Jang DY, Hong J, Kim H, Yoon KJ, et al. High-performance thin-film protonic ceramic fuel cells fabricated on anode supports with a non-proton-conducting ceramic matrix. J Mater Chem A 2016;4:6395–403. https://doi.org/10.1039/C5TA10670B.

[199] Lin Y, Ran R, Zheng Y, Shao Z, Jin W, Xu N, et al. Evaluation of Ba0.5Sr0.5Co0.8Fe0.2O3−δ as a potential cathode for an anode-supported proton-conducting solid-oxide fuel cell. J Power Sources 2008;180:15–22. https://doi.org/10.1016/j.jpowsour.2008.02.044.

[200] Lin Y, Ran R, Shao Z. Silver-modified Ba0.5Sr0.5Co0.8Fe0.2O3−δ as cathodes for a proton conducting solid-oxide fuel cell. Int J Hydrogen Energy 2010;35:8281–8. https://doi.org/10.1016/j.ijhydene.2009.12.017.

[201] Lin Y, Ran R, Zhang C, Cai R, Shao Z. Performance of PrBaCo2O5+δ as a Proton-Conducting Solid-Oxide Fuel Cell Cathode. J Phys Chem A 2010;114:3764–72. https://doi.org/10.1021/jp9042599.

[202] Lin Y, Zhou W, Sunarso J, Ran R, Shao Z. Characterization and evaluation of BaCo0.7Fe0.2Nb0.1O3−δ as a cathode for proton-conducting solid oxide fuel cells. Int J Hydrogen Energy 2012;37:484–97. https://doi.org/10.1016/j.ijhydene.2011.09.010.

[203] Tsvetkov N, Lu Q, Sun L, Crumlin EJ, Yildiz B. Improved chemical and electrochemical stability of perovskite oxides with less reducible cations at the surface. Nat Mater 2016;15:1010–6. https://doi.org/10.1038/nmat4659.

[204] Lai K-Y, Manthiram A. Effects of trivalent dopants on phase stability and catalytic activity of YBaCo4O7-based cathodes in solid oxide fuel cells. J Mater Chem A 2018;6:16412–20. https://doi.org/10.1039/C8TA01230J.

[205] Hayashi H, Kanoh M, Quan CJ, Inaba H, Wang S, Dokiya M, et al. Thermal expansion of Gd-doped ceria and reduced ceria. Solid State Ionics 2000;132:227–33. https://doi.org/10.1016/S0167-2738(00)00646-9.

[206] Du Y, Sammes NM, Tompsett GA, Zhang D, Swan J, Bowden M. Extruded Tubular Strontium- and Magnesium-Doped Lanthanum Gallate, Gadolinium-Doped Ceria, and Yttria-Stabilized Zirconia Electrolytes. J Electrochem Soc 2003;150:A74. https://doi.org/10.1149/1.1525268.

[207] Mori M, Yamamoto T, Itoh H, Inaba H, Tagawa H. Thermal Expansion of Nickel-Zirconia Anodes in Solid Oxide Fuel Cells during Fabrication and Operation. J Electrochem Soc 1998;145:1374–81. https://doi.org/10.1149/1.1838468.

[208] Kim J-H, Manthiram A. Low Thermal Expansion RBa(Co,M)4O7 Cathode Materials Based on Tetrahedral-Site Cobalt Ions for Solid Oxide Fuel Cells. Chem Mater 2010;22:822–31. https://doi.org/10.1021/cm9015244.

[209] Mori M. Mechanisms of Thermal Expansion and Shrinkage of La 0.8Sr 0.2MnO 3+δ] Perovskites with Different Densities during Thermal Cycling in Air. J Electrochem Soc 2005;152:A732. https://doi.org/10.1149/1.1864312.

[210] Ullmann H, Trofimenko N, Tietz F, Stöver D, Ahmad-Khanlou A. Correlation between thermal expansion and oxide ion transport in mixed conducting perovskite-type oxides for SOFC cathodes. Solid State Ionics 2000;138:79–90. https://doi.org/10.1016/S0167-2738(00)00770-0.

[211] McIntosh S, Vente JF, Haije WG, Blank DHA, Bouwmeester HJM. Oxygen Stoichiometry and Chemical Expansion of Ba0.5Sr0.5Co0.8Fe0.2O3-δ Measured by in Situ Neutron Diffraction. Chem Mater 2006;18:2187–93. https://doi.org/10.1021/cm052763x.

[212] Lee KT, Manthiram A. Comparison of Ln0.6 Sr0.4 Co O3-δ (Ln=La, Pr, Nd, Sm, and Gd) as cathode materials for intermediate temperature solid oxide fuel Cells. J Electrochem Soc 2006;153. https://doi.org/10.1149/1.2172572.

[213] Aguadero A, De La Calle C, Alonso JA, Escudero MJ, Fernández-Díaz MT, Daza L. Structural and electrical characterization of the novel SrCo 0.9Sb0.1O3.-δ perovskite: Evaluation as a solid oxide fuel cell cathode material. Chem Mater 2007;19:6437–44. https://doi.org/10.1021/cm071837x.

[214] Dong F, Chen D, Ran R, Park H, Kwak C, Shao Z. A comparative study of Sm0.5Sr0.5MO3−δ (M = Co and Mn) as oxygen reduction electrodes for solid oxide fuel cells. Int J Hydrogen Energy 2012;37:4377–87. https://doi.org/10.1016/j.ijhydene.2011.11.150.

[215] Swierczek K, Zheng K, Klimkowicz A. Optimization of Transport Properties of A-Site Ordered LnBa1-xSrxCo2-yFeyO5+ Perovskite-Type Cathode Materials. ECS Trans 2013;57:1993–2001. https://doi.org/10.1149/05701.1993ecst.

[216] Fossdal A, Menon M, Wærnhus I, Wiik K, Einarsrud M-A, Grande T. Crystal Structure and Thermal Expansion of La1−xSrxFeO3−δ Materials. J Am Ceram Soc 2004;87:1952–8. https://doi.org/10.1111/j.1151-2916.2004.tb06346.x.

[217] Dong F, Chen D, Chen Y, Zhao Q, Shao Z. La-doped BaFeO3-δ perovskite as a cobalt-free oxygen reduction electrode for solid oxide fuel cells with oxygen-ion conducting electrolyte. J Mater Chem 2012;22:15071–9. https://doi.org/10.1039/c2jm31711g.

[218] Xie D, Li K, Yang J, Yan D, Jia L, Chi B, et al. High-performance La0.5(Ba0.75Ca0.25)0.5Co0.8Fe0.2O3-δ cathode for proton-conducting solid oxide fuel cells. Int J Hydrogen Energy 2021;46:10007–14. https://doi.org/10.1016/j.ijhydene.2020.01.014.

[219] Shin JS, Park H, Park K, Saqib M, Jo M, Kim JH, et al. Activity of layered swedenborgite structured Y0.8Er0.2BaCo3.2Ga0.8O7+: δfor oxygen electrode reactions in at intermediate temperature reversible ceramic cells. J Mater Chem A 2021;9:607–21. https://doi.org/10.1039/d0ta11000k.

[220] Dayaghi AM, Haugsrud R, Stange M, Larring Y, Strandbakke R, Norby T. Increasing the thermal expansion of proton conducting Y-doped BaZrO3 by Sr and Ce substitution. Solid State Ionics 2021;359:115534. https://doi.org/https://doi.org/10.1016/j.ssi.2020.115534.

[221] Tolchard JR, Grande T. Chemical compatibility of candidate oxide cathodes for BaZrO3 electrolytes. Solid State Ionics 2007;178:593–9. https://doi.org/10.1016/j.ssi.2007.01.018.

[222] Lyagaeva YG, Medvedev DA, Demin AK, Tsiakaras P, Reznitskikh OG. Thermal expansion of materials in the barium cerate-zirconate system. Phys Solid State 2015;57:285–9. https://doi.org/10.1134/S1063783415020250.

[223] Zhu Z, Qian J, Wang Z, Dang J, Liu W. High-performance anode-supported solid oxide fuel cells based on nickel-based cathode and Ba(Zr0.1Ce0.7Y0.2)O3−δ electrolyte. J Alloys Compd 2013;581:832–5. https://doi.org/10.1016/j.jallcom.2013.07.210.

[224] Yu J, Ran R, Zhong Y, Zhou W, Ni M, Shao Z. Advances in Porous Perovskites: Synthesis and Electrocatalytic Performance in Fuel Cells and Metal–Air Batteries. ENERGY Environ Mater 2020;3:121–45. https://doi.org/10.1002/eem2.12064.

[225] Pers P, Mao V, Taillades M, Taillades G. Electrochemical behavior and performances of Ni-BaZr0·1Ce0·7Y0.1Yb0.1O3−δ cermet anodes for protonic ceramic fuel cell. Int J Hydrogen Energy 2018;43:2402–9. https://doi.org/10.1016/j.ijhydene.2017.12.024.

[226] Taillades G, Batocchi P, Essoumhi A, Taillades M, Jones DJ, Rozière J. Engineering of porosity, microstructure and electrical properties of Ni–BaCe0.9Y0.1O2.95 cermet fuel cell electrodes by gelled starch porogen processing. Microporous Mesoporous Mater 2011;145:26–31. https://doi.org/10.1016/j.micromeso.2011.04.020.

[227] Zhao F, Virkar A V. Dependence of polarization in anode-supported solid oxide fuel cells on various cell parameters. J Power Sources 2005;141:79–95. https://doi.org/10.1016/j.jpowsour.2004.08.057.

[228] Essoumhi A, Taillades G, Taillades-Jacquin M, Jones DJ, Rozière J. Synthesis and characterization of Ni-cermet/proton conducting thin film electrolyte symmetrical assemblies. Solid State Ionics 2008;179:2155–9. https://doi.org/10.1016/j.ssi.2008.07.025.

[229] Chevallier L, Zunic M, Esposito V, Di Bartolomeo E, Traversa E. A wet-chemical route for the preparation of Ni–BaCe0.9Y0.1O3−δ cermet anodes for IT-SOFCs. Solid State Ionics 2009;180:715–20. https://doi.org/10.1016/j.ssi.2009.03.005.

[230] Onishi T, Han D, Noda Y, Hatada N, Majima M, Uda T. Evaluation of performance and durability of Ni-BZY cermet electrodes with BZY electrolyte. Solid State Ionics 2018;317:127–35. https://doi.org/10.1016/j.ssi.2018.01.015.

[231] Atkinson A, Barnett S, Gorte RJ, Irvine JTS, McEvoy AJ, Mogensen M, et al. Advanced anodes for high-temperature fuel cells. Nat Mater 2004;3:17–27. https://doi.org/10.1038/nmat1040.

[232] Yamaguchi S, Shishido T, Yugami H, Yamamoto S, Hara S. Construction of fuel cells based on thin proton conducting oxide electrolyte and hydrogen-permeable metal membrane electrode. Solid State Ionics 2003;162–163:291–6. https://doi.org/10.1016/S0167-2738(03)00221-2.

[233] Ito N, Iijima M, Kimura K, Iguchi S. New intermediate temperature fuel cell with ultra-thin proton conductor electrolyte. J Power Sources 2005;152:200–3. https://doi.org/10.1016/j.jpowsour.2005.01.009.

[234] Yang S, Lu Y, Wang Q, Sun C, Ye X, Wen Z. Effects of porous support microstructure enabled by the carbon microsphere pore former on the performance of proton-conducting reversible solid oxide cells. Int J Hydrogen Energy 2018;43:20050–8. https://doi.org/10.1016/j.ijhydene.2018.09.011.

[235] Braun RJ, Dubois A, Ferguson K, Duan C, Karakaya C, Kee RJ, et al. Development of kW-Scale Protonic Ceramic Fuel Cells and Systems. ECS Trans 2019;91:997–1008. https://doi.org/10.1149/09101.0997ecst.

[236] Babilo P, Haile SM. Enhanced Sintering of Yttrium-Doped Barium Zirconate by Addition of ZnO. J Am Ceram Soc 2005;88:2362–8. https://doi.org/10.1111/j.1551-

2916.2005.00449.x.

[237] Morejudo SH, Zanón R, Escolástico S, Yuste-Tirados I, Malerød-Fjeld H, Vestre PK, et al. Direct conversion of methane to aromatics in a catalytic co-ionic membrane reactor. Science (80-) 2016;353:563 LP – 566. https://doi.org/10.1126/science.aag0274.

[238] Li J, Wang C, Wang X, Bi L. Sintering aids for proton-conducting oxides – A double-edged sword? A mini review. Electrochem Commun 2020;112:106672. https://doi.org/10.1016/j.elecom.2020.106672.

[239] Ricote S, Bonanos N, Manerbino A, Sullivan NP, Coors WG. Effects of the fabrication process on the grain-boundary resistance in BaZr0.9Y0.1O3-δ. J Mater Chem A 2014;2:16107–15. https://doi.org/10.1039/c4ta02848a.

[240] Clark D, Tong J, Morrissey A, Almansoori A, Reimanis I, O'Hayre R. Anomalous low-temperature proton conductivity enhancement in a novel protonic nanocomposite. Phys Chem Chem Phys 2014;16:5076–80. https://doi.org/10.1039/c4cp00468j.

[241] Costa R, Grünbaum N, Berger M-H, Dessemond L, Thorel A. On the use of NiO as sintering additive for BaCe0,9Y0,1O3−α. Solid State Ionics 2009;180:891–5. https://doi.org/10.1016/j.ssi.2009.02.018.

[242] Han D, Goto K, Majima M, Uda T. Proton Conductive BaZr0.8-xCexY0.2O3-δ: Influence of NiO Sintering Additive on Crystal Structure, Hydration Behavior, and Conduction Properties. ChemSusChem 2021;14:614–23. https://doi.org/10.1002/cssc.202002369.

[243] Han D, Uemura S, Hiraiwa C, Majima M, Uda T. Detrimental Effect of Sintering Additives on Conducting Ceramics: Yttrium-Doped Barium Zirconate. ChemSusChem

2018;11:4102–13. https://doi.org/10.1002/cssc.201801837.

[244] Braun RJ, Dubois A, Ferguson K, Duan C, Karakaya C, Kee RJ, et al. Development of kW-Scale Protonic Ceramic Fuel Cells and Systems. ECS Trans 2019;91:997–1008. https://doi.org/10.1149/09101.0997ecst.

[245] Chiara A, Giannici F, Pipitone C, Longo A, Aliotta C, Gambino M, et al. Solid-Solid Interfaces in Protonic Ceramic Devices: A Critical Review. ACS Appl Mater Interfaces 2020;12:55537–53. https://doi.org/10.1021/acsami.0c13092.

[247] Liu Y, Compson C, Liu M. Nanostructured and functionally graded cathodes for intermediate temperature solid oxide fuel cells. J Power Sources 2004;138:194–8. https://doi.org/10.1016/j.jpowsour.2004.06.035.

[248] Kumar V, Kaur M, Kaur G, Arya SK, Pickrell G. Stacking designs and sealing principles for IT-solid oxide fuel cell. INC; 2019. https://doi.org/10.1016/B978-0-12-817445-6.00011-9.

[249] Song Y, Liu J, Wang Y, Guan D, Seong A, Liang M, et al. Nanocomposites: A New Opportunity for Developing Highly Active and Durable Bifunctional Air Electrodes for Reversible Protonic Ceramic Cells. Adv Energy Mater 2021;2101899:1–9. https://doi.org/10.1002/aenm.202101899.

[250] Yan A, Cheng M, Dong Y, Yang W, Maragou V, Song S, et al. Investigation of a Ba0.5Sr0.5Co0.8Fe0.2O3- δ based cathode IT-SOFC. I. The effect of CO2 on the cell performance. Appl Catal B Environ 2006;66:64–71. https://doi.org/10.1016/j.apcatb.2006.02.021.

[251] Dubois A, Ricote S, Braun RJ. Benchmarking the expected stack manufacturing cost of next generation, intermediate-temperature protonic ceramic fuel cells with solid oxide fuel cell technology. J Power Sources 2017;369:65–77. https://doi.org/10.1016/j.jpowsour.2017.09.024.

[252] Dubois A, Ricote S, Braun RJ. Comparing the Expected Stack Cost of Next Generation Intermediate Temperature Protonic Ceramic Fuel Cells with Solid Oxide Fuel Cell Technology. ECS Trans 2017;78:1963–72. https://doi.org/10.1149/07801.1963ecst.

[253] Fehringer G, Janes S, Wildersohn M, Clasen R. Proton—conducting ceramics as electrode/electrolyte—materials for SOFCs: Preparation, mechanical and thermal-mechanical properties of thermal sprayed coatings, material combination and stacks. J Eur Ceram Soc 2004;24:705–15. https://doi.org/10.1016/S0955-2219(03)00262-0.

[254] Matzke T, Cappadonia M. Proton conductive perovskite solid solutions with enhanced mechanical stability. Solid State Ionics 1996;86–88:659–63. https://doi.org/10.1016/0167-2738(96)00231-7.

[255] de Vries KJ. Electrical and mechanical properties of proton conducting SrCe0.95Yb0.05O3 − α. Solid State Ionics 1997;100:193–200. https://doi.org/10.1016/S0167-2738(97)00350-0.

[256] Mu S, Hong Y, Huang H, Ishii A, Lei J, Song Y, et al. A novel laser 3D printing method for the advanced manufacturing of protonic ceramics. Membranes (Basel) 2020;10:1–17. https://doi.org/10.3390/membranes10050098.

[257] Tarutin A, Danilov N, Lyagaeva J, Medvedev D. One-step fabrication of protonic ceramic fuel cells using a convenient tape calendering method. Appl Sci 2020;10.

https://doi.org/10.3390/app10072481.

[258] Mercadelli E, Gondolini A, Montaleone D, Pinasco P, Sanson A. Innovative strategy for designing proton conducting ceramic tapes and multilayers for energy applications. J Eur Ceram Soc 2021;41:488–96. https://doi.org/10.1016/j.jeurceramsoc.2020.09.016.

[259] Chen D, Shao Z. Surface exchange and bulk diffusion properties of Ba0.5Sr 0.5Co0.8Fe0.2O3-δ mixed conductor. Int J Hydrogen Energy 2011;36:6948–56. https://doi.org/10.1016/j.ijhydene.2011.02.087.

[260] Chen Y, Hong T, Wang P, Brinkman K, Tong J, Cheng J. Investigate the proton uptake process of proton/oxygen ion/hole triple conductor BaCo0.4Fe0.4Zr0.1Y0.1O3-Δ by electrical conductivity relaxation. J Power Sources 2019;440:227122. https://doi.org/10.1016/j.jpowsour.2019.227122.

[261] Song S, Zhou J, Su X, Wang Y, Li J, Zhang L, et al. Operando X-ray spectroscopic tracking of self-reconstruction for anchored nanoparticles as high-performance electrocatalysts towards oxygen evolution. Energy Environ Sci 2018;11:2945–53. https://doi.org/10.1039/c8ee00773j.

[262] Hall JL. Cell components. Phytochemistry 1987;26:1235–6. https://doi.org/10.1016/s0031-9422(00)82398-5.

[263] Xu Q, Guo Z, Xia L, He Q, Li Z, Temitope I, et al. A comprehensive review of solid oxide fuel cells operating on various promising alternative fuels. Energy Convers Manag 2022;253:115175. https://doi.org/10.1016/j.enconman.2021.115175.

[264] Liu T, Zhao Y, Zhang X, Zhang H, Jiang G, Zhao W, et al. Robust redox-reversible

perovskite type steam electrolyser electrode decorated with: In situ exsolved metallic nanoparticles. J Mater Chem A 2020;8:582–91. https://doi.org/10.1039/c9ta06309a.

[265] Porras-Vazquez JM, Slater PR. Synthesis of oxyanion-doped barium strontium cobalt ferrites: Stabilization of the cubic perovskite and enhancement in conductivity. J Power Sources 2012;209:180–3. https://doi.org/10.1016/j.jpowsour.2012.02.105.

[266] Zeng Q, Zhang X, Wang W, Zhang D, Jiang Y, Zhou X, et al. A Zn-doped Ba0.5Sr0.5Co0.8Fe0.2o3-δ perovskite cathode with enhanced ORR catalytic activity for SOFCs. Catalysts 2020;10:1–12. https://doi.org/10.3390/catal10020235.

[267] Huang Y, Ding J, Xia Y, Miao L, Li K, Zhang Q, et al. Ba0.5Sr0.5Co0.8-xFe0.2NbxO3-δ (x≤0.1) as cathode materials for intermediate temperature solid oxide fuel cells with an electron-blocking interlayer. Ceram Int 2020;46:10215–23. https://doi.org/10.1016/j.ceramint.2020.01.013.

[268] Duan C, Hook D, Chen Y, Tong J, O’Hayre R. Zr and Y co-doped perovskite as a stable, high performance cathode for solid oxide fuel cells operating below 500°C. Energy Environ Sci 2017;10:176–82. https://doi.org/10.1039/c6ee01915c.

[269] Sun YR, Zhang X, Wang LG, Liu ZK, Kang N, Zhou N, et al. Lattice contraction tailoring in perovskite oxides towards improvement of oxygen electrode catalytic activity. Chem Eng J 2021;421:129698. https://doi.org/10.1016/j.cej.2021.129698.

[270] Shao Z, Yang W, Cong Y, Dong H, Tong J, Xiong G. Investigation of the permeation behavior and stability of a Ba0.5Sr0.5Co0.8Fe0.2O(3-δ) oxygen membrane. J Memb Sci 2000;172:177–88. https://doi.org/10.1016/S0376-7388(00)00337-9.

[271] Shao Z, Haile SM. A high-performance cathode for the next generation of solid-oxide fuel cells. Mater. Sustain. Energy, vol. 3, Co-Published with Macmillan Publishers Ltd, UK; 2010, p. 255–8. https://doi.org/10.1142/9789814317665_0036.

[272] Kim J, Choi S, Jun A, Jeong HY, Shin J, Kim G. Chemically stable perovskites as cathode materials for solid oxide fuel cells: La-Doped Ba0.5Sr0.5Co0.8Fe 0.2O3-δ. ChemSusChem 2014;7:1669–75. https://doi.org/10.1002/cssc.201301401.

[273] Wei B, Lü Z, Huang X, Li S, Ai G, Liu Z, et al. Electrochemical characteristics of Ba0.5Sr0.5Co0.8Fe0.2O3-δ-Sm0.2Ce0.8O1.9 composite materials for low-temperature solid oxide fuel cell cathodes. Mater Lett 2006;60:3642–6. https://doi.org/10.1016/j.matlet.2006.03.075.

[274] Li S, Lü Z, Wei B, Huang X, Miao J, Liu Z, et al. Performances of Ba0.5Sr0.5Co0.6Fe0.4O3-δ-Ce0.8Sm0.2O1.9 composite cathode materials for IT-SOFC. J Alloys Compd 2008;448:116–21. https://doi.org/10.1016/j.jallcom.2006.10.032.

[275] Kao WX, Lee MC, Lin TN, Wang CH, Chang YC. Fabrication and characterization of a Ba0.5Sr0.5Co0.8Fe0.2O3- δ-Gadolinia-doped ceria cathode for an anode-supported solid-oxide fuel cell. J Power Sources 2010;195:2220–3. https://doi.org/10.1016/j.jpowsour.2009.10.057.

[276] Li L, Yang H, Gao Z, Zhang Y, Dong F, Yang G, et al. Nickel-substituted Ba0.5Sr0.5Co0.8Fe0.2O3-δ: a highly active perovskite oxygen electrode for reduced-temperature solid oxide fuel cells. J Mater Chem A 2019;7:12343–9. https://doi.org/10.1039/c9ta02548k.

[277] Xu X, Su C, Shao Z. Fundamental Understanding and Application of Ba 0.5 Sr 0.5 Co 0.8

Fe 0.2 O 3−δ Perovskite in Energy Storage and Conversion: Past, Present, and Future . Energy & Fuels 2021;35:13585–609. https://doi.org/10.1021/acs.energyfuels.1c02111.

[278] Su C, Wang W, Shao Z. Cation-De fi cient Perovskites for Clean Energy Conversion 2021. https://doi.org/10.1021/accountsmr.1c00036.

[279] Escudero-Escribano M, Malacrida P, Hansen HM, Vej-Hansen U, Velazquez-Palenzuela A, Tripkovic V, et al. Dering That Can Enable the Engineering of Material Properties Through Spontaneous Ordering of Nanoparticles. Science (80-) 2016;352:73–6.

[280] Cai J, Song Y, Zang Y, Niu S, Wu Y, Xie Y, et al. N-induced lattice contraction generally boosts the hydrogen evolution catalysis of P-rich metal phosphides. Sci Adv 2020;6:1–9. https://doi.org/10.1126/sciadv.aaw8113.

[281] Liu J, Li Q, Sun L, Huo L, Zhao H, Jean-marc B. Tuning the high temperature properties of PrSrCoO 4 cathode with Cu 2 þ dopant for intermediate temperature solid oxide fuel cells 2020;159:486–93. https://doi.org/10.1016/j.renene.2020.06.032.

[282] Aguadero A, Alonso JA, Escudero MJ, Daza L. Evaluation of the La2Ni1−xCuxO4+δ system as SOFC cathode material with 8YSZ and LSGM as electrolytes. Solid State Ionics 2008;179:393–400. https://doi.org/https://doi.org/10.1016/j.ssi.2008.01.099.

[283] Nomura T, Nishimoto S, Kameshima Y, Miyake M. Electrode properties of doped Pr_2NiO_4-based oxide cathode for intermediate-temperature SOFCs. J Ceram Soc Japan 2012;120:534–8. https://doi.org/10.2109/jcersj2.120.534.

[284] Xie J, Ju Y-W, Matsuka M, Ida S, Ishihara T. Synergy effects of Pr1.91Ni0.71Cu0.24Ga0.05O4 and Ba0.5La0.5CoO3 composite on cathodic activity for

intermediate temperature solid oxide fuel cells. J Power Sources 2013;228:229–36. https://doi.org/https://doi.org/10.1016/j.jpowsour.2012.11.089.

[285] Fu YP, Subardi A, Hsieh MY, Chang WK. Electrochemical Properties of La0.5Sr0.5Co0.8M0.2O3-δ (M=Mn, Fe, Ni, Cu) Perovskite Cathodes for IT-SOFCs. J Am Ceram Soc 2016;99:1345–52. https://doi.org/10.1111/jace.14127.

[286] Wan Yusoff WNA, Somalu MR, Baharuddin NA, Muchtar A, Wei LJ. Enhanced performance of lithiated cathode materials of LiCo0.6X0.4O2 (X = Mn, Sr, Zn) for proton-conducting solid oxide fuel cell applications. Int J Energy Res 2020;44:11783–93. https://doi.org/10.1002/er.5819.

[287] Park J, Zou J, Yoon H, Kim G, Chung JS. Electrochemical behavior of Ba0.5Sr0.5Co 0.2-xZnxFe0.8O3-δ (x = 0-0.2) perovskite oxides for the cathode of solid oxide fuel cells. Int J Hydrogen Energy 2011;36:6184–93. https://doi.org/10.1016/j.ijhydene.2011.01.142.

[288] Li K, Xue D. Estimation of electronegativity values of elements in different valence states. J Phys Chem A 2006;110:11332–7. https://doi.org/10.1021/jp062886k.

[289] Slater JC. Atomic radii in crystals. J Chem Phys 1964;41:3199–204. https://doi.org/10.1063/1.1725697.

[290] Gagné OC, Hawthorne FC. Empirical Lewis acid strengths for 135 cations bonded to oxygen. Acta Crystallogr Sect B Struct Sci Cryst Eng Mater 2017;73:956–61. https://doi.org/10.1107/S2052520617010988.

[291] Liu D, Dou Y, Xia T, Li Q, Sun L, Huo L, et al. B-site La, Ce, and Pr-doped Ba0.5Sr0.5Co0.7Fe0.3O3-δ perovskite cathodes for intermediate-temperature solid oxide

fuel cells: Effectively promoted oxygen reduction activity and operating stability. J Power Sources 2021;494:229778. https://doi.org/10.1016/j.jpowsour.2021.229778.

[292] Wang X, Dou Y, Xie Y, Wang J, Xia T, Huo L, et al. A-Site Cation-Ordering Layered Perovskite EuBa0.5Sr0.5Co2-xFexO5+δas Highly Active and Durable Electrocatalysts for Oxygen Evolution Reaction. ACS Omega 2020;5:12501–15. https://doi.org/10.1021/acsomega.0c01383.

[293] Jin F, Liu X, Chu X, Shen Y, Li J. Effect of nonequivalent substitution of Pr3+/4+ with Ca2+ in PrBaCoFeO5+δ as cathodes for IT-SOFC. J Mater Sci 2021;56:1147–61. https://doi.org/10.1007/s10853-020-05375-y.

[294] Gao L, Zhu M, Li Q, Sun L, Zhao H, Grenier J-C. Electrode properties of Cu-doped Bi0.5Sr0.5FeO3−δcobalt-free perovskite as cathode for intermediate-temperature solid oxide fuel cells. J Alloys Compd 2017;700:29–36. https://doi.org/10.1016/j.jallcom.2017.01.026.

[295] Shen Y, Zhao H, Świerczek K, Du Z, Xie Z. Lattice structure, sintering behavior and electrochemical performance of La1.7Ca0.3Ni1−xCuxO4+Δ as cathode material for intermediate-temperature solid oxide fuel cell. J Power Sources 2013;240:759–65. https://doi.org/10.1016/j.jpowsour.2013.05.025.

[296] Zhang W, Zhang L, Guan K, Zhang X, Meng JJ, Wang H, et al. Effective promotion of oxygen reduction activity by rare earth doping in simple perovskite cathodes for intermediate-temperature solid oxide fuel cells. J Power Sources 2020;446:227360. https://doi.org/10.1016/j.jpowsour.2019.227360.

[297] Xu X, Wang H, Fronzi M, Wang X, Bi L, Traversa E. Tailoring cations in a perovskite

cathode for proton-conducting solid oxide fuel cells with high performance. J Mater Chem A 2019;7:20624–32. https://doi.org/10.1039/c9ta05300j.

[298] Sun L-P, Li H, Li Q, Huo L-H, Zhao H, Bassat J-M, et al. Evaluation of La2-xNiMnO6-Δ as cathode for intermediate temperature solid oxide fuel cells. J Power Sources 2018;392:8–14. https://doi.org/10.1016/j.jpowsour.2018.04.083.

[299] Gao L, Zhu M, Li Q, Sun L, Zhao H, Grenier JC. Electrode properties of Cu-doped Bi0.5Sr0.5FeO3−δcobalt-free perovskite as cathode for intermediate-temperature solid oxide fuel cells. J Alloys Compd 2017;700:29–36. https://doi.org/10.1016/j.jallcom.2017.01.026.

[300] Wang M, Jiang L, Kim EJ, Hahn SH. Electronic structure and optical properties of Zn(OH)2: LDA+U calculations and intense yellow luminescence. RSC Adv 2015;5:87496–503. https://doi.org/10.1039/c5ra17024a.

[301] Brown ID, Skowron A. Electronegativity and Lewis Acid Strength. J Am Chem Soc 1990;112:3401–3. https://doi.org/10.1021/ja00165a023.

[302] Yáng Z, Harvey AS, Infortuna A, Schoonman J, Gauckler LJ. Electrical conductivity and defect chemistry of Ba xSr 1-xCo yFe 1-yO 3-deltaperovskites. J Solid State Electrochem 2011;15:277–84. https://doi.org/10.1007/s10008-010-1208-4.

[303] Adler SB. Limitations of charge-transfer models for mixed-conducting oxygen electrodes. Solid State Ionics 2000;135:603–12. https://doi.org/10.1016/S0167-2738(00)00423-9.

[304] Strasser P, Koh S, Anniyev T, Greeley J, More K, Yu C, et al. core – shell fuel cell catalysts 2010;2:454–60. https://doi.org/10.1038/nchem.623.

[305] Nilsson A, Pettersson LGM, Hammer B, Bligaard T, Christensen CH, Nørskov JK. The electronic structure effect in heterogeneous catalysis 2005;100:111–4. https://doi.org/10.1007/s10562-004-3434-9.

[307] Almar L, Störmer H, Meffert M, Szász J, Wankmüller F, Gerthsen D, et al. Improved Phase Stability and CO2 Poisoning Robustness of Y-Doped Ba0.5Sr0.5Co0.8Fe0.2O3-δ SOFC Cathodes at Intermediate Temperatures. ACS Appl Energy Mater 2018;1:1316–27. https://doi.org/10.1021/acsaem.8b00028.

[308] Fabbri E, Bi L, Pergolesi D, Traversa E. High-performance composite cathodes with tailored mixed conductivity for intermediate temperature solid oxide fuel cells using proton conducting electrolytes. Energy Environ Sci 2011;4:4984–93. https://doi.org/10.1039/c1ee02361f.

[309] Serra JM, Vert VB. Compositional IMPROVEMENT of Ln0.435Ba0.145Sr 0.4Fe0.8Co0.2O3-δ IT-SOFC cathodes performance by multiple lanthanide substitution. J Electrochem Soc 2010;157. https://doi.org/10.1149/1.3465646.

[310] Wang J, Saccoccio M, Chen D, Gao Y, Chen C, Ciucci F. The effect of A-site and B-site substitution on BaFeO 3 À d : An investigation as a cathode material for intermediate-temperature solid oxide fuel cells. J Power Sources 2015;297:511–8. https://doi.org/10.1016/j.jpowsour.2015.08.016.

[311] Wan TH, Saccoccio M, Chen C, Ciucci F. Influence of the Discretization Methods on the Distribution of Relaxation Times Deconvolution: Implementing Radial Basis Functions with DRTtools. Electrochim Acta 2015;184:483–99. https://doi.org/10.1016/j.electacta.2015.09.097.

[312] Plekhanov SS, Kuzmin A V., Tropin ES, Korolev DA, Ananyev M V. New mixed ionic and electronic conductors based on LaScO3: Protonic ceramic fuel cells electrodes. J Power Sources 2020;449:227476. https://doi.org/10.1016/j.jpowsour.2019.227476.

[313] Sumi H, Ohshiro T, Nakayama M, Suzuki T, Fujishiro Y. Prevention of Reaction between (Ba,Sr)(Co,Fe)O3 Cathodes and Yttria-stabilized Zirconica Electrolytes for Intermediate-temperature Solid Oxide Fuel Cells. Electrochim Acta 2015;184:403–9. https://doi.org/10.1016/j.electacta.2015.10.092.

[314] Hashim SS, Liang F, Zhou W, Sunarso J. Cobalt-Free Perovskite Cathodes for Solid Oxide Fuel Cells. ChemElectroChem 2019;6:3549–69. https://doi.org/10.1002/celc.201900391.

[315] Chen Y, Yoo S, Choi Y, Kim JH, Ding Y, Pei K, et al. A highly active, CO2-tolerant electrode for the oxygen reduction reaction† 2018:2458–66. https://doi.org/10.1039/c8ee01140k.

[316] Liu M, Ding D, Bai Y, He T, Liu M. An Efficient SOFC Based on Samaria-Doped Ceria (SDC) Electrolyte. J Electrochem Soc 2012;159:B661–5. https://doi.org/10.1149/2.032206jes.

[317] Weber V, Meffert M, Wagner S, Störmer H, Unger LS, Ivers-Tiffée E, et al. Influence of B-site doping with Ti and Nb on microstructure and phase constitution of (Ba0.5Sr0.5)(Co0.8Fe0.2)O3−δ. J Mater Sci 2020;55:947–66. https://doi.org/10.1007/s10853-019-04102-6.

[318] Li S, Tu H, Li F, Anwar MT, Yu L. Investigation of Nd2Ni0.9M0.1O4+δ (M = Ni, Co, Cu, Fe, and Mn) cathodes for intermediate-temperature solid oxide fuel cell. J Alloys

Compd 2017;694:17–23. https://doi.org/10.1016/j.jallcom.2016.09.250.

[319] Xu C, Zhen S, Ren R, Chen H, Song W, Wang Z, et al. Cu-Doped Sr2Fe1.5Mo0.5O6−δ as a highly active cathode for solid oxide electrolytic cells 2019:8009–12. https://doi.org/10.1039/c9cc03455b.

[320] Zhang Z, Zhu Y, Zhong Y, Zhou W, Shao Z. Anion Doping: A New Strategy for Developing High-Performance Perovskite-Type Cathode Materials of Solid Oxide Fuel Cells. Adv Energy Mater 2017;7. https://doi.org/10.1002/aenm.201700242.

[321] Zhi M, Zhou G, Hong Z, Wang J, Gemmen R, et al. Single crystalline $La_{0.5}Sr_{0.5}MnO_3$ microcubes as cathode of solid oxidefuel cell**.** Energy & Environmental Science 2011:139–44. https://doi.org/10.1039/c0ee00300j.

[322] Al-Yousef YM, Ghouse M. Synthesis of Ba0.5Sr0.5Co0.2Fe0.8O3 (BSCF) Nanoceramic Cathode Powders by Sol-Gel Process for Solid Oxide Fuel Cell (SOFC) Application. World J Nano Sci Eng 2011;01:99–107. https://doi.org/10.4236/wjnse.2011.14016.

[323] Zhou W, Ran R, Shao Z, Zhuang W, Jia J, Gu H, et al. Barium- and strontium-enriched (Ba0.5Sr0.5)1+xCo0.8Fe0.2O3-δ oxides as high-performance cathodes for intermediate-temperature solid-oxide fuel cells. Acta Mater 2008;56:2687–98. https://doi.org/10.1016/j.actamat.2008.02.002.

[324] Li Z, Wei B, Lü Z, Zhang Y, Chen K, Miao J, et al. Evaluation of (Ba 0.5Sr 0.5) 0.85Gd 0.15Co 0.8Fe 0.2O 3-δ cathode for intermediate temperature solid oxide fuel cell. Ceram Int 2012;38:3039–46. https://doi.org/10.1016/j.ceramint.2011.12.001.

[325] Khan N, Kalair A, Abas N, Haider A. Review of ocean tidal, wave and thermal energy

technologies. Renew Sustain Energy Rev 2017;72:590–604. https://doi.org/https://doi.org/10.1016/j.rser.2017.01.079.

[326] Revankar ST, Majumdar P. Fuel Cells : Principles, Design, and Analysis 2016. https://doi.org/10.1201/B15965.

[327] Han D, Otani Y, Noda Y, Onishi T, Majima M, Uda T. Strategy to improve phase compatibility between proton conductive BaZr0.8Y0.2O3-δ and nickel oxide. RSC Adv 2016;6:19288–97. https://doi.org/10.1039/c5ra26947d.

[328] Iwahara H, Yajima T, Hibino T, Ozaki K, Suzuki H. Protonic conduction in calcium, strontium and barium zirconates. Solid State Ionics 1993;61:65–9. https://doi.org/10.1016/0167-2738(93)90335-Z.

[329] Han D, Kato K, Uda T. La2(Nb1-: XYx)2O7- δ: scovery of a novel fluorite structure-based ionic conductor. Chem Commun 2017;53:12684–7. https://doi.org/10.1039/c7cc07609f.

[330] Catlow CRA. Defect Processes and Migration Mechanisms in Solid State Ionics. Solid State Ionics 1992;12:219–31. https://doi.org/10.1016/b978-0-444-89354-3.50033-7.

[331] Merkle R, Hoedl MF, Raimondi G, Zohourian R, Maier J. Oxides with Mixed Protonic and Electronic Conductivity. Annu Rev Mater Res 2021;51:461–93. https://doi.org/10.1146/annurev-matsci-091819-010219.

[332] Tong H, Fu M, Yang Y, Chen F, Tao Z. A Novel Self-Assembled Cobalt-Free Perovskite Composite Cathode with Triple-Conduction for Intermediate Proton-Conducting Solid Oxide Fuel Cells. Adv Funct Mater 2022;32:2209695.

https://doi.org/10.1002/adfm.202209695.

[333] Hyuk J, Hong J, Lim D, Ahn S, Kim J, Kyu J. Water as Hole-Predatory Instrumental to Create Metal Nanoparticles on Triple-Conducting Oxides 2021.

[334] Song Y, Chen Y, Wang W, Zhou C, Zhong Y, Yang G, et al. Self-Assembled Triple-Conducting Nanocomposite as a Superior Protonic Ceramic Fuel Cell Cathode. Joule 2019;3:2842–53. https://doi.org/10.1016/j.joule.2019.07.004.

[335] Li W, Guan B, Yang T, Li Z, Shi W, Tian H, et al. Layer-structured triple-conducting electrocatalyst for water-splitting in protonic ceramic electrolysis cells: Conductivities vs. activity. J Power Sources 2021;495:229764. https://doi.org/10.1016/j.jpowsour.2021.229764.

[336] Zou D, Yi Y, Song Y, Guan D, Xu M, Ran R, et al. The BaCe 0.16 Y 0.04 Fe 0.8 O 3− δ nanocomposite: a new high-performance cobalt-free triple-conducting cathode for protonic ceramic fuel cells operating at reduced temperatures. J Mater Chem A 2022;10:5381–90. https://doi.org/10.1039/D1TA10652J.

[337] Song Y, Chen Y, Zhou W, Liu M, Song Y, Chen Y, et al. Self-Assembled Triple-Conducting Nanocomposite as a Superior Protonic Ceramic Fuel Cell Cathode Self-Assembled Triple-Conducting Nanocomposite as a Superior Protonic Ceramic Fuel Cell Cathode. Joule 2019;3:2842–53. https://doi.org/10.1016/j.joule.2019.07.004.

[338] Jiang Q, Cheng J, Wang R, Fan Y, Gao J. Novel triple-phase composite cathode materials for proton-conducting solid oxide fuel cells. J Power Sources 2012;206:47–52. https://doi.org/10.1016/j.jpowsour.2012.01.084.

[339] Seong A, Kim J, Jeong D, Sengodan S, Liu M, Choi S, et al. Electrokinetic Proton Transport in Triple (H+/O2−/e−) Conducting Oxides as a Key Descriptor for Highly Efficient Protonic Ceramic Fuel Cells. Adv Sci 2021;8:1–6. https://doi.org/10.1002/advs.202004099.

[340] Liu Z, Chen Y, Yang G, Yang M, Ji R, Song Y, et al. One-pot derived thermodynamically quasi-stable triple conducting nanocomposite as robust bifunctional air electrode for reversible protonic ceramic cells. Appl Catal B Environ 2022;319. https://doi.org/10.1016/J.APCATB.2022.121929.

[341] Xu D, Yan A, Xu S, Zhou Y, Yang S, Zhang R, et al. Self-Assembled Triple (H + / O 2 − / e −) Conducting Nanocomposite of Ba-Co-Ce-Y-O into an Electrolyte for Semiconductor Ionic Fuel Cells. Nanomaterials 2021;11:1–14. https://doi.org/10.3390/nano11092365.

[342] Bello IT, Yu N, Song Y, Wang J, Chan T, Zhao S, et al. Electrokinetic Insights into the Triple Ionic and Electronic Conductivity of a Novel Nanocomposite Functional Material for Protonic Ceramic Fuel Cells. Small 2022;18:2203207. https://doi.org/10.1002/smll.202203207.

[343] Shimada H, Yamaguchi Y, Sumi H, Mizutani Y. Performance Comparison of Perovskite Composite Cathodes with BaZr 0.1 Ce 0.7 Y 0.1 Yb 0.1 O 3– δ in Anode-Supported Protonic Ceramic Fuel Cells . J Electrochem Soc 2020;167:124506. https://doi.org/10.1149/1945-7111/abab26.

[344] Fabbri E, Bi L, Pergolesi D, Traversa E. High-performance composite cathodes with tailored mixed conductivity for intermediate temperature solid oxide fuel cells using

proton conducting electrolytes. Energy Environ Sci 2011;4:4984–93. https://doi.org/10.1039/c1ee02361f.

[345] Fabbri E, Licoccia S, Traversa E, Wachsman ED. Composite cathodes for proton conducting electrolytes. Fuel Cells 2009;9:128–38. https://doi.org/10.1002/fuce.200800126.

[346] Wei B, Lü Z, Huang X, Li S, Ai G, Liu Z, et al. Electrochemical characteristics of Ba0.5Sr0.5Co0.8Fe0.2O3-δ-Sm0.2Ce0.8O1.9 composite materials for low-temperature solid oxide fuel cell cathodes. Mater Lett 2006;60:3642–6. https://doi.org/10.1016/j.matlet.2006.03.075.

[347] Ni H, Yang Y, Tian Y, Wang X, Shen S, Zheng K, et al. Novel dual-phase symmetrical electrode materials for protonic ceramic fuel cells. J Mater Sci 2021;56:19651–62. https://doi.org/10.1007/s10853-021-06531-8.

[348] Kim JH, Jang K, Lim D-K, Ahn S, Oh D, Kim H, et al. Self-assembled nano-composite perovskites as highly efficient and robust hybrid cathodes for solid oxide fuel cells. J Mater Chem A 2022:23–5. https://doi.org/10.1039/d1ta08178k.

[349] Hu D, Kim J, Niu H, Daniels LM, Manning TD, Chen R, et al. High-performance protonic ceramic fuel cell cathode using protophilic mixed ion and electron conducting material. J Mater Chem A 2022;10:2559–66. https://doi.org/10.1039/d1ta07113k.

[350] Shin JF, Xu W, Zanella M, Dawson K, Savvin SN, Claridge JB, et al. Self-assembled dynamic perovskite composite cathodes for intermediate temperature solid oxide fuel cells. Nat Energy 2017;2. https://doi.org/10.1038/nenergy.2016.214.

[351] Zhao Z, Cui J, Zou M, Mu S, Huang H, Meng Y, et al. Novel twin-perovskite nanocomposite of Ba–Ce–Fe–Co–O as a promising triple conducting cathode material for protonic ceramic fuel cells. J Power Sources 2020;450:227609. https://doi.org/10.1016/j.jpowsour.2019.227609.

[352] Bello IT, Yu N, Zhai S, Song Y, Zhao S, Cheng C, et al. Effect of engineered lattice contraction and expansion on the performance and CO2 tolerance of Ba0.5Sr0.5Co0.7Fe0.3O3-δ functional material for intermediate temperature solid oxide fuel cells. Ceram Int 2022;48:21457–68. https://doi.org/10.1016/j.ceramint.2022.04.110.

[353] Bello IT, Yu N, Song Y, Wang J, Chan T-S, Zhao S, et al. Supporting Information Electrokinetic Insights into the Triple Ionic and Electronic Conductivity of a Novel Nanocomposite Functional Material for Protonic Ceramic Fuel Cells 2022. https://doi.org/10.1002/smll.202203207.

[354] Berger C, Bucher E, Merkle R, Nader C, Lammer J, Grogger W, et al. Influence of Y-substitution on phase composition and proton uptake of self-generated Ba(Ce,Fe)$O_{3-\delta}$ – Ba(Fe,Ce)$O_{3-\delta}$ composites. J Mater Chem A 2022;10:2474–82. https://doi.org/10.1039/D1TA07208K.

[355] Shannon RD. Revised effective ionic radii and systematic studies of interatomic distances in halides and chalcogenides. Acta Crystallogr Sect A 1976;32:751–67. https://doi.org/10.1107/S0567739476001551.

[356] LANGFORD JI, WILSON AJC. Scherrer after Sixty Years: A Survey and Some New Results in the Determination of Crystallite Size. J Appl Crystallogr 1978;11:102–13. https://doi.org/10.1107/S0021889878012844.

[357] Duan C, Hook D, Chen Y, Tong J, O’Hayre R. Zr and Y co-doped perovskite as a stable, high performance cathode for solid oxide fuel cells operating below 500°C. Energy Environ Sci 2017;10:176–82. https://doi.org/10.1039/c6ee01915c.

[358] Jiang L, Wei T, Zeng R, Zhang WX, Huang YH. Thermal and electrochemical properties of PrBa0.5Sr 0.5Co2-xFexO5+δ (x = 0.5, 1.0, 1.5) cathode materials for solid-oxide fuel cells. J Power Sources 2013;232:279–85. https://doi.org/10.1016/j.jpowsour.2013.01.064.

[359] Zohourian R, Merkle R, Maier J. Proton uptake into the protonic cathode material BaCo0.4Fe0.4Zr0.2O3-δ and comparison to protonic electrolyte materials. Solid State Ionics 2017;299:64–9. https://doi.org/10.1016/j.ssi.2016.09.012.

[360] Cheng S, Wang Y, Zhuang L, Xue J, Wei Y, Feldhoff A, et al. A Dual-Phase Ceramic Membrane with Extremely High H2Permeation Flux Prepared by Autoseparation of a Ceramic Precursor. Angew Chemie - Int Ed 2016;55:10895–8. https://doi.org/10.1002/anie.201604035.

[361] Chen S, Xie K, Dong D, Li H, Qin Q, Zhang Y, et al. A composite cathode based on scandium-doped chromate for direct high-temperature steam electrolysis in a symmetric solid oxide electrolyzer. J Power Sources 2015;274:718–29. https://doi.org/10.1016/j.jpowsour.2014.10.103.

[362] Song Y, Wang W, Ge L, Xu X, Zhang Z, Sérgio P, et al. Rational Design of a Water-Storable Hierarchical Architecture Decorated with Amorphous Barium Oxide and Nickel Nanoparticles as a Solid Oxide Fuel Cell Anode with Excellent Sulfur Tolerance 2017;1700337. https://doi.org/10.1002/advs.201700337.

[363] Cao J, Ji Y, Shao Z. Perovskites for protonic ceramic fuel cells: a review. Energy Environ

Sci 2022;15:2200–32. https://doi.org/10.1039/D2EE00132B.

[364] Hu X, Xie Y, Wan Y, Yang Y, Wu X, Xia C. Applied Catalysis B : Environmental Antimony-doped strontium cobalt oxide as promising cathode for low-temperature solid oxide fuel cell with excellent carbon dioxide tolerance. Appl Catal B Environ 2021;286:119901. https://doi.org/10.1016/j.apcatb.2021.119901.

[365] Crank J. THE MATHEMATICS OF DIFFUSION 1975.

[366] Westwater JW, Drickamer HG. The Mathematics of Diffusion. J Am Chem Soc 1957;79:1267–8. https://doi.org/10.1021/ja01562a072.

[367] Han D, Liu X, Bjørheim TS, Uda T. Yttrium-Doped Barium Zirconate-Cerate Solid Solution as Proton Conducting Electrolyte: Why Higher Cerium Concentration Leads to Better Performance for Fuel Cells and Electrolysis Cells. Adv Energy Mater 2021;11:1–11. https://doi.org/10.1002/aenm.202003149.

[368] Maradesa A, Py B, Quattrocchi E, Ciucci F. The probabilistic deconvolution of the distribution of relaxation times with finite Gaussian processes. Electrochim Acta 2022;413:140119. https://doi.org/10.1016/j.electacta.2022.140119.

[369] Ciucci F, Chen C. Analysis of electrochemical impedance spectroscopy data using the distribution of relaxation times: A Bayesian and hierarchical Bayesian approach. Electrochim Acta 2015;167:439–54. https://doi.org/10.1016/j.electacta.2015.03.123.

[370] Chen YY, Choi YM, Yoo S, Ding Y, Yan R, Pei K, et al. A Highly Efficient Multi-phase Catalyst Dramatically Enhances the Rate of Oxygen Reduction. Joule 2018;2:938–49. https://doi.org/10.1016/j.joule.2018.02.008.

[371] Tong Y, Tong Y, Meng X, Luo T, Cui C, Cui C, et al. Protonic Ceramic Electrochemical Cell for Efficient Separation of Hydrogen. ACS Appl Mater Interfaces 2020;12:25809–17. https://doi.org/10.1021/acsami.0c04024.

[372] Zhang X, Robertson M, Deĉes-Petit C, Qu W, Kesler O, Maric R, et al. Internal shorting and fuel loss of a low temperature solid oxide fuel cell with SDC electrolyte. J Power Sources 2007;164:668–77. https://doi.org/10.1016/J.JPOWSOUR.2006.10.087.

[373] Zhang H, Zhao F, Chen F, Xia C. Nano-structured Sm0.5Sr0.5CoO3 - δ electrodes for intermediate-temperature SOFCs with zirconia electrolytes. Solid State Ionics 2011;192:591–4. https://doi.org/10.1016/j.ssi.2010.05.024.

[374] Gu H, Yang G, Hu Y, Liang M, Chen S, Ran R, et al. Enhancing the oxygen reduction activity of PrBaCo2O5+δ double perovskite cathode by tailoring the calcination temperatures. Int J Hydrogen Energy 2020;45:25996–6004. https://doi.org/10.1016/j.ijhydene.2019.12.171.

[375] Zhang L, Shan J, Wang Q. BaCo0.4Fe0.4Zr0.2O3-δ: Evaluation as a cathode for ceria-based electrolyte IT-SOFCs. J Alloys Compd 2019;771:221–7. https://doi.org/10.1016/j.jallcom.2018.08.232.

[376] Gu B, Sunarso J, Zhang Y, Song Y, Yang G, Zhou W, et al. A high performance composite cathode with enhanced CO2 resistance for low and intermediate-temperature solid oxide fuel cells. J Power Sources 2018;405:124–31. https://doi.org/10.1016/j.jpowsour.2018.10.025.

[377] Wang S, Feng Y, Wang D. Electrochemical comparison of cobalt-free La0.5Sr 0.5Fe0.9Mo0.1O3-δ based cathode materials for intermediate-temperature solid oxide fuel

cells. Ceram Int 2014;40:6359–63. https://doi.org/10.1016/j.ceramint.2013.10.133.

[378] Zhao L, Zhang X, He B, Liu B, Xia C. Micro-tubular solid oxide fuel cells with graded anodes fabricated with a phase inversion method. J Power Sources 2011;196:962–7. https://doi.org/10.1016/j.jpowsour.2010.08.074.

[379] Liu Y, Guo Y, Ran R, Shao Z. A novel approach for substantially improving the sinterability of BaZr0.4Ce0.4Y0.2O3-δ electrolyte for fuel cells by impregnating the green membrane with zinc nitrate as a sintering aid. J Memb Sci 2013;437:189–95. https://doi.org/10.1016/J.MEMSCI.2013.03.002.

[380] Zhu A, Zhang G, Wan T, Shi T, Wang H, Wu M, et al. Evaluation of SrSc0.175Nb0.025Co0.8O3-δ perovskite as a cathode for proton-conducting solid oxide fuel cells: The possibility of in situ creating protonic conductivity and electrochemical performance. Electrochim Acta 2018;259:559–65. https://doi.org/10.1016/j.electacta.2017.11.037.

[381] Zhu C, Liu X, Yi C, Yan D, Su W. Electrochemical performance of PrBaCo2O5+δ</inf> layered perovskite as an intermediate-temperature solid oxide fuel cell cathode. J Power Sources 2008;185:193–6. https://doi.org/10.1016/j.jpowsour.2008.06.075.

[382] Kim J, Sengodan S, Kwon G, Ding D, Shin J, Liu M, et al. Triple-Conducting Layered Perovskites as Cathode Materials for Proton-Conducting Solid Oxide Fuel Cells. CHEMSUSCHEM Commun 1864564x 2014:10. https://doi.org/10.1002/cssc.201402351.

[383] Shang M, Tong J, O’Hayre R. A promising cathode for intermediate temperature protonic ceramic fuel cells: BaCo0.4Fe0.4Zr0.2O3-δ. RSC Adv 2013;3:15769–75. https://doi.org/10.1039/c3ra41828f.

[384] Zhu Y, Zhou W, Ran R, Chen Y, Shao Z, Liu M. Promotion of Oxygen Reduction by Exsolved Silver Nanoparticles on a Perovskite Scaffold for Low-Temperature Solid Oxide Fuel Cells. Nano Lett 2016;16:512–8. https://doi.org/10.1021/acs.nanolett.5b04160.

[385] Fabbri E, Pergolesi D, Traversa E. Electrode materials: A challenge for the exploitation of protonic solid oxide fuel cells. Sci Technol Adv Mater 2010;11. https://doi.org/10.1088/1468-6996/11/4/044301.

[386] Su R, Lü Z, Chen K, Ai N, Li S, Wei B, et al. Novel in situ method (vacuum assisted electroless plating) modified porous cathode for solid oxide fuel cells. Electrochem Commun 2008;10:844–7. https://doi.org/10.1016/j.elecom.2008.03.011.

[387] Lin Y, Zhou W, Sunarso J, Ran R, Shao Z. Characterization and evaluation of BaCo 0.7Fe 0.2Nb 0.1O 3-δ as a cathode for proton-conducting solid oxide fuel cells. Int J Hydrogen Energy 2012;37:484–97. https://doi.org/10.1016/j.ijhydene.2011.09.010.

[388] Radovic M, Lara-Curzio E. Mechanical properties of tape cast nickel-based anode materials for solid oxide fuel cells before and after reduction in hydrogen. Acta Mater 2004;52:5747–56. https://doi.org/10.1016/j.actamat.2004.08.023.

[389] Jun A, Yoo S, Ju Y-W, Hyodo J, Choi S, Jeong HYY, et al. Correlation between fast oxygen kinetics and enhanced performance in Fe doped layered perovskite cathodes for solid oxide fuel cells. J Mater Chem A 2015;3:15082–90. https://doi.org/10.1039/c5ta02158h.

[390] Peng R, Wu T, Liu W, Liu X, Meng G. Cathode processes and materials for solid oxide fuel cells with proton conductors as electrolytes. J Mater Chem 2010;20:6218–25. https://doi.org/10.1039/c0jm00350f.

[391] Merkle R, Poetzsch D, Maier J. (Invited) Oxygen Reduction Reaction at Cathodes on Proton Conducting Oxide Electrolytes: Contribution from Three Phase Boundary Compared to Bulk Path. ECS Meet Abstr 2015;MA2015-01:1608–1608. https://doi.org/10.1149/ma2015-01/27/1608.

[392] Chen D, Zhang Q, Lu L, Periasamy V, Tade MO, Shao Z. Multi scale and physics models for intermediate and low temperatures H+-solid oxide fuel cells with H+/e-/O2- mixed conducting properties: Part A, generalized percolation theory for LSCF-SDC-BZCY 3-component cathodes. J Power Sources 2016;303:305–16. https://doi.org/10.1016/j.jpowsour.2015.10.090.

[393] Yang BL, Zuo C, Wang S, Cheng Z, Liu M. A Novel Composite Cathode for Low-Temperature SOFCs Based on Oxide Proton Conductors 2008:3280–3. https://doi.org/10.1002/adma.200702762.

[394] Song Y, Chen Y, Wang W, Zhou C, Zhong Y, Yang G, et al. Supplementary Self-Assembled Triple-Conducting Nanocomposite as a Superior Protonic Ceramic Fuel Cell Cathode. Joule 2019;3:2842–53. https://doi.org/10.1016/j.joule.2019.07.004.

[395] Shin JF, Xu W, Zanella M, Dawson K, Savvin SN, Claridge JB, et al. Self-assembled dynamic perovskite composite cathodes for intermediate temperature solid oxide fuel cells. Nat Energy 2017;2:1–29. https://doi.org/10.1038/nenergy.2016.214.

[396] Berger C, Bucher E, Merkle R, Nader C, Lammer J, Grogger W, et al. Influence of Y-substitution on phase composition and proton uptake of self-generated Ba(Ce,Fe)O 3− δ –Ba(Fe,Ce)O 3− δ composites . J Mater Chem A 2022;10:2474–82. https://doi.org/10.1039/d1ta07208k.

[397] Nikitin SS, Markov AA, Leonidov IA, Patrakeev M V. Impact of Cerium Content on Ion and Electron Transport in Sr$_{1-x}$Ce$_{x}$FeO$_{3-\delta}$. J Phys Chem C 2021;125:17546–55. https://doi.org/10.1021/acs.jpcc.1c05144.

[398] Pagnier T, Charrier-Cougoulic I, Ritter C, Lucazeau G. Neutron diffraction study of BaCexZr1-xO3. EPJ Appl Phys 2000;9:1–9. https://doi.org/10.1051/epjap:2000192.

[399] Gushee BE, Katz L, Ward R. The Preparation of a Barium Cobalt Oxide and other Phases with Similar Structures. J Am Chem Soc 1957;79:5601–3. https://doi.org/10.1021/ja01578a004.

[400] Zhou W, Ran R, Shao Z. Progress in understanding and development of Ba0.5Sr0.5Co0.8Fe0.2O3-δ-based cathodes for intermediate-temperature solid-oxide fuel cells: A review. J Power Sources 2009;192:231–46. https://doi.org/10.1016/j.jpowsour.2009.02.069.

[401] Song Y, Chen Y, Xu M, Wang W, Zhang Y, Yang G, et al. A Cobalt-Free Multi-Phase Nanocomposite as Near-Ideal Cathode of Intermediate-Temperature Solid Oxide Fuel Cells Developed by Smart Self-Assembly. Adv Mater 2020;32:1–9. https://doi.org/10.1002/adma.201906979.

[402] Song Y, Wang W, Ge L, Xu X, Zhang Z, Julião PSB, et al. Rational Design of a Water-Storable Hierarchical Architecture Decorated with Amorphous Barium Oxide and Nickel Nanoparticles as a Solid Oxide Fuel Cell Anode with Excellent Sulfur Tolerance. Adv Sci 2017;4. https://doi.org/10.1002/advs.201700337.

[403] Bello IT, Yu N, Zhai S, Song Y, Zhao S, Cheng C, et al. Effect of engineered lattice contraction and expansion on the performance and CO2 tolerance of

Ba0.5Sr0.5Co0.7Fe0.3O3-δ functional material for intermediate temperature solid oxide fuel cells. Ceram Int 2022;48:21457–68. https://doi.org/10.1016/j.ceramint.2022.04.110.

[404] Liang M, Zhu Y, Song Y, Guan D, Luo Z, Yang G, et al. A New Durable Surface Nanoparticles-Modified Perovskite Cathode for Protonic Ceramic Fuel Cells from Selective Cation Exsolution under Oxidizing Atmosphere. Adv Mater 2021;34:2106379. https://doi.org/10.1002/adma.202106379.

[405] Soni S, Dave M, Dalela B, Alvi PA, Kumar S, Sharma SS, et al. Effect of defects and oxygen vacancies on the RTFM properties of pure and Gd-doped CeO2 nanomaterials through soft XAS. Appl Phys A Mater Sci Process 2020;126:1–11. https://doi.org/10.1007/s00339-020-03777-y.

[406] Amezawa K. X-ray absorption spectroscopic studies on solid oxide fuel cells and proton-conducting ceramic fuel cells. Curr Opin Electrochem 2020;21:250–6. https://doi.org/10.1016/j.coelec.2020.03.017.

[407] Orikasa Y, Ina T, Nakao T, Mineshige A, Amezawa K, Oishi M, et al. X-ray absorption spectroscopic study on La0.6Sr 0.4CoO3-δ cathode materials related with oxygen vacancy formation. J Phys Chem C 2011;115:16433–8. https://doi.org/10.1021/jp2029642.

[408] Bu Y, Joo S, Zhang Y, Wang Y, Meng D, Ge X, et al. A highly efficient composite cathode for proton-conducting solid oxide fuel cells. J Power Sources 2020;451:227812. https://doi.org/10.1016/j.jpowsour.2020.227812.

[409] Rioja-Monllor L, Ricote S, Bernuy-Lopez C, Grande T, O'Hayre R, Einarsrud M-A. High-Performance La0.5Ba0.5Co1/3Mn1/3Fe1/3O3−δ-BaZr1−zYzO3−δ Cathode Composites via an Exsolution Mechanism for Protonic Ceramic Fuel Cells. Inorganics

2018;6:83. https://doi.org/10.3390/inorganics6030083.

[410] Shao Z, Haile SM. A high-performance cathode for the next generation of solid-oxide fuel cells. Nature 2004;431:170–3. https://doi.org/10.1038/nature02863.

[411] Song Y, Chen J, Yang M, Xu M, Liu D, Liang M, et al. Realizing Simultaneous Detrimental Reactions Suppression and Multiple Benefits Generation from Nickel Doping toward Improved Protonic Ceramic Fuel Cell Performance 2022. https://doi.org/10.1002/smll.202200450.

[412] Song Y, Chen Y, Wang W, Zhou C, Zhong Y, Yang G, et al. Self-Assembled Triple-Conducting Nanocomposite as a Superior Protonic Ceramic Fuel Cell Cathode. Joule 2019;3:2842–53. https://doi.org/10.1016/j.joule.2019.07.004.

[413] Azad AK, Setsoafia DDY, Ming LC, Petra I. Synthesis and Characterization of High Density and Low Temperature Sintered Proton Conductor BaCe0.5Zr0.35In0.1Zn0.05O3-δ. Adv Mater Res 2015;1098:104–9. https://doi.org/10.4028/www.scientific.net/AMR.1098.104.

[414] Hong T, Lu W, Ren K, Liu T. The two-fold diffusion process for proton uptake reaction in BCFZY e-/H+/O2- triple conductor measured by electrical conductivity relaxation. Ionics (Kiel) 2020;26:5293–7. https://doi.org/10.1007/s11581-020-03757-5.

[415] Zhang Z, Wang J, Chen Y, Tan S, Shao Z, Chen D. In situ formation of a 3D core-shell and triple-conducting oxygen reduction reaction electrode for proton-conducting SOFCs. J Power Sources 2018;385:76–83. https://doi.org/10.1016/j.jpowsour.2018.03.029.

[416] Richter J, Holtappels P, Graule T, Nakamura T, Gauckler LJ. Materials design for

perovskite SOFC cathodes. Monatshefte Fur Chemie 2009;140:985–99. https://doi.org/10.1007/s00706-009-0153-3.

[417] Poetzsch D, Merkle R, Maier J. Stoichiometry variation in materials with three mobile carriers-Thermodynamics and transport kinetics exemplifi ed for protons, oxygen vacancies, and holes. Adv Funct Mater 2015;25:1542–57. https://doi.org/10.1002/adfm.201402212.

[418] Li Z, Wei B, Lü Z, Zhu X, Huang X, Zhang Y, et al. Ba and Gd doping effect in (Ba xSr 1-x) 0.95Gd 0.05Co 0.8Fe 0.2O 3-δ (x=0.1-0.9) cathode on the phase structure and electrochemical performance. Fuel Cells 2012;12:633–41. https://doi.org/10.1002/fuce.201100156.

[419] Ren R, Wang Z, Xu C, Sun W, Rooney DW, Sun K. Tuning the defects of the triple conducting oxide 2019:18365–72. https://doi.org/10.1039/c9ta04335g.

[420] He F, Liang M, Wang W, Ran R, Yang G, Zhou W, et al. High-Performance Proton-Conducting Fuel Cell with B-Site-Deficient Perovskites for All Cell Components. Energy and Fuels 2020;34:11464–71. https://doi.org/10.1021/acs.energyfuels.0c02370.

[421] Bu Y, Joo S, Zhang Y, Wang Y, Meng D, Ge X, et al. A highly efficient composite cathode for proton-conducting solid oxide fuel cells. J Power Sources 2020;451:227812. https://doi.org/10.1016/j.jpowsour.2020.227812.

[422] Hou J, Qian J, Bi L, Gong Z, Peng R, Liu W. The effect of oxygen transfer mechanism on the cathode performance based on proton-conducting solid oxide fuel cells. J Mater Chem A 2015;3:2207–15. https://doi.org/10.1039/c4ta04397a.